The Theory and Practice of Resonance Raman Spectroscopy

by

Dan Oprescu

A thesis submitted for the degree of
Doctor of Philosophy
of the University of London

Department of Chemistry
University College London
Bloomsbury, Gower Street, London WC1

March 1996

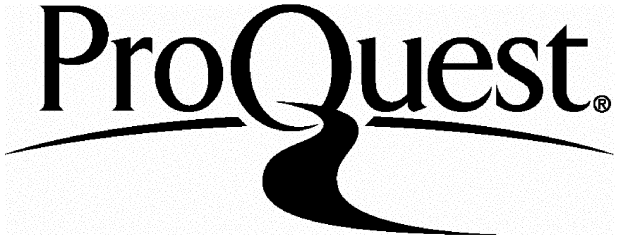

Abstract

The thesis proposes a new method of obtaining molecular structural data from resonance Raman spectroscopy; the experimental, theoretical and numerical aspects of the method are presented, and some of the results are included.

The first chapter describes Raman and resonance Raman scattering and introduces the instrumentation, methods and procedures used in obtaining Raman data. The sources of error in measuring band intensities and excitation profiles are analysed, and corrections to the errors are proposed. Some original experimental results are presented in Appendix 2 for the purpose of illustrating the technique and the sources of errors.

Chapter 2 describes an advanced theoretical model of secondary radiation, and its interpretation in terms of Raman and fluorescence radiation; in Chapter 3 the model is applied to relating resonance Raman data to molecular structure, by using the physical assumptions of the model and the corresponding mathematical approximations. The result is a set of equations relating microscopic parameters describing the molecular structure to the macroscopic quantities to be measured experimentally.

A new mathematical procedure for solving the equation set obtained at the end of Chapter 3 is proposed in Chapter 4; the numerical and computational implementation are described in this chapter and the computer programs used in practical applications are presented in appendices 4 and 5.

The results of applying the new method are presented in Chapter 5 in the form of tables containing the calculated parameters and of graphs comparing the experimental and the simulated excitation profiles; chemical systems belonging to three different geometries have been investigated.

Table of Contents

List of Tables

List of Figures

Acknowledgements

I would like to thank my parents, Elisabeta and Ion Oprescu, for their contribution to my early education, to my wife, Joan Geraldine Small, for her support during my research, and to my supervisor, Professor R.J.H. Clark, for offering me the opportunity to pursue the work leading to the present thesis.

It was a great privilege to have worked with Professor Andreas C. Albrecht, of Cornell University, during his stay in London in 1992 and subsequent visits. I am grateful to him for guiding me through the theory of resonance Raman spectroscopy, and particularly for introducing me to the transform theory.

At critical moments, my pursuit of academic accomplishment has drawn encouragement and strength from Rodica, Magda and Alexandru Oprescu, and from Professor Stelian Turbatu. I want also to thank a true friend and scientist, Dr Dan Ciomartan, for everything he gave me during our work together in University College London.

This thesis is dedicated to all those who have contributed to its conception.

I. Introduction to Resonance Raman Spectroscopy

Raman Scattering

The Raman effect was discovered in India in 1928 by C. V. Raman and, almost simultaneously, by G. Landsberg and L. Mandelstam in the Soviet Union. There was significant initial interest in the new discovery because its experimental observation happened at around the same time as its theoretical prediction [1,2], thus providing an early success for the young field of quantum physics.

The Raman effect gives rise to satellite lines, equidistant on each side of the exciting line in the spectrum of light scattered by a sample; as these satellite lines are produced by the interaction between light and the sample, they can provide a useful insight into the nature of the sample. The lines on the lower and higher energy side of the spectrum are called, respectively, "Stokes" and "anti-Stokes". The different positions of the satellite lines from that of the incident light means that the scattering undergone by the photons is inelastic; the intensity of the satellites is much lower than that of the incident beam, which means that the inelastic scattering has very low probability of occurring.

In fact, examining the interaction processes between light and matter, light can be transmitted, reflected or absorbed with much higher probability than it is scattered and most of the scattering takes place elastically; the transition probability for inelastic scattering of light is of the order of one in 10^8 photons. This low transition probability explains the complexity of the experiments designed to measure the intensity of Raman scattered light.

Inelastic scattering involves two different photons, one incident and one scattered; depending on the "collision" time and the degree of coherence between the two associated wave functions, two-photon processes have been

divided into Raman scattering and fluorescence. If the process can be considered instantaneous, in practice with a duration < 10^{-12} s, then it is called "Raman scattering"; otherwise, it is called "fluorescence". This aspect will be studied in detail in Chapter 2, where it will become obvious that the nomenclature is arbitrary, both processes being idealised parts of the same two-photon process.

The introduction will begin with the simplified picture in order to show the inadequacies of this nomenclature and to prepare the ground for the applications presented in the later chapters, which refer to the simultaneous part of the two-photon scattering. Figure 1.1 shows a basic diagram, based on quantum energy levels, of the infrared absorption (IR), Rayleigh (elastic) scattering, and Stokes and anti-Stokes Raman scattering processes, neglecting other processes such as visible and ultraviolet absorption, reflection, transmission or fluorescence. The diagram also ignores the relative intensities of the Stokes and anti-Stokes transitions, which depend on the relative thermal population of the starting levels (given by the Boltzmann statistical distribution).

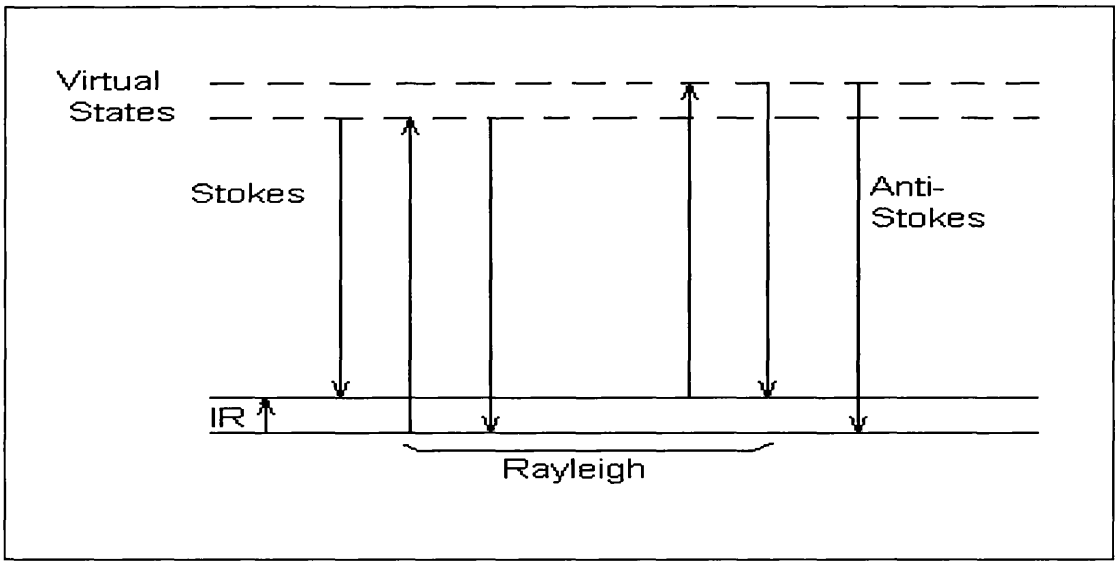

Figure 1.1 - Energy level diagram of vibrational scattering and absorption.

From Fig. 1.1 it can be seen that, after being excited to a virtual upper state by

an incident photon of energy $h\nu_0$, the system has the choice of relaxing back either to the initial level with the re-emission of a photon of the same energy $h\nu_0$ (Rayleigh scattering), or to another one, depending on the initial level, with the emission of a photon of a different energy: $h(\nu_0-\nu_1)$ (Stokes) or $h(\nu_0+\nu_1)$ (anti-Stokes). Here h represents Planck's constant, ν_0 the frequency of the incident photon, and $h\nu_1$ the energy difference between the two initial levels. In the case of infrared absorption and Raman (and resonance Raman) scattering, the initial levels correspond to the vibrational substates of the ground electronic state.

The Raman effect can be predicted by classical electrodynamics applied to polarisation and the argument has been transposed into quantum mechanical terms; the classical treatment starts with a beam of light of frequency ν_0 associated with a time-dependent electric field $\boldsymbol{E}$ of magnitude

$$E = E_0\cos(2\pi\nu_0 t), \tag{1.1}$$

where E_0 is the amplitude of the wave. When this field interacts with an isotropically polarisable medium, it induces a dipole moment

$$\boldsymbol{\mu} = \alpha\boldsymbol{E}, \tag{1.2}$$

where the polarizability depends on the n normal coordinates Q_k k=1,2,...,n as:

$$\alpha = \alpha^{(0)} + \left(\frac{\partial\alpha}{\partial Q_k}\right)_{Q_k^{(0)}} Q_k + \ldots, \quad k=1,2,\ldots,n\ ; \tag{1.3}$$

here $\alpha^{(0)}$ is the polarizability in the equilibrium position, i.e. in the absence of molecular deformation. The normal coordinates depend on time

$$Q_k = Q_k^{(0)}\cos(2\pi\nu_k t),\ k=1,2,\ldots,n \tag{1.4}$$

and substituting it back into Eqn (1.2) yields the expression for magnitude of the induced dipole

$$\boldsymbol{\mu} = \alpha^{(0)}E_0\cos(2\pi\nu_0 t) + E_0\left(\frac{\partial\alpha}{\partial Q_k}\right)_{Q_k^{(0)}} Q_k^{(0)}[\cos 2\pi(\nu_0+\nu_k)t + \cos 2\pi(\nu_0-\nu_k)t] + \ldots\ . \tag{1.5}$$

The first term represents the Rayleigh scattering, with the same frequency as the incident field, while the next two terms represent the anti-Stokes and Stokes terms, respectively. Equation (1.2) assumes that the polarizability is isotropic, which is not always the case in practice; taking its anisotropy into account leads to the following relations for the induced moment:

$$\mu_x = \alpha_{xx}E_x + \alpha_{xy}E_y + \alpha_{xz}E_z \tag{1.6a}$$

$$\mu_y = \alpha_{yx}E_x + \alpha_{yy}E_y + \alpha_{yz}E_z \tag{1.6b}$$

$$\mu_z = \alpha_{zx}E_x + \alpha_{zy}E_y + \alpha_{zz}E_z \tag{1.6c}$$

or, in matrix form,

$$\begin{pmatrix} \mu_x \\ \mu_y \\ \mu_z \end{pmatrix} = \begin{pmatrix} \alpha_{xx} & \alpha_{xy} & \alpha_{xz} \\ \alpha_{yx} & \alpha_{yy} & \alpha_{yz} \\ \alpha_{zx} & \alpha_{zy} & \alpha_{zz} \end{pmatrix} \begin{pmatrix} E_x \\ E_y \\ E_z \end{pmatrix} \quad <=> \quad \boldsymbol{\mu} = \hat{\alpha}\boldsymbol{E}. \tag{1.7}$$

In an experiment conducted in an anisotropic medium the components of the polarizability intervene directly, while in an isotropic medium only average quantities can be measured. For such an isotropic medium, the intensity I of the scattered Raman radiation in terms of the wavenumber $\tilde{\nu}_0$[1] and the irradiance I_0 of the incident radiation are related by the formula

$$I_{fi_{\pi/2}} = \frac{\pi^2}{\varepsilon_0^2}(\tilde{\nu}_0 \pm \tilde{\nu}_{fi})^4 |\alpha_{fi}|^2 I_0 \ , \tag{1.8}$$

where $\pi/2$ refers to light collected along a direction perpendicular to that of the incident beam and '*f*' and '*i*' to the final and initial states (Fig. 1.1) of the scattering system, respectively; α_{fi} is the polarizability associated with the inelastic scattering process and ε_0 is the permittivity of free space.

An important factor in determining the number of bands in a Raman spectrum

[1]- The wavenumber is linearly connected to the frequency ν by $\tilde{\nu}=\nu/v$, where v is the velocity of light in that medium.

is the selection rules imposed by the symmetry of the wave functions involved in a transition. These rules arise from the requirement that the transition probability per unit of time, given by Fermi's Golden Rule, be different from zero

$$W_{fi} = \frac{2\pi}{h}|\langle\psi_f|\hat{H}_T|\psi_i\rangle|^2 \neq 0 \quad <=> \quad \int_\tau \psi_i(\tau)\hat{H}_T\psi_f(\tau)d\tau \neq 0 \ , \tag{1.9}$$

where ψ_i and ψ_f are the wave functions of the initial and final states of the transition, $\hat{H}_T$ is the Hamiltonian operator of the transition, τ is the cartesian time-space continuum and *h* is Planck's constant. The integral is different from zero only when the integrand is non-zero, that is when the group theoretical product in the integrand contains a totally symmetric representation; the product of the three symmetries involved (initial state, final state and transition operator) has to be totally symmetric. This condition will remain in force under resonance Raman conditions as well, as it is valid for *any* transition between two states *i* and *f*; the transform method developed in chapter three will take it into account by concerning itself only with totally symmetric modes of vibration and symmetry-preserving transitions.

Resonance Raman Scattering

Raman scattering brings significant information about the structure of the *ground* electronic state, through vibrational data complementary to that obtained from infrared absorption spectroscopy. A subtle difference in the nature of the intermediate states (Fig. 1.1) produces very different data, characteristic of the *excited* electronic state and complementary to data obtained from visible and ultraviolet absorption spectroscopy. The effect occurring when the intermediate states are *real* instead of *virtual* is called resonance Raman scattering and gives rise to strongly enhanced bands at the same positions as regular Raman bands (ν_1, ν_2, ν_3, etc), and also as *overtones* - bands occurring at regular intervals throughout the spectrum ($2\nu_1$, $3\nu_1$, etc) - and as *combinations* (e.g. $\nu_2 + \nu_1$, $\nu_2 + 2\nu_1$, etc). Overtone and combination bands can be detected on both the Stokes and the anti-Stokes side of the Rayleigh line, with the same thermal

distribution as the Raman bands.

Resonance Raman spectra can be predicted by the time-dependent perturbative methods and a derivation of the transition probability will be given here in order to illustrate this approach and expose its shortcomings. The evolution of the wave function with respect to the time, *t*, is given by the time-dependent Schrödinger equation [3-5]

$$\hat{H}\psi = i\hbar\frac{\partial\psi}{\partial t} \ , \tag{1.10}$$

where it is assumed that the time-dependent Hamiltonian can be written as a sum between a stationary part $\hat{H}_0$ and a small time-dependent perturbation V

$$\hat{H} = \hat{H}_0 + \lambda V \ , \tag{1.11}$$

with λ denoting the perturbation parameter. It is also assumed that the unperturbed wave functions $\psi_n^{(0)}$ satisfy the Schrödinger equations

$$\hat{H}_0\psi_n^{(0)} = i\hbar\frac{\partial\psi_n^{(0)}}{\partial t} \ , \quad n = 1,2,3,... \tag{1.12}$$

and represent a product between a stationary part and a time-dependent exponential part

$$\psi_n^{(0)} = \psi_n e^{-itE_n/\hbar} \ , \tag{1.13}$$

where ψ_n (n = 1,2,3,...) are the eigenfunctions and E_n the eigenvalues of the time-independent equations

$$\hat{H}_0\psi_n = E_n\psi_n \ , \quad n = 1,2,3,... \ . \tag{1.14}$$

The wave function of the system, ψ, can be expanded in terms of the unperturbed basis set

$$\psi = \sum_n C_n(t)\psi_n^{(0)} \tag{1.15}$$

and substituting it into Eqn (1.10) gives [3-5]:

$$i\hbar\frac{\partial C_n}{\partial t} = \lambda\sum_m C_m\langle\psi_n^{(0)}|V|\psi_m^{(0)}\rangle \ . \qquad (1.16)$$

The coefficients C_n are set according to the usual practice of perturbation theory [4,5]:

$$C_n = C_n^{(0)} + \lambda C_n^{(1)} + \lambda^2 C_n^{(2)} + \ldots \qquad (1.18)$$

and substituting them into Eqn (1.16) gives, for the first three orders,

$$\frac{dC_n^{(0)}}{dt} = 0 \ , \qquad (1.18a)$$

$$i\hbar\frac{dC_n^{(1)}}{dt} = \sum_m C_m^{(0)}\langle\psi_n^{(0)}|V|\psi_m^{(0)}\rangle \ , \qquad (1.18b)$$

and

$$i\hbar\frac{dC_n^{(2)}}{dt} = \sum_m C_m^{(1)}\langle\psi_n^{(0)}|V|\psi_m^{(0)}\rangle \ . \qquad (1.18c)$$

Equations (1.18a-c) can be solved successively, assuming a time-independent perturbation V and the initial state i ; thus Eqn (1.18a) yields

$$C_i = 1, \quad C_m = 0 \ . \qquad (1.19a)$$

Substituting the above results into Eqn (1.18b) makes all but one term vanish

$$i\hbar\frac{dC_n^{(1)}}{dt} = \langle\psi_n^{(0)}|V|\psi_i^{(0)}\rangle$$

and yields the first order coefficient as

$$C_n^{(1)} = \frac{V_{ni}}{\hbar\omega_{ni}}[1-\exp(i t\omega_{ni})] \ . \qquad (1.19b)$$

Now substituting $C_n^{(1)}$ in Eqn (1.18c) yields the second order coefficient as

$$C_n^{(2)} = \sum_m \frac{V_{nm}V_{mi}}{\hbar\omega_{mi}}\left[\frac{1-\exp(it\omega_{nm})}{\hbar\omega_{nm}} - \frac{1-\exp(it\omega_{ni})}{\hbar\omega_{ni}}\right] . \qquad (1.19c)$$

In using Eqn (1.19c) for obtaining the transition probability, it is assumed that only the second term of the right-hand side, containing the initial state, makes a contribution in the long time limit. Hence

$$|C_n^{(2)}|^2 = \frac{2-2\cos(\omega_{ni}t)}{(\hbar\omega_{ni})^2}\left|\sum_m \frac{V_{nm}V_{mi}}{\hbar\omega_{mi}}\right|^2 \tag{1.20}$$

and by using the long-time limit for Dirac's function

$$\delta(\omega_{ni}) = \frac{1}{\pi}\lim_{t\to\infty}\left[\frac{1}{t}\frac{1-\cos(\omega_{ni}t)}{\omega_{ni}^2}\right] \tag{1.21}$$

the probability per unit time for a $n \leftarrow i$ second order transition is

$$W_{n\leftarrow i}^{(2)} = \frac{d}{dt}|C_n^{(2)}|^2 = \frac{2\pi}{\hbar^2}\left|\sum_m \frac{V_{nm}V_{mi}}{\hbar\omega_{mi}}\right|^2 \delta(\omega_{ni}) \ . \tag{1.22}$$

Similarly, the absorption probability per unit time is

$$W_{n\leftarrow i}^{(1)} = \frac{d}{dt}|C_n^{(1)}|^2 = \frac{2\pi}{\hbar^2}|V_{ni}|^2\delta(\omega_{ni}) \ . \tag{1.23}$$

In the quantum treatment of radiation [6,7] the electromagnetic field is considered to be an ensemble of non-interacting harmonic oscillator modes, with n_k photons in the k-th mode; each photon has the energy $\hbar\omega_k$, the polarisation $\hat{\mathbf{e}}_k$, and the propagation vector $\pm\mathbf{k}_k$, of magnitude

$$|\mathbf{k}_k| = \omega_k/c \tag{1.24}$$

(where c is the velocity of light) and perpendicular to the polarisation vector:

$$\hat{\mathbf{e}}_k \cdot \mathbf{k}_k = 0 \ . \tag{1.25}$$

This description of the radiation field, which neglects nuclear polarisation, leads to the following expression for the second-order transition probability (e_0 and m_0 being the electric charge and the mass of the electron):

$$W_{f\leftarrow i}^{(2)} = \frac{8\pi^3 e_0^4}{\hbar^2 m_0^4}\sum_l\sum_{l'}\frac{n_l n_{l'}}{\omega_l\omega_{l'}}\delta(\omega_{fi}-\omega_l+\omega_{l'}) \times\left|\sum_m\left[\frac{(\hat{\mathbf{e}}_{l'}\cdot\boldsymbol{P}_{fm})(\hat{\mathbf{e}}_l\cdot\boldsymbol{P}_{mi})}{\omega_{mi}-\omega_l}+\frac{(\hat{\mathbf{e}}_l\cdot\boldsymbol{P}_{fm})(\hat{\mathbf{e}}_{l'}\cdot\boldsymbol{P}_{mi})}{\omega_{mi}+\omega_{l'}}\right]\right|^2 \ . \tag{1.26a}$$

By using the relationship between the total linear momentum of the electrons

$\boldsymbol{P}$ and the total dipole transition moment $\boldsymbol{\mu}$, $\boldsymbol{P}_{fi}=(im_0\omega_{fi}/e_0)\boldsymbol{\mu}_{fi}$, and restricting the scope of Eqn (1.26a) to Raman scattering excited by a single-mode, monochromatic laser beam, the transition probability per unit time and unit volume becomes

$$W^{(2)}_{f\leftarrow i} = \frac{8\pi^3 e_0^4}{3\hbar^2 m_0^4}|\boldsymbol{\mu}_{fi}|^2\left|\sum_m\left(\frac{<f|m><m|i>}{\omega_{mi}-\omega_{laser}}+\frac{<i|m><m|f>}{\omega_{mi}+\omega_{laser}}\right)\right|^2 . \qquad (1.26b)$$

In the equation above, the transition moment has been assumed constant and the medium isotropic, such that $|\hat{e}_l\cdot\boldsymbol{\mu}_{fi}|^2=(|\boldsymbol{\mu}_{fi}|^2)/3$; ω_{laser} represents the circular frequency of the incident laser light beam.

Equation (1.26b) is very similar to the Kramers-Heisenberg dispersion formula [6]; a damping constant can be added on a "phenomenological" basis, and in the fast modulation limit it is insensitive to the different mechanisms for coherence loss encountered in experiments. It is, however, a good illustration for the idea of resonance; when $\omega_{laser}\rightarrow\omega_{mi}$ the denominator of the first term becomes infinitely small, the ratio becomes infinitely large, and that term dominates the sum, leading to a very intense band in the Raman spectrum.

Experimental Techniques for Resonance Raman Spectroscopy

As mentioned earlier in this chapter the Raman effect is weak, requiring special detection systems to separate Raman-scattered light from other effects, mainly Rayleigh scattering. In fact, Raman spectroscopy appears as a low signal-to-noise, high intensity range technique; the experimental setup consists of the following subsystems: a light source (usually a laser), a sampling subsystem, the optical analyzer (a monochromator and its collection optics), a detector, an electronic subsystem, and a computer which collects, processes and displays the data. Figure 1.2 shows the block diagram of such a spectroscopic system; the details of each subsystem will be discussed in the following paragraphs and are not included in the block diagram.

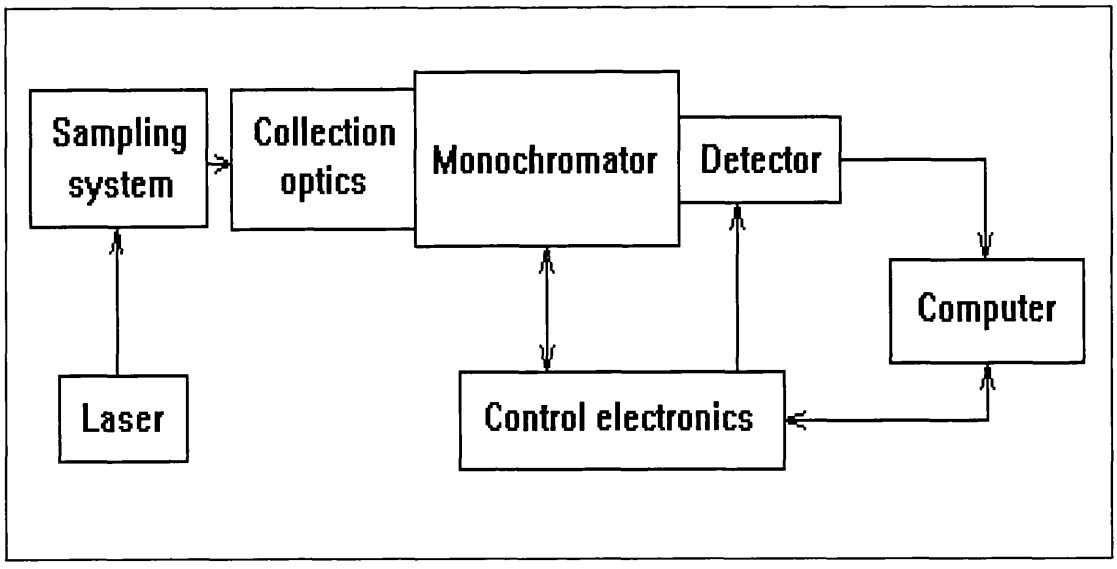

Figure 1.2 - Block diagram of a Raman spectroscopic system.

Lasers

The introduction of the laser as a light source for Raman spectroscopy is one of the factors credited with relaunching this technique in its use for collecting vibrational data, long dominated by infrared absorption spectroscopy, and it was based on the characteristic features of the laser radiation: monochromaticity, coherence and high intensity.

As the intensity of the scattered radiation is directly proportional to that of the incident beam (Eqn (1.8)) and the transition probability of the Raman effect is very low, a more intense incident beam is the most obvious way to boost the intensity of the signal to be collected. Even the low-power He-Ne laser, producing less than 10 mW output at 632.8 nm, was a significant improvement over high-pressure mercury lamps because it could be focused better and because all that low power was emitted in a very narrow spectral region; in fact, for conventional and resonance Raman spectroscopy the spectral bandwidth of gas lasers is considered infinitely narrow and the radiation they emit is considered to be monochromatic.

The introduction of other noble gases as lasing media, the most common of which are argon and krypton in the Ar^+, Kr^+ and mixed $Ar^+ + Kr^+$ ion lasers, has increased greatly the amount of power available; the lasers employed in the collection of data used in Chapter 5 can deliver routinely 100 mW of power and up to 10 W for certain experiments. The significantly increased output power is coupled with the availability of over 20 different output wavelengths between the two gases (as compared with only one for He-Ne), spanning the whole visible spectrum (406 - 799 nm).

The choice of exciting lines offered by the Ar^+ and Kr^+ lasers provided the first opportunity to investigate the frequency dependence of Raman scattering intensity, leading to Raman excitation profiles (REPs); resonance Raman spectra could be obtained as well, when the frequency of the incident beam matches the gap between the ground state and an upper electronic band (Eqn (1.25)). For full tunability, allowing the investigation of resonance Raman spectra with structured absorption bands (e.g. $KMnO_4$ [8], K_2MnO_4 [9], $[WS_4]^{2-}$ [10]), dye lasers pumped by high power Ar^+ or Kr^+ lasers can be used.

Another advantage of using the output of Ar^+ and Kr^+ lasers, especially the green and blue lines (530 - 458 nm), is the intensity gain produced by the proportionality of the intensity of the scattered radiation to the fourth power of the frequency (Eqn (1.8)). Increasing the frequency of the incident light by about 30 % (by using 488.0 nm excitation instead of 632.8 nm) leads to an almost three-fold increase in the intensity of the scattered light, in otherwise similar conditions.

However, when a higher incident frequency coincides with an absorption band of the sample, several effects which are normally neglected start to influence the intensity and sometimes the spectral composition of the scattered radiation; these effects will be dealt with in the next section, dedicated to sampling techniques and the interaction between the sample and the incoming laser radiation.

Samples and their interaction with the incident radiation

Sampling arrangements have the role of holding the sample in the optimal position for exposure to the laser beam and collection of the scattered radiation, while providing a controlled environment during the experiment. The most common requirement is low temperature for solid state samples, although sometimes the requirement is a very high pressure (> 1 MPa) for the study of minerals and other solid samples, or variable pressure for the study of gases.

As mentioned in the previous section there are several competing effects generated by irradiating a sample of material with high intensity laser light; the resonance Raman effect, while providing valuable information about the geometry of a molecule in a resonant electronic state, can obscure other vibrational features of the spectrum through the strong enhancement of the fundamental and overtone bands of only one mode. When the obtaining of conventional Raman data is the goal of the experiment, resonance can be avoided by choosing an exciting frequency away from the absorption bands of the sample; a higher frequency would take advantage of the $\tilde{\nu}^4$ factor and decrease the self-absorption, but if a higher frequency is not available or leads to increased absorption, a lower frequency would need to be chosen.

Relaxed and resonance fluorescence are effects which compete with the resonance Raman effect in relaxing the system from its excited state by dissipating some or all of the extra energy absorbed with the incident photon. They provide mechanisms for radiative energy dissipation that do not preserve the phase coherence with the incident field, leading to a high level of scattering radiation which arises from neither conventional nor resonance Raman effects and hence obscures the vibrational information. A common solution to this problem is to excite the Raman scattering with photons of a lower frequency than the energy gap between the ground and excited electronic states.

Self-absorption of the scattered radiation can reduce some of the gain obtained

by using higher incident frequencies, leading in extreme cases to thermal- or photo-decomposition of the sample; the Beer-Lambert law applies as for normal absorption

$$I = I_0 e^{-\mu x} \tag{1.27}$$

where I is the intensity of a light beam with the initial intensity I_0 after having passed through a layer of thickness x of material with the absorption coefficient μ. One possible solution to counter self-absorption is to decrease the thickness x by arranging the scattering geometry such that the scattered light travels as little as possible through the sample before exiting towards the collection optics [11,12]. Another solution is to decrease the intensity of the incident light I, decreasing both the absorbed intensity (Eqn (1.27)) and the intensity of the Raman scattered light (Eqn (1.8)); the signal-to-noise ratio of the Raman spectrum can then be improved by a longer integration time in the detection stage.

The most common sampling arrangement for liquids is a capillary tube, although the high intensity of the laser beam interacting with the sample can degrade the latter rapidly through photo- and thermal decomposition; the use of the rotating cell [13-16] and of the flow-through cell [17-19] solves this problem by providing a continuously fresh sample at the point of scattering.

A widely employed sampling condition is low temperature, which narrows the bandwidth and improves signal-to-noise and resolution, while at the same time protects the sample from thermal decomposition. Low-temperature sampling cells (cryostats) can be used for investigating various readily prepared samples, such as films, pellets and single crystals; these devices have been widely described in the literature and work by keeping the sample in thermal contact with liquid nitrogen, which is readily available, non-toxic, and has a very low boiling point - approximately 80 K.

More sophisticated cryostats may include temperature control through a heater

with variable output, and may replace liquid nitrogen with liquid helium in order to achieve temperatures in the range of 5 - 10 K. However complicated their design, all cryostats operating by keeping the sample in thermal contact with a cold liquid (at boiling point) are just sophisticated Dewar cells. A basic design for such a cryostat, essentially a Dewar recipient similar to the ones employed in our laboratory, is given in Fig. 1.3 for illustrative purposes.

The sample is positioned at the impact point, where only a very small volume is irradiated by the focused laser beam; the rest of the sample does not participate in the experiment and hence is not shown in Fig. 1.3.

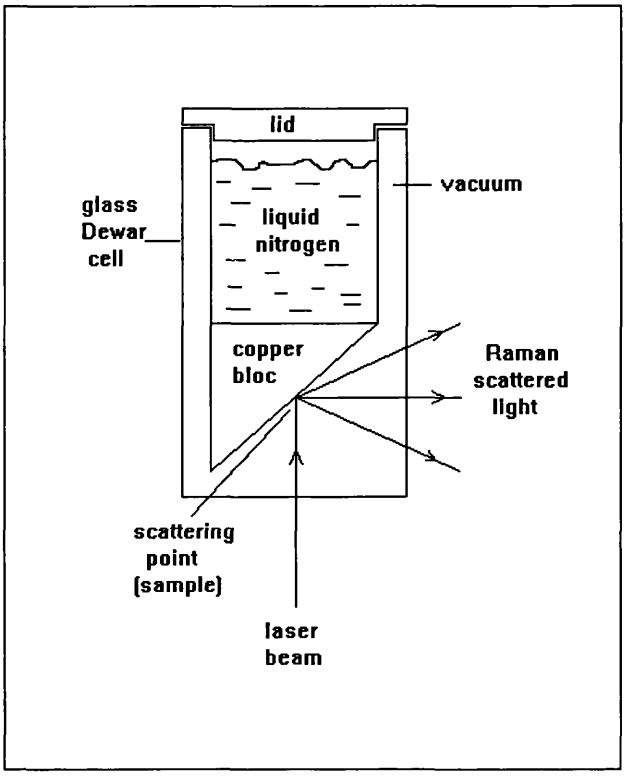

Figure 1.3 - Simple Dewar cryostat.

A different principle used in achieving low temperatures is that of adiabatic expansion of gases, used in the construction of domestic and laboratory refrigerators. Such a device (like the Air Products Displex) uses helium in a closed thermodynamic cycle and can achieve temperatures as low as 10 - 15 K; when fitted with a programable, variable output heater, closed-cycle helium refrigerators can be programmed to provide stable temperatures of between 10 and 350 K. Appendix 2 describes experiments that involve the preparation and spectroscopic analysis of a mixture of small, unstable sulphur clusters, isolated and trapped in a matrix of frozen argon obtained by using such a low-temperature sampling arrangement.

Collection of scattered light

After being scattered by the sample through various processes, light has to be spectrally analysed in order to separate the useful information from the very intense background; this requires a system that collects as much of the scattered light as possible without altering its spectral distribution, rejects very efficiently the background radiation (stray light and Rayleigh-scattered), and detects light at very low intensity levels.

The collection lens is usually a photographic camera lens, achromatic between 400 and 550 nm, and transmitting more than 70% of the incident light throughout the spectral range of interest for Raman scattering from chromophores (400 to 800 nm). Figure 1.4 shows the spectral transmittance curve for a typical such lens. The accurate positioning of the collection lens along the optical axis of the system is crucial, as more than 80% of the detected signal can be lost through a 5 μm misalignment of this very important optical element.

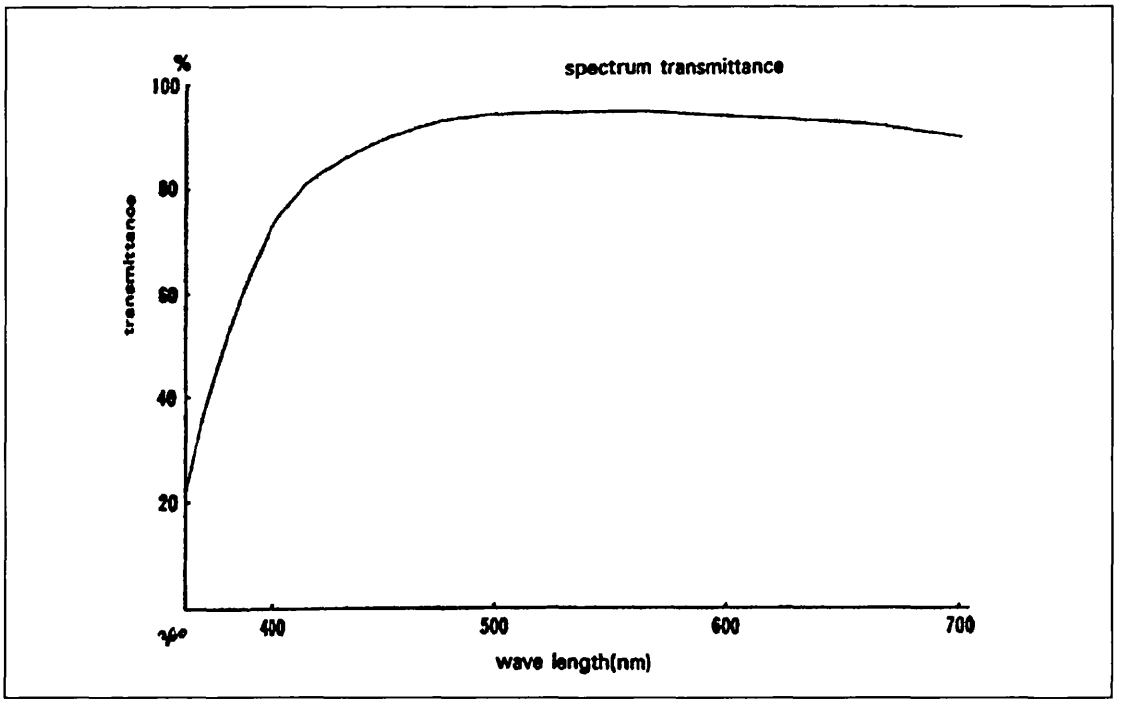

Figure 1.4 - Spectral transmittance of a typical photographic camera lens.

A particularly disturbing effect for resonance Raman scattering of high order overtones - leading to an overall Stokes shift of more than 1500 - 2000 cm^{-1} - is chromatic aberration; the lenses usually employed for light collection are corrected against this aberration only for blue and green light, between 400 and 550 nm. This aberration, affecting all lenses, produces differently sized focal "points" for different wavelengths, 1 and 2 in Fig. 1.5; if the collected light is focused onto the entrance aperture of the spectrometer, this aperture - usually a slit - will "cut" the focal disk to an extent dependant on the wavelength of the incident light, distorting the relative spectral distribution of the collected light.

This spectral distortion of the collected light before it is analysed propagates into a distortion of the band intensities in the measured spectrum; the study presented in Appendix 1 will show the extent of this aberration in a typical lens.

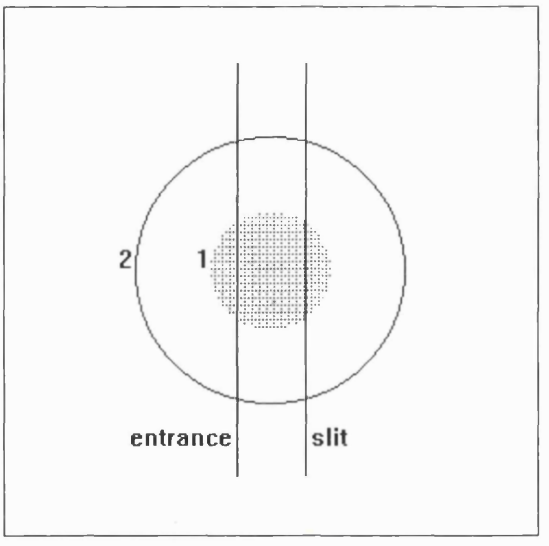

Figure 1.5 - The effect of chromatic aberration on the focusing of the collected light.

The chromatic aberration cannot be corrected satisfactorily throughout the whole spectral range, so its impact has to be minimised by minimising the spectral range to be analysed; thus, using more efficiently the information contained in the intensity of the first two or first four harmonics becomes even more important. The chromatic aberration can be eliminated completely by replacing the collection optics based on lenses by mirror-based optics but this experimental solution is very costly; by contrast, the transform method (to be discussed in Chapter 3) aims to provide an inexpensive tool, accessible to most laboratories.

Analysis of the scattered light

Typical single-channel Raman and resonance Raman spectrometers used are double monochromators, with the Czerny-Turner design shown in Fig. 1.6; a motorised precision mechanism positions the coordinated diffraction gratings G1 and G2 at a particular angle, allowing only light of a particular wavelength to pass through the entrance slit S_1, the middle slit S_2 and the exit slit S_3, and hit the detector.

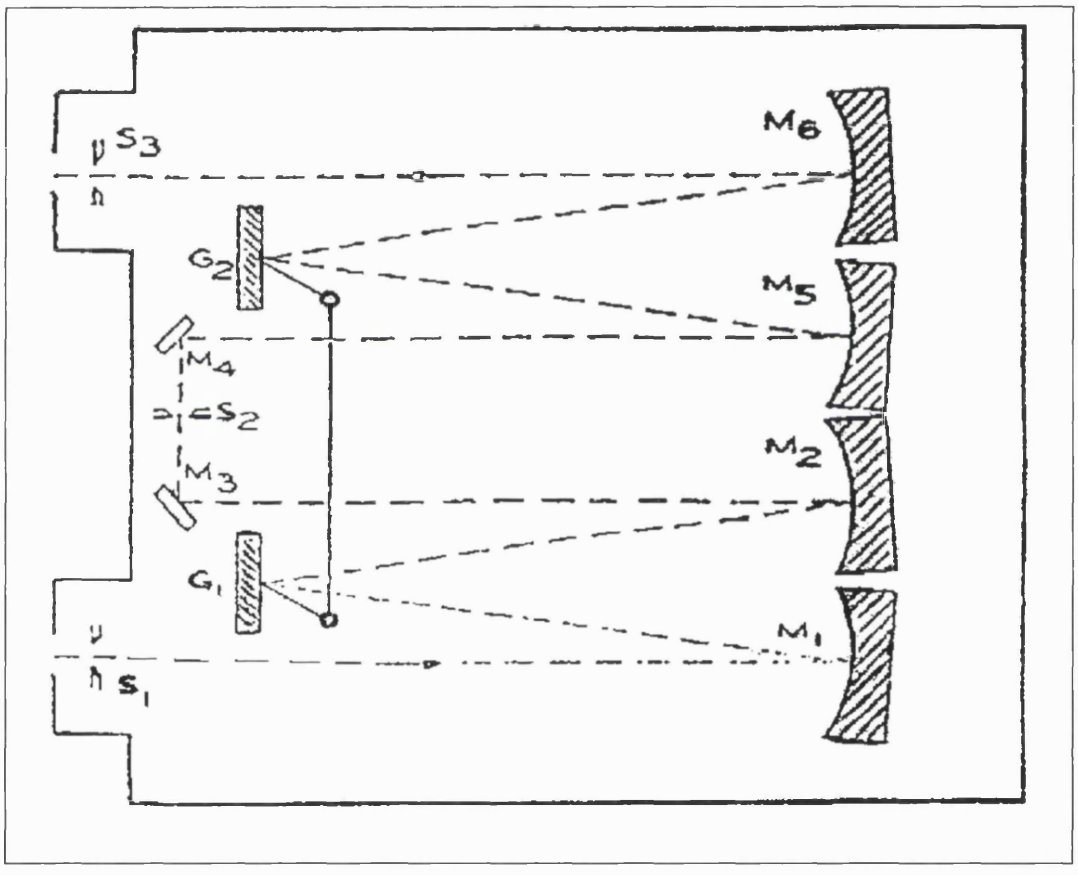

Figure 1.6 - Schematic diagram of a Czerny-Turner double monochromator.

The detector has a high sensitivity to light of low intensity, over a wide spectral range; typically, thermoelectrically-cooled photomultiplier tubes are used for single channel detection, while thermoelectrically-cooled photodiode arrays and charge-coupled detectors have become common for multichannel detection.

The photomultiplier tube is based on the photoelectric effect and on secondary electronic emission and transforms photon energy into the energy of electric pulses with an efficiency of around 15 %; pulses are collected at the anode and the signal is collected and processed by associated electronic circuitry which also provides stable high-voltage power for the cathode of the photomultiplier tubes. After being collected pulses are amplified, filtered against thermal and radioactive noise, formatted to a standard 5 V voltage and counted; modern counters are embedded in personal computers that process the resulting count into a spectrum, while controlling the mechanical parts of the monochromator as well. The computer software controlling modern spectrometers, most of which are fitted with multichannel detectors, also corrects the spectra collected for the spectral response of the instrument; the following section will be dedicated to the subject of spectral response.

Appendix 2 illustrates most of the experimental techniques described in this section through a series of spectroscopic experiments performed as a research project separate from the main body of the present work. This present work owes a number of ideas and a good amount of impetus to that project and other preliminary work.

Spectral response of the spectroscopic system

Light travelling between the laser and the detector interacts with many different systems including the sample, each with its own response to the incident radiation; the purpose of spectroscopy is to separate the response of the sample from the response of all other systems. The monochromator and the detector are the only two systems with a significant influence on the measured spectrum apart from the sample itself; the monochromator is *designed* to discriminate between different wavelengths and the detector will have a frequency-dependent efficiency from the quantum nature of the detection process.

It is usually assumed that the response of basic optical components (mirrors, lenses, prisms) is constant throughout near-infrared, visible and near ultraviolet; the spectral response of the collection optics, monochromator and detector is determined by replacing the sample and the laser source (Fig.1.2) with a standard calibration lamp with known spectral emissivity, calibrated by the National Physical Laboratory.

The calculation of the spectral response of an instrument starts with the assumption that the response of that system is linear in intensity and therefore responds to an oscillatory input of intensity

$$I_{input}(\omega) = I_{input_0} e^{it\omega} \tag{1.28a}$$

in a linear manner [20], producing an output of intensity

$$I_{output}(\omega) = I_{output_0} e^{it\omega} \tag{1.28b}$$

related to the input through the response function of the system, R, in the following relationship

$$I_{output}(\omega) = \frac{1}{\sqrt{2\pi}} \int_{-\infty}^{\infty} R(\omega - x)\, I_{input}(x)\, dx. \tag{1.29}$$

Recognising that Eqn (1.29) represents a convolution of the input intensity function, Eqn (1.29) can be written in a compact form as

$$I_{output} = I_{input} * R \tag{1.30}$$

or as a relationship between the corresponding inverse Fourier transforms

$$I^{-1}_{output}(x) = R^{-1}(x)\, I^{-1}_{input}(x) \ . \tag{1.31}$$

Writing the previous equation for the Raman scattered radiation R and for the standard source S gives

$$I^{-1}_{output_R}(x) = R^{-1}(x)\, I^{-1}_{input_R}(x) \tag{1.32a}$$

$$I^{-1}_{output_S}(x) = R^{-1}(x)\, I^{-1}_{input_S}(x) \tag{1.32b}$$

and the response of the system can be calculated from Eqn (1.32b) by performing the inverse Fourier transforms

$$R^{-1}(x) = \frac{I^{-1}_{output_S}}{I^{-1}_{input_S}} = \frac{\int_{-\infty}^{\infty} I_{output_S}(\nu)\, e^{-i\nu x} d\nu}{\int_{-\infty}^{\infty} I_{input_S}(\nu)\, e^{-i\nu x} d\nu} \tag{1.33}$$

and so the real input of the system can be calculated as a function of the known response of the system and of the measured output

$$I_{input_R}(\nu) = \frac{1}{\sqrt{2\pi}} \int_{-\infty}^{\infty} \frac{\int_{-\infty}^{\infty} I_{output_R}(\nu) e^{-i\nu x'} d\nu'}{R^{-1}(x)} e^{-i\nu x} dx \,. \tag{1.34}$$

The spectral response of the instrument is calculated in practice from the emissivity of the source and the measured spectrum of the lamp, by using fast Fourier algorithms in Eqn (1.34).

A method of estimating the result of the previous procedure would be very helpful for saving development and computer calculation time; by considering any spectral structure as a sum of an infinity of monochromatic lines of spectral width $d\nu'$, Eqn (1.29) can be written in its differential form

$$dI_{output}(\nu) = I_{input}(\nu)\, R(\nu - \nu')\, d\nu' . \tag{1.35}$$

The standard source S has a broad spectral emissivity function that can be taken to be Gaussian for illustrative purposes:

$$I_{input_S} = I^{(0)}_{input_S} \exp\left[-\frac{(\nu' - \nu_S)^2}{a_S^2} \right], \tag{1.36}$$

where ν_S is the maximum point and a_S = FWHH/$(2\sqrt{\ln 2})$ (where FWHH is the full-width at half-height of the Gaussian). The response of the instrument to monochromatic light of frequency ν' is taken to be also a Gaussian, centred on the frequency of the incident light

$$R(\nu) = R_{max} \exp\left[-\frac{\nu^2}{a_R^2} \right] \tag{1.37}$$

and with a_R defined in the same way as a_S.

Thus Eqn (1.35) becomes

$$dI_{output}(\nu) = I_{input}\exp\left[-\left(\frac{(\nu'-\nu_S)^2}{a_S^2}+\frac{(\nu-\nu')^2}{a_R^2}\right)\right]d\nu' \tag{1.38}$$

by taking into account that the maximum response can only be $R_{max} = 1$. After integration and rearranging the resulting expression, Eqn (1.38) becomes

$$I_{output_S}(\nu) = I^{(0)}_{input_S}\times const.\times\exp\left[-\frac{(\nu-\nu_S)^2}{a_S^2\left[1+\left(\frac{a_R}{a_S}\right)^2\right]}\right]. \tag{1.39}$$

As the Raman spectrometers are designed to have a narrow response function to incident monochromatic light, $a_R << a_S$ and Eqn (1.39) becomes

$$I_{output_S}(\nu) \approx I^{(0)}_{input_S}\times const.\times\exp\left[-\frac{(\nu-\nu_S)^2}{a_S^2}\right]. \tag{1.40}$$

Comparing Eqn (1.40) with Eqns (1.36) and (1.30) shows that, in Raman and resonance Raman practice, the convolution can be approximated with the multiplication of the input function by the response function *at every frequency point;* thus, the determination of the spectral response reduces to collecting the digital spectrum of a standard calibrated lamp and dividing each data point by the emissivity given in the calibration table of the lamp. Correcting a spectrum for the spectral response of the instrument consists then in dividing each data point in the spectrum by the value of the response function of the instrument.

The resulting spectral response curves of three typical spectrometers are shown in Fig. 1.7: two SPEX double monochromators operated in single-channel mode, fitted with 1800 mm^{-1} (for model R6) and 1200 mm^{-1} (for model 1401) holographic gratings and RCA GaAs photomultiplier tubes (type C-31034), and a DILOR triple monochromator operated in multichannel mode, fitted with three 1800 mm^{-1} gratings and a diode array detector.

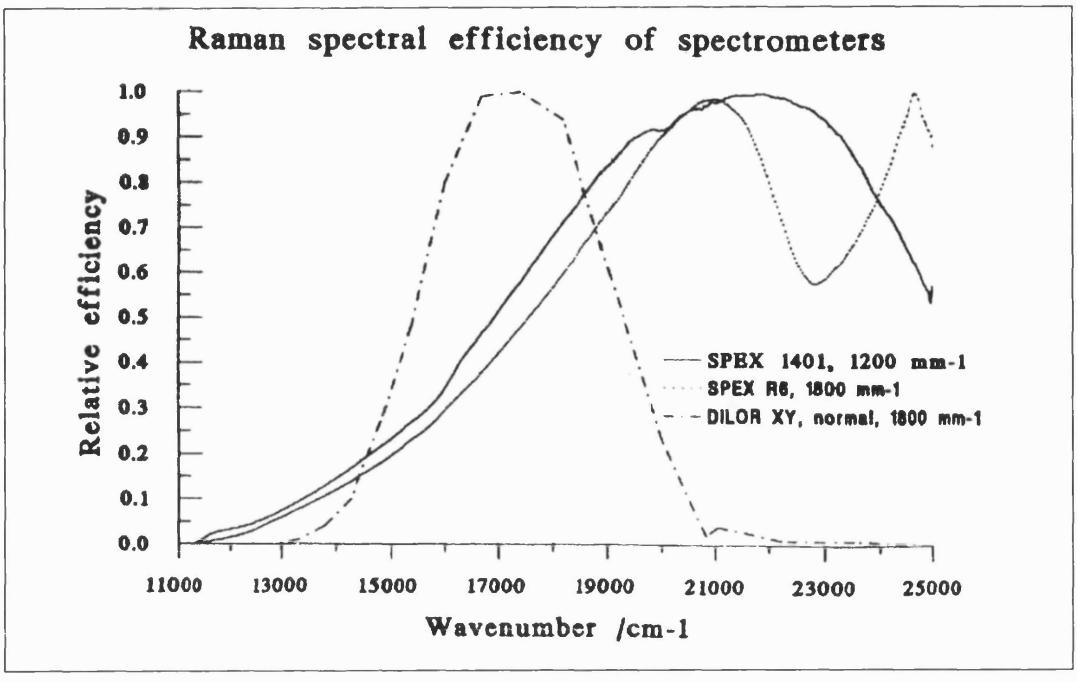

Figure 1.7 - Spectral response curves of different spectrometers.

It can be seen in Fig. 1.7 that even for a 1000 cm^{-1} scan the relative intensity of peaks will be altered by the non-linear spectral response; in the case of the resonance Raman spectrum of the 846 cm^{-1} vibration of $KMnO_4$, produced by excitation with light of 514.5 nm wavelength (19453 cm^{-1}) and collected by a SPEX 1401 instrument configured [8] as in the paragraph above, the relative change in the intensity of the third overtone is approximately 80 %. As shown in later chapters, using the transform method requires correcting the collected resonance Raman data for the spectral response of the instrumentation.

II. Density Matrix Formalism for Multiphoton Molecular Spectroscopies

Introduction

Chapter 1 has presented very briefly the traditional approach to optical spectroscopy - the second-order perturbation theory and the Kramers-Heisenberg formula - for both optical absorption and Raman scattering. While the Kramers-Heisenberg formula is correct in the case when all states of the chromophore and of its environment are included, in practice the latter are not known explicitly and have to be taken into account statistically. This approach introduces band shapes and widths on a strictly phenomenological basis, without taking into account the difference between different broadening mechanisms. For this reason, it is impossible for the Kramers-Heisenberg formula to discriminate between resonance Raman and resonance fluorescence and indeed, to predict any resonance fluorescence at all.

Theoretical studies [21-30] have shown that the mechanisms generating the loss of coherence between states control the nature of the secondary emission and the occurrence of resonance Raman scattering and resonance fluorescence. A recent study [31] has confirmed the theoretical results of [26-30,32] through experiments where either resonance Raman scattering or resonance fluorescence have been found to dominate the total intensity of secondary emission, depending on the dominant mechanism of coherence loss.

This chapter will show that resonance Raman scattering represents only a part of the laser-induced resonance secondary emission from electronically excited states, and is usually accompanied by a certain amount of resonance fluorescence. This is why the study of resonance Raman scattering has to start with a broader view of the two-photon processes, followed by an examination of the conditions under which resonance two-photon processes can occur and

resonance secondary radiation can be separated into resonance Raman scattering and resonance fluorescence.

The separation between resonance Raman scattering and resonance fluorescence will be based on the separation of the damping constant, and of its corresponding quantum operator, into terms of distinct phenomenological origin. The mathematical formalism required to achieve this separation is based on the density matrix of a multilevel system in interaction with a dissipative system (a "heat bath") [27]. The formalism thus developed will be extended to include the interaction with a radiation field [28-30,32] and then applied to the calculation of the transition probability for one- and two-photon processes.

This chapter will continue by separating the formulae for the transition probabilities into terms corresponding to one-photon absorption and emission, Raman scattering, and fluorescence. The role of different mechanisms will be discussed and conditions for the occurrence of various processes will be established. At the end of the chapter the experimental results of [31] will be examined in more depth , providing the ground for the approximation adopted in chapter 3 with regard to resonance fluorescence. Only then the theoretical basis for the transform relation between resonance Raman scattering and optical absorption spectra will be fully in place and the discussion can proceed towards establishing this transform relation, the aim of Chapter 3.

The Density Matrix Formalism

The starting point of this review of the formalism is the physical meaning of the density matrix, best illustrated by the case of a system with two levels, {1, 2}, the wave function [32]

$$\psi(\boldsymbol{r},t) = C_1(t)\psi_1(\boldsymbol{r}) + C_2(t)\psi_2(\boldsymbol{r}) \qquad (2.1)$$

and the Hamiltonian operator

$$\hat{H} = \hat{H}_0 + \hat{V} \ . \tag{2.2}$$

Here $\psi_1(r)$ and $\psi_2(r)$ are the eigenfunctions of the unperturbed Hamiltonian $\hat{H}_0$, $\hat{V}$ is the interaction Hamiltonian, and the coefficients $C_1(t)$ and $C_2(t)$ can be obtained from the solution of the time-dependent Schrödinger equation

$$\hat{H}\psi = i\hbar\frac{\partial\psi}{\partial t} \ . \tag{2.3}$$

It is found that the coefficients $C_1(t)$ and $C_2(t)$ satisfy the relations

$$\frac{dC_1}{dt} = -\frac{iE_1}{h}C_1 - \frac{iV_{12}}{h}C_2 \ , \tag{2.4a}$$

and

$$\frac{dC_2}{dt} = -\frac{iE_2}{h}C_2 - \frac{iV_{21}}{h}C_1 \ . \tag{2.4b}$$

The density matrix of a system with the wave function above is then defined as

$$\rho_{11} \equiv C_1C_1^*, \ \rho_{12} \equiv C_1C_2^*, \ \rho_{21} = C_2C_1^* = \rho_{12}^*, \ \rho_{22} \equiv C_2C_2^* \tag{2.5}$$

and the density *operator* corresponding to the matrix can be written then as

$$\hat{\rho} = |\psi><\psi| \ . \tag{2.6}$$

The density matrix can be used to calculate the expectation value of an operator $\hat{M}$, starting with the definition of its expectation value

$$\langle\hat{M}\rangle = <\psi(r,t)|\hat{M}|\psi(r,t)> \ ; \tag{2.7}$$

from the expression for the wave function (Eqn (2.1)) and the definition of the density matrix (Eqn (2.5)), it follows that

$$\langle\hat{M}\rangle = C_1^*C_1M_{11} + C_1^*C_2M_{12} + C_2^*C_1M_{21} + C_2^*C_2M_{22} \tag{2.8}$$

or, in matrix form, the expectation value of $\hat{M}$ will be the trace of the product between $\hat{M}$ and $\hat{\rho}$

$$\langle\hat{M}\rangle = Tr(\hat{\rho}\hat{M}) = Tr(\hat{M}\hat{\rho}) \ . \tag{2.9}$$

The time dependence of the density matrix of an isolated system is given by its equation of motion, which can be obtained by differentiating the density matrix with respect to time (Eqn (2.5))

$$\frac{d\rho_{11}}{dt} = C_1\frac{dC_1^*}{dt} + C_1^*\frac{dC_1}{dt} = C_1\left(\frac{iE_1}{\hbar}C_1^* + \frac{iV_{21}}{\hbar}C_2^*\right) - C_1^*\left(\frac{iE_1}{\hbar}C_1 + \frac{iV_{12}}{\hbar}C_2^*\right); \qquad (2.10)$$

cancelling the like terms yields

$$\frac{d\rho_{11}}{dt} = -\frac{i}{\hbar}(V_{12}\rho_{21} - \rho_{12}V_{21}) = -\frac{i}{\hbar}[\hat{V},\hat{\rho}]_{11} . \qquad (2.11a)$$

The other terms can be obtained similarly

$$\frac{d\rho_{22}}{dt} = -\frac{i}{\hbar}(V_{21}\rho_{12} - \rho_{21}V_{12}) = -\frac{i}{\hbar}[\hat{V},\hat{\rho}]_{22} , \qquad (2.11b)$$

$$\frac{d\rho_{12}}{dt} = -\frac{i}{\hbar}(E_1 - E_2)\rho_{12} + \frac{i}{\hbar}V_{12}(\rho_{11} - \rho_{22}) , \qquad (2.11c)$$

and

$$\frac{d\rho_{21}}{dt} = -\frac{i}{\hbar}(E_2 - E_1)\rho_{21} + \frac{i}{\hbar}V_{21}(\rho_{22} - \rho_{11}) \qquad (2.11d)$$

and the equation of motion for the density matrix can be written in operator form as

$$\frac{d\hat{\rho}}{dt} = -\frac{i}{\hbar}[\hat{H},\hat{\rho}] \equiv -i\hat{L}\hat{\rho} . \qquad (2.12)$$

Equation (2.12) is called also the Liouville equation and the Liouville operator is defined as

$$\hat{L} = \frac{1}{\hbar}[\hat{H},\cdot] . \qquad (2.13)$$

The above treatment for a pure-state, two-level system, is not very useful in practical terms because real systems are collections of multi-level systems. The extension of the previous approach to a mixed-state, multi-level system will start also with the wave function of a system in the state *j*:

$$\psi^{(j)}(r,t) = \sum_n C_n^{(j)}(t)\psi_n(r) \ . \tag{2.14}$$

Defining P_j as the probability of the system to be in the state with the wave function $\psi^{(j)}$ gives the following expression for the density matrix

$$\rho_{nm} = \sum_j P_j C_n^{(j)}(t)\left[C_m^{(j)}(t)\right]^* \ ; \tag{2.15}$$

in this case of a mixed-state, multi-level system, the density matrix element ρ_{nm} is a measure of the probability density that the state *m* mixes with the state *n*. The density operator is to be written as

$$\hat{\rho} = \sum_j P_j |\psi^{(j)}><\psi^{(j)}| \tag{2.16}$$

and the corresponding Liouville equation is

$$\frac{d\rho_{mn}}{dt} = -\frac{i}{\hbar}\sum_k (H_{mk}\rho_{kn} - \rho_{mk}H_{kn}) = -i\sum_{m'}\sum_{n'} L_{mn:m'n'}\rho_{m'n'} \ ; \tag{2.17}$$

the matrix element of the Liouville operator is given by

$$L_{mn:m'n'} = \frac{1}{\hbar}(H_{mm'}\delta_{nn'} - \delta_{mm'}H_{nn'}) \ , \tag{2.18}$$

where $\delta_{mm'}$ and $\delta_{nn'}$ are ordinary Kronecker symbols. In operator form the Liouville equation and operator are, respectively

$$\frac{d\hat{\rho}}{dt} = -i\hat{L}\hat{\rho} \tag{2.19}$$

and

$$\hat{L} = \frac{1}{\hbar}[\hat{H}, \cdot] \ . \tag{2.20}$$

Density Matrix Formalism for a Molecular System in Interaction with a Heat Bath

The review of the basis of the density matrix formalism establishes the terminology to be used in later work throughout this chapter and provides a connection between the physical reality to be modelled and the mathematical equations describing that model. However, a useful model needs to represent

an interesting problem in the simplest possible terms, so the next step of the present treatment is to separate the "reality", considered to be an isolated system, into two interacting parts: the system of interest - the "system" - and the rest -the "reservoir" or the "heat bath". Specifically, the "system" would represent the molecular system and the "bath" would represent all mechanisms through which the "system" interacts with its environment. This would account for all energy transfers, radiative or not, between the system and its environment, e.g. intermolecular collisions and low-frequency, internal modes of vibration.

The purpose of the separation between the "system" and the "bath" is to eliminate the "bath" part of the density matrix, so as to obtain a simpler equation of motion, involving only the reduced density matrix of the system of interest. Microscopic variables of the reservoir would not occur in this reduced equation, the effect of the reservoir on the "system" would be described conveniently through rate constants, and only a statistical assumption at the initial time would be required. The expressions for the rate constants will be derived and a phenomenological interpretation of the rate constants will be given.

For practical applications the "system" itself will be separated into another "system" and the radiation field but for the start there will be only a "system", with the Hamiltonian $\hat{H}_s$, and a "bath", with the Hamiltonian $\hat{H}_b$; the interaction between the system and the bath has the Hamiltonian $\hat{H}_1$. The Hamiltonian of the total system will be then

$$\hat{H} = \hat{H}_s + \hat{H}_b + \hat{H}_1 \equiv \hat{H}_0 + \hat{H}_1 \qquad (2.21)$$

and similarly for the corresponding Liouville operator

$$\hat{L} = \hat{L}_s + \hat{L}_b + \hat{L}_1 \equiv \hat{L}_0 + \hat{L}_1 \ . \qquad (2.22)$$

Applying the Laplace transform, defined by

$$\hat{\rho}(p) = \int_0^\infty e^{-pt}\,\hat{\rho}(t)dt\ , \tag{2.23}$$

to the Liouville equation for a mixed-state, multi-level system (Eqn (2.19)), yields [27,33]

$$\hat{\rho}(p) = \frac{\hat{\rho}(0)}{p + i\hat{L}}\ . \tag{2.24}$$

A transition operator $\hat{M}(p)$ will be defined as [27,28,33]

$$\frac{1}{p + i\hat{L}} = \frac{1}{p + i\hat{L}_0}\left[1 + \hat{M}(p)\frac{1}{p + i\hat{L}_0}\right], \tag{2.25}$$

which is to be substituted into the expression for the Laplace transform of the density operator (Eqn (2.24)), yielding

$$\hat{\rho}(p) = \frac{\hat{\rho}(0)}{p + i\hat{L}_0}\left[1 + \hat{M}(p)\frac{1}{p + i\hat{L}_0}\right]. \tag{2.26}$$

The density matrix of the "system" at time t can be found by calculating the trace of the total density matrix over the quantum states of the "bath"

$$\hat{\rho}^{(s)}(t) = \mathrm{Tr}_b\hat{\rho}(t)\ , \tag{2.27a}$$

$$\hat{\rho}^{(s)}(p) = \mathrm{Tr}_b\hat{\rho}(p)\ . \tag{2.27b}$$

To eliminate the "bath" variables, it is assumed [27] that at $t = 0$

$$\hat{\rho}(0) = \hat{\rho}^{(s)}(0)\hat{\rho}^{(b)}(0)\ ; \tag{2.28}$$

using this initial condition in the Laplace transform of the density matrix of the "system" yields

$$\hat{\rho}^{(s)}(p) = \frac{\hat{\rho}^{(s)}(0)}{p + i\hat{L}_s}\left[1 + \langle\hat{M}(p)\rangle\frac{1}{p + i\hat{L}_s}\right], \tag{2.29}$$

with the trace of the transition operator expressed as

$$\langle\hat{M}(p)\rangle = \mathrm{Tr}_b[\hat{M}(p)\hat{\rho}^{(b)}(0)]\ . \tag{2.30}$$

By introducing the memory function (or memory kernel) [28,34]

$$\langle \hat{M}_c(p) \rangle = -\frac{\langle \hat{M}(p) \rangle}{1 + \langle \hat{M}(p) \rangle (p + i\hat{L}_s)^{-1}} , \tag{2.31}$$

the Laplace transform of the density matrix of the "system" can also be expressed as [27]

$$\hat{\rho}^{(s)}(p) = \frac{\hat{\rho}^{(s)}(0)}{p + i\hat{L}_s + \langle \hat{M}_c(p) \rangle} \tag{2.32}$$

or rewritten as [27]

$$p\hat{\rho}^{(s)}(p) - \hat{\rho}^{(s)}(0) = -i\hat{L}_s\hat{\rho}^{(s)}(p) - \langle \hat{M}_c(p) \rangle \hat{\rho}^{(s)}(p) . \tag{2.33}$$

The Liouville equation of motion for the density matrix of the "system" can now be obtained by performing the inverse Laplace transform of Eqn (2.33)

$$\frac{d\hat{\rho}^{(s)}(t)}{dt} = -i\hat{L}_s\hat{\rho}^{(s)}(t) - \int_0^t d\tau \langle \hat{M}_c(\tau) \rangle \hat{\rho}^{(s)}(t-\tau) , \tag{2.34}$$

with

$$\langle \hat{M}(\tau) \rangle = \frac{1}{2\pi i} \int_{-i\infty+c}^{i\infty+c} dp \langle \hat{M}(p) \rangle \exp(p\tau) . \tag{2.35}$$

By using the identity

$$\exp\left(-\tau\frac{d}{dt}\right)\hat{\rho}^{(s)}(t) = \sum_{n=0}^{\infty} \frac{(-\tau)^n}{n!} \frac{d^n\hat{\rho}^{(s)}(t)}{dt^n} = \hat{\rho}^{(s)}(t-\tau) , \tag{2.36}$$

the Laplace transform of the density matrix of the "system" can also be written as

$$\frac{d\hat{\rho}^{(s)}(t)}{dt} = -i\hat{L}_s\hat{\rho}^{(s)}(t) - \int_0^t d\tau \langle \hat{M}_c(\tau) \rangle \exp\left(-\tau\frac{d}{dt}\right)\hat{\rho}^{(s)}(t) . \tag{2.37}$$

Approximating the time derivative operator by $-i\hat{L}_s$ under the exponential in Eqn (2.37) yields the generalised master equation for the density matrix of a system in contact with a heat bath

$$\frac{d\hat{\rho}^{(s)}(t)}{dt} = -i\hat{L}_s\hat{\rho}^{(s)}(t) - \int_0^t d\tau \langle \hat{M}_c(\tau) \rangle \exp(i\tau\hat{L}_s)\hat{\rho}^{(s)}(t) . \tag{2.38}$$

It is to be noted that the generalised master equation achieves the separation between the variables of the system of interest and those of the heat bath and depends only on the density matrix and the Liouville operator of the "system".

This equation provides the starting point for the treatment of any optical spectroscopy, as no assumption has been made about either the character or the magnitude of the interaction between the system of interest and its environment. The diagonal elements of the density matrix describe the time evolution of the population of the system, while the off-diagonal elements provide the information about the phase, bandwidth and band positions in the optical spectra.

In order to obtain relations applicable to spectroscopic problems, damping will be introduced through the Markov approximation: the duration of the interaction between the system and its environment is infinitely small compared with the time required by the density matrix to change, such that the time integral in the generalised master equation can be extended from zero to infinity. Thus the damping operator can be defined as

$$\hat{\Gamma} = \int_0^\infty d\tau \left\langle \hat{M}_c(\tau) \right\rangle \exp(i\tau \hat{L}_s) \tag{2.39}$$

and the equation of motion becomes

$$\frac{d\hat{\rho}^{(s)}(t)}{dt} = -i\hat{L}_s\hat{\rho}^{(s)}(t) - \hat{\Gamma}\hat{\rho}^{(s)}(t) \; . \tag{2.40}$$

The damping operator can be defined by correspondence with the time-independent damping constant only in the Markov approximation; when this approximation does not hold, one has to deal directly with the memory function. The physical quantity corresponding to the damping operator is the damping constant, to be derived in the following discussion; this will lead to the separation of the damping constant in two parts, of distinct phenomenological origins.

Applying the physical interpretation of the elements of the density matrix of the "system" leads, in the second order of approximation with respect to $\hat{H}_1$ [27], to the following equation for the diagonal matrix element

$$\frac{d\rho^{(s)}_{n_s n_s}}{dt} = -\sum_{n_s'} \Gamma_{n_s n_s; n_s' n_s'} \rho^{(s)}_{n_s' n_s'} \tag{2.41a}$$

and for the off-diagonal matrix element

$$\frac{d\rho^{(s)}_{m_s n_s}}{dt} = -(i\omega_{m_s n_s} + \Gamma_{m_s n_s; m_s n_s})\rho^{(s)}_{m_s n_s} \, . \tag{2.41b}$$

It can be seen in the previous equations that the time evolution of the diagonal elements of the density matrix depends only on the rate constants (Γ), characterising changes in the population of the state n_s ; the evolution of the off-diagonal elements between different states m_s and n_s depends on the band shifts (ω) as well as the rate constants (Γ) describing the population changes in both states involved.

The definition of the damping operator shows that calculating the matrix elements of this operator requires the calculation of the matrix elements of the memory function $\langle \hat{M}_c(\tau) \rangle$ (or equivalently $\langle \hat{M}_c(p) \rangle$). Thus, the Laplace transform of the memory function can be written as

$$\langle \hat{M}_c(p) \rangle^{(2)} = -\langle \hat{M}(p) \rangle^{(2)} = \left\langle \hat{L}_1 \frac{1}{p + i\hat{L}_0} \hat{L}_1 \right\rangle \tag{2.42}$$

or, for its diagonal matrix element

$$\langle \hat{M}_c(p) \rangle^{(2)}_{n_s n_s; n_s' n_s'} = \sum_{n_b} \sum_{n_b'} \rho^{(b)}_{n_b' n_b'}(0) \left(\hat{L}_1 \frac{1}{p + i\hat{L}_0} \hat{L}_1 \right)_{NN; N'N'} \, . \tag{2.43}$$

In the previous equation n_s, n'_s are quantum numbers corresponding to "system" states, n_b, n'_b are quantum numbers corresponding to "bath" states and the shorthand notation $N \equiv n_s n_b$, $N' \equiv n_s' n_b'$ has been used.

Using the definition of the Liouville operator and the assumption that the thermal average of the Liouville operator of the interaction is zero, $\langle \hat{L}_1 \rangle = 0$, and replacing for convenience the notation for the interaction Hamiltonian $\hat{H}' = \hat{H}_1$

in the previous equation yields

$$\left\langle \hat{M}_c(p)\right\rangle^{(2)}_{n_s n_s' : n_s' n_s'} = \sum_{n_b}\sum_{n_b'} \frac{\rho^{(b)}_{n_b' n_b'}(0)}{\hbar^2} \times \left[\delta_{NN'}\sum_M \left(\frac{|H'_{MN}|^2}{p+i\omega_{MN}} + \frac{|H'_{MN}|^2}{p+i\omega_{NM}}\right) - \frac{|H'_{NN}|^2}{p+i\omega_{N'N}} - \frac{|H'_{NN}|^2}{p+i\omega_{NN'}}\right], \tag{2.44}$$

which reduces for the case of $n_s \neq n_s'$ to

$$\left\langle \hat{M}_c(p)\right\rangle^{(2)}_{n_s n_s' : n_s' n_s'} = -\frac{1}{\hbar^2}\sum_{n_b}\sum_{n_b'} \rho^{(b)}_{n_b' n_b'}(0)\,|H'_{n_s n_b, n_s' n_b'}|^2 \left(\frac{1}{p+i\omega_{n_s n_b, n_s' n_b'}} + \frac{1}{p+i\omega_{n_s' n_b', n_s n_b}}\right) \tag{2.45}$$

or, by reversing the Laplace transform, to

$$\left\langle \hat{M}_c(\tau)\right\rangle^{(2)}_{n_s n_s' : n_s' n_s'} = -\frac{2}{\hbar^2}\sum_{n_b}\sum_{n_b'} \rho^{(b)}_{n_b' n_b'}(0)\,|H_{n_s n_b, n_s' n_b'}|^2 \cos(\omega_{n_s n_b, n_s' n_b'}\tau)\ . \tag{2.46}$$

The matrix element form of the definition of the damping operator now gives, in the case of $n_s \neq n_s'$,

$$\Gamma_{n_s n_s' : n_s' n_s'} = -\frac{2\pi}{\hbar^2}\sum_{n_b}\sum_{n_b'} \rho^{(b)}_{n_b' n_b'}(0)\,|H'_{n_s n_b, n_s' n_b'}|^2 \delta(\omega_{n_s n_b, n_s' n_b'}) \equiv -k_{n_s' \to n_s}\ . \tag{2.47}$$

The case for $n_s = n_s'$ yields similarly

$$\begin{aligned}\left\langle \hat{M}_c(p)\right\rangle^{(2)}_{n_s n_s' : n_s n_s} &= \frac{1}{\hbar^2}\sum_{n_b}\sum_{m_s}\sum_{m_b} \rho^{(b)}_{n_b n_b}(0)\,|H'_{m_s m_b, n_s n_b}|^2 \left(\frac{1}{p+i\omega_{m_s m_b, n_s n_b}} + \frac{1}{p+i\omega_{n_s n_b, m_s m_b}}\right) \\ &\quad - \frac{1}{\hbar^2}\sum_{n_b}\sum_{n_b'} \rho^{(b)}_{n_b' n_b'}(0)\,|H'_{n_s n_b, n_s' n_b'}|^2 \left(\frac{1}{p+i\omega_{n_s n_b', n_s' n_b}} + \frac{1}{p+i\omega_{n_s' n_b, n_s n_b'}}\right) \\ &= \frac{1}{\hbar^2}\sum_{n_b}\sum_{m_s \neq n_s}\sum_{m_b} \rho^{(b)}_{n_b n_b}(0)\,|H'_{m_s m_b, n_s n_b}|^2 \left(\frac{1}{p+i\omega_{m_s m_b, n_s n_b}} + \frac{1}{p+i\omega_{n_s n_b, m_s m_b}}\right)\end{aligned} \tag{2.48}$$

or, by reversing the Laplace transform,

$$\left\langle \hat{M}_c(\tau)\right\rangle^{(2)}_{n_s n_s' : n_s n_s} = \frac{2}{\hbar^2}\sum_{m_s \neq n_s}\sum_{n_b}\sum_{m_b} \rho^{(b)}_{n_b n_b}(0)\,|H_{m_s m_b, n_s n_b}|^2 (\cos\omega_{m_s m_b, n_s n_b}\tau)\ . \tag{2.49}$$

The matrix element form of the definition of the damping operator now gives, in the case of $n_s = n_s'$,

$$\Gamma_{n_s n_s : n_s n_s} = \frac{2\pi}{\hbar^2} \sum_{m_s \neq n_s} \sum_{n_b} \sum_{m_b} \rho^{(b)}_{n_b n_b}(0) |H'_{m_s m_b, n_s n_b}|^2 \delta(\omega_{m_s m_b, n_s n_b})$$
$$= - \sum_{m_s \neq n_s} \Gamma_{m_s m_s : n_s n_s} = - \sum_{n'_s \neq n_s} \Gamma_{n'_s n'_s : n_s n_s} = \sum_{n'_s \neq n_s} k_{n_s \to n'_s} \ . \qquad (2.50)$$

Combining the results for $n_s \neq n'_s$ and $n_s = n'_s$, the master equation for the diagonal elements of the density matrix of the "system" now becomes

$$\frac{d\rho^{(s)}_{n_s n_s}}{dt} = \sum_{n'_s}{}' (k_{n'_s \to n_s} \rho^{(s)}_{n'_s n'_s} - k_{n_s \to n'_s} \rho^{(s)}_{n_s n_s}) \ . \qquad (2.51)$$

The calculation of the off-diagonal matrix element of the damping operator is analogous to that of the diagonal element and starts with calculating the corresponding matrix element of the Laplace transform of the memory function

$$\left\langle \hat{M}_c(p) \right\rangle^{(2)}_{m_s n_s : m_s n_s} = \sum_{n_b} \sum_{n'_b} \rho^{(b)}_{n_b n'_b}(0) \left(\hat{L}_1 \frac{1}{p + i\hat{L}_0} \hat{L}_1 \right)_{MN:M'N'} \ , \qquad (2.52)$$

where the shorthand notation $M \equiv m_s n_b$, $N' \equiv n_s n'_b$, $N \equiv n_s n_b$, $M' \equiv m_s n'_b$ has been utilised. Again, as for the diagonal matrix element, using the definition of the Liouville operator and the assumption that the thermal average of the Liouville operator of the interaction is zero, $\left\langle \hat{L}_1 \right\rangle = 0$, and setting for convenience $\hat{H}' = \hat{H}_1$ in the previous equation yields

$$\left\langle \hat{M}_c(p) \right\rangle^{(2)}_{m_s n_s : m_s n_s} = \sum_{n_b} \sum_{n'_b} \frac{\rho^{(b)}_{n'_b n'_b}(0)}{\hbar^2} \times$$
$$\left[\sum_{M''} \left(\frac{H'_{MM''} H'_{M''M'}}{p + i\omega_{M''N}} \delta_{NN'} + \frac{H'_{N'M''} H'_{M''N}}{p + i\omega_{MM''}} \delta_{MM'} \right) - \frac{H'_{N'N} H'_{MM'}}{p + i\omega_{M'N}} - \frac{H'_{N'N} H'_{MM'}}{p + i\omega_{M'N}} \right] \qquad (2.53)$$

which, after expanding the sums over the Kronecker symbols and grouping the resultant terms, becomes

$$\left\langle \hat{M}_c(p)\right\rangle^{(2)}_{m_s n_s : m_s n_s} = \frac{1}{\hbar^2}\sum_{n_b}\sum_{m_s'}\sum_{m_b'} \rho^{(b)}_{n_b n_b}(0)\left(\frac{|H'_{m_s n_b, m_s' m_b'}|^2}{p + i\omega_{m_s' m_b', m_s n_b}} + \frac{|H'_{n_s n_b, m_s' m_b'}|^2}{p + i\omega_{n_s n_b, m_s' m_b'}} \right) \qquad (2.54)$$
$$- \frac{2}{\hbar^2}\sum_{n_b}\sum_{n_b'} \rho^{(b)}_{n_b' n_b'}(0) \frac{H'_{n_s n_b', n_s n_b} H'_{m_s n_b, m_s n_b}}{p + i\omega_{m_s n_b, m_s n_b}} .$$

Performing the inverse Laplace transform of the previous equation and substituting the result in the definition of the damping operator yields

$$\Gamma_{m_s n_s : m_s n_s} = \sum_{n_b}\sum_{m_s'}\sum_{m_b'} \frac{\rho^{(b)}_{n_b n_b}(0)}{\hbar^2}\left[|H'_{m_s n_b, m_s' m_b'}|^2 \eta(\omega_{m_s' m_b', m_s n_b}) + |H'_{n_s n_b, m_s' m_b'}|^2 \eta(\omega_{n_s n_b, m_s' m_b'}) \right] \qquad (2.55)$$
$$- \sum_{n_b}\sum_{n_b'} \frac{\rho^{(b)}_{n_b' n_b'}(0)}{\hbar^2} H'_{n_s n_b', n_s n_b} H'_{m_s n_b, m_s n_b'} \eta(\omega_{n_b', n_b}) ,$$

where the complex function η is defined as

$$\eta(\omega_{m_s' m_b', n_s n_b}) \equiv \int_0^\infty d\tau \exp(-i\tau\omega_{m_s' m_b', n_s n_b}) \qquad (2.56)$$

and can also be written as $\eta(x) = \pi\delta(x) - iP(1/x)$, where $P(1/x)$ is the principal value of $1/x$. Thus the matrix element of the damping operator can be separated into its real and imaginary parts

$$\Gamma_{m_s n_s : m_s n_s} = \mathrm{Re}[\Gamma_{m_s n_s : m_s n_s}] + i\,\mathrm{Im}[\Gamma_{m_s n_s : m_s n_s}] . \qquad (2.57)$$

The real part is called the dephasing rate constant and consists of the inelastic part $(\Gamma_{m_s m_s : m_s m_s} + \Gamma_{n_s n_s : n_s n_s})/2$ and the elastic part $\Gamma^{(d)}_{m_s n_s : m_s n_s}$; the matrix element of the damping operator is written now

$$\Gamma_{m_s n_s : m_s n_s} = \mathrm{Re}[(\Gamma_{m_s m_s : m_s m_s} + \Gamma_{n_s n_s : n_s n_s})/2 + \Gamma^{(d)}_{m_s n_s : m_s n_s}] + i\,\mathrm{Im}[\Gamma_{m_s n_s : m_s n_s}] . \qquad (2.58)$$

The elastic term $\Gamma^{(d)}_{m_s n_s : m_s n_s}$ is called pure dephasing because it does not accompany a population change and is written as

$$\Gamma^{(d)}_{m_s n_s : m_s n_s} = \frac{\pi}{\hbar^2}\sum_{n_b}\sum_{n_b'} \rho^{(b)}_{n_b n_b}(0)(H'_{n_s n_b, n_s n_b'} - H'_{m_s n_b', m_s n_b})^2 \delta(\omega_{n_b', n_b}) . \qquad (2.59)$$

The imaginary part represents the energy level shift due to the interaction between the system and the heat bath and can be written as

$$\mathrm{Im}\,\Gamma_{m_s n_s : m_s n_s} \equiv \Delta\omega_{m_s n_s} = -\frac{1}{\hbar^2} P \sum_{n_b} \sum_{m_s'} \sum_{m_b'} \rho^{(b)}_{n_b n_b}(0) \left(\frac{|H'_{m_s n_b, m_s' m_b'}|^2}{p + i\omega_{m_s' m_b', m_s n_b}} + \frac{|H'_{n_s n_b, m_s' m_b'}|^2}{p + i\omega_{n_s n_b, m_s' m_b'}} \right) \qquad (2.60)$$

$$- \frac{2}{\hbar^2} P \sum_{n_b} \sum_{n_b'} \rho^{(b)}_{n_b' n_b'}(0) \frac{H'_{n_s n_b', n_s n_b} H'_{m_s n_b, m_s n_b}}{p + i\omega_{m_s n_b, m_s n_b}} \, .$$

The equation of motion for the off-diagonal element of the density matrix is now obtained by replacing the real and imaginary part of the corresponding matrix element of the damping operator in Eqn (2.41b)

$$\frac{d\rho^{(s)}_{m_s n_s}}{dt} = -i(\omega_{m_s n_s} + \Delta\omega_{m_s n_s})\rho^{(s)}_{m_s n_s} - \left[\frac{1}{2} (\Gamma_{m_s m_s : m_s m_s} + \Gamma_{n_s n_s : n_s n_s}) + \Gamma^{(d)}_{m_s n_s : m_s n_s} \right] \rho^{(s)}_{m_s n_s} \, . \qquad (2.61)$$

The above equation shows that the spectral position of each band, through the energy level shift, is temperature-dependent. As the phase information about the system is contained in the off-diagonal element of its density matrix, the above equation also shows that the Lorentzian spectral bandwidth of a molecular system depends not only on the total decay rate of each molecular state, but also on the pure dephasing characterising each pair of molecular states. This fact is not captured by any other method of treating molecular spectroscopy and represents the key advantage of the density matrix method over all the others.

Density Matrix Formalism for a Molecular System in Interaction with a Radiation Field and a Heat Bath

The formalism developed in the previous section will be extended now by including the interaction between the system and the radiation field. The results will then be applied to the specific cases of one- and two-photon spectroscopy, leading to expressions of the transition probability for optical absorption and resonant secondary radiation. These expressions are the two components of the transform relation, to be established in Chapter 3.

The starting point of this application is the definition of the probability rate for a *j*-photon transition of a multilevel molecular system from the initial state belonging to the manifold {*a*} to all possible final states belonging to manifold {*n*}, in the Markov approximation [29]

$$W^{(j)} = \lim_{t \to \infty} \sum_{n} \frac{d(\rho_j)^{(s)}_{nn}(t)}{dt} , \tag{2.62}$$

requiring the derivation of the master equation for one- and two-photon processes involving the system, the radiation field and the heat bath.

The derivation will proceed as in the earlier discussion of a system in contact with a heat bath, starting with the equation of motion for the whole system

$$\frac{\partial \hat{\rho}}{\partial t} = -i\hat{L}\hat{\rho} \tag{2.63}$$

with the Liouville operator defined as

$$\hat{L} \equiv \frac{1}{\hbar}[\hat{H}, \cdot\,] \tag{2.64}$$

and the Hamiltonian of the total system

$$\hat{H} = \hat{H}_0 + \hat{H}' . \tag{2.65}$$

The total unperturbed and interaction Hamiltonians are, respectively,

$$\hat{H}_0 = \hat{H}_s + \hat{H}_b + \hat{H}_r \tag{2.66a}$$

and

$$\hat{H}' = \hat{H}'_{sr} + \hat{H}_{sb} . \tag{2.66b}$$

The Hamiltonians and the corresponding Liouville operators of the molecular system, the heat bath, the radiation field, the system-radiation field interaction and system-heat bath interaction are denoted by the subscripts *s, b, r, sr* and *sb*, respectively.

The derivation will seek to isolate the density matrix of the system by eliminating both the bath and the radiation field variables; this will be achieved by applying the appropriate projection operator to both sides of the Laplace

transform of the Liouville equation (Eqn (2.63))

$$(p + i\hat{L})\hat{\rho}(p) = \hat{\rho}(0). \tag{2.67}$$

Applying the projection operator $\hat{A}=\hat{\rho}^{(b)}(0)Tr_b$ to both sides of Eqn (2.67), and assuming that $\hat{\rho}(0) = \hat{\rho}^{(s)}(0)\hat{\rho}^{(b)}(0)\hat{\rho}^{(r)}(0)$, yields [32]

$$[p+i\hat{L}_s+i\hat{L}_r+\langle\sum(p)\rangle_b]\hat{\rho}^{(sr)}(p) = \hat{\rho}^{(sr)}(0)\ , \tag{2.68}$$

where $\hat{\rho}^{(sr)}=Tr_b\hat{\rho}$ and

$$\langle\sum(p)\rangle_b=Tr_b[i\hat{L}'_{sb}+i\hat{L}'_{sb}(1-\hat{A})(p+i\hat{L})^{-1}(1-\hat{A})\hat{L}'_{sb}]\hat{\rho}^{(b)}(0). \tag{2.69}$$

A second projection operator $\hat{\alpha}=\hat{\rho}^{(r)}(0)Tr_r$ is applied to the intermediate result (Eqn (2.68)) in order to obtain the reduced density matrix of the molecular system

$$[p+i\hat{L}_s+\{\hat{M}(p)\}]\hat{\rho}^{(s)}(p) = \hat{\rho}^{(s)}(0). \tag{2.70}$$

In the previous equation $\{...\}=Tr_r...\hat{\rho}^{(r)}(0)$ and

$$\begin{aligned}\hat{M}(p) = {} & i\hat{L}_{sr'} + \langle\sum(p)\rangle_b - [i\hat{L}_{sr'}+\langle\sum(p)\rangle_b](1-\alpha) \\ & \times[p+i\hat{L}_s+i\hat{L}_r+i\hat{L}'_{sr}+\langle\sum(p)\rangle_b]^{-1}(1-\alpha)[i\hat{L}'_{sr}+\langle\sum(p)\rangle_b]\ .\end{aligned} \tag{2.71}$$

Applying the inverse Laplace transform to the reduced density matrix (Eqn (2.70)) yields the equation of motion of the molecular system

$$\frac{d\hat{\rho}^{(s)}(t)}{dt}=-i\hat{L}_s\hat{\rho}^{(s)}(t)-\int_0^t d\tau\{\hat{M}(\tau)\}\hat{\rho}^{(s)}(t-\tau)\ , \tag{2.72}$$

where

$$\{\hat{M}(\tau)\} = \frac{1}{2\pi i}\int_{-i\infty+c}^{i\infty+c} dp\{\hat{M}(p)\}\exp(p\tau). \tag{2.73}$$

In the Markov approximation - when changes in the density matrix of the system happen in an infinitely short time - the time integral in Eqn (2.72) can be extended to infinity and the equation of motion can be written as

$$\frac{d\hat{\rho}^{(s)}(t)}{dt} = (-i\hat{L}_s-\hat{k})\hat{\rho}^{(s)}(t)\ , \tag{2.74}$$

where

$$\hat{k} = \lim_{t\to\infty} \int_0^t d\tau \{\hat{M}(\tau)\} \exp(i\hat{L}_s\tau). \tag{2.75}$$

Equation (2.74) is the master equation for multiphoton processes involving a multilevel molecular system coupled to a heat bath; it is the starting point for applying the density matrix formalism to processes involving any number of photons. The transition operator can be expanded as

$$\{\hat{M}(p)\} = \{\hat{M}^{(0)}(p)\} + \{\hat{M}^{(1)}(p)\} + \{\hat{M}^{(2)}(p)\} + \{\hat{M}^{(3)}(p)\} + \ldots , \tag{2.76}$$

where the superscripts correspond to the number of photons involved in the process. The transition operators for one-, two- and three-photon processes are, respectively,

$$\{\hat{M}^{(1)}(p)\} = \{\hat{L}'_{sr}\hat{G}(p)\hat{L}'_{sr}\} , \tag{2.77a}$$

$$\{\hat{M}^{(2)}(p)\} = -\{\hat{L}'_{sr}\hat{G}(p)\hat{L}'_{sr}\hat{G}(p)\hat{L}'_{sr}\hat{G}(p)\hat{L}'_{sr}\} \tag{2.77b}$$

and

$$\{\hat{M}^{(3)}(p)\} = \{\hat{L}'_{sr}\hat{G}(p)\hat{L}'_{sr}\hat{G}(p)\hat{L}'_{sr}\hat{G}(p)\hat{L}'_{sr}\hat{G}(p)\hat{L}'_{sr}\hat{G}(p)\hat{L}'_{sr}\} , \tag{2.77c}$$

where the resolvent operator $\hat{G}(p)$ is

$$\hat{G}(p) = [p + i\hat{L}_s + i\hat{L}_r + \langle \sum (p) \rangle_b]^{-1}. \tag{2.78}$$

For an arbitrary number $k \geq 2$ of photons, the transition operators are connected through the following recurrence relationship

$$\hat{M}^{(k)}(p) = -\hat{L}'_{sr}\hat{C}^{(k-1)}(p)\hat{L}'_{sr} , \tag{2.79}$$

where

$$\hat{C}^{(k-1)}(p) = \hat{G}(p)\hat{M}^{(k-1)}(p)\hat{G}(p). \tag{2.80}$$

Using these relationships, the matrix element of the k-th order transition operator between the initial state A and the final state N of the system in the presence of the radiation field is

$$\begin{aligned}\hat{M}^{(k)}(p)_{NN:AA} = \frac{1}{\hbar^2}\sum_L \sum_M [&H'_{NM}H'_{LA}\hat{C}^{(k-1)}(p)_{MN:LA} + H'_{MN}H'_{AL}\hat{C}^{(k-1)}(p)_{NM:AL} \\ &- H'_{NM}H'_{AL}\hat{C}^{(k-1)}(p)_{MN:AL} + H'_{MN}H'_{LA}\hat{C}^{(k-1)}(p)_{NM:LA}] ,\end{aligned} \tag{2.81}$$

where $\hat{H}' = \hat{H}'_{sr}$, $N = nn_r$, $M = mm_r$, $A = aa_r$ and $L = ll_r$ and the subscript s for the

molecular system has been omitted; the matrix element of the Liouville operator is

$$(\hat{L}'_{sr})_{NN:LM} = \frac{1}{\hbar}[(\hat{H}'_{sr})_{NL}\delta_{NM} - (\hat{H}'_{sr})_{MN}\delta_{NL}] \ . \tag{2.82}$$

Taking the trace of the matrix element of the transition operator over the radiation field variables, Eqn (2.81) can be written as

$$\{\hat{M}^{(k)}(p)\}_{nn:aa} = \sum_{n_r}\sum_{a_r} \rho^{(r)}_{a,a_r}(0)[\hat{M}^{(k)}(p)]_{nn_r nn_r:aa_r aa_r} = \sum_{n_r}\sum_{a_r} \rho^{(r)}_{a,a_r}(0)[\hat{M}^{(k)}(p)]_{NN:AA} \ . \tag{2.83}$$

Any application of the matrix density formalism to the spectroscopy of optical processes involving an arbitrary number of photons will be a particular case of the system of equations (2.74, 75, 77a-c). The number of photons involved in the process to be studied will determine the order of the transition moment (Eqn (2.76)) to be employed, while the nature of the states *A, N, M* and *L* will determine the shape of its matrix element. The nature of the molecule-field and molecule-heat bath interaction will determine the shape of the trace operators and of the Hamiltonians and hence, through the dephasing rate constants and the spectral positions, the final form of the transition probability.

One-Photon Processes: Absorption and Emission

Regardless of the nature of the initial and final states (absorption or emission), the derivation of the formula of the transition probability rate for a one-photon process starts with its definition, in the Markov approximation [29,30,32]

$$W^{(1)} = \lim_{t\to\infty} \sum_n \frac{d\rho^{(s)}_{nn}(t)}{dt} = \sum_a \sum_n \lim_{t\to\infty} \int_0^t d\tau \{\hat{M}^{(1)}(\tau)\}_{nn:aa} \hat{\rho}^{(s)}_{aa}(0) \ , \tag{2.84}$$

where the trace of the transition operator (Eqn 2.77a) over the field variables is

$$\{\hat{M}^{(1)}(p)\}_{nn:aa} = \{\hat{L}'_{sr}\hat{G}(p)\hat{L}'_{sr}\}_{nn:aa} \ . \tag{2.85}$$

By neglecting in the resolvent operator the effect of the interaction between the molecule and the radiation field, $\hat{G}(p)$ can be written as

$$\hat{G}(p) \approx \hat{G}^{(0)}(p) = \left[p + i\hat{L}_s + i\hat{L}_r + \left\langle \sum^{(0)}(p) \right\rangle_b\right]^{-1} , \tag{2.86}$$

where

$$\left\langle \sum^{(0)}(p) \right\rangle_b = \left\langle \hat{L}'_{sb}(p + i\hat{L}_s + i\hat{L}_b)^{-1}\hat{L}'_{sb} \right\rangle . \tag{2.87}$$

With this approximation for the resolvent operator, the trace of the transition operator (Eqn (2.85)) can be written as

$$\begin{aligned} \{\hat{M}^{(1)}(p)\}_{nn:aa} \approx \{\hat{L}'_{sr}\hat{G}^{(0)}(p)\hat{L}'_{sr}\}_{nn:aa} &= \sum_{n_r}\sum_{a_r} \rho^{(r)}_{a,a_r}(0)[\hat{L}'_{sr}\hat{G}^{(0)}(p)\hat{L}'_{sr}]_{nn,n_rn_r:aa,a_ra_r} \\ &= \sum_{n_r}\sum_{a_r} \rho^{(r)}_{a,a_r}(0)[M^{(1)}(p)]_{NN:AA} . \end{aligned} \tag{2.88}$$

and its matrix element between the initial state A and the final state N as

$$\begin{aligned} M^{(1)}_{NN:AA}(p) = -\frac{1}{\hbar^2}\sum_L\sum_M [&\{H'_{NM}H'_{LA}G^{(0)}_{MA}(p) + H'_{MN}H'_{AL}G^{(0)}_{AM}(p)\}\delta_{NA}\delta_{ML} \\ &- \{H'_{NM}H'_{AL}G^{(0)}_{AN}(p) + H'_{MN}H'_{LA}G^{(0)}_{NA}(p)\}\delta_{MA}\delta_{NL}] , \end{aligned} \tag{2.89}$$

where the matrix element of the resolvent operator is [29,30,32]

$$G^{(0)}_{NA}(p) = G^{(0)}_{NA:NA}(p) = (p + i\omega_{nn_r,aa_r} + \Gamma_{na})^{-1} \tag{2.90}$$

and the dephasing rate constant between the a and n molecular states, calculated in the previous section, is $\Gamma_{na} \equiv \left\langle \sum^{(0)}(0) \right\rangle_{na:na}$.

For a one-photon process A and N are different states, so the matrix element of the one-photon transition operator is

$$[M^{(1)}(p)]_{NN:AA} = \frac{2}{\hbar^2}|H'_{NA}|^2 \mathrm{Re}[G^{(0)}_{NA}(p)] . \tag{2.91}$$

Performing the inverse Laplace transform on the previous equation, with Eqn (2.90) for the matrix element of the resolvent operator, yields

$$\{\hat{M}^{(1)}(p)\}_{nn:aa} = \frac{1}{\hbar^2}\sum_{n_r}\sum_{a_r} \rho^{(r)}_{a,a_r}(0)\,\mathrm{Re}\,|H'_{nn_r:aa_r}|^2 \exp[-\tau(i\omega_{nn_r,aa_r} + i\Delta\omega_{na} + \Gamma_{na})] . \tag{2.92}$$

This leads to the following expression for the transition probability rate of a one-photon process:

$$W^{(1)} = \frac{1}{\hbar^2}\sum_{n}\sum_{a}\sum_{n_r}\sum_{a_r}\rho^{(s)}_{aa}(0)\rho^{(r)}_{a_r a_r}(0)|H'_{NA}|^2\,\mathrm{Re}\left[\int_0^\infty e^{-i\tau(\omega_{nn_r aa_r}+\Delta\omega_{na}-i\Gamma_{na})}d\tau\right] \tag{2.93}$$

or, by using the identity $i\int_0^\infty d\tau e^{[-i\tau(a-ib)]} \equiv (a-ib)^{-1}$, $b>0$:

$$W^{(1)} = \frac{1}{\hbar^2}\sum_{n}\sum_{a}\sum_{n_r}\sum_{a_r}\rho^{(s)}_{aa}(0)\rho^{(r)}_{a_r a_r}(0)|H'_{NA}|^2\frac{\Gamma_{na}}{(\omega_{NA}+\Delta\omega_{na})^2+\Gamma_{na}^2} \ . \tag{2.94}$$

The expression above will be used in the next chapter towards a transform relation between the one- and the two-photon transition probability rates. Further assumptions on the actual shape of the interaction Hamiltonian and of the density matrix of the radiation field will lead to a more detailed formula for the one-photon transition probability rate, to be derived in the following paragraphs.

In the dipole approximation for the quantized field description (Eqns (1.24-27)), the Hamiltonian of the molecule-radiation field interaction is [29,30,32]

$$\hat{H}'_r = -\sum_l (\hat{\mathbf{e}}\cdot\boldsymbol{P})\frac{e_0}{m_0}\left(\frac{2\pi\hbar}{\omega_l L^3}\right)^{1/2}(\hat{a}_l+\hat{a}_l^\dagger) \ . \tag{2.95}$$

This leads to the following expression for the trace of the Laplace transform of the transition operator:

$$\begin{aligned}\{\hat{M}^{(1)}(p)\}_{nn:aa} = {} & \frac{2\pi e_0^2}{m_0^2\hbar L^3}\mathrm{Re}\sum_{n_r}\sum_{a_r}\rho^{(r)}_{a_r a_r}(0)\exp[-\tau(i\omega_{nn_r aa_r}+i\Delta\omega_{na}+\Gamma_{na})] \\ & \times\sum_l\sum_{l'}\frac{<aa_r|\hat{\mathbf{e}}_l\cdot\boldsymbol{P}(\hat{a}_l+\hat{a}_l^\dagger)|nn_r><nn_r|(\hat{a}_{l'}^\dagger+\hat{a}_{l'})\hat{\mathbf{e}}_{l'}\cdot\boldsymbol{P}|aa_r>}{(\omega_l\omega_{l'})^{1/2}} \ ,\end{aligned} \tag{2.96}$$

where the subscript l is associated with the photon mode and the polarisation and $\hat{a}$ and $\hat{a}^\dagger$ are the photon creation and annihilation operators which satisfy the commutation relation $[\hat{a},\hat{a}^\dagger]=1$. Expanding the matrix elements and using the relations $\hat{a}|n>=n^{1/2}|n-1>$, $\hat{a}^\dagger|n>=(n+1)^{1/2}|n+1>$ and $<n|n'>=\delta_{nn'}$ in the equation above yields

$$\{\hat{M}^{(1)}(p)\}_{nn';aa'} = \frac{2\pi e_0^2}{m_0^2\hbar L^3}\mathrm{Re}\sum_{n_r}\sum_{a_r}\rho^{(r)}_{a_r a_r}(0)\exp[-\tau(i\omega_{nn_r aa_r}+i\Delta\omega_{na}+\Gamma_{na})] \times\sum_l \frac{[a_l\delta_{n_r,a_l-1}+(a_l+1)\delta_{n_r,a_l+1}]|\hat{\mathbf{e}}_l\cdot\boldsymbol{P}_{na}|^2}{\omega_l} \tag{2.97}$$

and, after performing the summation over the Kronecker tensor elements,

$$\{\hat{M}^{(1)}(p)\}_{nn';aa'} = \frac{2\pi e_0^2}{m_0^2\hbar L^3}\mathrm{Re}\sum_l \frac{|\hat{\mathbf{e}}_l\cdot\boldsymbol{P}_{na}|^2}{\omega_l}\sum_{a_l}\rho^{(r)}_{a_l a_l}(0)\exp[-\tau(i\Delta\omega_{na}+\Gamma_{na})] \times\{a_l\exp[-i\tau(\omega_{na}-\omega_l)]+(a_l+1)\exp[-i\tau(\omega_{na}+\omega_l)]\} . \tag{2.98}$$

Using the relationship between the *fi*-th matrix element of the total linear momentum operator of the electrons $\boldsymbol{P}$ and that of the total dipole moment $\boldsymbol{\mu}$, $\boldsymbol{P}_{fi}=(i m_0\omega_{fi}/e_0)\boldsymbol{\mu}_{fi}$, in Eqn (2.98) gives the final form of the one-photon transition operator:

$$\{\hat{M}^{(1)}(p)\}_{nn';aa'} = \frac{4\pi}{\hbar L^3}\mathrm{Re}\sum_l \frac{\omega_{na}^2}{\omega_l}|\hat{\mathbf{e}}_l\cdot\boldsymbol{\mu}_{na}|^2\sum_{a_l}\rho^{(r)}_{a_l a_l}(0)\exp[-\tau(i\Delta\omega_{na}+\Gamma_{na})] \times\{a_l\exp[-i\tau(\omega_{na}-\omega_l)]+(a_l+1)\exp[-i\tau(\omega_{na}+\omega_l)]\} . \tag{2.99}$$

The first and second terms represent one-photon absorption and one-photon emission processes, respectively. By using the first term of the previous equation for the trace of the transition operator, the formula of the transition probability rate for one-photon absorption becomes

$$W^{(1)}_{abs} = \frac{4\pi}{\hbar L^3}\sum_n\sum_a\sum_l\sum_{a_l}\rho^{(s)}_{aa}(0)\rho^{(r)}_{a_l a_l}(0)\omega_{na}|\hat{\mathbf{e}}_l\cdot\boldsymbol{\mu}_{na}|^2 a_l\frac{\Gamma_{na}}{(\bar{\omega}_{na}-\omega_l)^2+\Gamma_{na}^2} , \tag{2.100}$$

where $\bar{\omega}_{na} = \omega_{na}+\Delta\omega_{na}$ and $\omega_{na}^2/\omega_l \approx \omega_{na}$ have been used.

Considering the statistical nature of the radiation field, the density matrix for the thermal excitation of photons in a single mode at temperature T is (k_B is Boltzmann's constant)

$$\hat{\rho}^{(r)}(0) = [1-\exp(-\hbar\omega_r/k_BT)]\sum_{a_r}\exp(-a_r\hbar\omega_r/k_BT)|a_r><a_r| , \tag{2.101}$$

with the diagonal matrix element

$$\rho^{(r)}_{a_r a_r}(0) = [1-\exp(-\hbar\omega_r/k_BT)]\exp(-a_r\hbar\omega_r/k_BT) \ . \tag{2.102}$$

By using the identities

$$\sum_k^\infty ke^{-kx} \equiv \sum_k^\infty -\frac{\partial}{\partial x}e^{-kx} = -\frac{\partial}{\partial x}\sum_k^\infty (e^{-x})^k \rightarrow \frac{\partial}{\partial x}(e^{-x}-1)^{-1} = -\frac{e^{-x}}{(1-e^{-x})^2} \tag{2.103}$$

and the mean photon number $\bar{a}_r = 1/[\exp(\hbar\omega_r/k_BT)-1]$, the transition probability for one-photon absorption becomes

$$W^{(1)}_{abs} = \frac{4\pi\bar{a}_r}{\hbar L^3}\sum_n\sum_a \rho^{(s)}_{aa}(0)\omega_{na}|\hat{\mathbf{e}}_r\cdot\boldsymbol{\mu}_{na}|^2\frac{\Gamma_{na}}{(\bar{\omega}_{na}-\omega_r)^2+\Gamma^2_{na}} \ . \tag{2.104}$$

The absorption cross-section can be obtained, in units of cm^2, by using the formula for the intensity of light, $I=\hbar\omega_r\bar{a}_r c/L^3$ in units of erg s^{-1} cm^{-2} (c is the velocity of light):

$$\alpha^{(1)}_{abs} = \frac{4\pi}{\hbar c}\sum_n\sum_a \rho^{(s)}_{aa}(0)\omega_{na}|\hat{\mathbf{e}}_r\cdot\boldsymbol{\mu}_{na}|^2\frac{\Gamma_{na}}{(\bar{\omega}_{na}-\omega_r)^2+\Gamma^2_{na}} \ . \tag{2.105}$$

For randomly oriented systems, the average over all orientations of the dipole vector has to be carried out, yielding

$$\alpha^{(1)}_{abs} = \frac{4\pi}{3\hbar c}\sum_n\sum_a \rho^{(s)}_{aa}(0)\omega_{na}|\boldsymbol{\mu}_{na}|^2\frac{\Gamma_{na}}{(\bar{\omega}_{na}-\omega_r)^2+\Gamma^2_{na}} \ . \tag{2.106}$$

Two-Photon Processes: Secondary Radiation, Raman Scattering and Fluorescence

As it has been seen already in the case of one-photon processes, the density matrix formalism yields the transition probability for *all* processes involving the same number of photons. In the case of two-photon processes this means that the distinction between Raman and fluorescence scattering does not exist *a priori* and, depending on the experimental circumstances, these two aspects of secondary radiation may or may not be separated.

The derivation of the two-photon transition probability rate starts with its

definition

$$W^{(2)} = \lim_{t\to\infty} \sum_n \frac{d\rho^{(s)}_{nn}(t)}{dt} = \sum_a \sum_n \lim_{t\to\infty} \int_0^t d\tau \{\hat{M}^{(2)}(\tau)\}_{nn:aa} \hat{\rho}^{(s)}_{aa}(0) \ , \tag{2.107}$$

where the trace of the matrix element of the transition operator (Eqn (2.77b)) over the field variables is

$$\{\hat{M}^{(2)}(p)\}_{nn:aa} = -\{\hat{L}'_{sr}\hat{G}(p)\hat{L}'_{sr}\hat{G}(p)\hat{L}'_{sr}\hat{G}(p)\hat{L}'_{sr}\}_{nn:aa} \ . \tag{2.108}$$

By neglecting in the resolvent operator the effect of the interaction between the molecule and the radiation field, $\hat{G}(p)$ can be written as

$$\hat{G}(p) \approx \hat{G}^{(0)}(p) = \left[p + i\hat{L}_s + i\hat{L}_r + \left\langle \sum^{(0)}(p) \right\rangle_b\right]^{-1} \ , \tag{2.109}$$

where

$$\left\langle \sum^{(0)}(p) \right\rangle_b = \left\langle \hat{L}'_{sb}(p + i\hat{L}_s + i\hat{L}_b)^{-1}\hat{L}'_{sb} \right\rangle \ . \tag{2.110}$$

From the recurrence relation between the transition operators corresponding to consecutive numbers of photons (Eqn (2.81)) the two-photon operator can be expressed as a combination of the appropriate one-photon operators:

$$\begin{aligned} M^{(2)}_{NN:AA}(p) = \frac{1}{\hbar^2}\sum_L \sum_M [&H'_{NM}H'_{LA}G^{(0)}_{MN}(p)G^{(0)}_{LA}(p)M^{(1)}_{MN:LA}(p) \\ &+ H'_{MN}H'_{AL}G^{(0)}_{NM}(p)G^{(0)}_{AL}(p)M^{(1)}_{NM:AL}(p) \\ &- H'_{NM}H'_{AL}G^{(0)}_{MN}(p)G^{(0)}_{AL}(p)M^{(1)}_{MN:AL}(p) \\ &- H'_{MN}H'_{LA}G^{(0)}_{NM}(p)G^{(0)}_{LA}(p)M^{(1)}_{NM:LA}(p)] \end{aligned} \tag{2.111}$$

or, by using $M^{(1)}_{NM:AL} = M^{(1)*}_{MN:LA}$ and $G^{(0)}_{NM}(p) = G^{(0)*}_{MN}(p)$ [29,30,32],

$$\begin{aligned} M^{(2)}_{NN:AA}(p) = \frac{2}{\hbar^2}\mathrm{Re}\sum_L \sum_M [&H'_{NM}H'_{LA}G^{(0)}_{MN}(p)G^{(0)}_{LA}(p)M^{(1)}_{MN:LA}(p) \\ &- H'_{NM}H'_{AL}G^{(0)}_{MN}(p)G^{(0)}_{AL}(p)M^{(1)}_{MN:AL}(p)] \ . \end{aligned} \tag{2.112}$$

With $H'_{AN} \neq 0$ the two matrix elements of the one-photon transition operator in the equation above are, respectively

$$M^{(1)}_{MN:LA}(p) = \frac{1}{\hbar^2}\sum_I H'_{IN}H'_{AI}G^{(0)}_{MI}(p)\delta_{ML} \tag{2.113}$$

and

$$M^{(1)}_{MN:AL}(p) = \frac{1}{\hbar^2}\sum_I [\delta_{NL}H'_{MI}H'_{IA}G^{(0)}_{IN}(p) + \delta_{MA}H'_{IN}H'_{LI}G^{(0)}_{AI}(p)] - \frac{1}{\hbar^2}H'_{MA}H'_{LN}[G^{(0)}_{ML}(p) + G^{(0)}_{AN}(p)] \ . \tag{2.114}$$

Replacing these two matrix elements in Eqn (2.112) yields the matrix element of the two-photon operator [27,29-31]

$$M^{(2)}_{NN:AA}(p) = -\frac{2}{\hbar^2}\mathrm{Re}\sum_L\sum_M H'_{AL}H'_{LN}H'_{NM}H'_{MA}\,[G^{(0)}_{MN}(p)G^{(0)}_{AL}(p)G^{(0)}_{AN}(p) + G^{(0)}_{MN}(p)G^{(0)}_{ML}(p)\,(G^{(0)}_{MA}(p) + G^{(0)}_{AL}(p))] \ . \tag{2.115}$$

It has been shown [32,35] that, by using the relation

$$\begin{aligned} G^{(0)}_{MN}G^{(0)}_{AL}G^{(0)}_{AN} &= G^{(0)}_{MA}G^{(0)}_{LA}G^{(0)}_{AN} + G^{(0)}_{AL}G^{(0)}_{AN}(G^{(0)}_{MN} - G^{(0)}_{MA}(p)) \\ &= G^{(0)}_{MA}G^{(0)}_{AL}G^{(0)}_{AN} + G^{(0)}_{MN}G^{(0)}_{MA}G^{(0)}_{AL}[-1 + (\Gamma_{MA} - \Gamma_{MN} + \Gamma_{AN})G^{(0)}_{AN}] \ , \end{aligned} \tag{2.116}$$

where p has been omitted for simplicity, the transition operator can be separated into three parts, corresponding to three different processes - simultaneous, sequential and mixed - according to the timing between their component one-photon processes. The terms are described, respectively, by:

$$[M^{(2)}_{sim}(p)]_{NN:AA} = \frac{2}{\hbar^4}\mathrm{Re}\,G^{(0)}_{AN}(p)\,|\sum_M H'_{NM}G^{(0)}_{MA}(p)H'_{MA}|^2 \ , \tag{2.117}$$

$$[M^{(2)}_{seq}(p)]_{NN:AA} = \frac{2}{\hbar^4}\mathrm{Re}\sum_L\sum_M H'_{AL}H'_{LN}H'_{NM}H'_{MA}(\Gamma_{MA} - \Gamma_{ML} + \Gamma_{AL}) \times G^{(0)}_{MN}(p)G^{(0)}_{AL}(p)G^{(0)}_{ML}(p)G^{(0)}_{MA}(p) \tag{2.118}$$

and

$$[M^{(2)}_{mix}(p)]_{NN:AA} = \frac{2}{\hbar^4}\mathrm{Re}\sum_L\sum_M H'_{AL}H'_{LN}H'_{NM}H'_{MA}(\Gamma_{MA} - \Gamma_{MN} + \Gamma_{AN}) \times G^{(0)}_{AN}(p)G^{(0)}_{MN}(p)G^{(0)}_{MA}(p)G^{(0)}_{AL}(p) \ . \tag{2.119}$$

By inserting Eqn (2.115) into the relation of definition (Eqn (2.107)) and performing the direct and inverse Laplace transforms involved, the two-photon transition probability rate is given by the formula

$$W^{(2)} = \frac{2}{\hbar^4}\mathrm{Re}\sum_a\sum_{a_r}\sum_N\sum_M\sum_L \rho^{(s)}_{aa}(0)\rho^{(r)}_{a_r a_r}(0)\frac{H'_{AL}H'_{LN}H'_{NM}H'_{MA}}{i\omega_{MA}+\Gamma_{MA}} \times\left[\frac{1}{(i\omega_{AL}+\Gamma_{AL})(i\omega_{AN}+\Gamma_{AN})}+\frac{1}{i\omega_{ML}+\Gamma_{ML}}\left(\frac{1}{i\omega_{MA}+\Gamma_{MA}}+\frac{1}{i\omega_{AL}+\Gamma_{AL}}\right)\right]. \quad (2.120)$$

The transition probability rates for simultaneous, sequential and mixed two-photon processes are, respectively,

$$W^{(2)}_{sim} = \frac{2}{\hbar^4}\sum_a\sum_{a_r}\rho^{(s)}_{aa}(0)\rho^{(r)}_{a_r a_r}(0)\sum_N\frac{\Gamma_{NA}}{\omega^2_{NA}+\Gamma^2_{NA}}\left|\sum_M\frac{H'_{NM}H'_{MA}}{i\omega_{MA}+\Gamma_{MA}}\right|^2, \quad (2.121a)$$

$$W^{(2)}_{seq} = \frac{2}{\hbar^4}\mathrm{Re}\sum_a\sum_{a_r}\rho^{(s)}_{aa}(0)\rho^{(r)}_{a_r a_r}(0)\sum_N\sum_M\sum_L H'_{AL}H'_{LN}H'_{NM}H'_{MA} \times\frac{\Gamma_{MA}-\Gamma_{ML}+\Gamma_{AL}}{(i\omega_{MA}+\Gamma_{MA})(i\omega_{AL}+\Gamma_{AL})(i\omega_{MN}+\Gamma_{MN})(i\omega_{ML}+\Gamma_{ML})} \quad (2.121b)$$

and

$$W^{(2)}_{mix} = \frac{2}{\hbar^4}\mathrm{Re}\sum_a\sum_{a_r}\sum_N\rho^{(s)}_{aa}(0)\rho^{(r)}_{a_r a_r}(0)\frac{\Gamma_{AN}}{\omega^2_{AN}+\Gamma^2_{AN}}\sum_M\sum_L H'_{AL}H'_{LN}H'_{NM}H'_{MA} \times\frac{\Gamma_{MA}-\Gamma_{MN}+\Gamma_{AN}}{(i\omega_{MA}+\Gamma_{MA})(i\omega_{AL}+\Gamma_{AL})(i\omega_{MN}+\Gamma_{MN})}. \quad (2.121c)$$

Separating the elastic and inelastic terms in the damping constants (Eqn (2.58)) in the denominators in Eqns (2.122) and (2.123) yields

$$\Gamma_{MA}-\Gamma_{ML}+\Gamma_{AL} = \Gamma_{AA}+\Gamma^{(d)}_{MA}-\Gamma^{(d)}_{ML}+\Gamma^{(d)}_{AL} \quad (2.122a)$$

and

$$\Gamma_{MA}-\Gamma_{MN}+\Gamma_{AN} = \Gamma_{AA}+\Gamma^{(d)}_{MA}-\Gamma^{(d)}_{MN}+\Gamma^{(d)}_{AN}. \quad (2.122b)$$

If the initial state of the system is stable (most common case) then $\Gamma_{AA}\rightarrow 0$ and

$$\Gamma_{MA}-\Gamma_{ML}+\Gamma_{AL} \rightarrow \Gamma^{(d)}_{MA}-\Gamma^{(d)}_{ML}+\Gamma^{(d)}_{AL} \quad (2.123a)$$

and

$$\Gamma_{MA}-\Gamma_{MN}+\Gamma_{AN} \rightarrow \Gamma^{(d)}_{MA}-\Gamma^{(d)}_{MN}+\Gamma^{(d)}_{AN}. \quad (2.123b)$$

This result shows the extent to which pure-dephasing, the origin of the elastic part of the damping constant, controls the intensity of the sequential and mixed

two-photon processes. It can be seen that the separation of secondary radiation (all two-photon scattering processes) into pure Raman, pure stimulated emission and mixed processes cannot be achieved except for the special case of no pure-dephasing present, when only the value of the pure Raman scattering term is different from zero.

This is the most important conclusion of this chapter, as the need for separation between pure Raman scattering and pure stimulated emission intensities has occurred during some of my early experimental work (Appendix 2). The interpretation of the results will not be possible on the basis of the transform theory, used in interpreting the rest of the experimental data (chapter 5).

Pure-dephasing and Secondary Radiation: an experimental view

Examining the three terms (Eqns (2.121a-c)) of the two-photon transition probability, it can be noticed that $W_{sim}^{(2)}$ leads to a spectrum with resonances at the ground electronic state vibrational frequencies ω_{NA}, while $W_{seq}^{(2)}$ leads to resonances at frequencies corresponding to the spacing between vibrational levels of the excited and ground electronic states ω_{MA}, ω_{AL} and ω_{MN}; $W_{mix}^{(2)}$ shows resonances of both types, hence its "mixed" character. $W_{sim}^{(2)}$ (Eqn (2.121a)) is very similar to the Kramers-Heisenberg formula and corresponds to the Raman part of a two-photon process. $W_{seq}^{(2)}$ and $W_{mix}^{(2)}$ exist only in the presence of pure-dephasing and it is generally accepted [31,35-37] that the mixed term can be neglected.

Experimental studies [31] have confirmed this conclusion and identified two main mechanisms for pure-dephasing: quasi-elastic collisions of the "system" molecules, undergoing resonance scattering, with the molecules of the "solvent" (material-induced pure-dephasing) and stochastic fluctuations of the exciting radiation field interacting with the "system" (radiation-induced pure-dephasing).

Quasi-elastic collisions can make a noticeable contribution to the coherence loss (damping) between two states involved in a transition when the mean collision time is comparable with the lifetime of the states involved. This contribution will not be noticeable in low density or low temperature samples, when the mean collision time is relatively long. Experiments presented in Part I of [31] show that material-induced pure-dephasing is negligible in the absence of collisions - the mean time between collisions is much longer than the lifetime of the excited state decay. For solid state samples, this means that this pure-dephasing mechanism can be neglected, which is particularly relevant for the experimental cases studied in chapter 5.

Random fluctuations in the exciting radiation field can contribute to the line broadening when the linewidth of the exciting radiation is comparable with the reciprocal of the lifetime of the states involved in the transition. Experiments presented in Part II of [31] show that pure-dephasing of transitions with corresponding bandwidths of 1 cm^{-1} is negligible for excitation with lines narrower than 1 cm^{-1} - both single-mode dye lasers and noble gas ion lasers (Ar^+, Kr^+) fall into this category. This is particularly relevant to the experimental cases studied in chapter 5, as the Raman linewidths observed there are much greater than the linewidths of the laser light producing the excitation and so the radiation-induced pure-dephasing can be neglected.

The work will proceed towards a transform relation by assuming that both main mechanisms of pure-dephasing produce negligible contributions to damping. Hence, the resonance secondary radiation observed experimentally is assumed to contain only resonance Raman radiation, with a transition probability being given by $W_{sim}^{(2)}$. Experimental cases which do not fit this assumption can be studied as in [36] by employing a multimode, "total simulation" approach, based on the equations derived in [37]; this approach requires ample computing resources and it will not be pursued here.

III. Transform Relation between Resonance Raman and Absorption Spectra

Introduction

H. A. Kramers and R. de L. Kronig [38,39] have shown that the real and imaginary parts of the complex electric susceptibility are related through a pair of simple mathematical relations, called dispersion relations, analogous to the transform relation between a Hilbert pair. As a consequence, the complex polarizability is fully determined when the absorption coefficient is known at all frequencies and it has been shown [40-52] that, under certain assumptions, the *absorption and resonance Raman scattering cross-sections* can be related through a Kramers-Kronig dispersion (or transform) relation.

Resonance Raman scattering intensity and cross-section are usually calculated under certain "standard assumptions": resonance Raman scattering involves only one excited electronic state and one vibrational mode; the vibrational Hamiltonian is quadratic in the normal coordinate of the mode in resonance (the mode is not coupled with any others and its vibrational frequency is the same in the ground and excited electronic states); the electronic transition moment does not depend on the normal coordinate of the mode undergoing resonance (the Condon approximation); the electronic and vibronic (nuclear) variables are independent of each other (the Born-Oppenheimer approximation).

The aim of this chapter is to establish a transform relation between resonance Raman scattering and optical absorption cross-sections, in the least restrictive model possible. The assumptions of a single electronic state (Albrecht's A-term [53] scattering only) and a single, uncoupled mode involved in resonance Raman scattering will be preserved. Beyond that, the Born-Oppenheimer approximation will be relaxed to a very large extent, the electronic transition moment will be allowed to depend in the first order on the normal coordinate of the mode undergoing resonance (*linear* non-Condon contributions) and the

vibrational force constant will be allowed to depend *linearly* on the same normal coordinate (the vibrational frequency will be allowed to change by up to 20% between the ground and excited electronic states).

The transform relation will be established here for an arbitrary order of scattering, employing the time-correlator formalism developed by Hizhnyakov and Tehver [41] according to the assumptions listed in the previous paragraph. The result will be a multivariable, non-linear, non-analytic equation which will be solved numerically, using the method to be developed in Chapter 4, and the results will be given in Chapter 5 for a number of experimental cases.

The Kramers-Kronig Dispersion Relations

In the linear approximation of the electromagnetic theory, the polarisation $\boldsymbol{P}(t)$ of a physical system is related *linearly* to an applied electric field $\boldsymbol{E}(t)$ through

$$\boldsymbol{P}(t) = (2\pi)^{-1/2} \int_{-\infty}^{\infty} \chi(t-t')\boldsymbol{E}(t')\mathrm{d}t' . \tag{3.1}$$

By using the convolution theorem [20] between Fourier transforms, Eqn (3.1) becomes

$$\boldsymbol{P}(\omega) = \chi(\omega) * \boldsymbol{E}(\omega) , \tag{3.2}$$

where $\chi(\omega)$ is the complex linear polarizability. H. D. Kramers and R. L. Kronig have shown [38,39] that the real and imaginary parts of $\chi(\omega)$ form a Hilbert pair

$$\mathrm{Re}[\chi(\omega)] = \frac{1}{\pi} \mathrm{P} \int_{-\infty}^{\infty} \frac{\mathrm{Im}[\chi(x)]}{x-\omega} \mathrm{d}x \tag{3.3a}$$

$$\mathrm{Im}[\chi(\omega)] = -\frac{1}{\pi} \mathrm{P} \int_{-\infty}^{\infty} \frac{\mathrm{Re}[\chi(x)]}{x-\omega} \mathrm{d}x , \tag{3.3b}$$

where P represents the principal value of the integral; for experimentally viable frequencies (real and positive), Eqns (3.3a) and (3.3b) become

$$\mathrm{Re}[\chi(\omega)] = \frac{2}{\pi} \mathrm{P} \int_{0}^{\infty} \frac{x\,\mathrm{Im}[\chi(x)]}{x^2-\omega^2} \mathrm{d}x , \tag{3.4a}$$

$$\mathrm{Im}[\chi(\omega)] = -\frac{2\omega}{\pi}\mathrm{P}\int_0^\infty \frac{\mathrm{Re}[\chi(x)]}{x^2-\omega^2}dx \ . \tag{3.4b}$$

Equations (3.4a) and (3.4b) represent the Kramers-Kronig dispersion relations; in conjunction with the relationship between the absorption coefficient $\mu(\omega)$ (from the Beer-Lambert law, Eqn (1.27)) and the complex linear polarizability, $\mu(\omega) = (2\omega/c)\,\mathrm{Im}[1+4\pi\chi(\omega)]^{1/2}$, they yield the following relationship between the complex polarizability $\chi(\omega)$ and the absorption cross-section ABS(ω) [40-42,55]:

$$\chi(\omega) \equiv \Phi(\omega) = \frac{2}{\pi}\mathrm{P}\int_0^\infty \frac{\mathrm{ABS}(x)}{x^2-\omega^2}dx + \mathrm{i}\frac{\mathrm{ABS}(\omega)}{\omega} \ . \tag{3.5}$$

Obtaining the detailed relationship between the resonance Raman scattering cross-section and the absorption cross-section will be the scope of the time correlator formalism described in the following sections.

The Resonance Raman and Absorption Time-Correlators

The calculation of the time correlators starts by considering the Raman scattering from a sample of randomly oriented molecules, between an initial molecular eigenstate *i*, and a final molecular eigenstate *f*; the incident laser frequency is ω_L and all the light scattered in all polarizations over 4π steradians at $\omega_L - \omega_{fi}$ (integrated over the linewidth) is measured. The scattering cross-section per molecule is given as [53]

$$\sigma_R^{fi}(\omega_L) = \frac{8\pi(\omega_L-\omega_{fi})^4}{9c^4\hbar^2}\sum_{\rho,\sigma} |[\alpha_{\rho\sigma}(\omega_L)]_{fi}|^2 \ , \tag{3.6}$$

in which $[\alpha_{\rho\sigma}(\omega_L)]_{fi}$ is just the *f,i*-th matrix element of the molecule-based $\rho\sigma$-th Cartesian tensor element of the complex molecular electrical susceptibility (the "molecular polarizability") and the circular Bohr frequency corresponding to the *f,i*-th energy gap is $\omega_{fi} = \Delta E_{fi}/\hbar$. The frequency domain expression for $[\alpha_{\rho\sigma}(\omega_L)]_{fi}$ is the anisotropic version of the transition probability rate $W_{sim}^{(2)}$ (Eqn (2.121a)) expressed as cross-section, in which the incident field has been assumed to be monochromatic and the thermal population of all other molecular levels apart from $a \equiv i$, is taken to be negligible at equilibrium:

$$[\alpha_{\rho\sigma}(\omega_L)]_{fi} = \sum_e \left(\frac{\langle f|\rho|e\rangle\langle e|\sigma|i\rangle}{\omega_{ei} - \omega_L - i\gamma_{ei}} + \frac{\langle f|\sigma|e\rangle\langle e|\rho|i\rangle}{\omega_{ef} + \omega_L + i\gamma_{ie}} \right); \quad (3.7)$$

the sum is over all molecular eigenstates e, γ_{ei} represents the dephasing rate constant for an e,i coherence, and ρ and σ are molecule-based Cartesian components of the macroscopic electric dipole operator.

When near- or in-resonance with an electronic transition, the principal contribution to $[\alpha_{\rho\sigma}(\omega_L)]_{fi}$ will be from the resonance that arises in the first term of Eqn (3.7). To arrive at general transform expressions for the resonant scattering of fundamentals and overtones, including non-Condon effects, by employing the recursion relations developed by Hizhnyakov and Tehver [52], the terms of Eqn (3.7) that are near resonant are placed in the time-domain by writing the complex denominator through its half-Fourier transform:

$$[\alpha_{\rho\sigma}(\omega_L)]_{fi} = i\int_0^\infty d\tau e^{i\tau\omega_L} \sum_e \langle f|\rho|e\rangle\langle e|\sigma|i\rangle \exp[-i\tau(\omega_{ei} - i\gamma_{ei})] \; . \quad (3.8)$$

The sum on e in Eqn (3.8) can be closed provided that the dephasing rate constant, γ_{ei}, is algebraically separable ($\gamma_{ei} = \gamma_e + \gamma$), as already is the frequency difference ($\omega_{ei} \equiv \omega_e - \omega_i$). In the most general case, when the pure-dephasing constant $\gamma_{ei}^{(d)}$ depends on both indices e and i, the separation is made impossible by the very notion of pure-dephasing (Eqns (2.58), (2.61)). The separation is achieved only in the assumption of negligible pure-dephasing, as discussed at the end of Chapter 2.

A non-Hermitian Hamiltonian is introduced, H, which consists of the full (Hermitian) molecular Hamiltonian, H, and an anti-Hermitian damping operator, D, such that (in circular frequency):

$$H|e\rangle = \omega_e|e\rangle, \quad D|e\rangle = i\gamma_e|e\rangle; \quad \text{or} \quad H|e\rangle = (\omega_e + i\gamma_e)|e\rangle \; . \quad (3.9)$$

Introducing H defined in this way into Eqn (3.8) and closing on the complete

molecular eigenstate basis set {|*e*>}, yields

$$\left[\alpha_{\rho\sigma}(\omega_L)\right]_{fi} = i\int_0^\infty d\tau e^{i\tau\omega_L} <f|\rho e^{-i\tau H^\dagger} \sigma e^{i\tau H}|i> \ . \tag{3.10}$$

By defining the time correlator $[A_{\rho\sigma}]_{fi}$ as [40-42,55,56] (see also [52] for conjugate form)

$$[A_{\rho\sigma}]_{fi} = i\theta(\tau) <f|\rho e^{-i\tau H^\dagger} \sigma e^{i\tau H}|i> \ , \tag{3.11}$$

where $\theta(\tau)$ is the Heaviside step function, the matrix element of the molecular susceptibility (Eqn (3.6)) for the two photon $f \leftarrow i$ transition can be written as

$$[\alpha_{\rho\sigma}(\omega_L)]_{fi} = \int_{-\infty}^\infty d\tau e^{i\tau\omega_L} [A_{\rho\sigma}]_{fi} \ . \tag{3.12}$$

Within the same assumptions as for resonance Raman scattering, and using Eqn (2.94), the matrix element of the molecular susceptibility for a one-photon transition from the *i*-th *molecular* level into all reasonably excited states in an isotropic medium can be written as

$$[\alpha_{\rho\rho}(\omega_L)]_{ii} = \int_{-\infty}^\infty d\tau e^{i\tau\omega_L} [A_{\rho\rho}]_{ii} \ , \tag{3.13}$$

with the absorption correlator being given by

$$[A_{\rho\rho}]_{ii} = i\theta(\tau) <i|\rho e^{-i\tau H^\dagger} \rho e^{i\tau H}|i> \ . \tag{3.14}$$

With the relations above, the task of connecting the resonance Raman and absorption scattering cross-sections has been reduced to expressing the resonance Raman correlator as a function of the absorption correlator. This will be achieved by letting the exponential operators in the correlators to operate on the *i* and *f* eigenstates, which will require the consideration of two issues: the nature of the molecular states *i* and *f* - and hence the need for some form of Born-Oppenheimer approximation - and the particular shape of the Hamiltonians, i.e. the nature of the vibronic coupling. Before proceeding with these two issues, a brief look at the temperature and ensemble effects is needed, for it may affect the relationship between the absorption and resonance Raman scattering cross-sections.

The Limited Born-Openheimer Approximation

Considering the $3N$-6 nuclear coordinates of a polyatomic molecule, electronic absorption and Raman scattering are multimode in essence, often involving a significant part of this $3N$-6 dimensional space. On the other hand, Raman scattering can focus on the scattering of a single mode at a time, the remaining $3N$-7 space participating in the REP much as it does in ABS. This can be formalised [55] in a most general form by requiring that the molecular Hamiltonian be parameterized only in the normal coordinate of the scattered vibration, the remaining $3N$-7 nuclear coordinates and all electronic coordinates serving as true variables.

This limited Born-Oppenheimer approximation rests upon the assumption that mode-mixing (Duschinsky rotation) between the mode of interest and the $3N$-7 space is negligible; when this not the case, the Born-Oppenheimer approximation limited to one coordinate must be relieved and extended to include the full sub-space of the mixing modes. In fact the present one-dimensional adiabatic approximation might be thought of as the usual complete ($3N$-6 space) parameterization of the electronic Hamiltonian, followed by perturbative corrections of the eigenstates and eigenvalues to all orders in the $3N$-7 displacement coordinates. The molecular eigenstates can be separated now between the mode of interest and the $3N$-7 space:

$$|i\rangle \rightarrow |g'\rangle|i\rangle, \tag{3.15a}$$

$$|f\rangle \rightarrow |g'\rangle|f\rangle \tag{3.15b}$$

and

$$|e\rangle \rightarrow |e'\rangle|e\rangle\ . \tag{3.15c}$$

This limited adiabatic approach [55,59] allows considerable generality in the ($3N$-7) non-Raman space, including variable damping parameters as well as non-adiabatic effects to all orders. The usual potential energy hypersurfaces are formally absent, leaving only one-dimensional potential energy curves in the

scattered coordinate. The molecular eigenenergies are parametric only in Q_a (the normal coordinate of the scattered mode) and are expanded in Q_a around equilibrium positions. The molecular eigenstates will cluster in groups $\{e'\}$, $\{g'\}$ to produce (normally) nearly harmonic potential curves $V_{e'}(Q_a)$ and $V_{g'}(Q_a)$ with well-defined equilibrium positions and second derivatives (force constants). This grouping corresponds to the conventional concept of a resonant and a ground electronic state each with well defined vibrational levels.

The Effect of Temperature and Ensemble Averaging

In the laboratory, an observed linear absorption cross-section, ABS(ω), represents an ensemble-averaged cross-section over all initial states recognizing both the thermal distribution of molecules over initial states as well as a possible site distribution, or inhomogeneity of vibronic frequencies. Thus for $\Omega_{g',j}$, representing the weighting of thermal and other broadening effects of the initial state $\{|g'\rangle|j\rangle\}$, the observable absorption cross-section is [55]

$$\mathrm{ABS}(\omega) = \frac{3c}{4\pi}\sum_{g',j}\Omega_{g',j}\sigma_A^{\,jj}(\omega) \qquad (3.15d)$$

and similarly for the observed resonance Raman spectrum or Raman excitation profile (REP(ω)):

$$\mathrm{REP}(\omega) = \sum_{g',j}\Omega_{g',j}\sigma_R^{\,j(j+n)}(\omega)\ . \qquad (3.15e)$$

In both cases the g' label on the cross-sections is suppressed for convenience.

As the absorption cross-section (Eqn (3.13)) is *linear* in the correlator while the resonance Raman scattering cross-section is *quadratic* in the correlator (Eqns (3.6) and (3.14)), Eqns (3.15) and (3.16) represent ensemble averaging of the correlator on the linear and quadratic level, respectively. The link between ABS and REP is formally ensemble and temperature dependent; this problem has been addressed by the early studies of the transform relation [41,55], where sample cases have been explored. Further work by Chan and Page [57,58] has found that the temperature averaging implied in ABS represents a good

approximation for the REP, for systems with many thermally-populated low-frequency modes which lead to absorption spectra with overlapping vibronic structures . This conclusion has been accepted here, and the systems studied in Chapter 5 are deemed suitable from this point of view.

It has to be pointed out that temperature averaging is implicitly present at amplitude level in the 3*N*-7 space, in the limited adiabatic treatment used here. It is expected that for the systems treated here — scattering from modes whose frequencies are considerably larger than kT (see Chapter 5) — this approach to temperature and ensemble averaging is satisfactory.

The Correlators in the Limited Born-Oppenheimer Approximation

For resonance Raman scattering, two potential energy curves are involved [52,60], $V_2(Q_a)$ (upper) and $V_1(Q_a)$ (lower), with the Hermitian nuclear Hamiltonians H_2 and H_1. For harmonic potentials these operators are

$$H_2 = T_2 + V_2 = \omega_2\left(\hat{a}_2^\dagger \hat{a}_2 + \frac{1}{2}\right) \tag{3.16a}$$

$$H_1 = T_1 + V_1 = \omega_1\left(\hat{a}_1^\dagger \hat{a}_1 + \frac{1}{2}\right), \tag{3.16b}$$

having eigenkets $\{|j_2\rangle\}$ and $\{|j_1\rangle\}$, respectively.

Furthermore, for the *n*-th overtone transition of a given mode in the ground electronic state the molecular states can be written as (Eqn (3.15a,b)):

$$|i\rangle \rightarrow |g')|j_1\rangle \equiv |g')|j\rangle \tag{3.17a}$$

$$|f\rangle \rightarrow |g')|j_1 + n_1\rangle \equiv |g')|j + n\rangle \ , \tag{3.17b}$$

in which the subscripts 1 for the ground state are henceforth removed for simplicity. For the molecular eigenstate associated with resonances, Eqn (3.15c) becomes:

$$|e\rangle \rightarrow |e')|j_2\rangle \ . \tag{3.17c}$$

Equations (3.17a,b) recognize the partitioning of the molecular Hamiltonian, H:

$$H \rightarrow H_{g'} + H_1 \ , \quad \text{with } H_{g'}|g') = \omega_{g'}|g') \ , \tag{3.18a}$$

and Eqn (3.17c) the partitioning of H:

$$H \rightarrow H_{e'} + H_2 \ , \quad \text{with } H_{e'}|e') = \omega_{e'}|e') \ , \tag{3.18b}$$

in which $H_{g'}$ and $H_{e'}$ are not just the electronic Hamiltonians evaluated at ground and excited state equilibrium positions of the Raman-active normal coordinate, but also include the full $3N$-7 nuclear coordinates of the non-Raman space without further approximation. The sum over molecular eigenstates also recognizes this factoring of state space with:

$$\sum_{e} \rightarrow \sum_{e'} \sum_{j_2} \ , \tag{3.19a}$$

in which the states $\{e'\}$ are those that carry transition dipole strength between the ground state and the resonant electronic band. Furthermore, whenever the damping parameter appears, it, too, is partitioned into the two spaces (in the limit of negligible pure-dephasing):

$$\gamma_{ei} \rightarrow \gamma_{e'i'} + \gamma_{j_2 j_1} = \gamma_{e'i'} + \gamma \ , \tag{3.19b}$$

in which $\gamma_{j_2}\gamma_{j_1}$ represents the damping contribution from the Raman sub-space only and it is conventionally taken to be a constant, γ, for all relevant $\{j_2 j_1\}$. For many applications at ordinary temperature j_1 is often a Raman mode with negligible thermal excitation, whose $\gamma_{j_1} = 0$. In that case $\gamma_{j_2} = \gamma$ and the decay parameter of the Raman mode in the excited 'electronic' state does not change with its degree of excitation; however, the $\gamma_{e'i'}$ contribution to the damping can vary with the energy of excitation in an unconstrained manner. Li and Champion have explored a model that relieves the constant γ assumption as applied to transform theory [61].

The limited Born-Oppenheimer approximation leads now to the relabelling of the scattering cross-section:

$$\sigma_R^{fi} \rightarrow \sigma_R^{(j+n)j} \ . \tag{3.19c}$$

With this limited adiabatic point of view (Eqns (3.15, 3.17-3.19)) and the harmonic oscillator Hamiltonians (Eqns (3.16, 3.18)), closing the sum on j_2, but

not on e' in Eqn (3.8) gives

$$[\alpha_{\rho\sigma}(\omega_L)]_{g'(j+n),g'j} = i\int_0^\infty d\tau e^{i\tau\omega_L} e^{-\tau\gamma} \times \sum_{e'} \langle j+n|(g'|\rho|e')e^{-i\tau H_2}(e'|\sigma|g')e^{i\tau H_1}|j\rangle \exp[-i\tau(\omega_{e'g'} - i\gamma_{e'g'})] \ . \tag{3.20}$$

Writing the Cartesian components of the electric transition moment in the non-Raman space as $(M_\rho)_{g'e'} \equiv (g'|\rho|e')$, $(M_\sigma)_{e'g'} \equiv (e'|\sigma|g')$, the Raman correlator (Eqn (3.11)) becomes:

$$[A_{\rho\sigma}(\tau)]_{j+n,j} = i\theta(\tau)e^{-\gamma\tau}\sum_{e'} e^{-i\tau(\omega_{e'g'} - i\gamma_{e'g'})}\langle j+n|(M_\rho)_{g'e'}e^{-i\tau H_2}(M_\sigma)_{e'g'}e^{i\tau H_1}|j\rangle \tag{3.21}$$

and the matrix element of the molecular polarisability (Eqn (3.6)) becomes now

$$[\alpha_{\rho\sigma}(\omega_L)]_{j+n,j} = \int_{-\infty}^{\infty} d\tau\, e^{i\tau\omega_L}[A_{\rho\sigma}(\tau)]_{j+n,j} \ . \tag{3.22}$$

Equation (3.21) is close to the expression given by [52] except for the use of the limited Born-Oppenheimer approximation and a more conventional expression for the Raman polarizability (Eqn (3.7)). Throughout this work the development is consistently the (negative) conjugate of that presented in [52]; wherever the phase of the representation of correlators and polarisabilities is ϕ in [52], here it is $\pi - \phi$. This remark will allow the use of the recursion relations developed in [52], although formally their starting equation is the complex conjugate form of the more conventional form employed in Eqn (3.7).

At the same time the absorption correlator (Eqn (3.14)) becomes

$$[A_{\rho\rho}(\tau)]_{j,j} = i\theta(\tau)e^{-\gamma\tau}\sum_{e'} e^{-i\tau(\omega_{e'g'} - i\gamma_{e'g'})}\langle j|(M_\rho)_{g'e'}e^{-i\tau H_2}(M_\rho)_{e'g'}e^{i\tau H_1}|j\rangle \tag{3.23}$$

and the corresponding matrix element (Eqn (3.13)) can be written as

$$[\alpha_{\rho\rho}(\omega_L)]_{j,j} = \int_{-\infty}^{\infty} d\tau e^{i\tau\omega_L}[A_{\rho\rho}(\tau)]_{j,j} \ . \tag{3.24}$$

This is just the diagonal matrix element of the $\rho\rho$-th Cartesian tensor

component of the vibronic absorption correlator. The crucial point of the derivation of a transform relation is to link the ρρ-th Cartesian tensor component of the diagonal [(*j*,*j*)] vibronic absorption correlator (Eqn (3.23)) to the off-diagonal version [(*j*+*n*,*j*)] (Eqn (3.21)). In the present case, the next step will be to establish a relationship between the resonance Raman and absorption correlators in the non-Condon approximation (Eqn (3.23), (3.21)) and the correlators written in the Condon approximation, for which recurrence relations exist in all orders [52]. Recognizing that the ladder operators of two different harmonic oscillators are linearly related, Hizhnyakov and Tehver have presented a particularly succinct algebra for accomplishing this task [52].

The Relationship between Non-Condon and Condon Correlators

The *n*-th order Raman correlator (Eqn (3.21)) will be examined while considering only the resonance with a uniquely polarized transition (ρ = σ) and a linear dependence of the molecular transition moment $(M_\rho)_{g'e'}$ on the coordinate of the Raman- active vibration - a linear non-Condon coupling. Thus

$$(M_\rho)_{g'e'} = (M_\rho)^{(0)}_{g'e'}[1 + m(\hat{a}_1 + \hat{a}_1^\dagger)] \ , \qquad (3.25)$$

in which *m* is the dimensionless vibronically induced transition moment in units of the allowed transition moment and $\hat{a}_1$ and $\hat{a}_1^\dagger$ are the raising and lowering (ket side) operators in the space of the ground state oscillator. The parameter *m* is a dimensionless average parameter representing the linear non-Condon coupling of the transition moment to the Raman-active mode (whose ground state harmonic potential is characterized by the raising and lowering operators $\hat{a}_1^\dagger$ and $\hat{a}_1$). This non-Condon coupling parameter, *m*, can be read also as the fractional change of the transition moment caused by one rms displacement along the Raman mode coordinate in the ground state [55]. $(M_\rho)^{(0)}_{g'e'}$ continues to contain implicitly all of the nuclear coordinates of the (3*N*-7) non-Raman space including their unconstrained 'Condon' and 'non-Condon' role [55,62]. It is only the Raman active coordinate that has been treated explicitly at the linear non-Condon level.

In considering a specific molecule-based Cartesian transition moment (ρ), the possibility of a rotating moment with (*e'*, *g'*) has been excluded; also, to maintain the separability of the Raman space from the non-Raman space the dimensionless non-Condon coupling constant, *m*, has to be assumed independent of the 3*N*-7 variables (*e'*, *g'*), being therefore an "average" non-Condon coupling parameter in (e', g'). These constraints, however, are standard in the usual full Born-Oppenheimer approach to the problem.

The derivation will proceed with the introduction of a simplified notation:

$$\hat{M} \equiv [1 + m(\hat{a}_1 + \hat{a}_1^{\dagger})] \ , \qquad \hat{B} \equiv e^{-i\tau H_2} \ , \qquad \hat{C} \equiv e^{i\tau H_1} \ . \tag{3.26}$$

The matrix element in the correlator (Eqn (3.21)) can be written now as

$$<j+n|\,(M_\rho)_{g'e'}\, e^{-i\tau H_2} (M_\rho)_{e'g'}\, e^{i\tau H_1}|j> \;=\; \left|(M_\rho)^{(0)}_{g'e'}\right|^2 <j+n|\hat{M}\hat{B}\hat{M}\hat{C}|j> \tag{3.27}$$

and then the *n*-th order resonance Raman correlator (Eqn (3.21)) becomes

$$A_n^{NC}(\tau) \;=\; i\theta(\tau) e^{-\gamma\tau} \sum_{e'} e^{-i\tau(\omega_{e'g'} - i\gamma_{e'g'})} \left|(M_\rho)^{(0)}_{g'e'}\right|^2 <j+n|\hat{M}\hat{B}\hat{M}\hat{C}|j> \ , \tag{3.28}$$

where $[A_{\rho\sigma}(\tau)]_{j,j+n} \approx A_n^{NC}(\tau)$ for the single polarisation considered in the present linear non-Condon approximation.

Given that $<n| = <0|(\hat{a}_1)^n (n!)^{-1/2}$, the powers of the ladder operators are written for convenience as $(\hat{a}_1)^n \equiv \hat{A}_n(1)$; by taking $j = 0$ to dominate the correlator for the j part of the thermal average in Eqs. (3.15), (3.16) ($\hbar\omega_1 >> k_B T$) the resonance Raman correlator in the present model becomes

$$A_n^{NC}(\tau) \approx i\theta(\tau)(n!)^{-1/2} e^{-\gamma\tau} \sum_{e'} e^{-i\tau(\omega_{e'g'} - i\gamma_{e'g'})} \left|(M_\rho)^{(0)}_{g'e'}\right|^2 <0|\hat{A}_n(1)\hat{M}\hat{B}\hat{M}\hat{C}|0> \tag{3.29}$$

and the absorption correlator ($n = 0$)

$$A_0^{NC}(\tau) \approx i\theta(\tau) e^{-\gamma\tau} \sum_{e'} e^{-i\tau(\omega_{e'g'} - i\gamma_{e'g'})} \left|(M_\rho)^{(0)}_{g'e'}\right|^2 <0|\hat{M}\hat{B}\hat{M}\hat{C}|0> \ . \tag{3.30}$$

The approximate thermal averaging achieved at the correlator level [52,63], remains in effect here as well, as far as the 3*N*-7 non-Raman space (the averaging over *g'*) is concerned; it is only the Raman space (the *j* space) that

has been truncated to the unexcited level.

The derivation will proceed now by first transforming $\hat{M}$ into a function only of $\hat{a}_2$ and $\hat{a}_2^\dagger$, the raising and lowering operators for the harmonic potential of the excited electronic state. The second $\hat{M}$ in the non-Condon matrix element is passed through $\hat{B}$ by using a commutation relation, the result is reconverted to a function of $\hat{a}_1$ and $\hat{a}_1^\dagger$, then together with the remaining $\hat{M}$ the net operation is performed on the left upon $\hat{A}_n(1)$.

The general linear relationship between the two sets of raising and lowering operators of two harmonic potential energy curves 1 and 2 is [52,60]

$$\hat{a}_2^\dagger = p + q\hat{a}_1^\dagger + r\hat{a}_1 \tag{3.31a}$$

and its complex conjugate

$$\hat{a}_2 = p + q\hat{a}_1 + r\hat{a}_1^\dagger \ , \tag{3.31b}$$

where $\{p, q, r\}$ are dimensionless constants fixed by the Manneback equations (Appendix 3); p relates to the displacement for the two potential energy curves, q and r to the changes in their characteristic frequencies. Combining Eqns (3.31a,b) in Eqn (3.25) yields

$$\hat{M} = 1 - \frac{2mp}{q+r} + \frac{m}{q+r}(\hat{a}_2^\dagger + \hat{a}_2) \ . \tag{3.32}$$

Using the completeness relation $\sum_n |n><n| = 1$ and the effect of operators on molecular eigenstates it follows that

$$\begin{aligned} \hat{a}_2 e^{-i\tau H_2} &= \sum_{n_2} \hat{a}_2 |n_2><n_2| e^{-i\tau H_2} = \sum_{n_2} n_2^{1/2} e^{-i\tau n_2\omega_2} |n_2 - 1><n_2| \\ &= e^{-i\tau\omega_2} \sum_{n_2} e^{-i\tau H_2} n_2^{1/2} |n_2 - 1><n_2| = e^{-i\tau\omega_2} e^{-i\tau H_2} \hat{a}_2 \sum_{n_2} |n_2><n_2| \\ &= e^{-i\tau\omega_2} e^{-i\tau H_2} \hat{a}_2 \ , \end{aligned} \tag{3.33}$$

which can be used to prove the identity

$$\langle i|\hat{B}\hat{A}_n(1)\hat{C}|i\rangle = e^{-i\tau n\omega_1}\langle i|\hat{B}\hat{C}\hat{A}_n(1)|i\rangle = \langle i|\hat{C}\hat{A}_n^{\dagger}(1)\hat{B}|i\rangle = e^{i\tau n\omega_1}\langle i|\hat{A}_n^{\dagger}(1)\hat{C}\hat{B}|i\rangle \quad (3.34)$$

and consequently

$$\hat{B}\hat{M} = \hat{B}\left(1-\frac{2mp}{q+r}\right) + \frac{m}{q+r}\left(\hat{a}_2^{\dagger}e^{-i\tau\omega_2} + \hat{a}_2 e^{i\tau\omega_2}\right)\hat{B} \ . \quad (3.35)$$

Reverting now to the $\hat{a}_1$ and $\hat{a}_1^{\dagger}$ operators by using Eqns (3.31a,b) yields

$$\begin{aligned}\hat{B}\hat{M} = &\left[1-\frac{2mp}{q+r}+\frac{mp}{q+r}\left(e^{-i\tau\omega_2}+e^{i\tau\omega_2}\right)\right]\hat{B} \\ &+m\left(\frac{q}{q+r}e^{-i\tau\omega_2}+\frac{r}{q+r}e^{i\tau\omega_2}\right)\hat{a}_1^{\dagger}\hat{B}+m\left(\frac{r}{q+r}e^{-i\tau\omega_2}+\frac{q}{q+r}e^{i\tau\omega_2}\right)\hat{a}_1\hat{B} \ .\end{aligned} \quad (3.36)$$

With Eqn (3.36) for $\hat{B}\hat{M}$, $\langle 0|\hat{A}_n(1)\hat{M}\hat{B}\hat{M}\hat{C}|0\rangle$ is constructed as

$$\begin{aligned}\langle 0|\hat{A}_n(1)\hat{M}\hat{B}\hat{M}\hat{C}|0\rangle = &\left[1+\frac{mp}{q+r}\left(e^{i\tau\omega_2}+e^{-i\tau\omega_2}-2\right)\right]\langle 0|\hat{A}_n(1)\hat{B}\hat{C}|0\rangle \\ &+m\left(1+\frac{q}{q+r}e^{i\tau\omega_2}+\frac{r}{q+r}e^{-i\tau\omega_2}\right)\langle 0|\hat{A}_{n+1}(1)\hat{B}\hat{C}|0\rangle \\ &mn\left(1+\frac{q}{q+r}e^{-i\tau\omega_2}+\frac{r}{q+r}e^{i\tau\omega_2}\right)\langle 0|\hat{A}_{n-1}(1)\hat{B}\hat{C}|0\rangle,\end{aligned} \quad (3.37)$$

in which all terms of order m^2 have been neglected .

Setting $n = 0$ in Eqn (3.37) leads to the non-Condon expression for the absorption (with $\langle 0|\hat{A}_{-1}(1)\hat{B}\hat{C}|0\rangle \equiv 0$):

$$\begin{aligned}\langle 0|\hat{M}\hat{B}\hat{M}\hat{C}|0\rangle = &\left[1+\frac{mp}{q+r}\left(e^{i\tau\omega_2}+e^{-i\tau\omega_2}-2\right)\right]\langle 0|\hat{A}_0(1)\hat{B}\hat{C}|0\rangle \\ &+m\left(1+\frac{q}{q+r}e^{i\tau\omega_2}+\frac{r}{q+r}e^{-i\tau\omega_2}\right)\langle 0|\hat{A}_1(1)\hat{B}\hat{C}|0\rangle \ .\end{aligned} \quad (3.38)$$

Using the definition of the correlator (Eqn (3.210) in Eqn (3.37) leads to the relation expressing the *n*-th order non-Condon correlator in terms of the *n*-th order Condon correlator for which recurrence relations exist [52]:

$$A_n^{NC}(\tau) = \left[1+\frac{mp}{q+r}\left(e^{i\tau\omega_2}+e^{-i\tau\omega_2}-2\right)\right]A_n^{C}(\tau) + m(n+1)^{1/2}\left[1+\frac{q}{q+r}e^{i\tau\omega_2}+\frac{r}{q+r}e^{-i\tau\omega_2}\right]A_{n+1}^{C}(\tau) + mn^{1/2}\left[1+\frac{q}{q+r}e^{-i\tau\omega_2}+\frac{r}{q+r}e^{i\tau\omega_2}\right]A_{n-1}^{C}(\tau) \quad . \tag{3.39}$$

Equation (3.39) coincides, for n = 1, with that obtained by Hizhnyakov and Tehver for $A_1^{NC}(\tau)$, the first-order Raman correlator with non-Condon effects [52]; however, they have not obtained the general expression, for an arbitrary order, presented here and in [60]. Setting n = 0 in Eqn (3.40) gives the non-Condon absorption correlator

$$A_0^{NC}(\tau) = \left[1+\frac{mp}{q+r}\left(e^{i\tau\omega_2}+e^{-i\tau\omega_2}-2\right)\right]A_0^{C}(\tau) + m\left(1+\frac{q}{q+r}e^{i\tau\omega_2}+\frac{r}{q+r}e^{-i\tau\omega_2}\right)A_1^{C}(\tau) \quad . \tag{3.40}$$

From Appendix 3 the parameters {p, q, r} in Eqns (3.31) - (3.40) are given by

$$p = -\Delta\left(\frac{\pi c}{\hbar}\right)^{1/2}\mu^{1/2}\tilde{\nu}_2^{1/2} \quad , \quad q = \frac{\tilde{\nu}_2+\tilde{\nu}_1}{2(\tilde{\nu}_2\tilde{\nu}_1)^{1/2}} \quad , \quad r = \frac{\tilde{\nu}_2-\tilde{\nu}_1}{2(\tilde{\nu}_2\tilde{\nu}_1)^{1/2}} \quad , \tag{3.41}$$

in which Δ is the displacement of the equilibrium position of the excited-state one-dimensional potential energy curve, R_{e_2}, with respect to that of the ground state curve, R_{e_1}, along the Raman mode coordinate ($\Delta = R_{e_2} - R_{e_1}$), μ is the reduced mass of the Raman oscillator, and $\tilde{\nu}_2$ and $\tilde{\nu}_1$ are the wavenumbers of the Raman mode in the excited and ground states respectively, in cm^{-1}.

Equations (3.39) and (3.40) establish the desired relationship between non-Condon and Condon correlators for n-th order RRS, preparing the ground for the introduction of the recursion relations among the Condon Raman correlators developed in [52] and finally to link the non-Condon Raman correlators at any order to the non-Condon absorption correlator. Using the result in conjunction with Eqns (3.20) - (3.23) will then yield the transform relation between the

respective cross-sections, which constitute the goal of this chapter.

The Transform Relation

Hizhnyakov and Tehver have given recursion formulae for the Condon correlators derived from the $(\alpha_{\rho\sigma})_{if}$ polarizability component. As mentioned earlier in this chapter, a more conventional choice of phase, the $(\alpha_{\rho\sigma})_{fi}$ matrix element, is used here instead. Hence it is the complex conjugates of the HT correlators which are required; thus for n even ($n = 2k$):

$$A^{C}_{2k}(\tau) = [(2k)!]^{1/2}\sum_{s=0}^{k}\frac{\xi^{2s}\zeta^{k-s}}{(k-s)!2^{k-s}(2s)!}A^{C}_{0}(\tau) \qquad (3.42a)$$

and for n odd ($n = 2k + 1$)

$$A^{C}_{2k+1}(\tau) = [(2k+1)!]^{1/2}\sum_{s=0}^{k}\frac{\xi^{2s+1}\zeta^{k-s}}{(k-s)!2^{k-s}(2s+1)!}A^{C}_{0}(\tau)\ . \qquad (3.42b)$$

Because the present treatment is consistently conjugate to that of [52], the parameters in Eqns (3.42a,b) must be the conjugates of those found in [52]:

$$\xi = \bar{\xi}\frac{e^{-i\tau\omega_2}-1}{1-\delta e^{-i\tau\omega_2}} \quad \text{and} \quad \zeta = \delta\frac{e^{-2i\tau\omega_2}-1}{1-\delta^2 e^{-2i\tau\omega_2}}\ , \qquad (3.43a)$$

with

$$\bar{\xi} \equiv \frac{p}{q} \quad \text{and} \quad \delta \equiv \frac{r}{q}\ . \qquad (3.43b)$$

The parameters $\{p, q, r\}$ are given in Eqns (3.41). The other two parameters, $\bar{\xi}$ and δ in Eqns (3.43a,b), become:

$$\bar{\xi} = \frac{p}{q} = -\left(\frac{8\pi^2 c}{h}\right)^{1/2}(\mu\tilde{\nu}_1)^{1/2}\Delta\frac{\tilde{\nu}_2}{\tilde{\nu}_1+\tilde{\nu}_2} \approx -2.43557\times10^{-3}(\mu\tilde{\nu}_1)^{1/2}\Delta\frac{\tilde{\nu}_2}{\tilde{\nu}_1+\tilde{\nu}_2}\ , \qquad (3.44a)$$

with $[\mu]=1\,\text{amu}$, $[\tilde{\nu}]=1\,\text{cm}^{-1}$, $[\Delta]=1\,\text{pm}$, and

$$\delta = \frac{r}{q} = \frac{\tilde{\nu}_2-\tilde{\nu}_1}{\tilde{\nu}_2+\tilde{\nu}_1}\ . \qquad (3.44b)$$

The expression of the non-Condon absorption correlator (Eqn (3.23)) can be

greatly simplified. For $n = 1$ ($k = 0$) Eqn (3.42b) becomes:

$$A_1^C(\tau) = \xi A_0^C(\tau) . \tag{3.45a}$$

Rearranging the terms in Eqn (3.40) and using the approximations

$$\delta^2 << 1, \quad \delta << 1 \Rightarrow (\delta^2 e^{-2i\tau\omega_2} \to 0), \quad m\delta << 1, \quad m^2 << 1 , \tag{3.45b}$$

the non-Condon absorption correlator in terms of the Condon one (Eqn 3.40) becomes

$$A_0^{NC}(\tau) = (1 + 2m\xi) A_0^C(\tau) \tag{3.45c}$$

or, to order $m\xi$,

$$A_0^C(\tau) \approx (1 - 2m\xi) A_0^{NC}(\tau). \tag{3.45d}$$

For a wide range of real cases (Chapter 5), where the approximations formulated in Eqn (3.45b) are valid, the parameters ξ and ζ can be written as:

$$\xi \approx \bar{\xi}(e^{-i\tau\omega_2} - 1)(1 + \delta e^{-i\tau\omega_2}) \tag{3.46a}$$

and

$$\zeta \approx \delta(e^{-2i\tau\omega_2} - 1) . \tag{3.46b}$$

Thus, Eqn (3.39) becomes for $n = n_e$ (even):

$$A_{n_e}^{NC}(\tau) = \sum_{s=0}^{\frac{n_e}{2}} \left[\frac{n_e^{1/2}}{2s} C + \frac{[(n_e+1)n_e]^{1/2}}{(2s+1)\,2s} (n_e+1)^{1/2} C_+ + n_e^{1/2} C_- \right] \times (1-2m\xi)[(n_e-1)!]^{1/2} \frac{\xi^{2s-1} \zeta^{\frac{n_e}{2}-s}}{\left(\frac{n_e}{2}-s\right)!\, 2^{\frac{n_e}{2}-s} (2s-1)!} A_0^{NC}(\tau) \tag{3.47a}$$

and for $n = n_o$ (odd):

$$A_{n_o}^{NC}(\tau) = \sum_{s=0}^{\frac{n_o-1}{2}} \left[\frac{n_o^{1/2}}{2s+1} C + \frac{[(n_o+1)n_o]^{1/2}}{(2s+2)(2s+1)} (n_o+1)^{1/2} C_+ + n_o^{1/2} C_- \right] \times (1-2m\xi)[(n_o-1)!]^{1/2} \frac{\xi^{2s} \zeta^{\frac{n_o-1}{2}-s}}{\left(\frac{n_o-1}{2}-s\right)!\, 2^{\frac{n_o-1}{2}-s} (2s)!} A_0^{NC}(\tau) , \tag{3.47b}$$

where the coefficients C, C_+ and C_- are given by:

$$C = \xi\left[1+\frac{m\bar{\xi}}{1+\delta}\left(e^{i\tau\omega_2}+e^{-i\tau\omega_2}-2\right)\right], \tag{3.48a}$$

$$C_+ = \xi^2 m\left(1+\frac{e^{i\tau\omega_2}}{1+\delta}+\frac{\delta e^{-i\tau\omega_2}}{1+\delta}\right), \tag{3.48b}$$

and

$$C_- = m\left(1+\frac{e^{-i\tau\omega_2}}{1+\delta}+\frac{\delta e^{i\tau\omega_2}}{1+\delta}\right). \tag{3.48c}$$

Replacing the coefficients C, C_+ and C_- (Eqns (3.48a-c)) in the non-Condon correlators (Eqns (3.47a,b)), expanding all terms, cancelling the small terms by using the approximations formulated in Eqn (3.45b) and introducing the notations $\hat{\beta} \equiv e^{-i\tau\omega_2}$, $k_e \equiv n_e/2$, $k_o \equiv (n_o-1)/2$, $x_e \equiv 2m\bar{\xi}(k_e-s)/(2s+1)$ and $x_o \equiv m\bar{\xi}(k_o-s)/(s+1)$, Eqns (3.47a,b) become, respectively, for $n = n_e$ (even):

$$A_{n_e}^{NC}(\tau) = (n_e!)^{1/2}\bar{\xi}A_0^{NC}(\tau)\sum_{s=0}^{k_e}\frac{\xi^{2s-1}\zeta^{k_e-s}}{(k_e-s)!\,2^{k_e-s}(2s)!}\times \left[(\delta+x_e)\hat{\beta}^2+\left(1-\delta+2s\frac{m}{\xi}-x_e\right)\hat{\beta}+\left(2s\frac{m}{\xi}-1-x_e\right)+(x_e)\hat{\beta}^{-1}\right] \tag{3.49a}$$

and for $n = n_o$ (odd):

$$A_{n_o}^{NC}(\tau) = (n_o!)^{1/2}\bar{\xi}A_0^{NC}(\tau)\sum_{s=0}^{k_o}\frac{\xi^{2s}\zeta^{k_o-s}}{(k_o-s)!\,2^{k_o-s}(2s+1)!}\times \left[(\delta+x_o)\hat{\beta}^2+\left(1-\delta+(2s+1)\frac{m}{\xi}-x_o\right)\hat{\beta}+\left((2s+1)\frac{m}{\xi}-1-x_o m\bar{\xi}\right)+x_o\hat{\beta}^{-1}\right]. \tag{3.49b}$$

Using Eqns (3.46a,b) for ξ and ζ, expanding ξ^{2s}, and ζ^k, ($k = k_e$, k_o) and approximating $(1+\delta\hat{\beta})^j$ as $1+j\delta\hat{\beta}$, yields the final form of the relationship between the resonance Raman and absorption correlators, respectively, for $n = n_e$ (even):

$$A_{n_e}^{NC}(\tau) = (n_e!)^{1/2}\sum_{s=0}^{k_e}\frac{\bar{\xi}^{2s}\delta^{k_e-s}(k_e+s-1)!}{2^{k_e-s}(2s)!}\sum_{t=0}^{k_e+s-1}\frac{(-1)^t}{t!(k_e+s-1-t)!}\sum_{u=0}^{k_e-s}\frac{1}{u!(k_e-s-u)!}$$

$$\times\{(2s\delta+x_e)\hat{\beta}^{n_e-t-u+1}+[1-2s(\delta-\frac{m}{\xi})-x_e]\hat{\beta}^{n_e-t-u} \qquad (3.50a)$$

$$+(2s\frac{m}{\xi}-1-x_e)\hat{\beta}^{n_e-t-u-1}+x_e\hat{\beta}^{n_e-t-u-2}\}A_0^{NC}(\tau)$$

and for $n = n_o$ (odd):

$$A_{n_o}^{NC}(\tau) = (n_o!)^{1/2}\sum_{s=0}^{k_o}\frac{\bar{\xi}^{2s+1}\delta^{k_o-s}(k_o+s)!}{2^{k_o-s}(2s+1)!}\sum_{t=0}^{k_o+s}\frac{(-1)^t}{t!(k_o+s-t)!}\sum_{u=0}^{k_o-s}\frac{1}{u!(k_o-s-u)!}$$

$$\times\{[(2s+1)\delta+x_o]\hat{\beta}^{n_o-t-u+1}+[1-(2s+1)(\delta-\frac{m}{\xi})-x_o]\hat{\beta}^{n_o-t-u} \qquad (3.50b)$$

$$+[(2s+1)\frac{m}{\xi}-1-x_o]\hat{\beta}^{n_o-t-u-1}+x_o\hat{\beta}^{n_o-t-u-2}\}A_0^{NC}(\tau)\ .$$

This is the desired link between the n-th order Raman correlator and the absorption correlator at the non-Condon level (in its linear approximation). The transform relation for n-th Raman excitation profiles, developed by using the Fourier transform (Eqn (3.12)) of the non-Condon n-th order Raman correlator (Eqn (3.39)), produces the n-th order non-Condon polarizability ($\rho\rho$-th tensor element) (with $\omega_L \equiv \omega$)

$$\alpha_n^{NC}(\omega) = \int_{-\infty}^{\infty}d\tau e^{i\tau\omega}A_n^{NC}(\tau)\ . \qquad (3.51)$$

The frequency displacement operator $\hat{\beta}\equiv e^{-i\tau\omega_2}$ appears in $A_n^{NC}(\tau)$ as various powers through Eqns (3.50a,b) and it simply shifts the frequency of the Fourier kernel (Eqn (3.51)); thus [60]

$$\int_{-\infty}^{\infty}d\tau e^{i\tau\omega}\hat{\beta}^s\ldots = \int_{-\infty}^{\infty}d\tau e^{i\tau(\omega-s\omega_2)}\ldots \qquad (3.52)$$

and the Fourier transform of the Raman correlator (Eqn (3.51)) in the presence of a term containing $\hat{\beta}^s$ (Eqns (3.50a,b)) will produce a Raman polarizability whose frequency argument has been down-shifted by $s\omega_2$ from the incident

laser frequency, ω. The Fourier transform of Eqns (3.50a,b) yields for $n = n_e$:

$$\alpha_{n_e}^{NC}(\omega) = (n_e!)^{1/2}\sum_{s=0}^{k_e}\frac{\bar{\xi}^{2s}\delta^{k_e-s}(k_e+s-1)!}{2^{k_e-s}(2s)!}\sum_{t=0}^{k_e+s-1}\frac{(-1)^t}{t!(k_e+s-1-t)!}\sum_{u=0}^{k_e-s}\frac{1}{u!(k_e-s-u)!}$$

$$\times\{(2s\delta+x_e)\Phi[\omega-(n_e-t-u+1)\omega_2] + [1-2s(\delta-m/\bar{\xi})-x_e]\Phi[\omega-(n_e-t-u)\omega_2] + (2sm/\bar{\xi}-1-x_e)\Phi[\omega-(n_e-t-u-1)\omega_2] + x_e\Phi[\omega-(n_e-t-u-2)\omega_2]\} \quad (3.53a)$$

and for $n = n_o$:

$$\alpha_{n_o}^{NC}(\omega) = (n_o!)^{1/2}\sum_{s=0}^{k_o}\frac{\bar{\xi}^{2s+1}\delta^{k_o-s}(k_o+s)!}{2^{k_o-s}(2s+1)!}\sum_{t=0}^{k_o+s}\frac{(-1)^t}{t!(k_o+s-t)!}\sum_{u=0}^{k_o-s}\frac{1}{u!(k_o-s-u)!}$$

$$\times\{[(2s+1)\delta+x_o]\Phi[\omega-(n_o-t-u+1)\omega_2] + [1-(2s+1)(\delta-m/\bar{\xi})-x_o]\Phi[\omega-(n_o-t-u)\omega_2] + [(2s+1)m/\bar{\xi}-1-x_o]\Phi[\omega-(n_o-t-u-1)\omega_2] + x_o\Phi[\omega-(n_o-t-u-2)\omega_2]\}\ . \quad (3.53b)$$

Finally, the *n*-th order Raman excitation profile, $REP_n(\omega)$, as the *measured* value of the scattering cross-section relative to frequency, is obtained by using Eqns (3.53a,b) in Eqn (3.6):

$$REP_n(\omega) = const|\alpha_n^{NC}(\omega)|^2. \quad (3.54)$$

The proportionality constant depends on many different factors involved in the detection process used and is difficult to calculate in practice. Also, although it is assumed to be a constant, frequency-dependent effects like the self-absorption of the scattered resonance Raman radiation in the sample or the spectral response of the detection system can invalidate this assumption. Carefully designed and executed experiments, including various corrections (Chapter 1, Appendix 1), alleviate this problem to the extent that the proportionality constant in Eqn (3.54) is indeed a constant in most cases; also, it is an essential requirement only for absolute REP measurements and it will be shown in Chapter 4 how this can be circumvented at no loss of generality.

The polarizability function in Eqns (3.53a,b), $\Phi(\omega)$, is available from the experimental absorption spectrum (Eqn (3.5)); it can be seen from Eqns (3.53a,b) that the *n*-th order complex polarizability, and hence the resonance Raman scattering cross-section in the *n*-th order, depends on *four* different zero order quantities, each of them to be calculated at a different frequency. This imposes certain requirements on the absorption data employed in the calculation of the *n*-th order resonance Raman scattering cross-sections and of the excited state parameters, as it will be seen in chapters 4 and 5.

It can be seen also from Eqns (3.53a,b) that the leading term is the one corresponding to $s=0$, with no frequency shift; this observation shows that the result obtained here is consistent with previously published work [40-52,55], where the change of the vibrational frequency between the ground and the excited electronic state has been neglected. A comparison between the magnitude of the variously shifted polarisabilities would show however (Chapter 5), that the other terms cannot always be neglected; the reason is the frequency shift, which leads to the calculation of the polarizability in points of higher or lower intensity on the absorption curve. Especially for spectra exhibiting overlapping vibronic structure, this effect can be significant and has a bearing on the extent and the resolution of the absorption spectra to be collected and used in the calculations.

IV. Numerical Implementation of the Transform Method

The mathematical problem as a system of equations in several variables

Practical applications of the transform method in resonance Raman spectroscopy are based around Eqns (3.53a,b) and (3.54); they establish the relationship between the measured value of the scattering cross-section of a resonance Raman transition as a function of molecular parameters and the value of the absorption coefficient measured across the visible spectrum. The instrumental parameters involved in this relationship are contained in the constant appearing in Eqn (3.54) and will be taken into account here.

The interpretation of resonance Raman spectra in terms of the molecular geometry and force constants in the excited electronic state involves the values of three parameters, controlling the intensity distribution between different harmonics of the spectrum and the overall intensity of the resonance Raman scattering: the bond length change Δ between the ground and the excited electronic states, the force constant as reflected in the vibrational wavenumber $\tilde{\nu}_e$ in the excited electronic state and the non-Condon factor *m*. Thus, treating these three parameters and the instrumental constant as unknowns of a system of simultaneous equations, a minimum of four equations is required in order to have a fully, albeit minimally, determined solution. The four equations represent four different instances of Eqn (3.54), corresponding to four different values of the measured scattering cross-section; they can be obtained by using two different approaches, depending on the experimental situation.

In the first approach the resonance Raman spectrum exhibits at least four harmonics, measurable with a sufficient degree of accuracy, and Eqn (3.54) can be written in turn for each harmonic of order one to four:

$$const\left|\alpha_1^{NC}(\omega_L,\tilde{\nu}_e,\Delta,m)\right|^2 = REP(\omega_L-\omega_g) \tag{4.1a}$$

$$const\left|\alpha_2^{NC}(\omega_L,\tilde{\nu}_e,\Delta,m)\right|^2 = REP(\omega_L-2\omega_g) \tag{4.1b}$$

$$const\left|\alpha_3^{NC}(\omega_L,\tilde{\nu}_e,\Delta,m)\right|^2 = REP(\omega_L-3\omega_g) \tag{4.1c}$$

$$const\left|\alpha_4^{NC}(\omega_L,\tilde{\nu}_e,\Delta,m)\right|^2 = REP(\omega_L-4\omega_g)\ , \tag{4.1d}$$

where ω_L is the circular frequency of the exciting radiation, $REP(\omega_L - j\omega_g)$ is the Raman excitation profile and ω_g is the circular Raman frequency corresponding to the vibrational energy gap in the ground state. The instrumental constant (which must be independent of the scattering order) can be eliminated by dividing Eqns (4.1b,c,d) by Eqn (4.1a); the system (4.1a-d) can be written as:

$$\frac{\left|\alpha_2^{NC}(\omega_L,\tilde{\nu}_e,\Delta,m)\right|^2}{\left|\alpha_1^{NC}(\omega_L,\tilde{\nu}_e,\Delta,m)\right|^2} = \frac{REP(\omega_L-2\omega_g)}{REP(\omega_L-\omega_g)} \tag{4.2a}$$

$$\frac{\left|\alpha_3^{NC}(\omega_L,\tilde{\nu}_e,\Delta,m)\right|^2}{\left|\alpha_1^{NC}(\omega_L,\tilde{\nu}_e,\Delta,m)\right|^2} = \frac{REP(\omega_L-3\omega_g)}{REP(\omega_L-\omega_g)} \tag{4.2b}$$

$$\frac{\left|\alpha_4^{NC}(\omega_L,\tilde{\nu}_e,\Delta,m)\right|^2}{\left|\alpha_1^{NC}(\omega_L,\tilde{\nu}_e,\Delta,m)\right|^2} = \frac{REP(\omega_L-4\omega_g)}{REP(\omega_L-\omega_g)}\ . \tag{4.2c}$$

The second approach is suitable to the situations in which several resonance Raman spectra can be collected, corresponding to several different wavelengths for the exciting light, but in which no spectrum exhibits at least four well defined harmonics; this is a very common experimental situation,therefore making the second approach very useful for practical applications. For example, if only the fundamental and the first overtone are observed in the spectrum, the system of simultaneous equations (4.2a-c) can be written as:

$$\frac{\left|\alpha_2^{NC}(\omega_{L_1},\tilde{\nu}_e,\Delta,m)\right|^2}{\left|\alpha_1^{NC}(\omega_{L_1},\tilde{\nu}_e,\Delta,m)\right|^2} = \frac{REP(\omega_{L_1}-2\omega_g)}{REP(\omega_{L_1}-\omega_g)} \tag{4.3a}$$

$$\frac{\left|\alpha_2^{NC}(\omega_{L_2},\tilde{\nu}_e,\Delta,m)\right|^2}{\left|\alpha_1^{NC}(\omega_{L_2},\tilde{\nu}_e,\Delta,m)\right|^2} = \frac{REP(\omega_{L_2}-2\omega_g)}{REP(\omega_{L_2}-\omega_g)} \tag{4.3b}$$

and

$$\frac{\left|\alpha_2^{NC}(\omega_{L_3}, \tilde{\nu}_e, \Delta, m)\right|^2}{\left|\alpha_1^{NC}(\omega_{L_3}, \tilde{\nu}_e, \Delta, m)\right|^2} = \frac{REP(\omega_{L_3} - 2\omega_g)}{REP(\omega_{L_3} - \omega_g)} \,. \tag{4.3c}$$

The nature of Eqns (4.2a-c) and (4.3a-c) will determine the choice of method for solving them; examining the expressions of α_n^{NC} for n = 1 - 4 (Eqn (3.53a,b)) reveals that some of the unknowns appear at powers higher than three, making an analytic solution impossible to obtain. With the aid of the Mathematica(R) computer program[2], Eqns (3.50a,b) - the precursors of Eqns (3.53a,b) - yield:

```
A1^NC = m - xi + (d*xi) / b^2 + [m + (1 - d) * xi] / b;

A2^NC = {-d - 2*m*xi + xi^2 + (2*d*xi^2) / b^3 + [(-2 +
2*d) * xi^2] / b + [d + 2*m*xi + (1 - 4*d) * xi^2] / b^2}
/ 2^(1/2);

A3^NC = {3*d*xi + 3*m*xi^2 - xi^3 + (3*d*xi^3) / b^4 +
[3*d*xi + 3*m*xi^2 + (1 - 9*d) * xi^3] / b^3 + [-3*d*xi
- 3*m*xi^2 + (3 - 3*d) * xi^3] / b + [-3*d*xi - 3*m*xi^2
+ (-3 + 9*d) * xi^3] / b^2} / 6^(1/2);

A4^NC = {-6*d*xi^2 - 4*m*xi^3 + xi^4 + [(6 - 16*d) * xi^4]
/ b^2 + (4*d*xi^4) / b^5 + [6*d*xi^2 + 4*m*xi^3 + (1 -
16*d) * xi^4] / b^4 + [12*d*xi^2 + 8*m*xi^3 + (-4 + 4*d)
* xi^4] / b + [-12*d*xi^2 - 8*m*xi^3 + (-4 + 24*d) *
xi^4] / b^3 } / 24^(1/2) ,
```

where `d` = δ of Eqns (3.43b, 3.44b), `xi` = $\bar{\xi}$ of Eqns (3.43b, 3.44a), `b` = $\hat{\beta} \equiv e^{-i\tau\omega_\bullet}$ of Eqns (3.49a,b) and `m` = m is the non-Condon factor. It can be seen from the Mathematica output and from Eqns (3.53a,b), (3.54) and (4.2a-c)

[2] - Mathematica(R) has the capability of manipulating mathematical expressions and performing algebraic calculations in symbolic (as opposed to numeric) form [52]. Mathematica textual output included here is highlighted by being presented in a different font (lighter and fixed-spaced) from that of the main text.

that none of the three unknowns can be eliminated analytically, while one of the unknowns, $\tilde{\nu}_e$, appears both explicitly, in δ and in $\bar{\xi}$, and *implicitly* in the expression of Re[$\Phi(\omega)$] (Eqns (3.5), (3.53a,b)).

Converting a system to a single equation in several variables

The previous section has shown that the systems (4.2a-c) and (4.3a-c) can be solved only numerically so the next step will be to adapt the problem to a numerical treatment and to assess the problem from a numerical point of view; only the system (4.2a-c) will be considered in this section, as all the conclusions and procedures developed here will apply equally to both systems (Eqns 4.2a-c and 4.3a-c).

There are no established methods for solving non-linear systems of simultaneous equations similar to (4.2a-c) [64,65]; however, there are several general methods for solving one non-linear equation in several variables, e.g. Newton's method and its derivations. The system (4.2a-c) will be converted into a single equation in several variables by moving both terms of each Eqn (4.2) onto the same side of the equals sign:

$$\frac{\left|\alpha_2^{NC}(\omega_L,\tilde{\nu}_e,\Delta,m)\right|^2}{\left|\alpha_1^{NC}(\omega_L,\tilde{\nu}_e,\Delta,m)\right|^2} - \frac{REP(\omega_L-2\omega_g)}{REP(\omega_L-\omega_g)} = 0 \qquad (4.4a)$$

$$\frac{\left|\alpha_3^{NC}(\omega_L,\tilde{\nu}_e,\Delta,m)\right|^2}{\left|\alpha_1^{NC}(\omega_L,\tilde{\nu}_e,\Delta,m)\right|^2} - \frac{REP(\omega_L-3\omega_g)}{REP(\omega_L-\omega_g)} = 0 \qquad (4.4b)$$

$$\frac{\left|\alpha_4^{NC}(\omega_L,\tilde{\nu}_e,\Delta,m)\right|^2}{\left|\alpha_1^{NC}(\omega_L,\tilde{\nu}_e,\Delta,m)\right|^2} - \frac{REP(\omega_L-4\omega_g)}{REP(\omega_L-\omega_g)} = 0\ . \qquad (4.4c)$$

It is known from classical algebra that three quantities A, B, C are null simultaneously when and only when the sum of their squares $A^2 + B^2 + C^2$ is also null and therefore Eqns (4.4a-c) are equivalent to:

$$\left[\frac{\left|\alpha_2^{NC}(\omega_L,\tilde{\nu}_e,\Delta,m)\right|^2}{\left|\alpha_1^{NC}(\omega_L,\tilde{\nu}_e,\Delta,m)\right|^2}-\frac{REP(\omega_L-2\omega_g)}{REP(\omega_L-\omega_g)}\right]^2+$$

$$\left[\frac{\left|\alpha_3^{NC}(\omega_L,\tilde{\nu}_e,\Delta,m)\right|^2}{\left|\alpha_1^{NC}(\omega_L,\tilde{\nu}_e,\Delta,m)\right|^2}-\frac{REP(\omega_L-3\omega_g)}{REP(\omega_L-\omega_g)}\right]^2+ \qquad (4.5)$$

$$\left[\frac{\left|\alpha_4^{NC}(\omega_L,\tilde{\nu}_e,\Delta,m)\right|^2}{\left|\alpha_1^{NC}(\omega_L,\tilde{\nu}_e,\Delta,m)\right|^2}-\frac{REP(\omega_L-4\omega_g)}{REP(\omega_L-\omega_g)}\right]^2=0\ .$$

By defining the function $X(\tilde{\nu}_e,\Delta,m)$ as

$$X(\tilde{\nu}_e,\Delta,m)\equiv\left[\frac{\left|\alpha_2^{NC}(\omega_L,\tilde{\nu}_e,\Delta,m)\right|^2}{\left|\alpha_1^{NC}(\omega_L,\tilde{\nu}_e,\Delta,m)\right|^2}-\frac{REP(\omega_L-2\omega_g)}{REP(\omega_L-\omega_g)}\right]^2+$$

$$\left[\frac{\left|\alpha_3^{NC}(\omega_L,\tilde{\nu}_e,\Delta,m)\right|^2}{\left|\alpha_1^{NC}(\omega_L,\tilde{\nu}_e,\Delta,m)\right|^2}-\frac{REP(\omega_L-3\omega_g)}{REP(\omega_L-\omega_g)}\right]^2+ \qquad (4.6)$$

$$\left[\frac{\left|\alpha_4^{NC}(\omega_L,\tilde{\nu}_e,\Delta,m)\right|^2}{\left|\alpha_1^{NC}(\omega_L,\tilde{\nu}_e,\Delta,m)\right|^2}-\frac{REP(\omega_L-4\omega_g)}{REP(\omega_L-\omega_g)}\right]^2,$$

Eqn (4.5) can be written simply as:

$$X(\tilde{\nu}_e,\Delta,m)=0\ , \qquad (4.7)$$

with ω_L, ω_g as given parameters. As a numerical solution to the Eqn (4.7) implies a finite resolution for the values of the unknowns, the problem becomes to find the set $(\tilde{\nu}_e,\Delta,m)$ that *minimises* X rather than makes it exactly null; thus, the problem of solving a system of three simultaneous equations in three unknowns is reduced to minimising a function of three independent variables.

At this point it would be useful to inspect the four-dimensional space where the minimum of X lies. This will be accomplished by assigning to each point in a three-dimensional space $(\tilde{\nu}_e,\Delta,m)$ a shade of grey from a palette corresponding to the *logarithmic* scale of values for (X/X_{max}) and plotting all the points so

defined. The logarithmic scale has the advantage of preserving the monotony (trend) of the function and increasing the resolution at small values of the argument (around the minimum) while "compressing" the range of larger, uninteresting values. The palette has been chosen with black corresponding to the minimum and white to values larger than a certain threshold and up to the maximum value of *X*. Figure 4.1 illustrates the procedure by plotting *X* for $KMnO_4$ (see also chapter 5) across the region of space containing the minimum of X[3], with a low resolution for the three coordinates: 12 cm^{-1} for the vibrational wavenumber in the excited electronic state, 1.2 pm for the bond length change and 0.05 for the non-Condon factor.

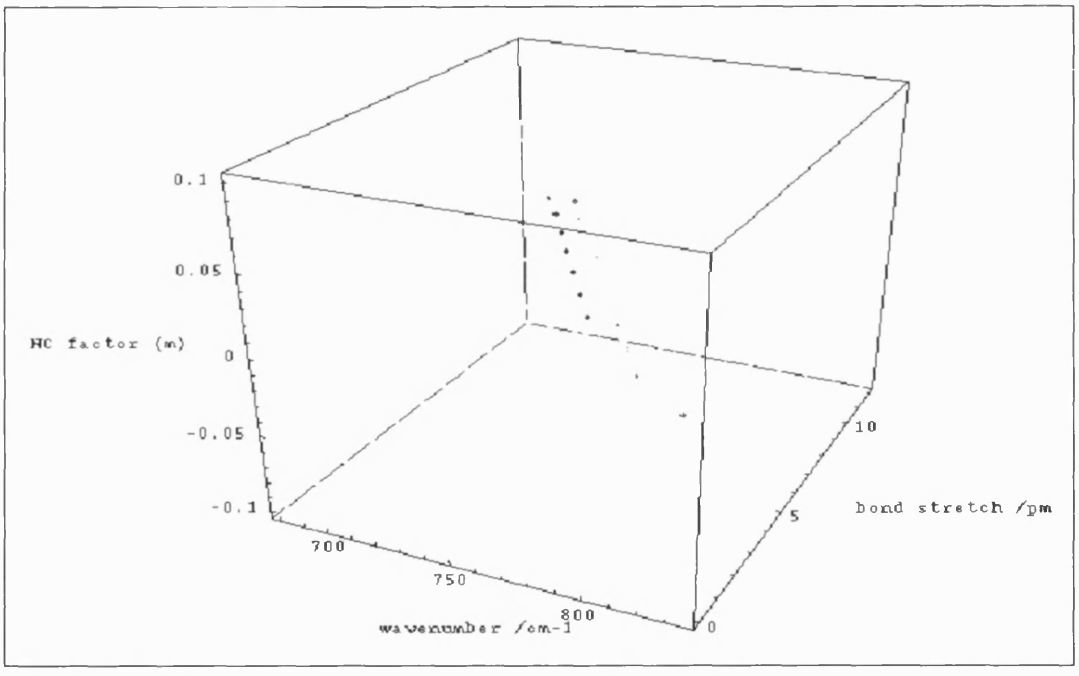

Figure 4.1 - General view of a low-resolution plot of *X* (Eqn (4.6)) for $KMnO_4$.

The Mathematica(R) script used to produce Fig. 4.1 is based on the graphics object `Graphics3D[list{primitives,directives},list{options}]`, constructed of `Point[{x,y,z}]` primitives with the `GrayLevel[i]` graphics

[3] - Early work has tried to extend the search for *negative* Δ and $\tilde{\nu}_e > \tilde{\nu}_g$, for several of the cases presented in chapter 5; the results have always been consistent with the conventional view of bond length *increase* and vibrational wavenumber *decrease* between the ground and excited electronic states. The plot of the search space has thus been restricted to its meaningful part, for the sake of clarity.

directive and some graphics options [66]; the coordinates `(x,y,z)` correspond to $(\tilde{\nu}_e, \Delta, m)$ and the grey shade `i`, a number between 0 and 1, to $\log(X/X_{min})$. The script is computer-generated by a program written in the C programming language; only a sample is shown bellow, the full script containing 880 lines:

```
Graphics3D[{
{ GrayLevel[1.0], Point[{650.0, 0.0, -0.100}] },
{ GrayLevel[1.0], Point[{650.0, 0.0, -0.050}] },
...
{ GrayLevel[1.0], Point[{840.0, 12.0, 0.100}] } },
Axes->True, BoxRatios->{1,1.2,1}, ViewPoint->Automatic }]
```

The region of the solution space depicted in Fig. 4.1 can be viewed from different angles in order to facilitate the visual inspection and the location of the minimum of X; Figs. 4.2a-c show the same region, viewed along each of the three independent axes. It should be stressed at this point that the viewing angles shown here are not necessarily the most suitable and that the choice of view depends on the case studied and on the preference of the observer.

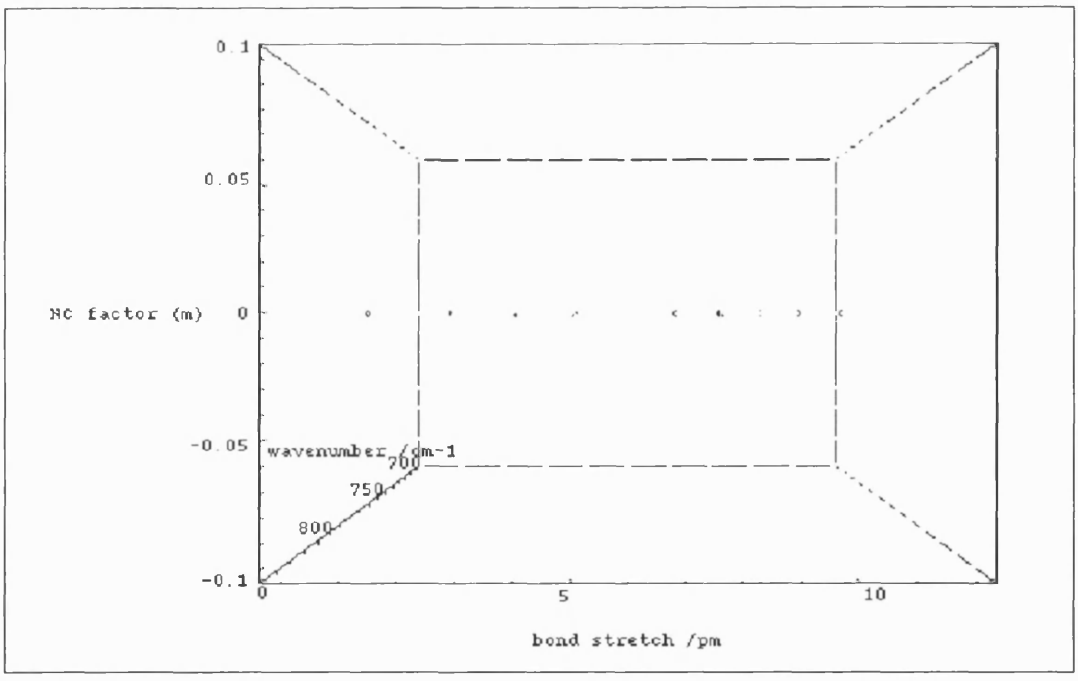

Figure 4.2a - View along the wavenumber axis of the plot in Fig. 4.1.

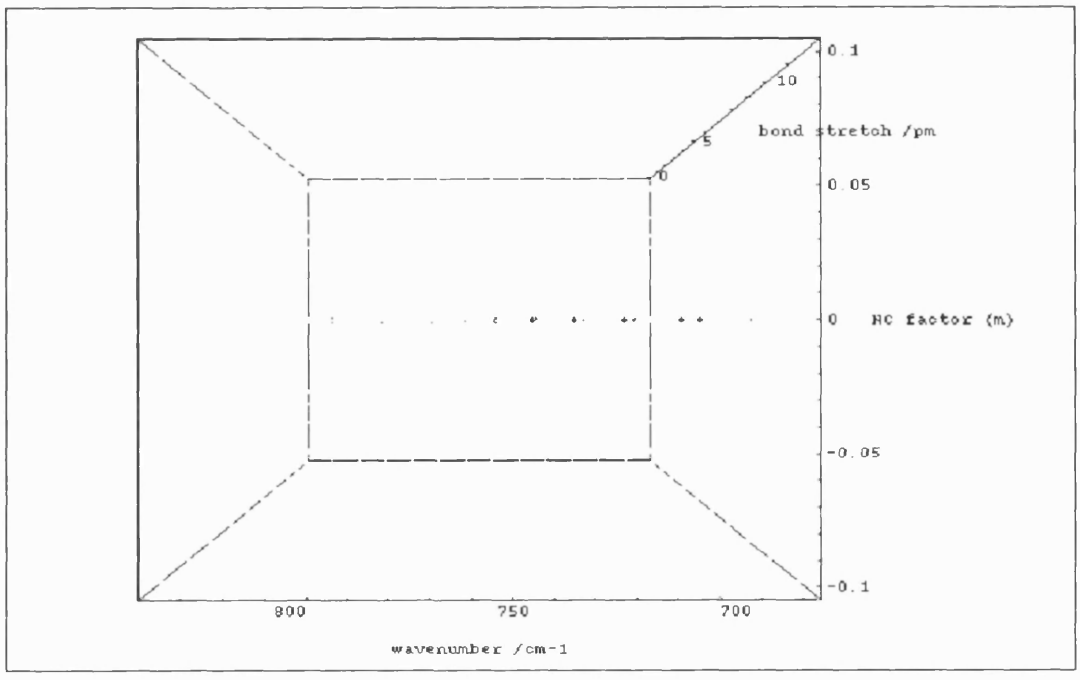

Figure 4.2b - View along the bond-stretch axis of the plot in Fig. 4.1.

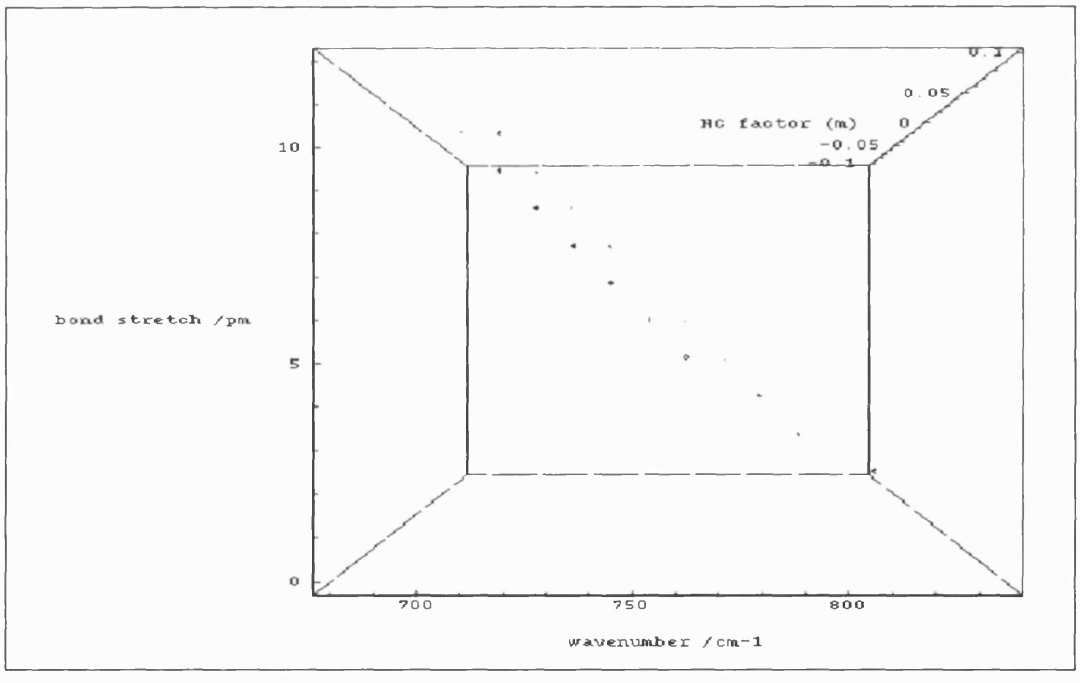

Figure 4.2c - View along the *m* axis of the plot in Fig. 4.1.

It can be seen in Figs. 4.2a,b that the scale along the *m* coordinate is not well chosen and the points appear to cluster around the plane defined by $m = 0$;

Fig. 4.3 and Figs. 4.4a-c provide a more detailed view of the solution space than Figs. 4.1, 4.2a-c, by focusing on a smaller range of values for *m*.

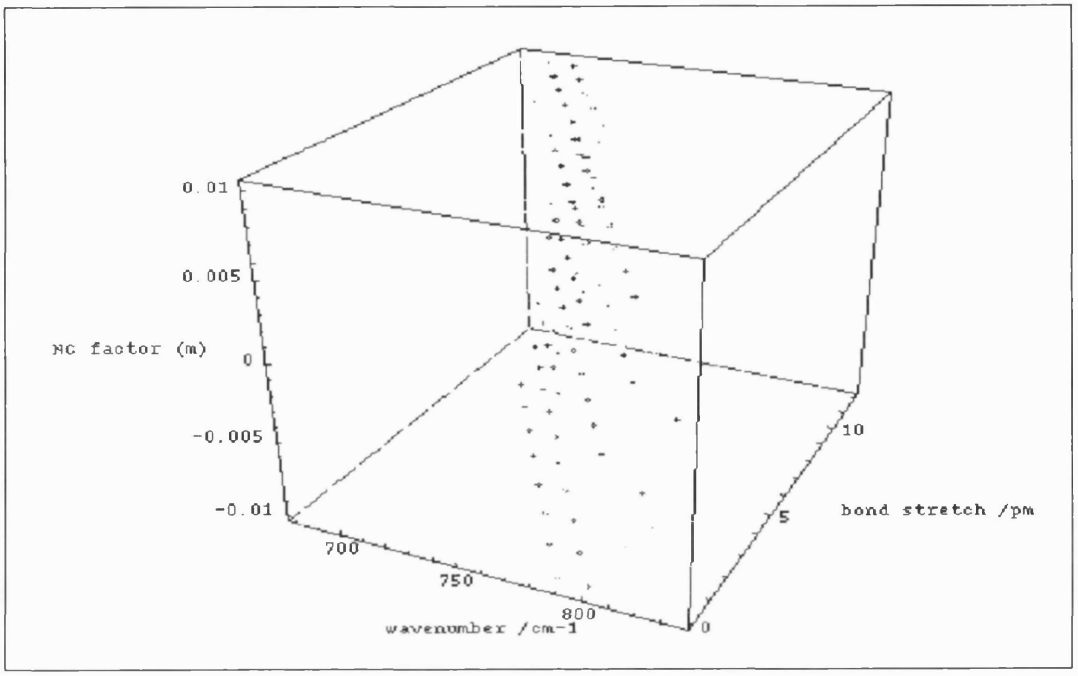

Figure 4.3 - Full view of a high resolution plot of *X* (Eqn (4.6)) for $KMnO_4$.

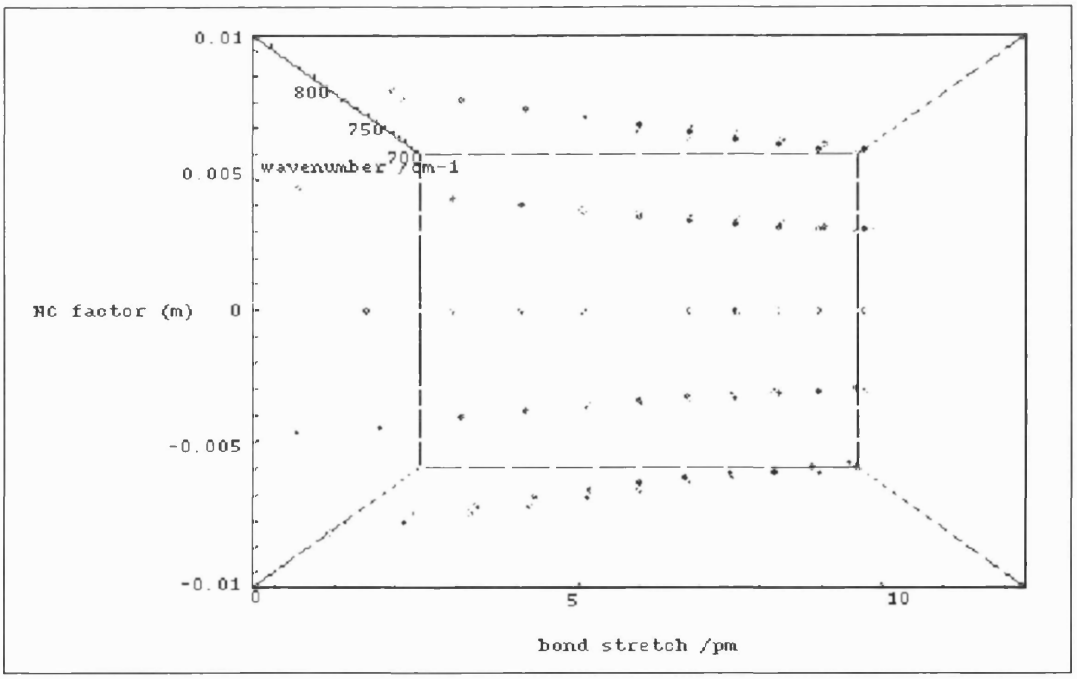

Figure 4.4a - View along the wavenumber axis of the plot in Fig. 4.3.

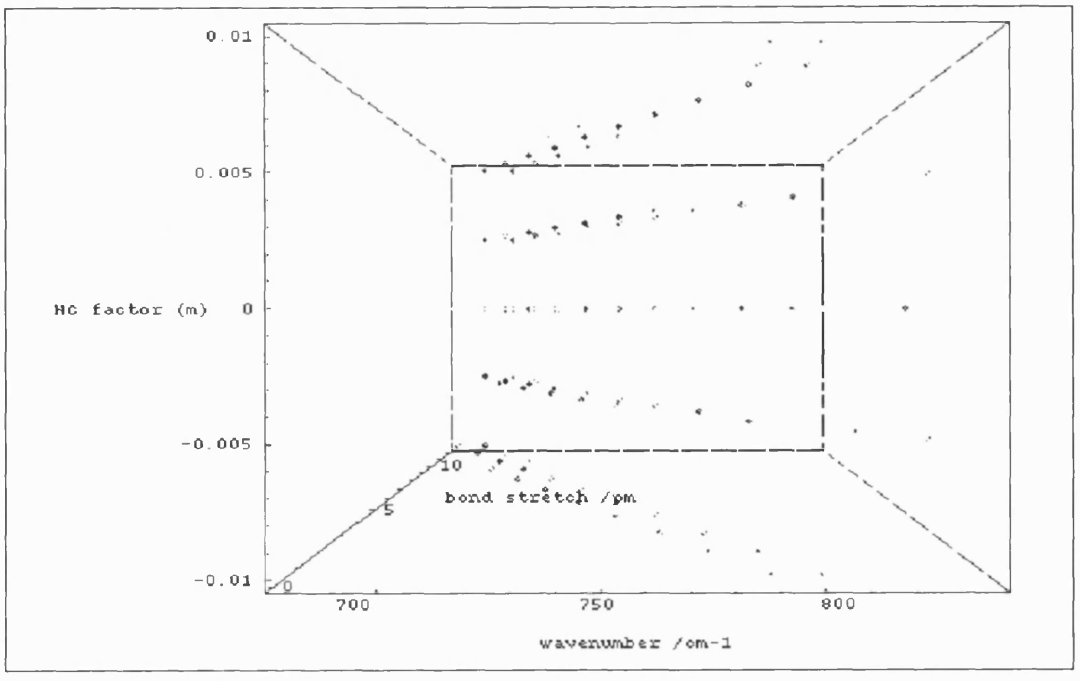

Figure 4.4b - View along the bond-stretch axis of the plot in Fig. 4.3.

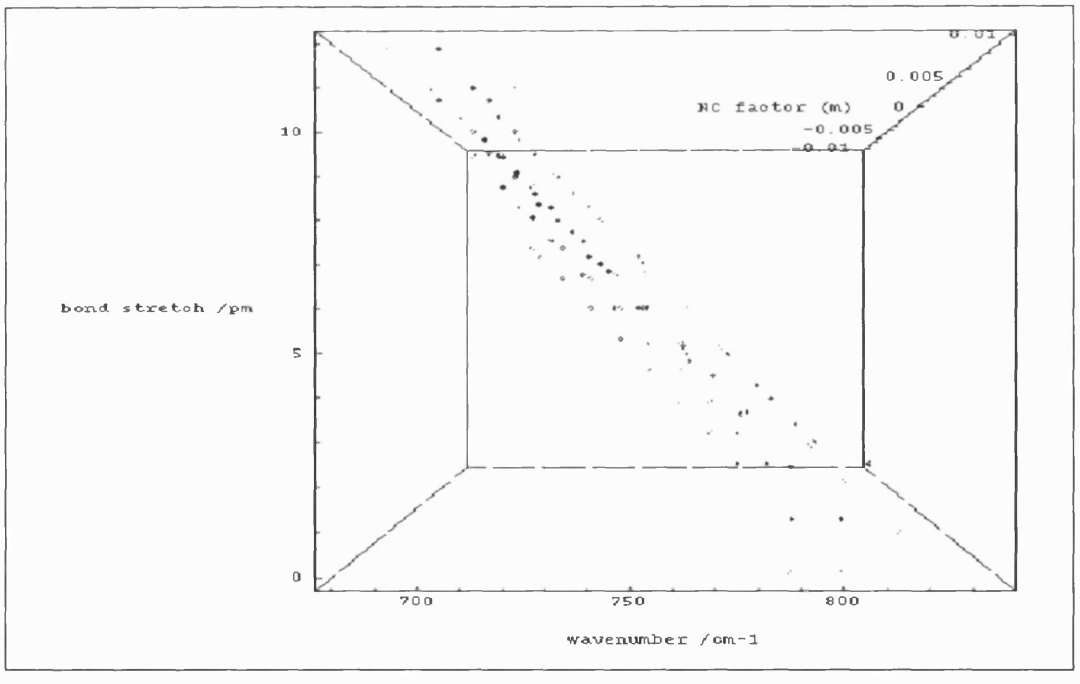

Figure 4.4c - View along the *m* axis of the plot in Fig. 4.3.

The three-dimensional diagrams in Figs. 4.1 - 4.4 suggest another useful way

of inspecting the solution space: representing each point in a two-dimensional space by considering m to be a fixed parameter, and associating a grey palette to the scale of values of $\log(X/X_{min})$. This procedure would be equivalent to 'slicing' a three-dimensional representation across the m coordinate with planes of a fixed value for m, the resulting series of density plots being entirely equivalent to the original three-dimensional representation.

The main advantage of two-dimensional relative to three-dimensional images is that they are much easier to inspect visually; the price to be paid for this facility is the large number of such plots needed to cover an equivalent region of the $(\tilde{\nu}_e, \Delta, m)$ space. As will be shown in later sections, dealing with such large number of similar objects is a job computers are most suited to, and this will be the approach that will eventually emerge.

Another advantage of the two-dimensional relative to three-dimensional images is that the former require fewer resources than the later, allowing a higher resolution and a wider range of values for each coordinate: 550.0 to 800.0, in steps of 5.0 cm^{-1}, for the vibrational wavenumber in the excited electronic state, and 0.0 to 40.0, in steps of 0.5 pm, for the bond length change upon excitation.

The Mathematica(R) script used to produce Figs. 4.5a-e is computer-generated by a program written in C and is shown below in an abbreviated form:

```
Graphics3D[{
{ GrayLevel[1.0], Point[{550.0, 0.0}] },
{ GrayLevel[1.0], Point[{550.0, 0.5}] },
...
{ GrayLevel[1.0], Point[{555.0, 0.0}] },
{ GrayLevel[0.9], Point[{550.0, 0.5}] },
...
{ GrayLevel[1.0], Point[{800.0, 40.0}] } },
Axes->False, Frame->True }]
```

The script is based on the graphic object `Graphics[list{primitives, directives}, list{options}]`, constructed of `Point[{x,y}]` primitives with the `GrayLevel[i]` graphic directive and some graphic options [66]; the coordinates `(x,y)` correspond to $(\tilde{\nu}_e, \Delta)$ and the grey shade `i`, a number between 0 and 1, to $\log(X/X_{min})$.

Figures 4.5a-e will show five two-dimensional diagrams with the corresponding non-Condon factor displayed in the top right corner of each frame; these diagrams illustrate the important point that the non-Condon factor can have a significant influence on the resonance Raman spectrum, by visualising the changing position of the minima of X with the changing non-Condon factor m. Also, another important observation to be drawn from Figs. 4.5a-e is that sometimes the minimum of $X(\tilde{\nu}_e, \Delta, m)$ is not unique, a fact that will be further discussed in this chapter.

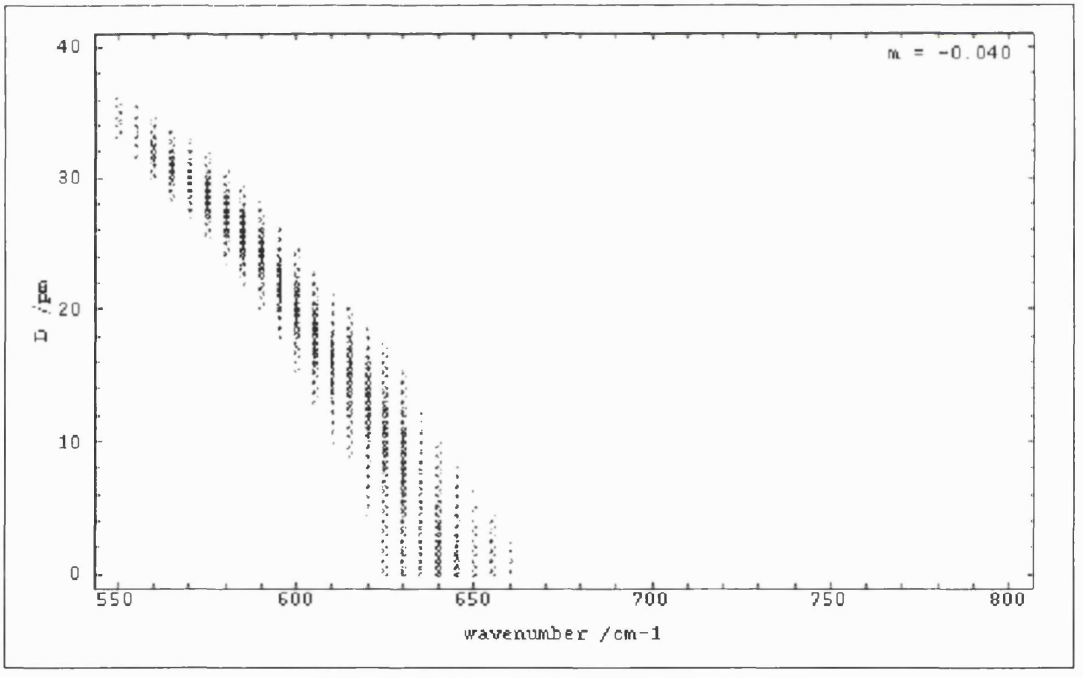

Figure 4.5a - 2D plot of X (Eqn (4.6)) for $KMnO_4$, m = -0.040.

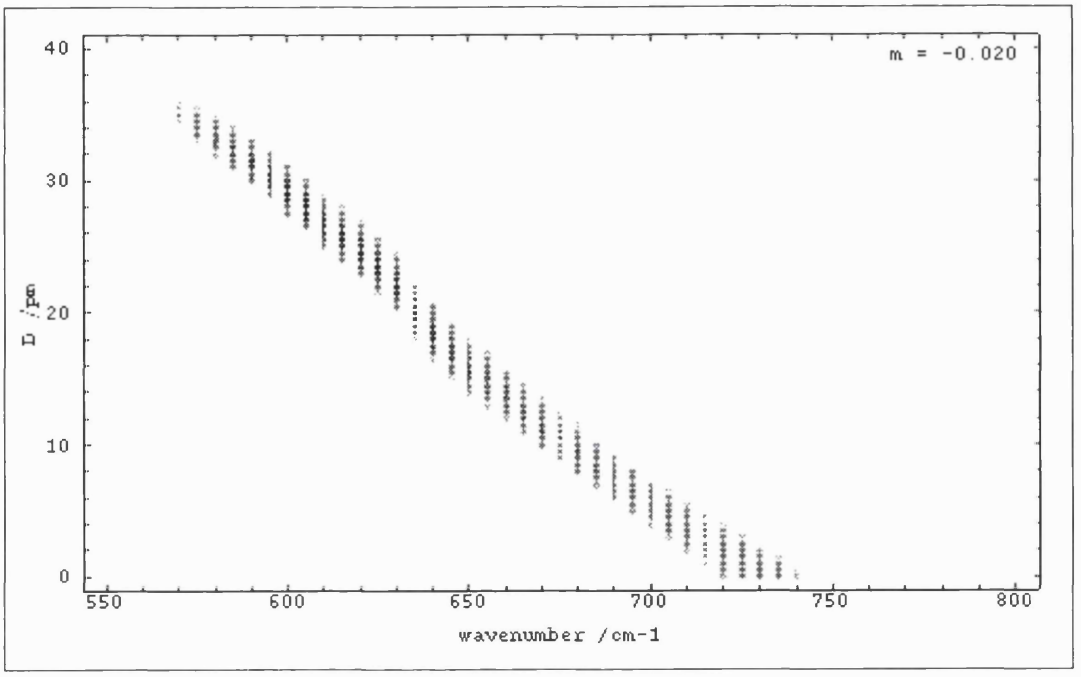

Figure 4.5b - 2D plot of X (Eqn (4.6)) for $KMnO_4$, m = -0.020.

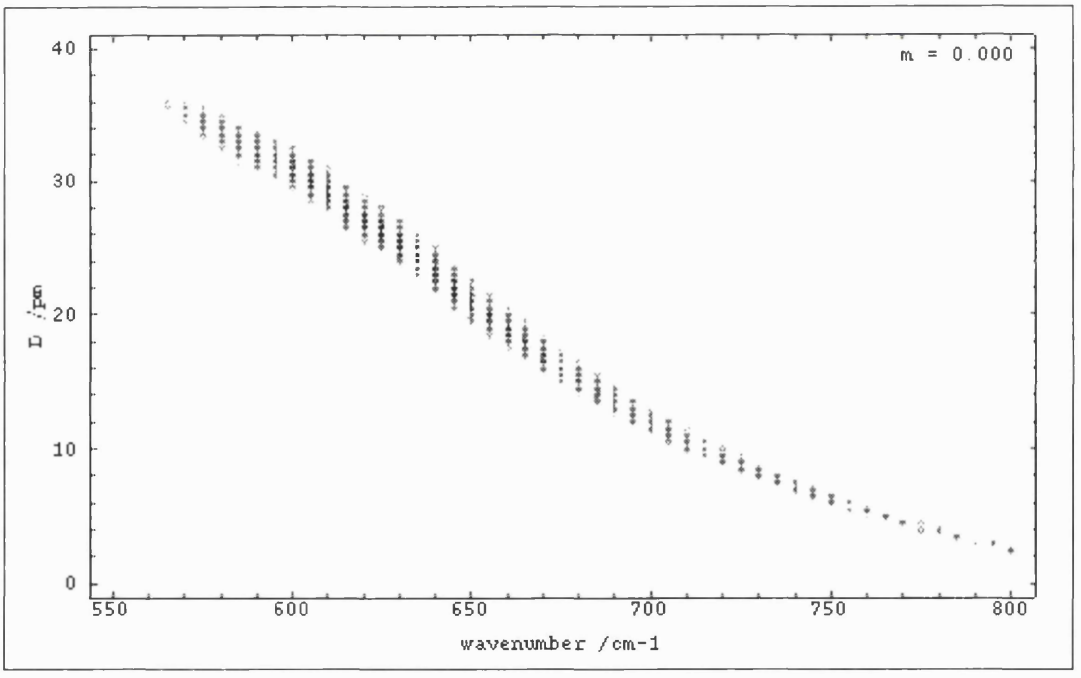

Figure 4.5c - 2D plot of X (Eqn (4.6)) for $KMnO_4$, m = -0.000.

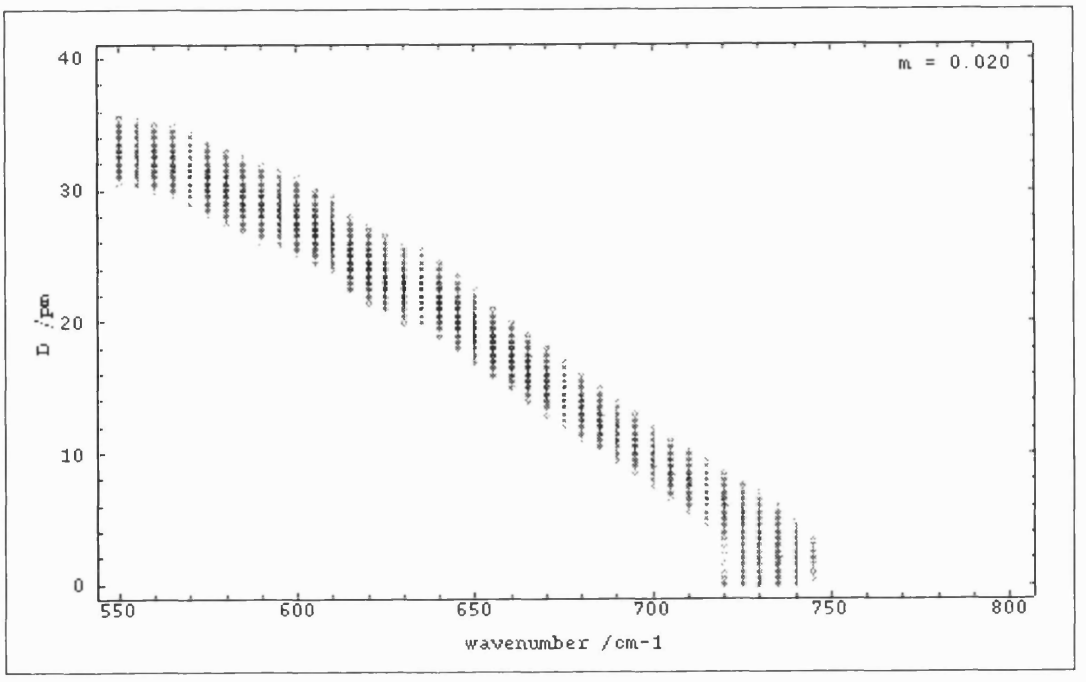

Figure 4.5d - 2D plot of X (Eqn (4.6)) for $KMnO_4$, m = 0.020.

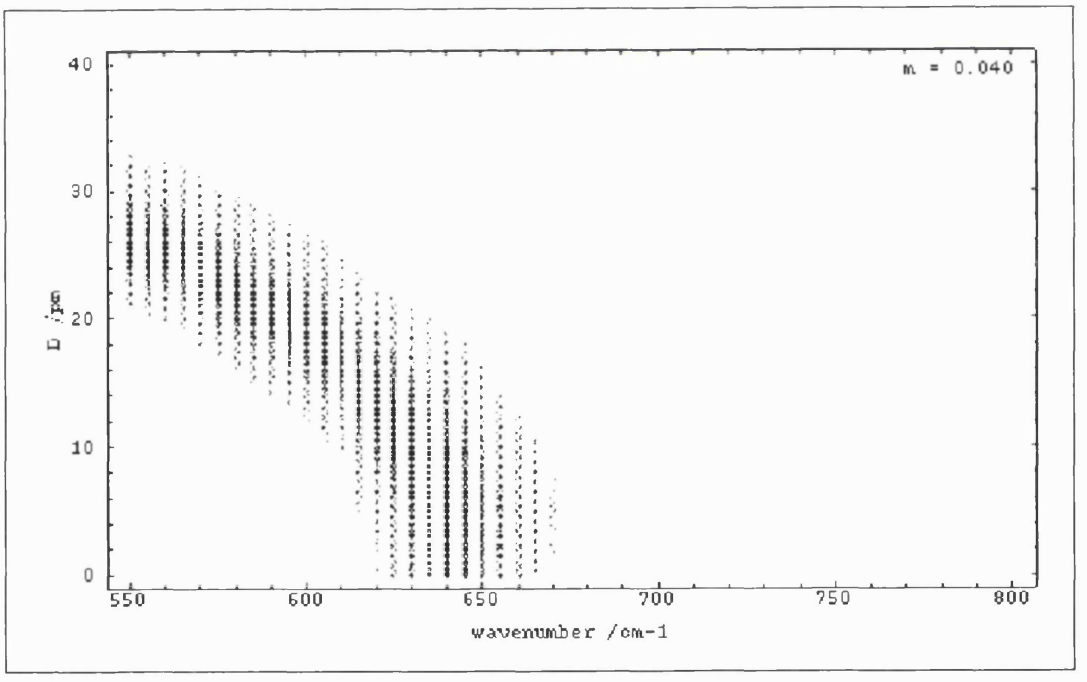

Figure 4.5e - 2D plot of X (Eqn (4.6)) for $KMnO_4$, m = 0.040.

Having inspected the solution space, the next step would be to choose a

numerical method for minimising $X(\tilde{v}_e, \Delta, m)$, or for solving $X = 0$; the next section is a brief review of some established methods, all of them iterative, that could be employed for this task.

Numerical methods for solving equations in several variables

The original problem of solving a system of three simultaneous equations in three unknowns (Eqns (4.2a-c), (4.3a-c)) has been converted first into solving a single equation in three unknowns (Eqn (4.5)) and then into minimising a function of three independent variables (Eqn (4.6)); as the minimum value of this function is zero, the methods used to find its minimum and its zeros will be completely equivalent.

Thus, the review of the numerical methods will refer to the equation

$$f(\boldsymbol{x}) = 0, \quad \boldsymbol{x} = (x_1, x_2, \ldots, x_n) \tag{4.8}$$

or to the minimisation of $f(\boldsymbol{x})$, $f : D \subset R^3 \rightarrow R$; D is the domain where the function f is defined, positive when defined by Eqn (4.6), assumed to be continuous, and its first derivative assumed to exist and to be continuous. Normally the domain can be larger than the actual region of interest so it will be chosen such as to contain at least one minimum of $f(\boldsymbol{x})$; in applications it will be restricted also by the conditions imposed on individual components of $\boldsymbol{x}$, such as the approximations formulated in Eqn (3.45b).

All numerical methods employed in solving equations or in minimising functions improve an assumed solution into a new assumed solution iteratively, starting with an initial guess for the solution of the problem, and testing against a convergence criterium and the number of iterations. An iterative process is said to converge when the difference between two successive iterations becomes smaller than a preset value, within fewer iterations than a preset number.

In view of this definition of convergence, there are no methods with a good

global convergence in several variables; when a good initial guess is available, as provided by the visual inspection procedure outlined in the previous section, the first method to be considered is Newton-Raphson [64,65], based on the Taylor expansion of a function $f(\boldsymbol{x})$ in the neighbourhood of $\boldsymbol{x}$:

$$f(\boldsymbol{x}+\delta\boldsymbol{x}) = f(\boldsymbol{x}) + \sum_{j=1}^{n} \frac{\partial f}{\partial x_j}\delta x_j + O(\delta\boldsymbol{x}^2). \tag{4.9}$$

By identifying the partial derivatives matrix in Eqn (4.9) as the Jacobian row matrix $\boldsymbol{J}$ of $f(\boldsymbol{x})$

$$J_i \equiv \frac{\partial f}{\partial x_i} \tag{4.10}$$

and by neglecting higher order terms $O(\delta\boldsymbol{x}^2)$, Eqn (4.9) becomes:

$$f(\boldsymbol{x}+\delta\boldsymbol{x}) = f(\boldsymbol{x}) + \boldsymbol{J}\cdot\delta\boldsymbol{x} \tag{4.11}$$

In a converging process $\boldsymbol{x}+\delta\boldsymbol{x}$ is much closer to the solution than $\boldsymbol{x}$ so that $f(\boldsymbol{x}+\delta\boldsymbol{x}) = 0$ ($f(\boldsymbol{x}_{new}) << f(\boldsymbol{x}_{old})$) and thus Eqn (4.10) becomes an equation for the correction to $\boldsymbol{x}$, $\delta\boldsymbol{x}$:

$$\boldsymbol{J}\cdot\delta\boldsymbol{x} = -f(\boldsymbol{x}) \tag{4.12}$$

and the new assumed solution becomes:

$$\boldsymbol{x}_{new} = \boldsymbol{x}_{old} + \delta\boldsymbol{x} \; . \tag{4.13}$$

The Newton-Raphson method works very well for smooth functions with well-defined solutions for which a good initial guess exists; however, it can be seen from Figs. 4.4 and 4.5 that $f(\boldsymbol{x}) \equiv X(\tilde{v}_e, \Delta, m)$ is not a smooth function and that there can be several solutions (minima) close to each other. Under such circumstances the Newton-Raphson method would have a significant chance of failing and there would be no indication of this happening; clearly, more refined versions of the method would be required to improve the level of confidence in its results.

A quasi-Newton method proposed in [65] checks at every iteration that some progress towards the solution is being made i.e. $f(\boldsymbol{x}_{new}) << f(\boldsymbol{x}_{old})$ and whenever

this is not the case the full correction to $\boldsymbol{x}$, $\delta\boldsymbol{x}$, is replaced with a smaller step *in the same direction* $\lambda\cdot\delta\boldsymbol{x}$, $0<\lambda<1$. Finding the appropriate λ becomes then a sub-task to be performed at every iteration, thus increasing the computational load per iteration and the number of iterations required to reach a solution and eventually cancelling the advantage of the fast convergence of the original Newton-Raphson method.

Another method for solving equations in several variables is Broyden's method, which reduces to the secant method in the one-dimensional case [64,65]; it is more robust than Newton-Raphson's method and offers better, but slower, global convergence. It is not significantly better than Newton-Raphson because it cannot cope with noisy functions and thus it does not provide a method suitable for the variety of equations that the transform method produces. The compromise between global convergence, robustness and speed is a recurrent problem of all established methods of solving equations in several variables, caused by the complexity of calculating a gradient (or equivalently the Jacobian matrix) and then correcting the existing vector $\boldsymbol{x}_{old}$ into another vector $\boldsymbol{x}_{new}$.

The nature of the problem can be changed by replacing the search for a solution of Eqn (4.8) with the search for a minimum of $f(\boldsymbol{x})$; there are several established minimisation methods in several variables and in principle any function has a minimum over a given interval. The restriction still to be observed is that the minimum be zero and well within the boundaries of the domain; in the case of several minima, all null within the preset precision, visual inspection of the solution space will sort out singularities from real minima, to be further sorted along physical considerations.

One common problem of all established minimisation methods is that the search for a minimum ends on local as well as on true, domain-wide minima; the method of the steepest descent will be reviewed briefly for illustrative purposes, its failure in the early stages of my work having been the main reason for proposing a new method in the next section.

The Steepest Descent method for minimising $f(\boldsymbol{x})$ calculates the local gradient of f at $\boldsymbol{x}_i$ for the i-th iteration and finds the new solution $\boldsymbol{x}_{i+1}$ corresponding to the minimum value of f along the local gradient; then a new local gradient is calculated at $\boldsymbol{x}_{i+1}$ and the procedure is reiterated until the local gradient is less than a preset value, i.e. a minimum has been found. As with other methods, the Steepest Descent ends on a minimum regardless of its being local or domain-wide, or of the number and position of other minima in the domain.

Proposed grid method for minimising multidimensional functions

Having reviewed the numerical methods considered for the solution of Eqn (4.7), either directly or as a minimisation problem, it becomes clear that a suitable numerical method has to:

1. - find and list all local minima within the domain;
2. - be able to cope with noisy functions;
3. - be fast enough for implementation as an independent program on personal computers.

As no method could be found to fulfil all of the above criteria, a new method is proposed [67], consisting of high resolution calculation and sorting of the values of $X(\tilde{\nu}_e, \Delta, m)$ across a $\{\tilde{\nu}_e, \Delta, m\}$ grid of suitable step size along each coordinate, spanning a sub-domain chosen by visually inspecting a low-resolution three-dimensional image of the whole domain.

The starting point of the method is the inspection of figures analogous to Figs. 4.1 and 4.2a-c; in the case chosen as example, $KMnO_4$, this eliminates a sizeable portion of the domain, towards larger absolute values of the non-Condon factor m and wavenumbers larger than 800 cm^{-1}. It would be premature to draw any conclusions from the visual inspection of a low-resolution image with regard to the position of the minima within the chosen sub-domain; the noise in the data is such that only a high-resolution computer search can find the minima with any degree of confidence. The visual

inspection and the computer search complement each other, none of these two procedures being reliable enough when used individually.

The grid method is very fast, as it calculates only the value of the function $X(\tilde{\nu}_e, \Delta, m)$ along the nodes of the grid and the small program required is very sensitive to optimisation as will be shown in a later section dedicated to the computer program. However, the search for ever better precision can cancel the benefits of simplicity and speed of the method; halving the step size along each of the three coordinates increases the computing time roughly by a factor of eight and there can be no program optimisation that could keep pace with such an increase in workload. A balance has to be maintained between precision, performance and intrinsic data noise, by use of the visual inspection before and after each computer search; at the end, when a number of possible minima have been identified, a significance test based on physical arguments will decide the solution.

The robustness of the method with respect to experimental uncertainty has been tested at an early stage, by comparing two calculated Raman Excitation Profiles, corresponding to two different data sets. The sets differed by the estimated experimental error in measuring the band intensities of Eqns (3.54) and (4.1a-d). The tests have been performed for every set of results presented in chapter 5; there always was a visible difference between the two plots and hence the method was deemed to be able to cope with experimental error.

The grid method compares well with the established minimisation methods, being more thorough than any other method and therefore fulfilling the first criterion listed at the beginning of this section. Its ability to cope with data-induced noise is good, as the grid can always be shifted by an amount smaller than the step size along any one of or even all coordinates and the new set of results compared with the previous set; thus, the method fulfils the second criterion formulated above.

Finally, the calculation and sorting program runs on any personal computer of the IBM PC type, under any DOS compatible operating system, and after recompilation on any computer with a C compiler - virtually any computer in use today. Obviously, the faster the computer the faster the program will run and Appendix 4 contains test data which show the significant effect a faster computer can have on the execution speed of the program. However, all of the practical applications shown in Chapter 5 have been run on a less powerful machine, no run taking more than 2 -3 hours. As regards the visual inspection part of the method, the Mathematica package has been ported also on most computers in use today, running at an acceptable speed even on less powerful machines, like the one employed for the applications in Chapter 5.

Having defined the problem, in Eqns (4.1) to (4.7), and a numerical method to solve it, one last but important mathematical point needs to be addressed before describing the actual computer program: the Kramers-Kronig transform itself, relating the experimental absorption to the real and imaginary parts of the complex electronic polarizability (Eqn (3.5)).

Numerical Kramers-Kronig transform of the absorption spectrum

The absorption spectrum is a tabulated function, with values measured at regular intervals along either a frequency or a wavelength scale; the standard Kramers-Kronig transform relation (Eqn (3.5)) needs to be modified by taking into account that electronic absorption is significant only across some region of the frequency spectrum and virtually zero everywhere else. Thus, the real part of Eqn (3.5) can be written as

$$\begin{aligned} \mathrm{Re}[\Phi(\omega)] &= P\int_{-\infty}^{+\infty}\frac{\mathrm{ABS}(x)}{x(x-\omega)}dx \\ &= \sum_{j=0}^{j_0-1}\int_{x_j}^{x_{j+1}}\frac{\mathrm{ABS}(x)}{x(x-\omega)}dx + \int_{x_{j_0}}^{x_{j_0+3}}\frac{\mathrm{ABS}(x)}{x(x-\omega)}dx + \sum_{j=j_0+3}^{N-1}\int_{x_j}^{x_{j+1}}\frac{\mathrm{ABS}(x)}{x(x-\omega)}dx\,, \end{aligned} \tag{4.14}$$

as any part of a definite integral with a zero integrand is null; here N is the number of data points in the absorption file and $x_{j_0+1} < \omega < x_{j_0+2}$.

The integrals under the summation signs of Eqn (4.14) can be calculated analytically, assuming that the data points are sufficiently close to each other such that $\frac{\mathrm{ABS}(x)}{x}$ can be approximated by a straight line between any two adjacent data points. The remaining integral will be calculated also analytically, but assuming a quadratic fit for $\frac{\mathrm{ABS}(x)}{x}$ across the integration domain; now Eqn (4.14) can be written as

$$\mathrm{Re}[\Phi(\omega)] = \sum_{j=0}^{j_0-1} \int_{x_j}^{x_{j+1}} \frac{a_j x + b_j}{x-\omega} dx + \int_{x_{j_0}}^{x_{j_0+3}} \frac{ax^2+bx+c}{x-\omega} dx + \sum_{j=j_0+3}^{N-1} \int_{x_j}^{x_{j+1}} \frac{a_j x + b_j}{x-\omega} dx \,, \tag{4.15}$$

where the coefficients a_j, b_j come from the linear interpolation

$$\begin{aligned} a_j x_j + b_j &= \frac{\mathrm{ABS}(x_j)}{x_j} \,, \\ a_j x_{j+1} + b_j &= \frac{\mathrm{ABS}(x_{j+1})}{x_{j+1}} \end{aligned} \tag{4.16}$$

and a, b, c from the quadratic interpolation

$$\begin{aligned} a x_{j_0}^2 + b x_{j_0} + c &= \frac{\mathrm{ABS}(x_{j_0})}{x_{j_0}} \\ a x_{j_0+1}^2 + b x_{j_0+1} + c &= \frac{\mathrm{ABS}(x_{j_0+1})}{x_{j_0+1}} \\ a x_{j_0+2}^2 + b x_{j_0+2} + c &= \frac{\mathrm{ABS}(x_{j_0+2})}{x_{j_0+2}} \,. \end{aligned} \tag{4.17}$$

At the time of reading the absorption data file, the program defines and populates two arrays, $x_j \equiv \tilde{\nu}_j$ and $y_j \equiv [\mathrm{ABS}(x_j)]/x_j$; with this notation and after performing the integrals in Eqn (4.15), the real part of the complex polarizability becomes

$$\mathrm{Re}[\Phi(\omega)] = y_N - y_0 + y_{j_0+3} - y_{j_0} +$$
$$\sum_{j=0}^{j_0-1} \frac{y_{j+1}(\omega - x_j) - y_j(\omega - x_{j+1})}{x_{j+1} - x_j} \ln\left(\frac{\omega - x_{j+1}}{\omega - x_j}\right) +$$
$$\frac{a}{2}(x_{j_0+3}^2 - x_{j_0}^2) + (a\omega + b)(x_{j_0+3} - x_{j_0}) + (a\omega^2 + b\omega + c)\ln\left(\frac{\omega - x_{j_0+3}}{x_{j_0} - \omega}\right) + \qquad (4.18)$$
$$\sum_{j=j_0+3}^{N-1} \frac{y_{j+1}(\omega - x_j) - y_j(\omega - x_{j+1})}{x_{j+1} - x_j} \ln\left(\frac{\omega - x_{j+1}}{\omega - x_j}\right).$$

Equation (4.18) is similar to that obtained by Chan and Page in [57], apart from two different points: their interpolation across the asymptote $x=\omega$ is linear rather than quadratic and their extrapolation of the absorption spectrum at the 'tails' is linear rather than quadratic. The difference between a linear and a quadratic interpolation can be up to 10 % of the value of $\mathrm{Re}[\Phi(\omega)]$, so the quadratic solution has been adopted in this work in spite of the extra computational time required.

Computer programming of the Transform Method

The implementation of the transform method and its application to the calculation of excited state parameters consists of several programs, each performing a specific task; these programs have been designed, written and maintained separately, as required by their different functionality. Throughout this section, programs written in the C programming language will be referred to as 'C programs' in the same way that the 'Mathematica scripts' are programs written in the language of the Mathematica(R) interpreter. The Mathematica scripts have been shown in earlier sections; they have not been integrated with C programs in order to avoid problems associated with increased complexity.

C has been chosen as the programming language of this work after performance tests involving different languages and different types of computer (Appendix 4), simulating the kinds of calculation deriving from the transform method; although the availability of technology has been a restrictive factor, it

was the speed and portability of C that has recommended it for this work.

The main C program calculates and sorts the values of $X(\tilde{\nu}_e, \Delta, m)$ at the nodes of a $\{\tilde{\nu}_e, \Delta, m\}$ grid, listing the local minima encountered and writing their position to a file for later inspection; as mentioned in an earlier section, the program is organised such as to maximise its execution speed by minimising the number of operations needed to scan the whole grid and a few optimisation techniques will be described in the following paragraphs.

The order of nesting the loops corresponding to each of the three parameters can change the execution time by a large factor, especially the position of the $\tilde{\nu}_e$ loop; the Kramers-Kronig transform needs to be performed at every step along the $\tilde{\nu}_e$ coordinate and it is very time-consuming. Positioning it as the outermost loop ensures that it is not performed unnecessarily; the calculated values of the real and imaginary part of the complex polarizability are stored in two arrays, part of a structure that can be accessed by calculations performed within the inner loops.

The speed of access to this structure is optimised by passing the pointer to the structure, and then pointers to the array elements within, rather than the elements themselves; it is significantly more efficient to pass a pointer of two or four bytes long than several hundred elements eight bytes each; earlier versions of the program, prior to the use of this technique, were considerably slower.

The program has a command line interface where it receives the name of the system to process and all the information required and produced by the program is read from, and written to, data files tagged with the name of the system, e.g. KMN.ABS, KMN41.DAT and KMN41.OUT for $KMnO_4$. The domain is defined in the file KMN.SRC, that can be edited very easily with any text editor; the absorption and the resonance Raman data files are never changed,

except in case of reassessment of the experimental data they contain.

As mentioned in an earlier section, a calculation can run over a period of two to three hours, the machine being unable to perform other tasks during this time or interact with its operator. A more efficient way of operation has been employed, by grouping several calculations in a batch, often run overnight without the intervention of the operator; the results are saved during each calculation in separate output data files, tagged with the name of each system.

Four other programs have been designed and written to provide feed-back on the results of the calculations of the main program but, as the main program, all calculate the values of $X(\tilde{\nu}_e, \Delta, m)$. Two programs closely related to each other have been mentioned already, in the section describing the solution space and the Mathematica scripts; they generate the scripts by calculating $X(\tilde{\nu}_e, \Delta, m)$ at every point $\{\tilde{\nu}_e, \Delta, m\}$ throughout the specified domain. One other program generates the Raman excitation profile for a given set of $\{\tilde{\nu}_e, \Delta, m\}$ parameters and order of scattering by calculating $X(\tilde{\nu}_e, \Delta, m)$ at different frequencies and another program generates resonance Raman intensities for the first four harmonics in the RRS spectrum, again for a given set of parameters $\{\tilde{\nu}_e, \Delta, m\}$; the data sets generated by these two programs are then plotted out by using a commercial graphics package. The complete listing of the main program is given in Appendix 5.

V. Applications of the Transform Method

Introduction

The purpose of this chapter is to apply the transform method developed in chapters 3 and 4 to real chemical systems. There are two main applications proposed: first, to calculate the changes in bond length and vibrational wavenumber upon excitation and second, to check on the extent to which the assumptions of the model hold, for each of the systems studied.

It was thought previously [40,43] that the transform method would be suitable only as a supplementary check on the assumptions used in multimode simulation models, based on the sum-over-states [36,37] or on the time evolution of the wave packet [59,68,69] approaches. It will be shown here (as in [60,68]) that the applications of the transform relation extend to the direct calculation of the excited state parameters.

Also, the assumptions will be tested by simulating the band intensities of the first, second, third and fourth order harmonics and the RRS excitation profiles of the fundamental and first overtone, and by comparing them with the experimental values. The availability of published data will be a limiting factor in the latter comparison, excitation profiles being usually recorded only up to the second overtone.

Data Requirements and Methodology

All transform calculations require the absorption spectrum (in digital form), the value of the reduced mass of the oscillator representing the mode of interest, and the vibrational wavenumber of that mode in the ground electronic state. The choice of procedure for the multidimensional fit determines what additional data may be required. Minimal requirements for the procedures used here are

either:

a) - intensity data at one excitation wavelength and the intensities of the first three overtones of the resonance Raman spectrum relative to that of the fundamental, or

b) - intensity data at three excitation wavelengths and the intensity of the first overtone relative to that of the fundamental for each of the three wavelengths.

Data can be obtained either from papers already published, subject to some restrictions and corrections, or directly from experiment. While for testing purposes both possibilities can be considered, only the latter is open for new systems.

The choice of data already published over those freshly recorded balances two criteria, convenience versus data quality. The quality of the data already published cannot be improved upon, but it can determine which cases will be selected for testing. Proper choice of systems and well executed experiments should offer excellent testing grounds; however, after being rigorously tested and where appropriate, corrected as necessary, published data offered the desired balance between convenience and reliability. The fact that all data have been produced in the same laboratory, using the same well known and understood standards, increases confidence in its quality.

The suitability of published data is assessed by calculating the real and imaginary parts of the complex polarizability from the optical absorption data and by examining the change of their value when changing the number of data points employed (i.e. the resolution of the data). The example presented in Table 5.1 shows that, past an optimum value, increasing the number of data points will not increase the precision of the calculation, limited by the approximations of the model (Chapter 3, Eqn (3.45b)). Each system has been tested individually for the optimum number of data points, as a structured absorption spectrum will require a higher resolution than a featureless one.

Table 5.1

The effect of the number of data points on the precision of Re(α) and Im(α)

Number of data points	Re(α) /(er)^2 s	Im(α) /(er)^2 s
10	9.985 x 10^{-9}	2.083 x 10^{-8}
20	8.012 x 10^{-9}	1.676 x 10^{-8}
30	8.107 x 10^{-9}	1.681 x 10^{-8}
40	8.093 x 10^{-9}	1.680 x 10^{-8}
50	8.095 x 10^{-9}	1.680 x 10^{-8}
100	8.095 x 10^{-9}	1.680 x 10^{-8}
2000	8.095 x 10^{-9}	1.680 x 10^{-8}

Excitation wavenumber: 20000 cm^{-1}.

Excited state vibrational wavenumber: 400 cm^{-1}

Re(α), Im(α) - the real and imaginary parts of the calculated complex polarizability, for $[NBu_4]_2[MoS_4]$

Corrections have been made, where appropriate, for two factors influencing the measured band intensity in the resonance Raman spectrum and in excitation profiles: the spectral response (efficiency) of the spectrometer and the ν^4 factor (Eqn (3.6)). As published data have been corrected already for one or both of these factors, care has been exercised in handling the data.

The smallest value accepted in the literature for the relative error in the band intensity is ± 5 %; on bands of lower intensity, as in the wings of an excitation profile or for higher order overtones, the error can be ± 10 % and even up to ± 20 %, depending on the signal-to-noise ratio. This means that fitting the more intense bands in the spectrum or the points of higher relative intensity in the excitation profile becomes relatively more important. As no quantitative measure exists for the relative error of the data employed, no estimate has

replaced it in the graphs displayed at the end of each section.

The systems used throughout this chapter have been selected according to the likelihood that they will satisfy the assumptions of the model, presented in Chapter 3; only few of the examples chosen will exhibit features leading to the conclusion that one or several of the initial assumptions have been invalidated. Systems likely to fit these assumptions well have either linear or tetrahedral symmetry and examples analysed here, of tetrahedral (MX_4), linear chain or multiply-bonded (M≡M) structure, have such symmetry.

MX_4 Systems

The systems tested here belong to the T_d point group, of tetrahedral symmetry, and consist of a central metal atom surrounded equidistantly by four identical atoms belonging to the groups VIa or VIIa (Fig. 5.1). The complexes involving the metal atom (M) can be neutral, as in titanium and tin tetrahalides, or negatively charged (all the other systems studied). The counterions are usually ammonium derivatives (potassium only in $KMnO_4$).

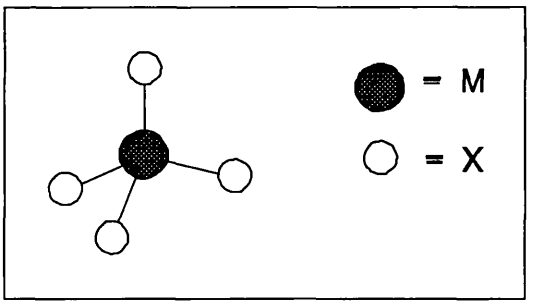

Figure 5.1 - T_d geometry.

Due to their T_d geometry, the MX_4 systems analysed here possess only one totally symmetric mode of vibration so the assumption that the mode of interest does not mix with other modes should hold well. Their geometry also makes them susceptible to Jahn-Teller distortions [71] and to splitting of the excited state into substates, breaking the assumption of a single electronic state. As long as the Jahn-Teller distortions and induced splittings are small, resonance with a single electronic state is assumed.

The nature and temperature of the samples are presented in Table 5.2,

together with some of the data employed in the calculations.

Table 5.2

Data employed in the calculations on MX_4 systems

System	Absorption spectrum			RR spectrum			μ_r /amu
	Sample	T /K	$\tilde{\nu}_{max}$/cm^{-1}	Sample	T /K	$\tilde{\nu}_{laser}$/cm^{-1}	
$KMnO_4$:$KClO_4$ [71]	solid	293	17950*	solid	293	19435	16
$[NBu_4]_2[WS_4]$ [10]	solid	14	25000	solid	80	24585	32
$[NH_4]_2[WS_4]$ [10]	solid	14	25000	solid	80	24585	32
$[NBu_4]_2[MoS_4]$ [72]	solid	14	21300	solid	80	20986	32
$[NEt_4][FeCl_4]$ [73]	sol.	293	27500	sol.	293	27488	35.5
$[NBu_4][FeBr_4]$ [73]	sol.	293	21200	solid	80	20986	79.9
$TiBr_4$ [74]	sol.	293	28600	sol.	293	27488	79.9
SnI_4 [75]	sol.	293	27500	sol.	293	N/A**	127
TiI_4 [76]	sol.	293	19400	sol.	293	19435	127

* - $\tilde{\nu}_{00}$, as the absorption spectrum is highly structured

** - several excitation wavelengths and the respective intensity of the first overtone relative to that of the fundamental have been used.

solid - pressed powder; the sample is mixed with KBr, KCl, CsI, KNO_3 or K_2SO_4

sol. - solution in cyclohexane or nitromethane.

μ_r - the reduced mass of the totally symmetric mode

It can be seen in Table 5.3 that the assumption of linear dependence of the electronic transition moment on the normal coordinate of the totally symmetric mode also holds, the linear correction parameter m being less than 0.1 in all cases. However, some of the examples show a change of more than 18.2 %

(Appendix 3) in the vibrational wavenumber of the totally symmetric mode, breaking the assumption that the force constant is linear in the normal coordinate. The paucity of experimental data points in the respective excitation profile hinders the comparison between experimental and calculated results, leaving those cases open to further investigation and discussion.

Table 5.3

Results for MX_4 systems

System	$\tilde{\nu}_R \equiv \tilde{\nu}_g$ /cm^{-1}	$\tilde{\nu}_e$ /cm^{-1}	$\lvert\delta\tilde{\nu}\rvert/\tilde{\nu}_R$ %	r(M-X) /Å	Δ(M-X) /pm	Δr %	m
$KMnO_4$:$KClO_4$	848.6 ± 0.5	747.0 ± 5.0	11.9	1.59	4.4 ± 1.0	2.7	0.00 ± 0.01
$[NBu_4]_2[WS_4]$	477.6 ± 0.5	413.0 ± 5.0	13.5	2.32[1]	11.5 ± 1.0	4.9	-0.01 ± 0.01
$[NH_4]_2[WS_4]$	488.0 ± 0.5	417.0 ± 5.0	14.5	2.32[1]	11.2 ± 1.0	4.8	-0.01 ± 0.01
$[NBu_4]_2[MoS_4]$	451.1 ± 0.5	395.0 ± 5.0	12.4	2.32[2]	10.0 ± 1.0	4.3	0.01 ± 0.01
$[NEt_4][FeCl_4]$	334.2 ± 0.5	258.0 ± 5.0	22.7*	2.30[3]	29.0 ± 1.0	12.5	0.01 ± 0.01
$[NBu_4][FeBr_4]$	203.2 ± 0.5	142.0 ± 5.0	30.0*	2.35[4]	33.0 ± 1.0	14.0	0.00 ± 0.01
$TiBr_4$	232.7 ± 0.5	155.0 ± 5.0	33.2*	2.31	30.5 ± 1.0	13.2	0.00 ± 0.01
SnI_4	151.2 ± 0.5	136.5 ± 5.0	10.0	2.64	8.3** ± 1.0	3.1	0.00 ± 0.01
TiI_4	161.2 ± 0.5	142.0 ± 5.0	11.8	2.72[5]	8.0 ± 1.0	2.9	0.01 ± 0.01

* - technically outside the limits of the model, 18.2 % (Appendix 3)

** - using the ratio between the intensity of the first overtone and of the fundamental

Estimates [77,78]:

[1] - from r(W-Cl) = 2.26 Å in WCl_6

[2] - from r(Mo-Cl) = 2.27 Å in $MoCl_5$

[3] - from r(Fe-Cl) = 2.30 Å in $[FeCl_6]^-$

[4] - from r(Fe-Cl) = 2.30 Å in $[FeCl_6]^-$ and r(Br-Br) = 2.28 Å in Br_2

[6] - from r(Ti-Br) = 2.31 Å in $TiBr_4$, r(Br-Br) = 2.28 Å in Br_2 and r(I-I) = 2.66 Å in I_2

Notes to symbols:

$\tilde{\nu}_R \equiv \tilde{\nu}_g$ = vibrational wavenumber in the ground electronic state

$\tilde{\nu}_e$ = vibrational wavenumber in the resonant excited electronic state

$\delta\tilde{\nu} \equiv (\tilde{\nu}_g - \tilde{\nu}_e)/\tilde{\nu}_g$ = the relative wavenumber change in the mode of interest between the ground and excited states

r(M-X) = metal-ligand bond length. M = Mn, W, Mo, Fe, Ti or Sn; X: O, S, Cl, Br or I

Δ(M-X) = metal-ligand bond length change upon excitation

m = linear non-Condon correction parameter (Eqn (3.25))

The results in Table 5.3 compare well with those given in other sources, where data were available for comparison; unfortunately such data were available for only few of the systems considered, as the parameters calculated here may not have been measured directly in any study before. Table 5.4 compares the results of the present method applied to MX_4 systems with previously published results; graphs comparing the simulated and experimental resonance Raman spectrum and excitation profile for each system are grouped at the end of this section (Figs. 5.2-5.10,(a,b)).

Table 5.4

Comparison between present and previously published results for MX_4 systems

System	$\tilde{\nu}_e$/cm^{-1}		Δ /pm	
	present work	other work	present work	other work
$KMnO_4$:$KClO_4$	747.0 ± 5.0	740.0 ± 5.0 [71]	4.4 ± 0.5	4.6 ± 0.5 [58]
$[NBu_4]_2[WS_4]$	413.0 ± 5.0	410.0 ± 10.0 [10]	11.5 ± 1.0	10.0 ± 1.0 [59]
$[NBu_4]_2[MoS_4]$	395.0 ± 5.0	410.0 ± 10.0 [72]	10.0 ± 1.0	10.0 ± 1.0 [60]
TiI_4	142.0 ± 5.0	145.0[1] [79]	8.0 ± 1.0	7.8 ± 1.0 [61]

[1] - assumed in the calculation in [79]

The vibronic structure present in some absorption spectra ($KMnO_4$, $[NBu_4]_2[WS_4]$ and $[NBu_4]_2[WS_4]$) permits the direct measurement of the vibrational wavenumber of the totally symmetric mode in the excited electronic state. In all cases mentioned, the results of the present method match, within the errors, those obtained directly from the absorption spectrum. The results for the bond length change also match, within the errors, those obtained by other workers [10,71,72,79] through total simulation using a sum-over-states approach.

A problem present in some graphs (like those for $[NEt_4][FeCl_4]$, $TiBr_4$ and SnI_4), is the relative error (as discussed in a previous section) of the experimental data points in the excitation profiles. $[NEt_4][FeBr_4]$ is also the only system for which the intensity of the first overtone relative to that of the fundamental increases monotonously, even beyond 1.0, with the wavenumber of the exciting radiation. Assuming that the experimental data set is reliable, the $[FeBr_4]^-$ ion appears to undergo drastic changes upon excitation, which cannot be modelled within the present approach. This conclusion appears to be confirmed by the

exceedingly large values obtained for $\tilde{\nu}_e$ and for Δ; the fact that they appear to parallel those for $[NEt_4][FeCl_4]$ and $TiBr_4$ is not relevant, as the latter have very few points on the excitation profile to compare with.

Tin tetraiodide has given very different results for each of the two procedures outlined in Chapter 4 and in an earlier section of this chapter. The final result has been determined by comparison with a similar system (TiI_4) and between the experimental and calculated resonance Raman spectrum and excitation profiles (at the end of the present section). There have been two attempts to calculate $\tilde{\nu}_e$ and Δ for TiI_4; the results of the present method are consistent with one set of results [79], the other set [80] not being even self consistent (a linear correction of 30 %, m = -0.3, requires a *quadratic* rather than the *linear* model employed in [80]).

A similar situation appeared for $[NBu_4]_2[MoS_4]$, albeit with a smaller discrepancy between the results of the two procedures. The corresponding graph at the end of this section shows the difference between the experimental and calculated resonance Raman spectrum; the non-Condon result is comparable with the result of a pure Franck-Condon model, but the experimental data appear far from fitting either model. Comparison with similar systems ($[NH_4]_2[WS_4]$, $[NBu_4]_2[WS_4]$) indicate that the results obtained solely from the band intensities of the first four harmonics in the resonance Raman spectrum are not reliable. The explanation could be that the $\tilde{\nu}_1$ and $\tilde{\nu}_3$ wavenumbers differ by only 4 %, leading to the overlapping of the main $v_1\tilde{\nu}_1$ progression with the $\tilde{\nu}_3 + v_1\tilde{\nu}_1$ - or maybe with a $v_3\tilde{\nu}_3$ progression - and to unreliable band intensities. As this overlap disappears when excitation takes place away from the maximum of the $\tilde{\nu}_1$ excitation profile, the band intensities can be measured more accurately and so the results of the second procedure are definitely the more reliable.

$KMnO_4$:$KClO_4$

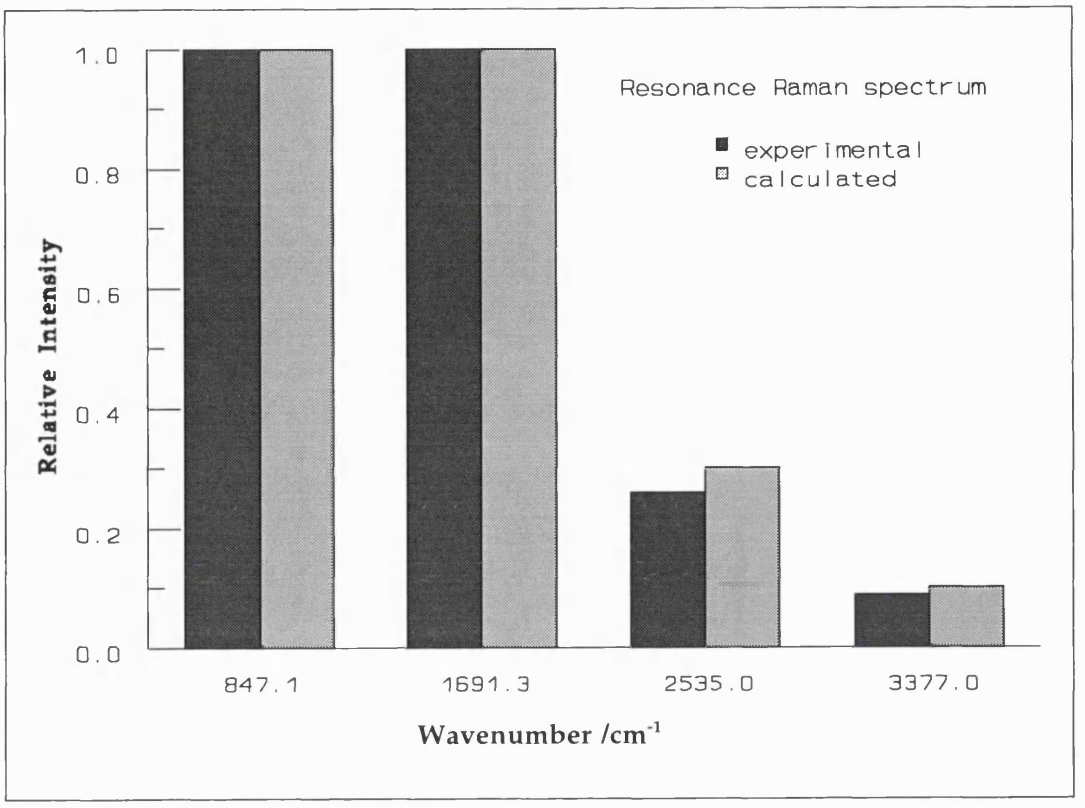

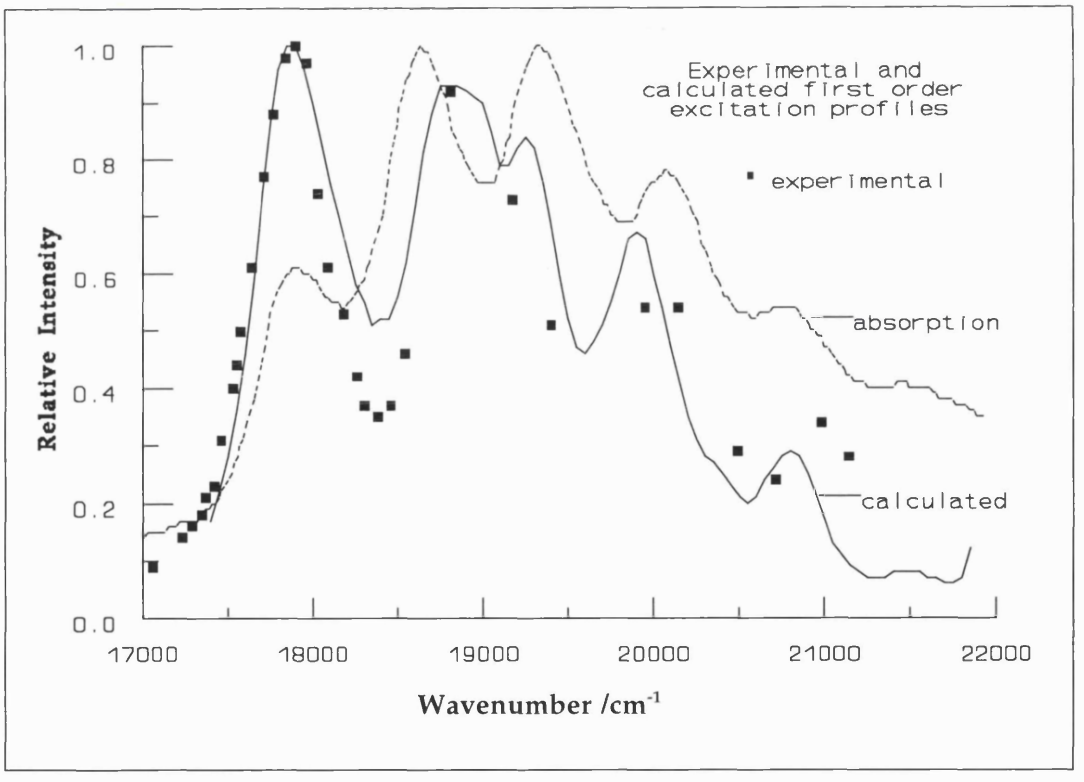

Figures 5.2a (top), 5.2b (bottom).

$[NBu_4]_2[WS_4]$

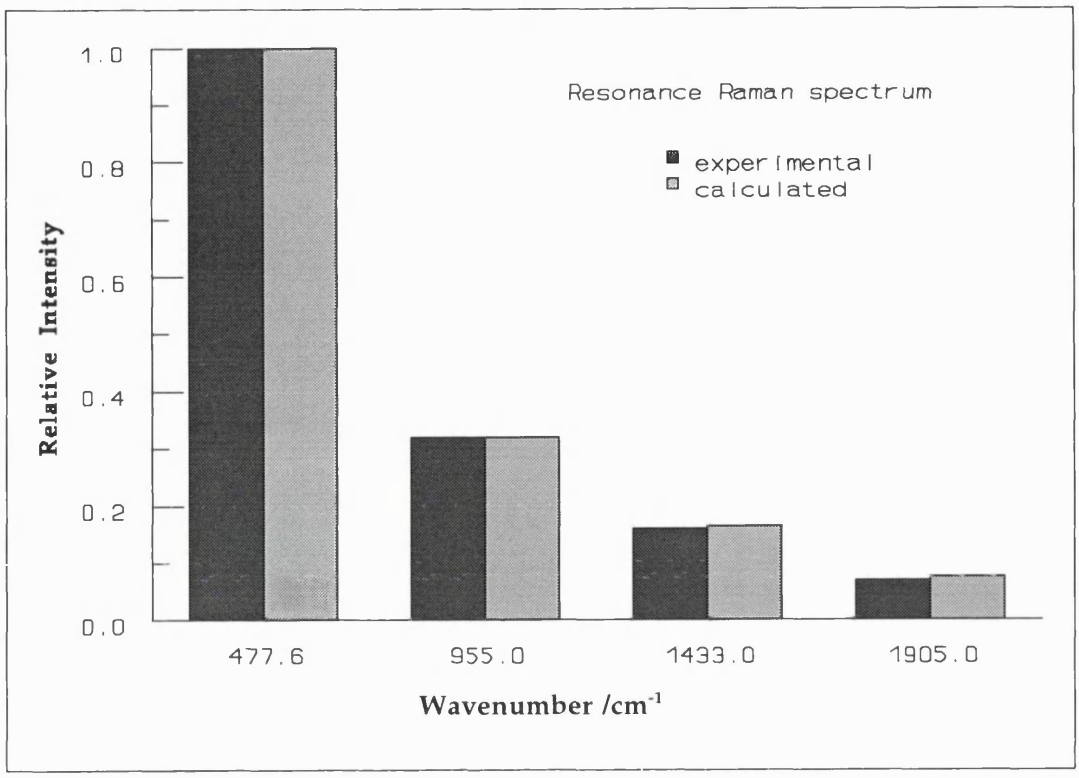

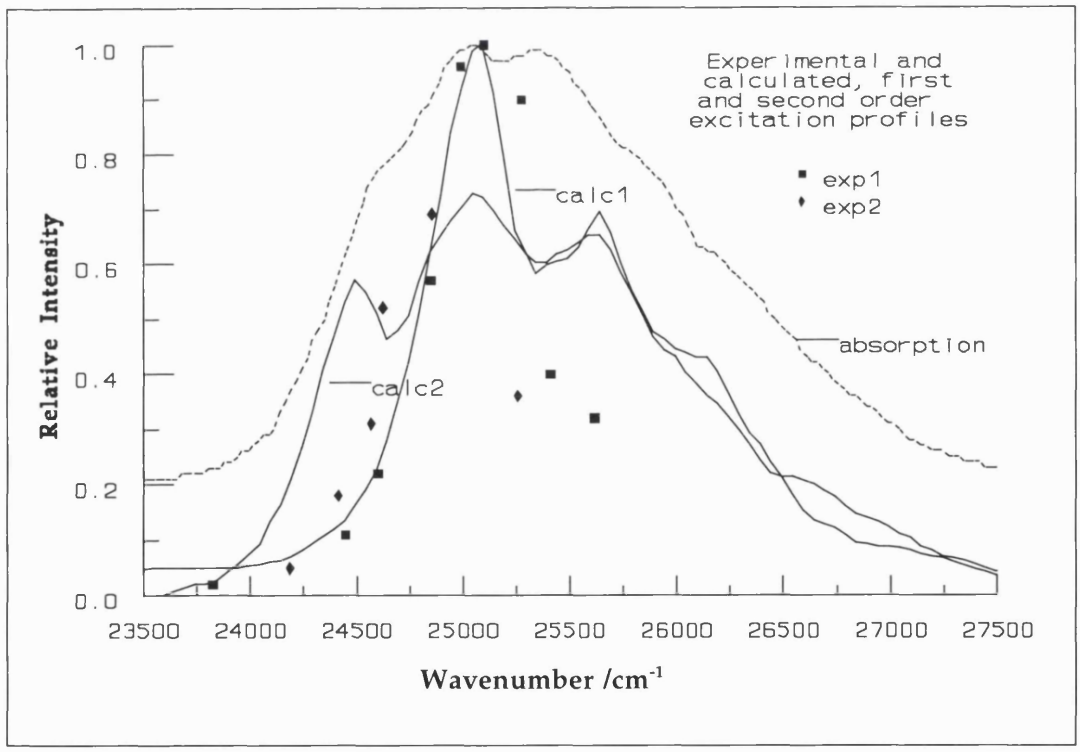

Figures 5.3a (top), 5.3b (bottom).

$[NH_4]_2[WS_4]$

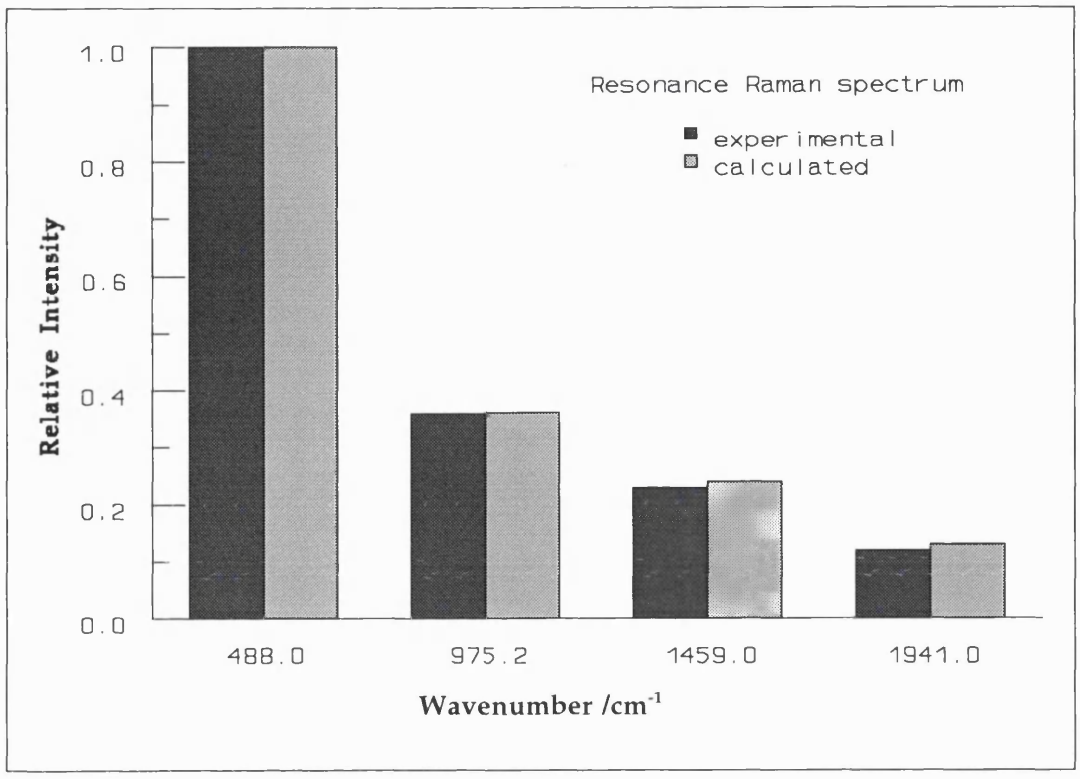

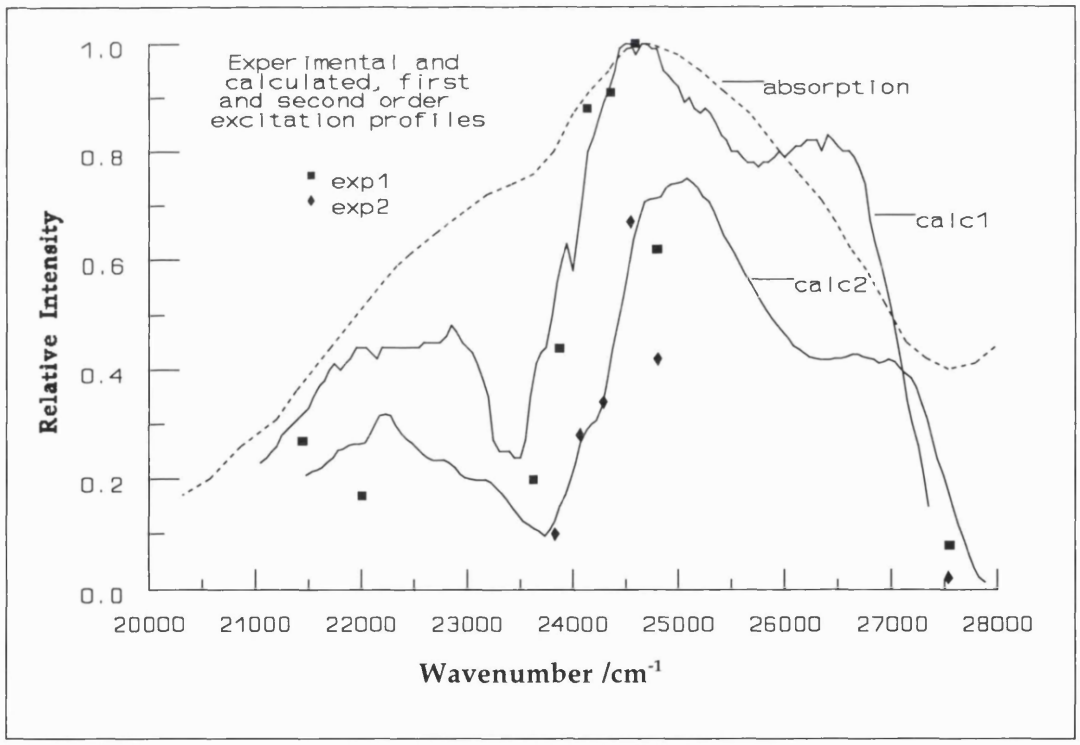

Figures 5.4a (top), 5.4b (bottom).

$[NBu_4]_2[MoS_4]$

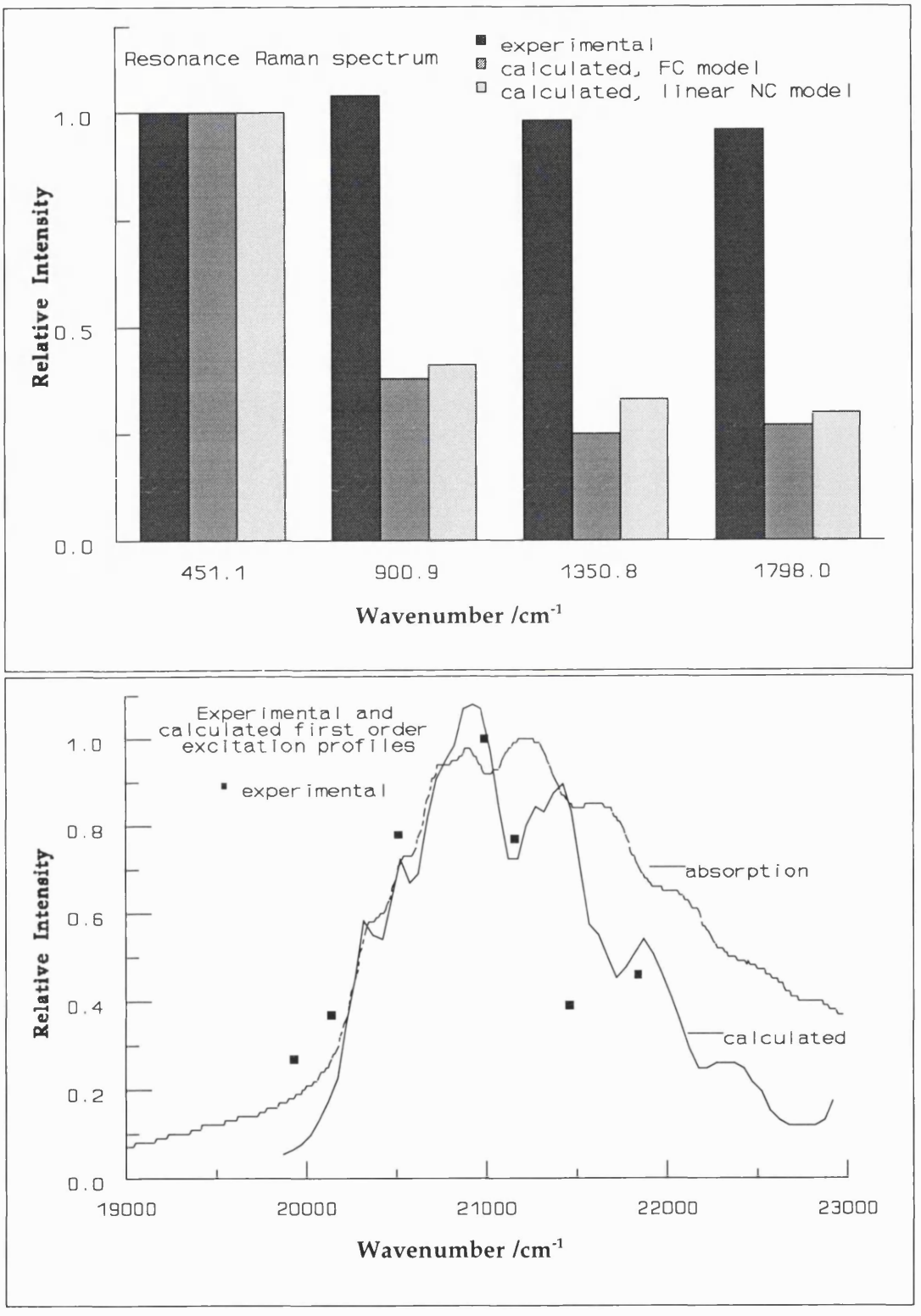

Figures 5.5a (top), 5.5b (bottom).

$[NEt_4][FeCl_4]$

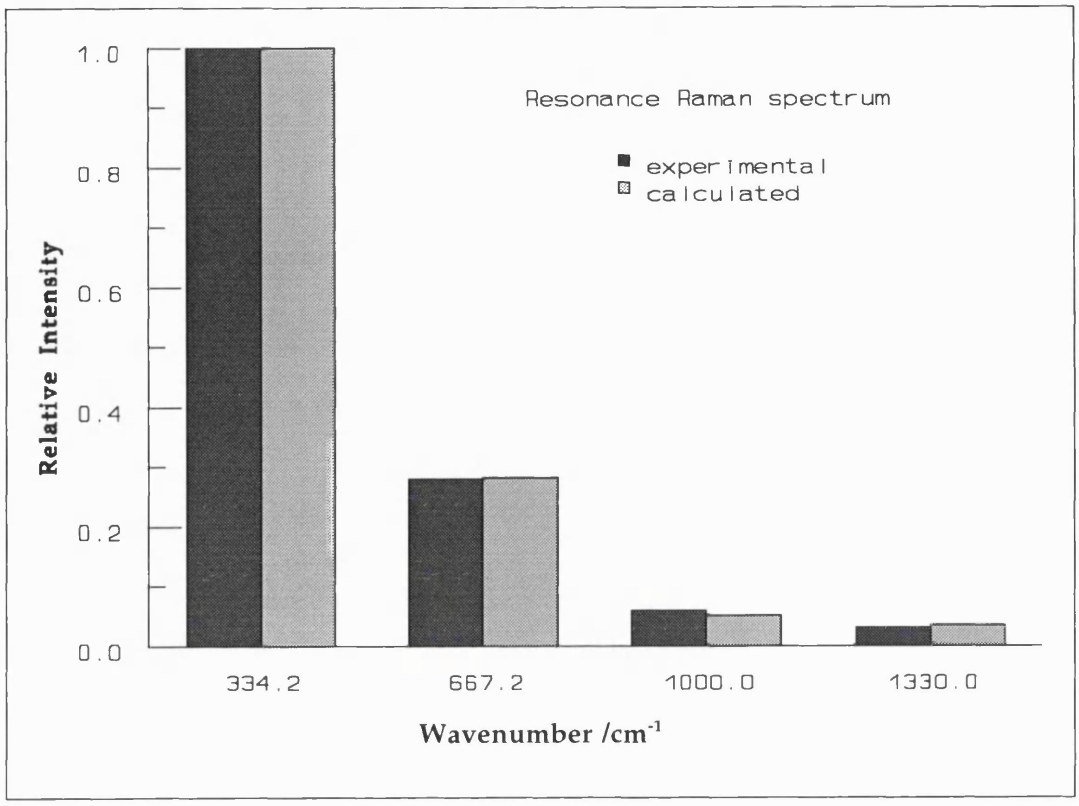

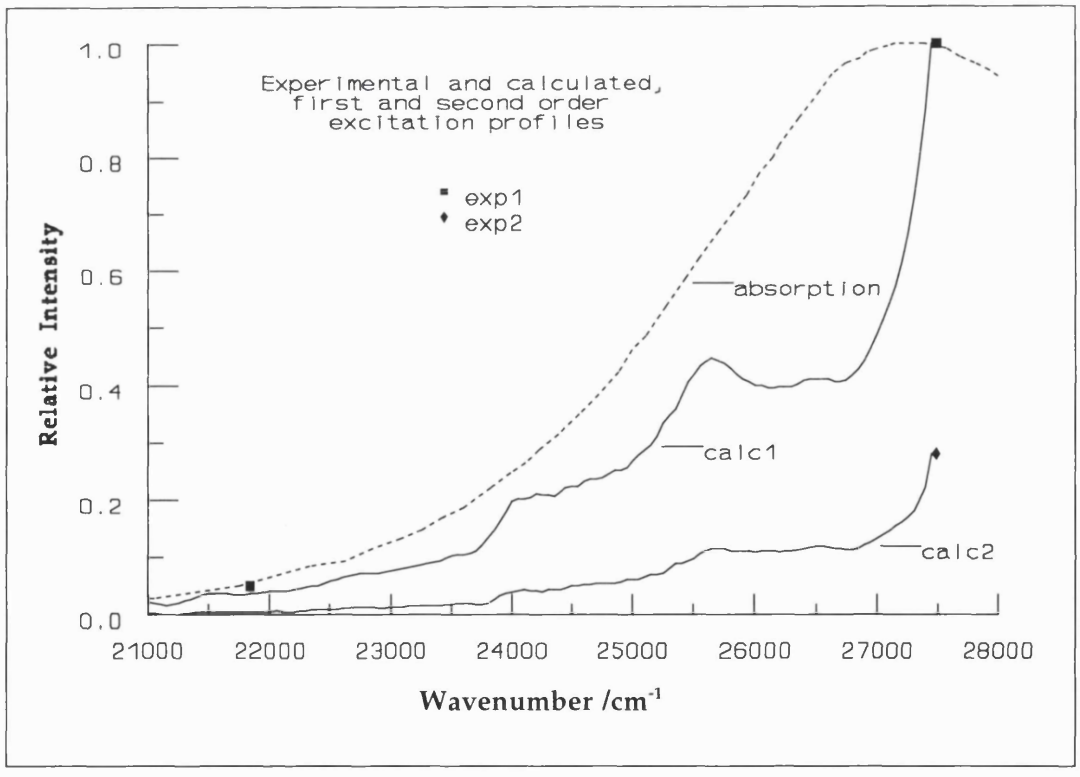

Figures 5.6a (top), 5.6b (bottom).

$[NBu_4][FeBr_4]$

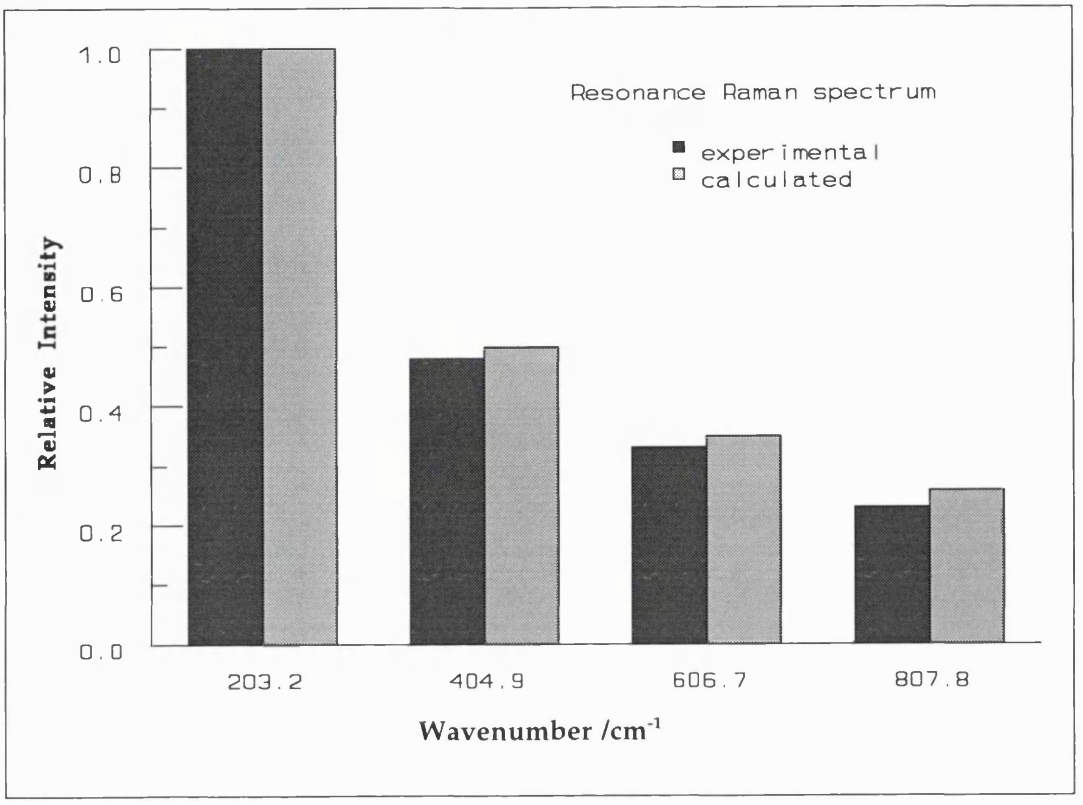

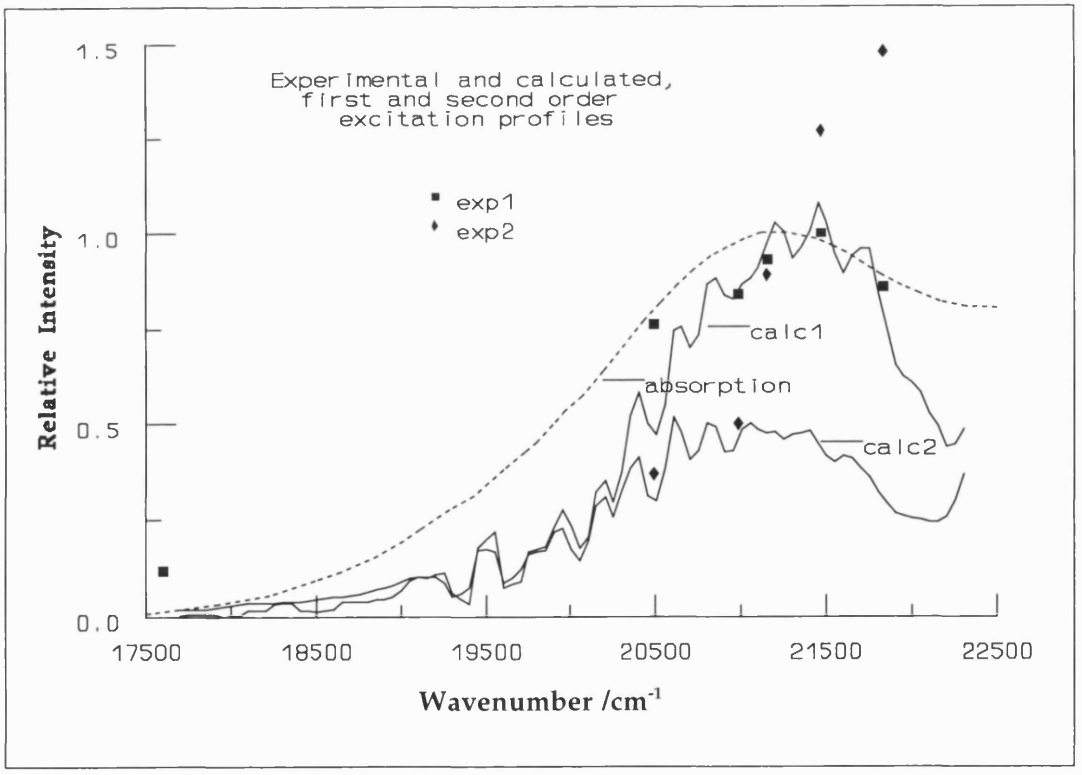

Figures 5.7a (top), 5.7b (bottom).

$TiBr_4$

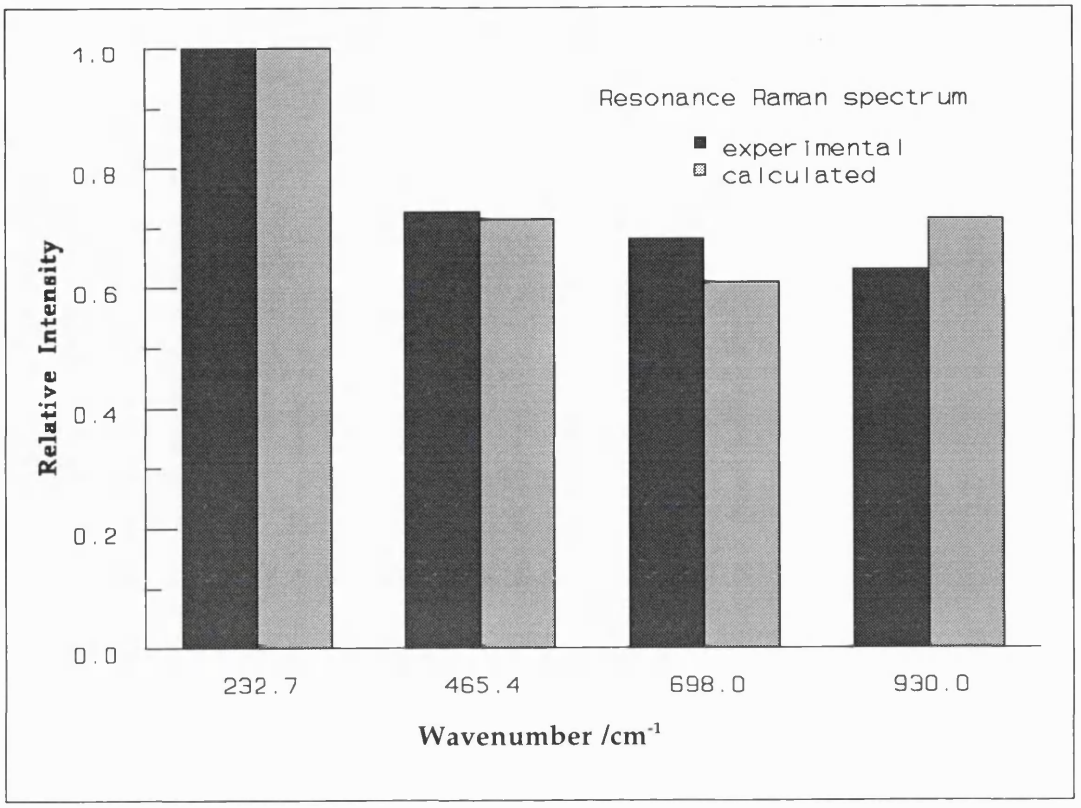

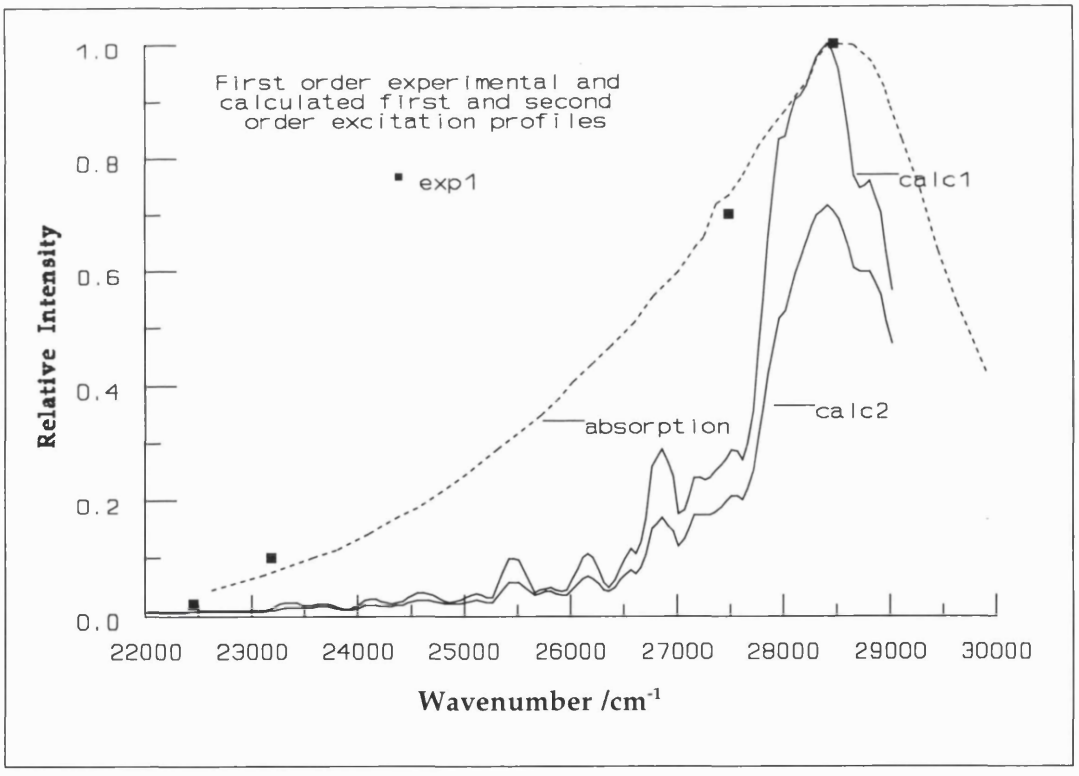

Figures 5.8a (top), 5.8b (bottom).

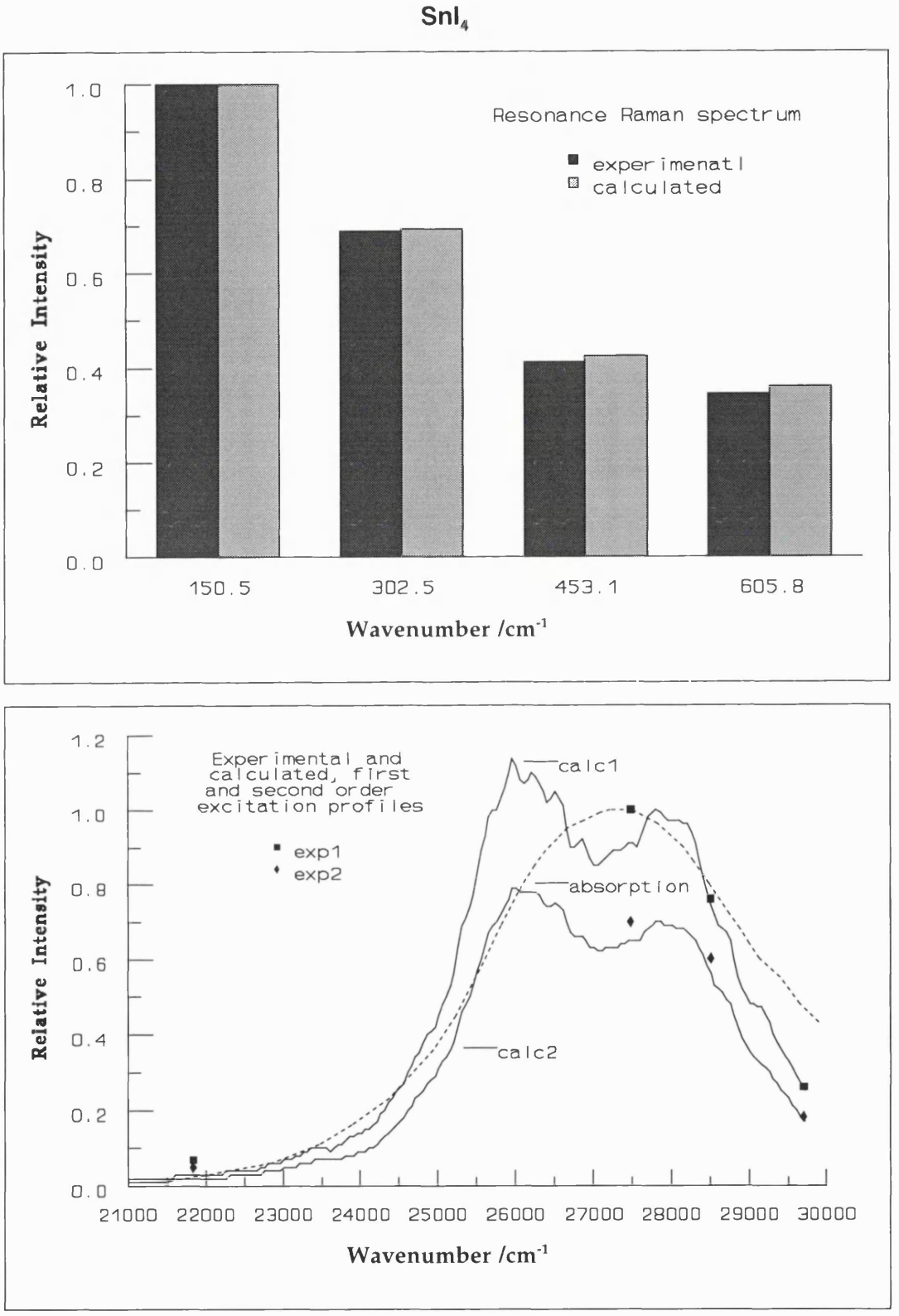

Figures 5.9a (top), 5.9b (bottom).

TiI_4

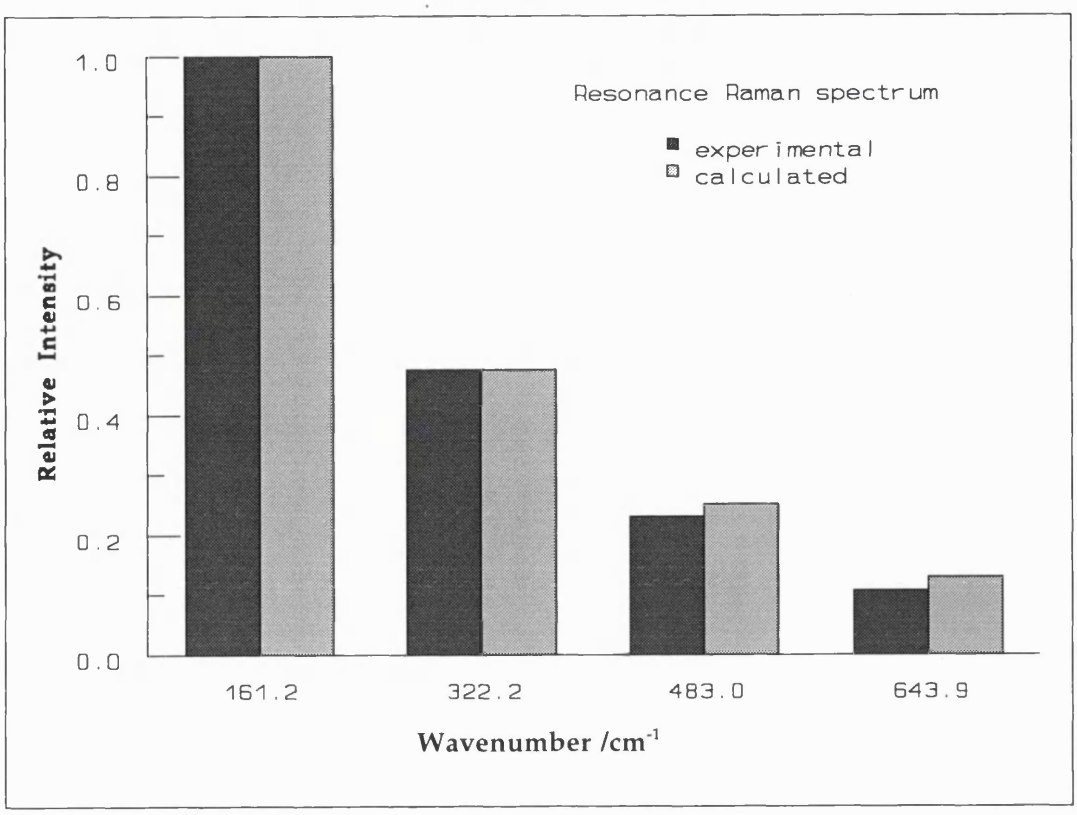

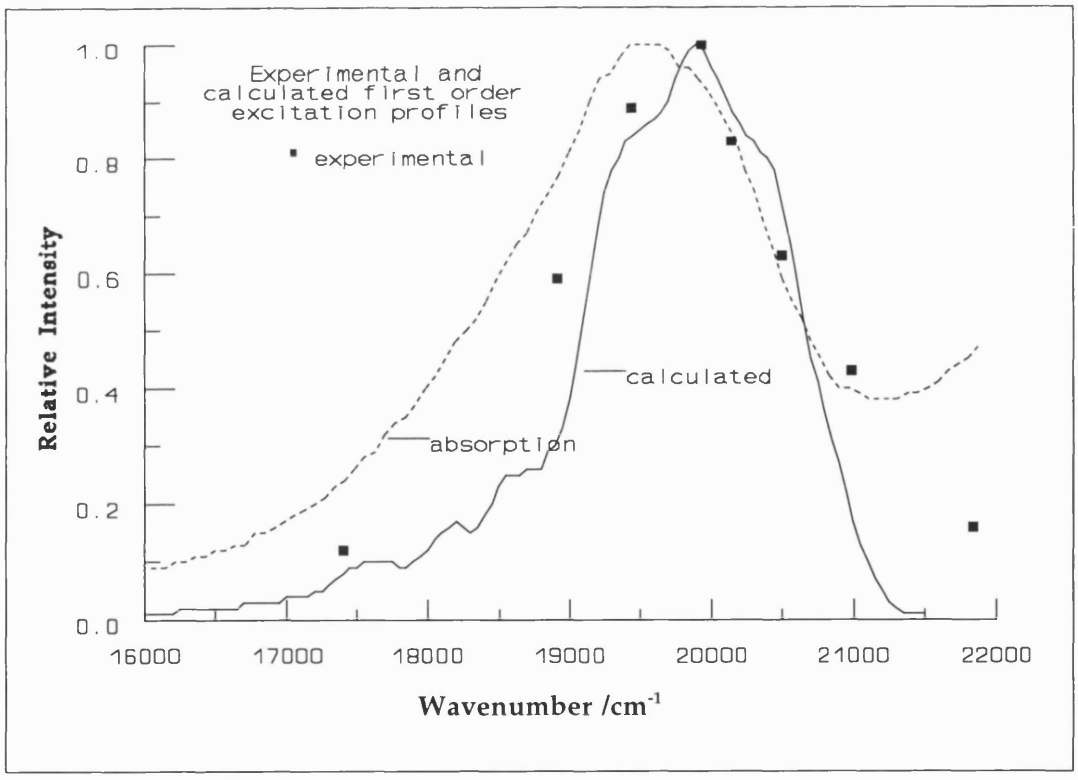

Figures 5.10a (top), 5.10b (bottom).

M≡M Multiply Bonded Systems

The systems tested consist of two triply bonded metal atoms (Os or Rh) bridged by a 'cage' of four identical ligands (O_2CCH_3 or O_2CCH_2Cl) and one axial ligand attached to each metal atom (either a Cl atom or PPh_3). Thus the systems belong to the D_{4h} point group (Fig. 5.11).

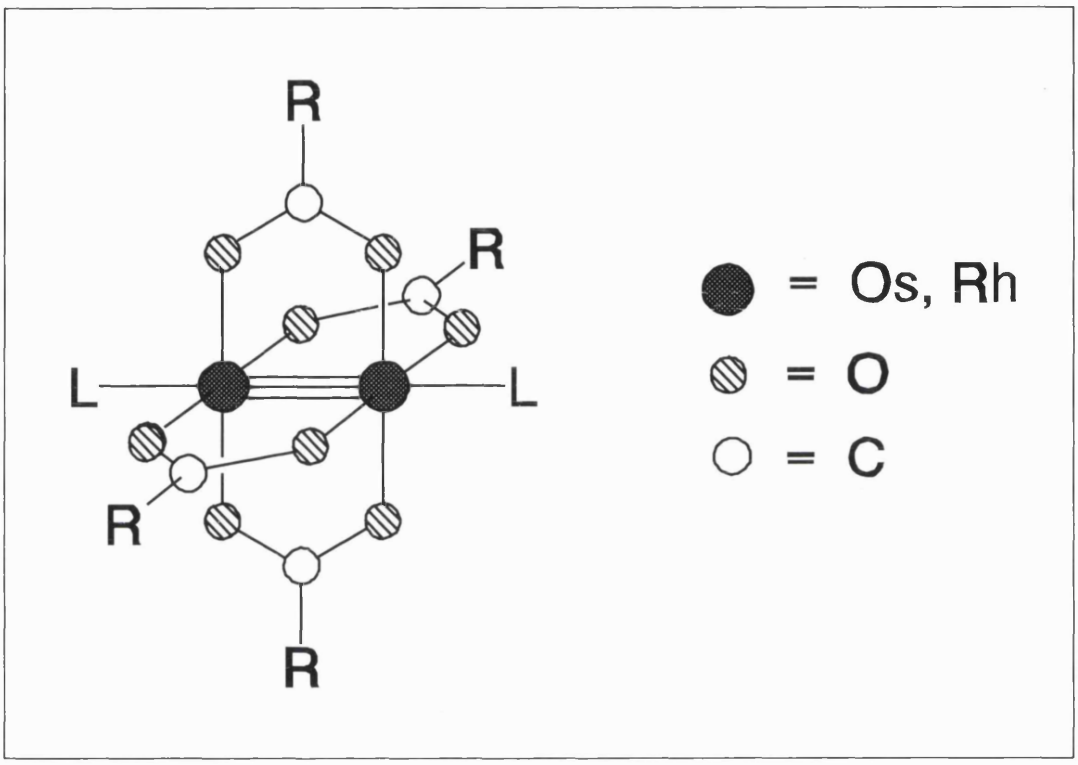

Figure 5.11 - Geometry of M≡M systems.

The angle between the metal-oxygen and the metal-metal bonds is almost 90°, which should prevent the metal-metal stretching mode from mixing with any of the 'cage' modes; however, mixing with the axial metal-ligand stretch should be expected. The excitation profiles [81-83] show, however, that the intensities of these other bands are much lower than that of the metal-metal stretch, and so the present treatment will neglect any mode mixing.

The absorption spectrum shows only one band in the visible region of the spectrum (with a very weak shoulder in the case of $Os_2(O_2CCH_2Cl)_4Cl_2$) so

resonance with a single electronic band is assumed. The nature and temperature of the samples are described in Table 5.5, together with some of the data employed in the calculations.

Table 5.5

Data employed in the calculations on metal-metal multiply bonded systems

System	Absorption spectrum			RR spectrum			μ_r /amu
	Sample	T /K	$\tilde{\nu}_{max}$ /cm^{-1}	Sample	T /K	$\tilde{\nu}_{laser}$ /cm^{-1}	
$Os_2(O_2CCH_3)_4Cl_2$ [81]	solid	20	26000	solid	80	24585	95.1
$Os_2(O_2CCH_2Cl)_4Cl_2$ [82]	solid	20	24500	solid	80	24070	95.1
$Rh_2(O_2CCH_3)_4(PPh_3)_2$ [83]	solid	20	27000	solid	80	28056	51.5

Table 5.6

Results for metal-metal multiply bonded systems

System	$\tilde{\nu}_R \equiv \tilde{\nu}_g$ /cm^{-1}	$\tilde{\nu}_e$ /cm^{-1}	$\lvert\delta\tilde{\nu}\rvert/\tilde{\nu}_R$ %	r(M≡M) /Å	Δ(M≡M) /pm	Δ/r %	m
$Os_2(O_2CCH_3)_4Cl_2$	229.0 ± 0.5	205.0 ± 5.0	10.4	2.314	15.0 ± 1.0	6.5	-0.01 ± 0.01
$Os_2(O_2CCH_2Cl)_4Cl_2$	236.0 ± 0.5	188.0 ± 5.0	20.3*	2.32[1]	21.8 ± 1.0	9.4	0.00 ± 0.01
$Rh_2(O_2CCH_3)_4(PPh_3)_2$	289.0 ± 0.5	261.0 ± 5.0	9.7	2.450 [66]	23.4 ± 1.0	9.5	0.02 ± 0.01

* - technically outside the limits of the model, 18.2 % (Appendix 3); if the precision margin is taken into account, the result is within the limits.

[1] - estimated from r(M≡M) = 2.314 Å in $Os_2(O_2CCH_3)_4Cl_2$.

Notes to symbols:

$\tilde{\nu}_R$, $\tilde{\nu}_e$, $\delta\tilde{\nu}$, m - same as the symbols in Table 5.2

r(M-M) = metal-metal bond length (Os-Os, Rh-Rh)

Δ(M-M) = metal-metal bond length change upon excitation.

The relative bond length change for the M≡M tested here is larger than for the MX_4 systems but similar to the values obtained for linear chains (presented in the next section). It appears that the relative bond stretch upon electronic excitation is larger in systems with axial symmetry than for centrosymmetric ones.

The simulations of the resonance Raman spectra and of the excitation profiles compare well with the experimental data, especially for $Os_2(O_2CCH_2Cl)_4Cl_2$ for which also better defined excitation profiles are available. A comparison between the experimental resonance Raman spectra and Raman excitation profiles, and those calculated with the transform method is given in Figs. 5.12-5.14(a,b), presented at the end of this section.

Unfortunately, there are no results in the literature with which to compare those of the present section; those of Woodruff et al. [84] have been obtained for *non*-bridged multiply-bonded systems ($[Re_2Br_8]^{2-}$) and thus a direct comparison between the results is not possible.

$Os_2(O_2CCH_3)_4Cl_2$

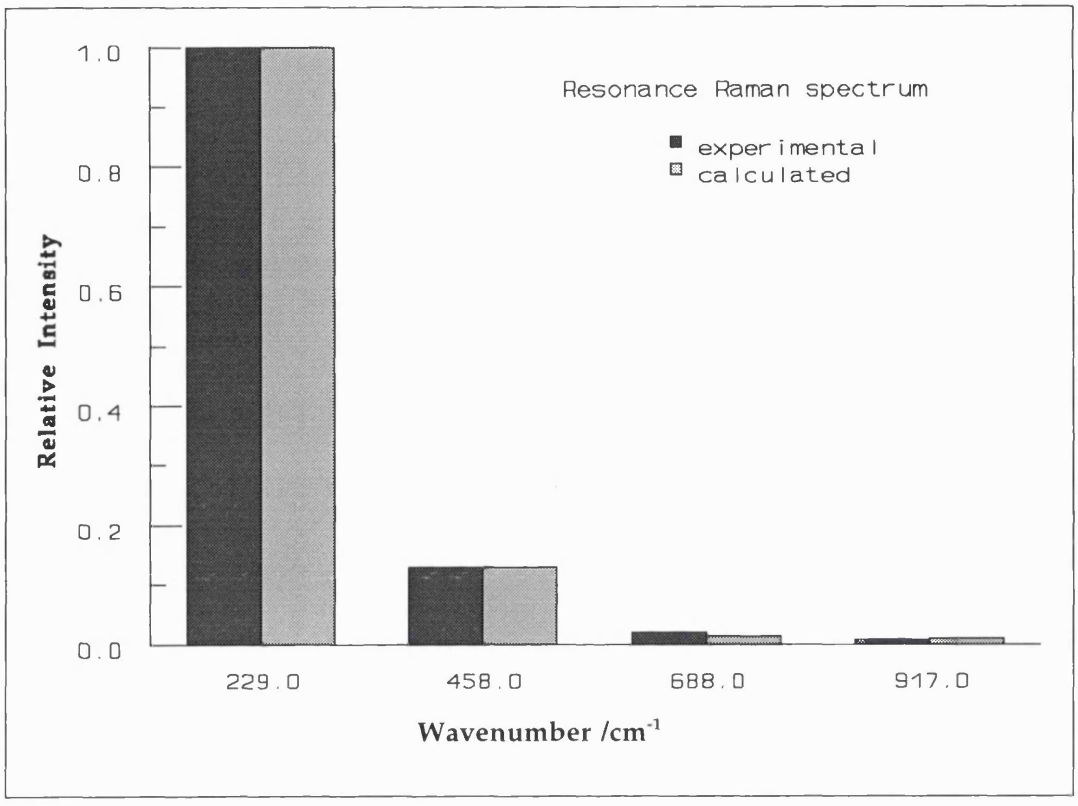

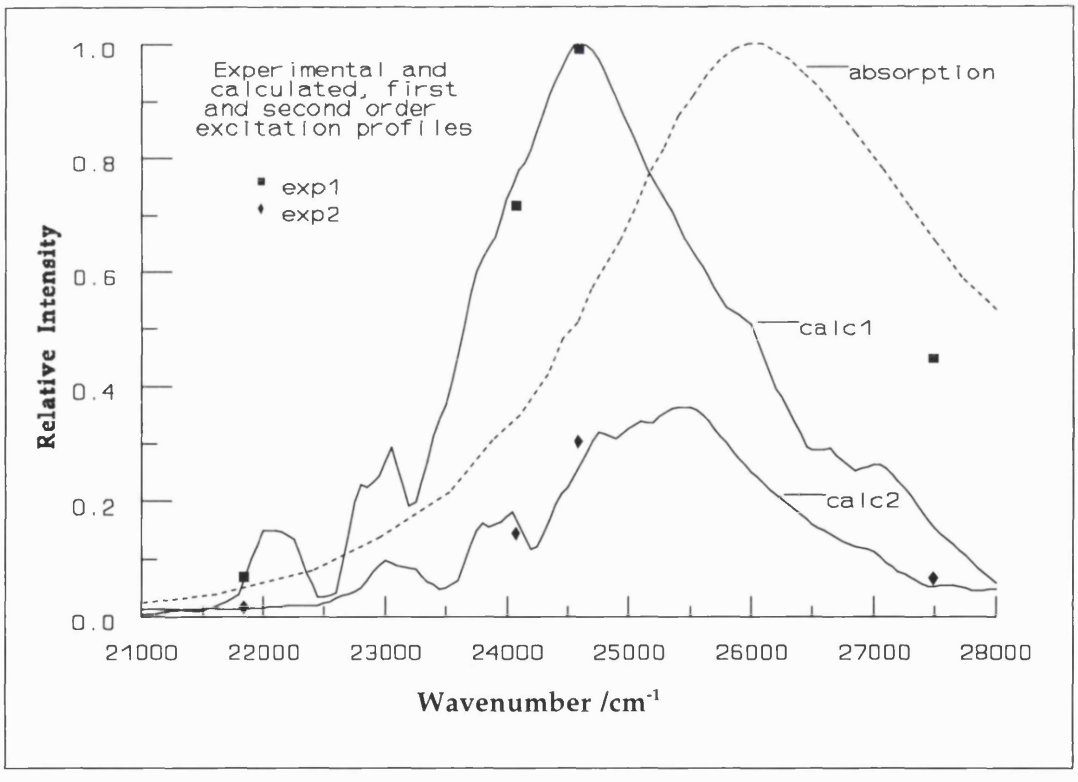

Figures 5.12a (top), 5.12b (bottom).

$Os_2(O_2CCH_2Cl)_4Cl_2$

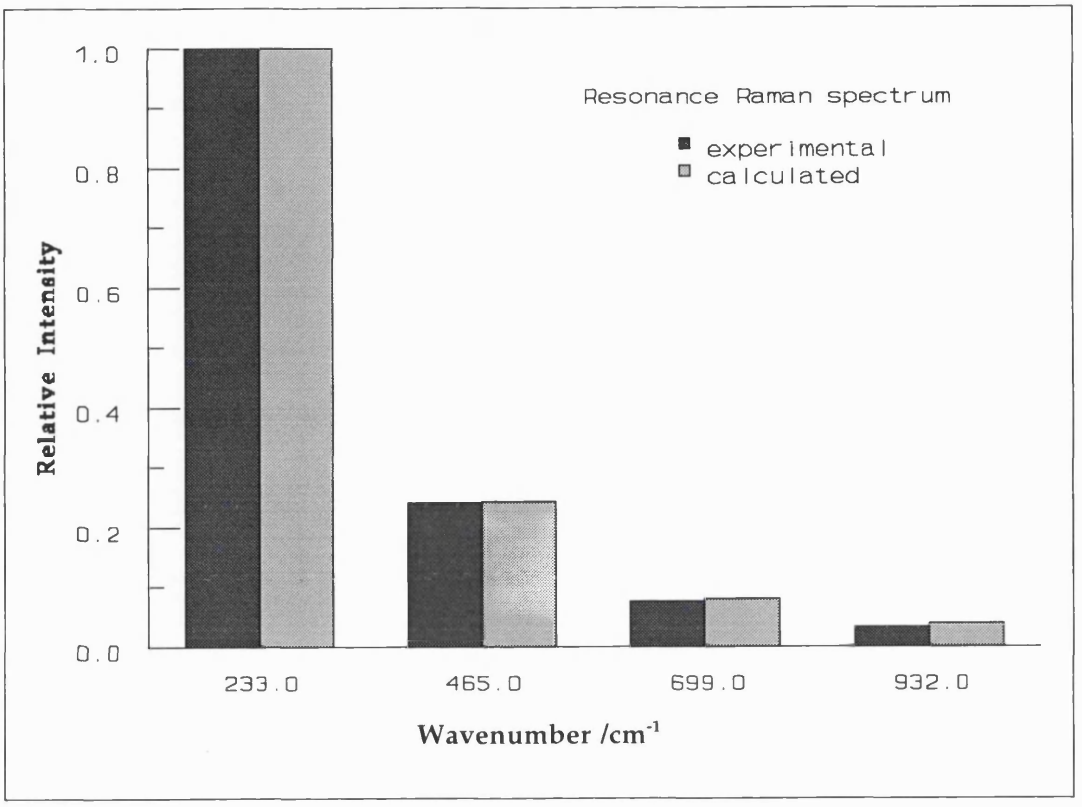

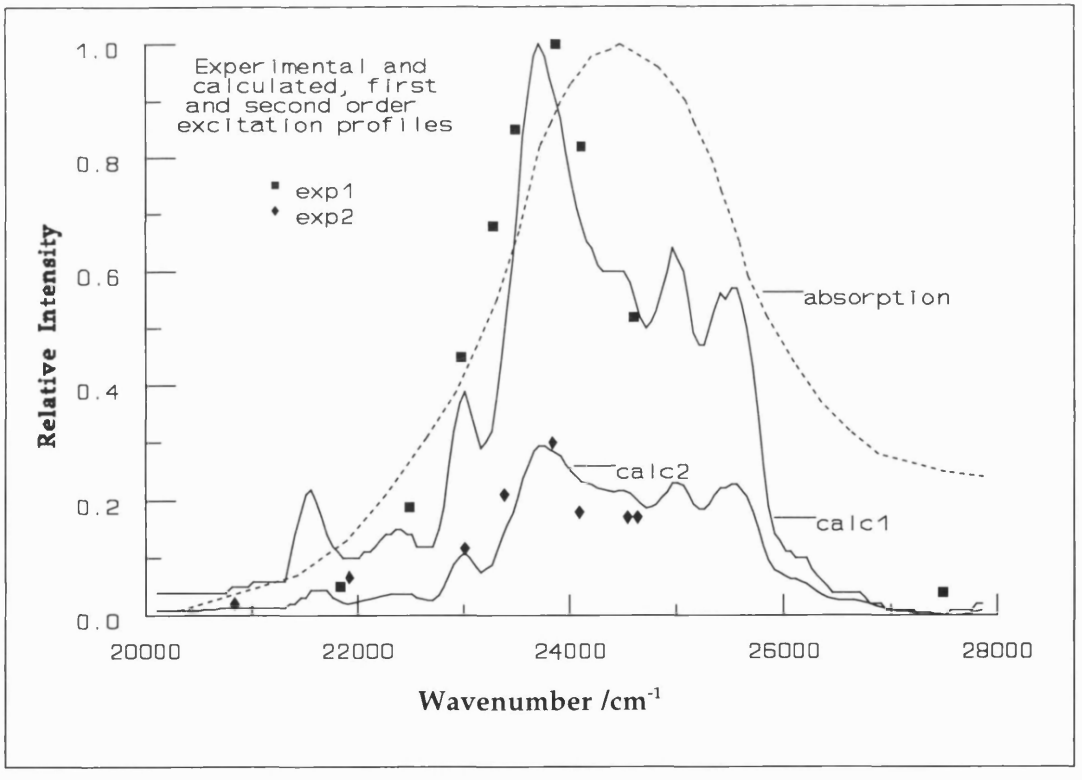

Figures 5.13a (top), 5.13b (bottom).

$Rh_2(O_2CCH_3)_4Cl_2$

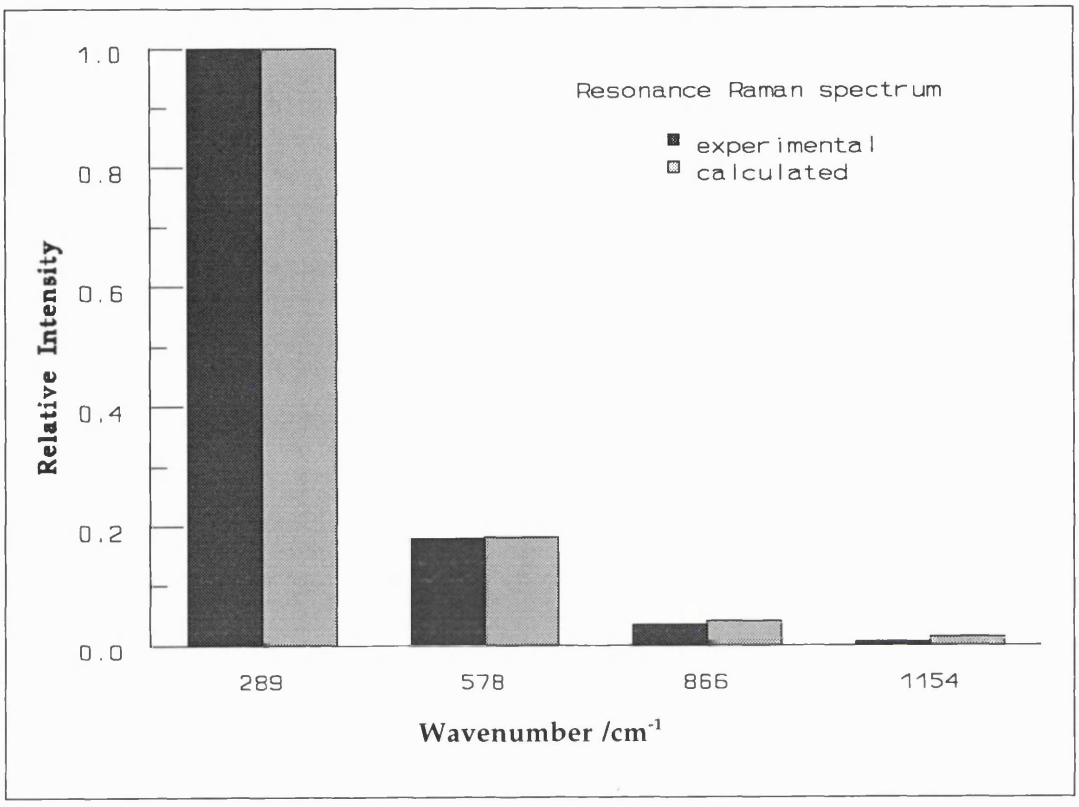

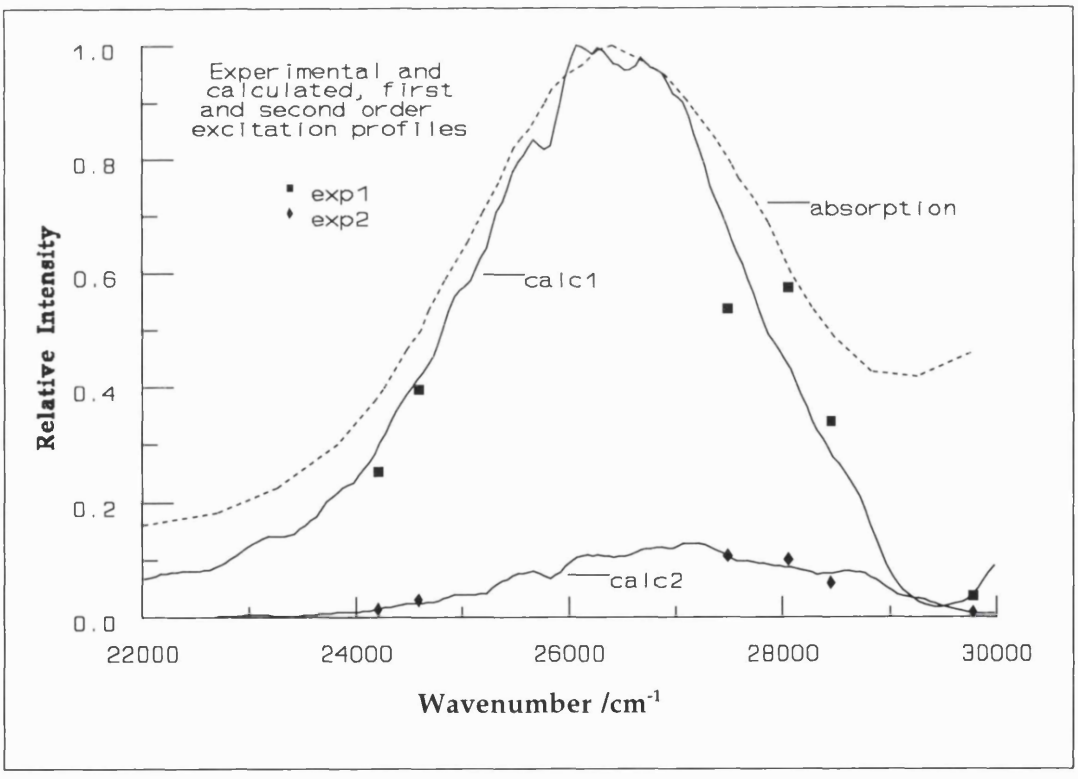

Figure 5.14a (top), 5.14b (bottom).

Halogen-Bridged, Mixed-Valence Linear Chain Systems

The systems tested consist of chains of Pt^{II}-Pt^{IV} dimers (Fig. 5.15a) which upon excitation become chains of --Pt^{III}-- monomers (Fig. 5.15b), a model proposed by Piepho, Krausz and Schatz [85] and further extended by Prassides and Schatz [86,87]. This model has been used successfully by Prassides and Schatz [87] to calculate the location of the intervalence band and the resonance secondary radiation (resonance Raman scattering and luminescence) spectrum for Wolffram's red salt, $[Pt(EtNH_2)_4][Pt(EtNH_2)_4Cl_2]Cl_4 \cdot 4H_2O$.

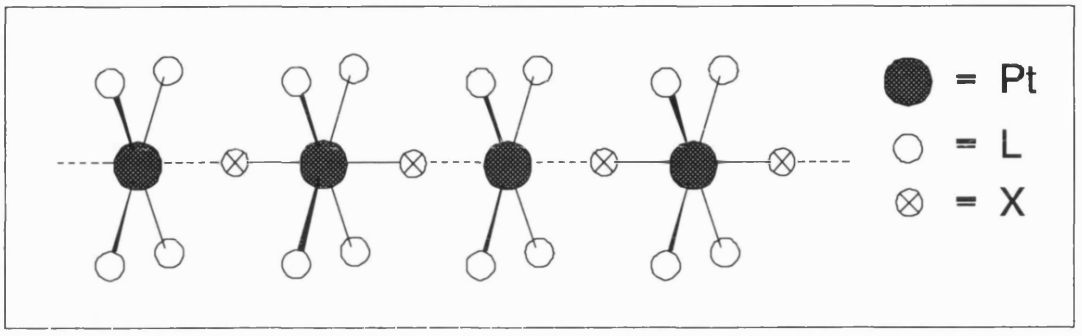

Figure 5.15a - Ground state geometry of linear chain systems [85,86].

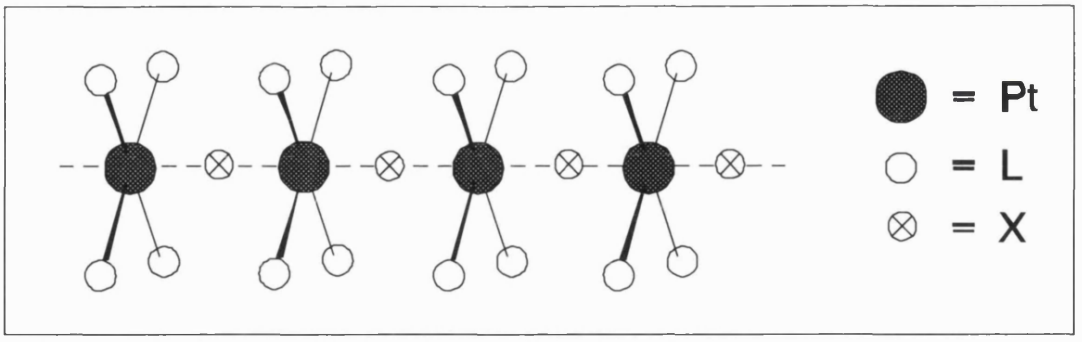

Figure 5.15b - Excited state geometry of linear chain systems [85,86].

The totally symmetric mode of interest of the systems studied here is the axial stretch X-Pt^{IV}-X; the polymeric structure of the molecular chain amplifies the vibration, leading to long progressions in $\tilde{\nu}_{sym}$(X-Pt^{IV}-X) which totally dominate the resonance Raman spectrum. Substitution of the equatorial amines by other amines [88] does not change the wavenumber of the mode of interest by more than a few cm^{-1}, so it can be assumed that that mode does not mix with others.

Table 5.7

Data employed in the calculations on mixed-valence linear chain systems

System	Absorption spectrum			RR spectrum			μ_r /amu
	Sample[1]	T /K	$\tilde{\nu}_{max}$ /cm^{-1}	Sample[2]	T /K	$\tilde{\nu}_{laser}$ /cm^{-1}	
$[Pt(pn)_2][Pt(pn)_2Cl_2](ClO_4)_4$ [88]	solid	293	25000	solid	80	21836	35.5
$\{[Pt(en)_2][Pt(en)_2Cl_2]\}_3 \cdot [CuCl_4]_4$ [88]	solid	293	19100	solid	80	17599	35.5
$\{[Pt(en)_2][Pt(en)_2Br_2]\}_3 \cdot [CuBr_4]_4$ [88]	solid	293	15870	solid	80	15453	79.9
$[Pt((-)\text{-dach})_2] \cdot [Pt((-)\text{-dach})_2Br_2]Br_4$ [88]	solid	293	15900	solid	80	13288	79.9
$[Pt((-)\text{-dacp})_2] \cdot [Pt((-)\text{-dacp})_2Br_2]Br_4$ [88]	solid	293	14300	solid	80	13288	79.9
$[Pt(pn)_2][Pt(pn)_2Br_2](ClO_4)_4$ (red) [88]	solid[3]	293	19600	solid	80	17599	79.9
$[Pt(pn)_2][Pt(pn)_2Br_2](ClO_4)_4$ (blue) [88]	solid[3]	293	16950	solid	80	17599	79.9
$[Pt(NH_3)_2(SCN)_2] \cdot [Pt(NH_3)_2(SCN)_2I_2]$ [88]	solid	293	18200	solid	80	17599	127
$[Pt(pn)_2][Pt(pn)_2I_2](ClO_4)_4$ [88]	solid	293	12800	solid	80	13288	127

[1] - mixture with alkali halides

[2] - mixture with alkali halides and an internal standard (K_2SO_4 or KNO_3)

[3] - suspension in chloroform

The absorption spectrum contains only the intervalence band in the visible region and there is also little evidence of Jahn-Teller distortion of the systems studied so resonance with a single excited electronic state can be assumed.

Table 5.8

Results for mixed-valence linear chain systems

System	$\tilde{\nu}_R \equiv \tilde{\nu}_g$ /cm^{-1}	$\tilde{\nu}_e$ /cm^{-1}	$\lvert\delta\tilde{\nu}\rvert/\tilde{\nu}_R$ %	r(Pt-X) /Å	Δ(Pt-X) /pm	Δr %	m
$[Pt(pn)_2][Pt(pn)_2Cl_2](ClO_4)_4$	313.2 ± 0.5	232.0 ± 5.0	25.8*	2.31	31.0 ± 1.0	13.4	0.00 ± 0.01
$\{[Pt(en)_2][Pt(en)_2Cl_2]\}_3 \cdot [CuCl_4]_4$	300.5 ± 0.5	230.0 ± 5.0	23.3*	2.33	25.2 ± 1.0	10.8	0.00 ± 0.01
$\{[Pt(en)_2][Pt(en)_2Br_2]\}_3 \cdot [CuBr_4]_4$	168.6 ± 0.5	133.0 ± 5.0	21.1*	2.54[1]	16.5 ± 1.0	6.5	0.00 ± 0.01
$[Pt((-)\text{-dach})_2] \cdot [Pt((-)\text{-dach})_2Br_2]Br_4$	161.4 ± 0.5	129.0 ± 5.0	20.0*	2.70[2]	21.6 ± 1.0	8.0	0.00 ± 0.01
$[Pt((-)\text{-dacp})_2] \cdot [Pt((-)\text{-dacp})_2Br_2]Br_4$	163.1 ± 0.5	124.0 ± 5.0	23.9*	2.70[2]	18.4 ± 1.0	6.8	0.00 ± 0.01
$[Pt(pn)_2][Pt(pn)_2Br_2](ClO_4)_4$ (red)	174.5 ± 0.5	154.0 ± 5.0	11.5	2.71[3]	15.4 ± 1.0	5.6	0.00 ± 0.01
$[Pt(pn)_2][Pt(pn)_2Br_2](ClO_4)_4$ (blue)	174.8 ± 0.5	147.6 ± 5.0	15.5	2.71[3]	17.9 ± 1.0	6.6	0.00 ± 0.01
$[Pt(NH_3)_2(SCN)_2] \cdot [Pt(NH_3)_2(SCN)_2I_2]$	120.4 ± 0.5	92.3 ± 5.0	23.3*	2.70[4]	25.7 ± 1.0	9.5	0.00 ± 0.01
$[Pt(pn)_2][Pt(pn)_2I_2](ClO_4)_4$	121.4 ± 0.5	109.0 ± 5.0	10.2	2.77	10.9 ± 1.0	3.9	0.00 ± 0.01

* - technically outside the limits of the model, 18.2 %; if the precision margin is taken into account, the result is within the limits.

[1] - estimated from r(Pt-Br) = 2.42 Å in $[Pt(etn)_4][Pt(etn)_4Br_2]Br_4 \cdot 4H_2O$ [89];

[2] - estimated from r(Pt-Br) = 2.67 Å in $[Pt(pn)_2][Pt(pn)_2Br_2]Br_4$ [90];

[3] - estimated from r(Pt-Br) = 2.42 Å in $[Pt(en)_2][Pt(en)_2Br_2](ClO_4)_4$ [91] and

[4] - estimated from r(Pt-I) = 2.69 Å in $[Pt(NH_3)_4][Pt(NH_3)_4I_2][HSO_4]_3[OH] \cdot H_2O$ [88]

Notes to symbols:

$\tilde{\nu}_R$, $\tilde{\nu}_e$, $\delta\tilde{\nu}$, *m* - same as the symbols in Table 5.2

r(Pt-X) = platinum-halogen bond length (X = Cl,Br,I)

Δ(Pt-X) = platinum-halogen bond length change upon excitation

The values obtained for the vibrational wavenumber of the totally symmetric mode in the excited electronic state are large, some of them falling just outside the limits of the model, but consistent with large bond length changes. These large changes are in broad agreement with a bond length change of 22 pm for $r(Pt^{IV}\text{-X})$ obtained by Prassides and Schatz [87] for Wolffram's red salt. The good agreement between the results of the two methods should consolidate the acceptance of a large change in the Pt^{IV}-X bond length in linear-chain compounds and, by implication, in other systems.

The simulations based on the transform method fit well the experimental data, with the exception of $[Pt(NH_3)_2(SCN)_2][Pt(NH_3)_2(SCN)_2I_2]$; the graphs are given at the end of this section (Figs. 5.16-5.24(a,b)). In that case the experimental excitation profile appears as if resonance takes place also with a second, 'dark' electronic state and the values obtained for the (assumed single) excited electronic state are not consistent with the rest of the results.

The good agreement between the results of Prassides and Schatz [87] and the experimental data, and the very different nature of their model calculations provides a good check for the present work. The advantage of the transform method is that it requires much less computational power than the dynamic

solution of the vibronic Schrödinger equation and it yields not only the bond length change, but also the vibrational wavenumber of the mode of interest in the excited electronic state and the linear non-Condon correction parameter.

$[Pt(pn)_2][Pt(pn)_2Cl_2](ClO_4)_4$

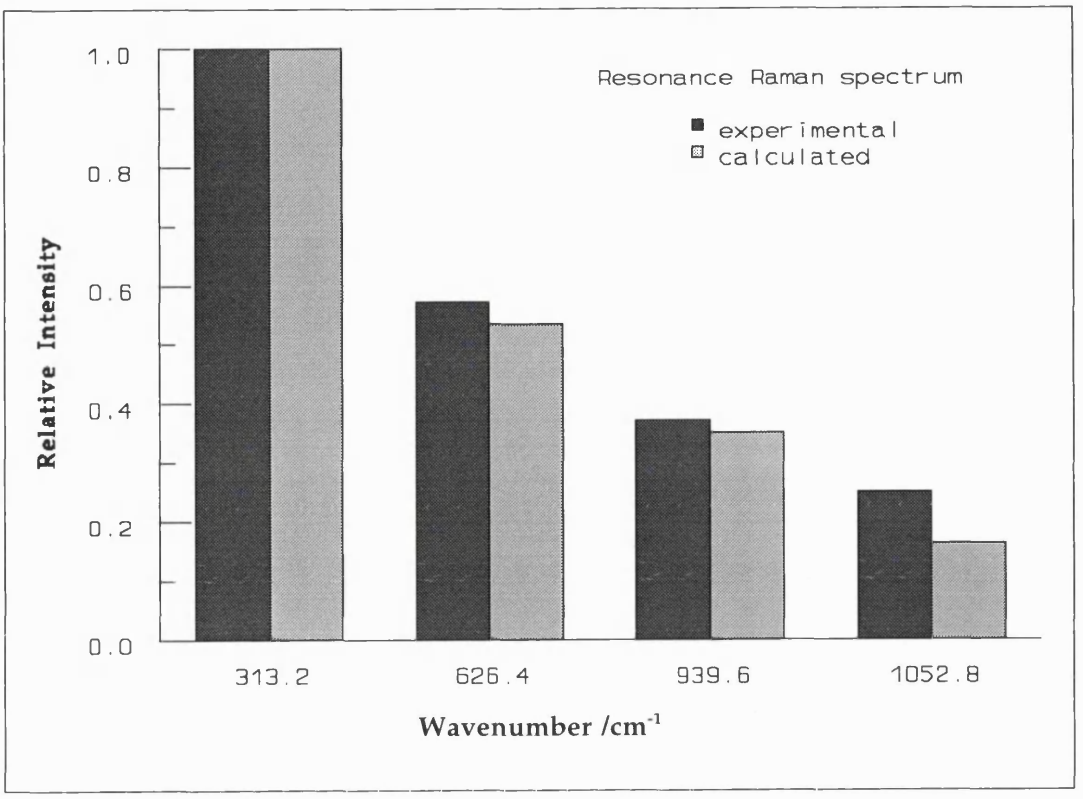

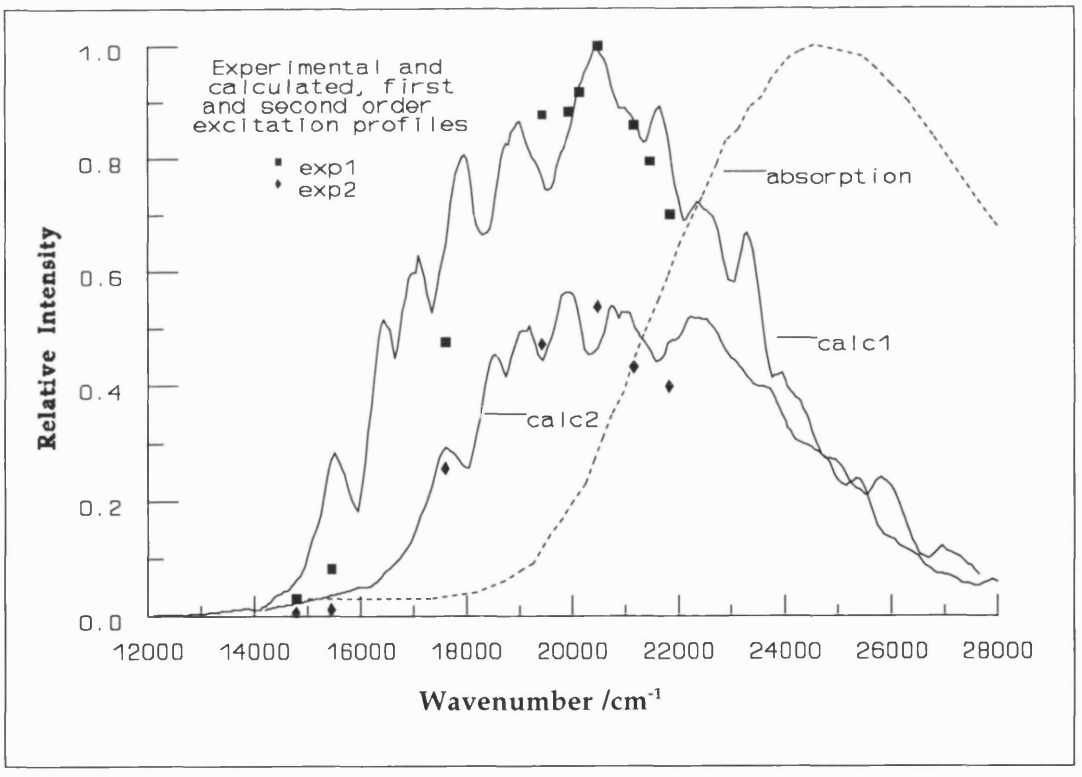

Figures 5.16a (top), 5.16b (bottom).

$\{[Pt(en)_2][Pt(en)_2Cl_2]\}_3(CuCl_4)_4$

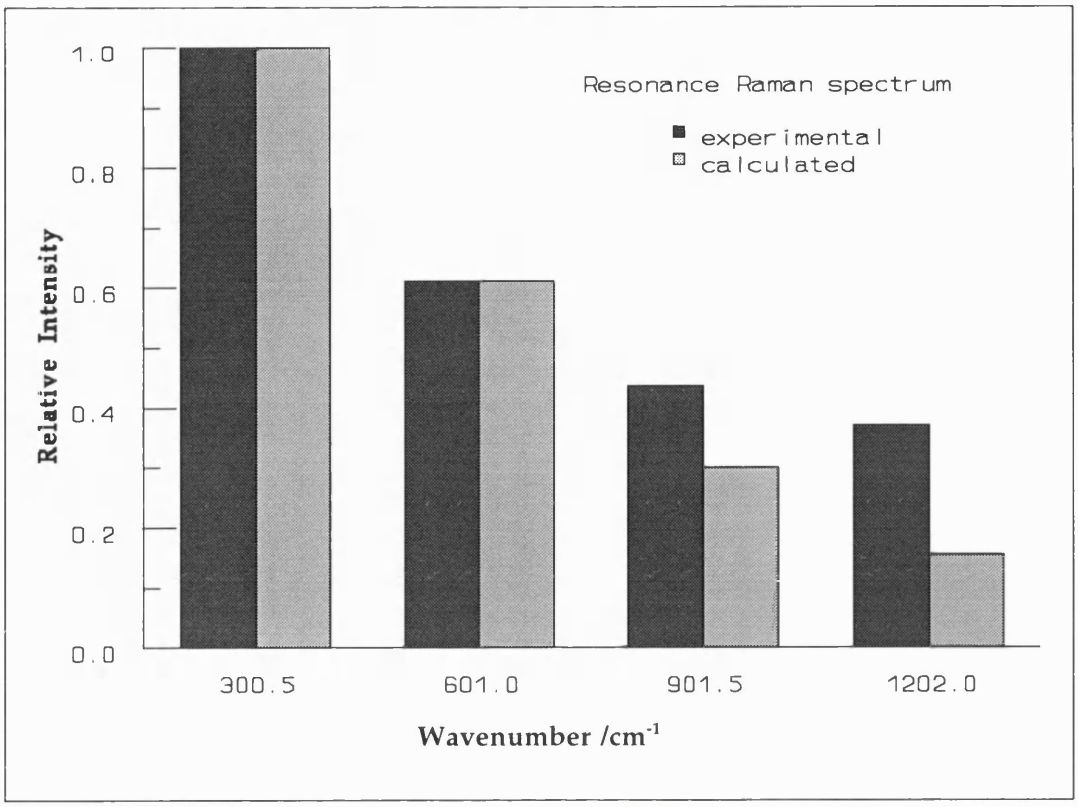

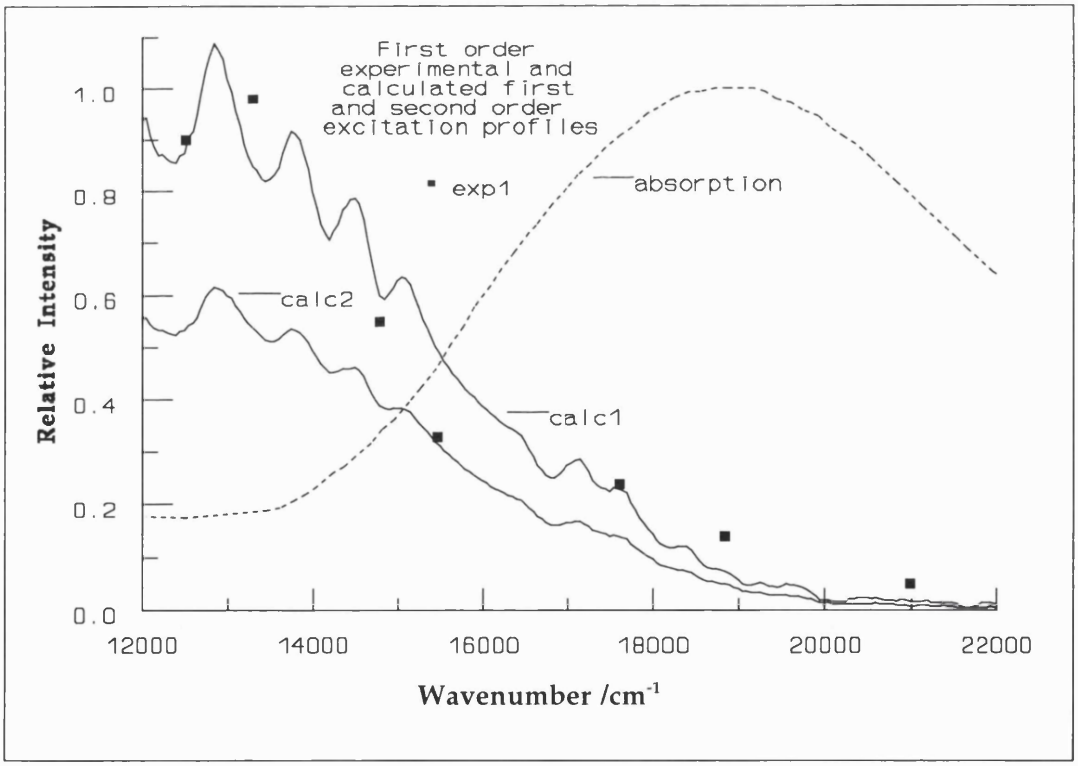

Figures 5.17a (top), 5.17b (bottom).

$\{[Pt(en)_2][Pt(en)_2Br_2]\}_3(CuBr_4)_4$

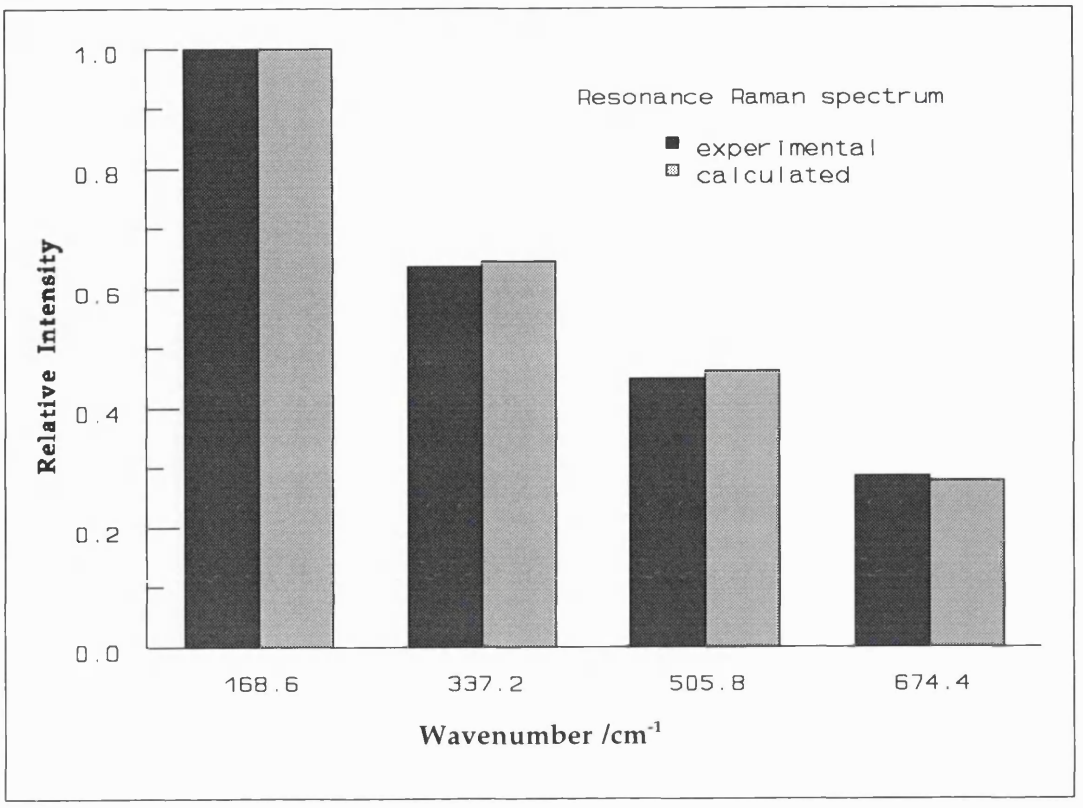

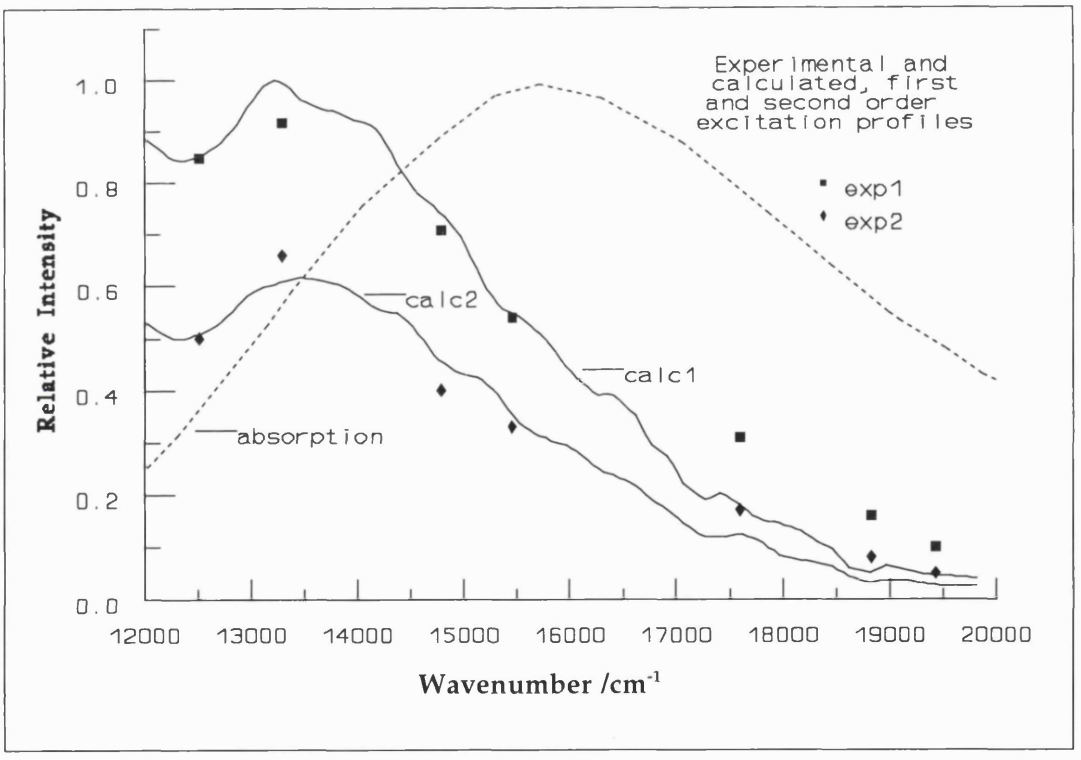

Figures 5.18a (top), 5.18b (bottom).

$[Pt((-)\text{-dach})_2][Pt((-)\text{-dach})_2Br_2]Br_4$

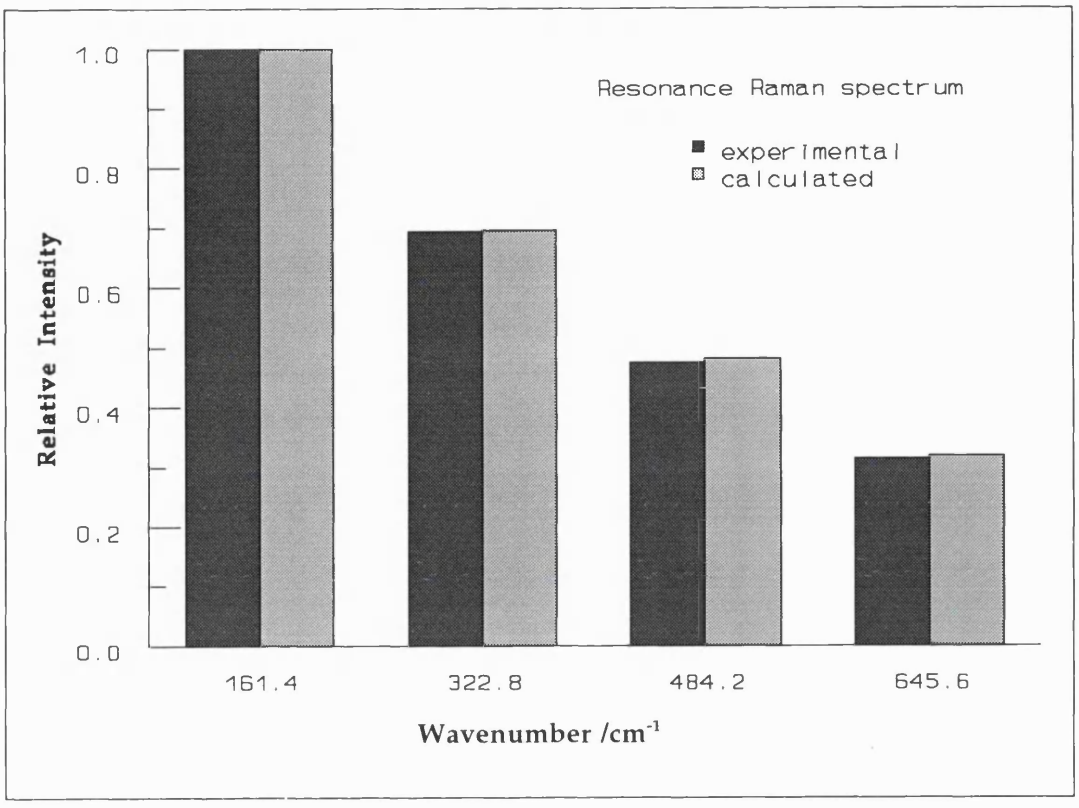

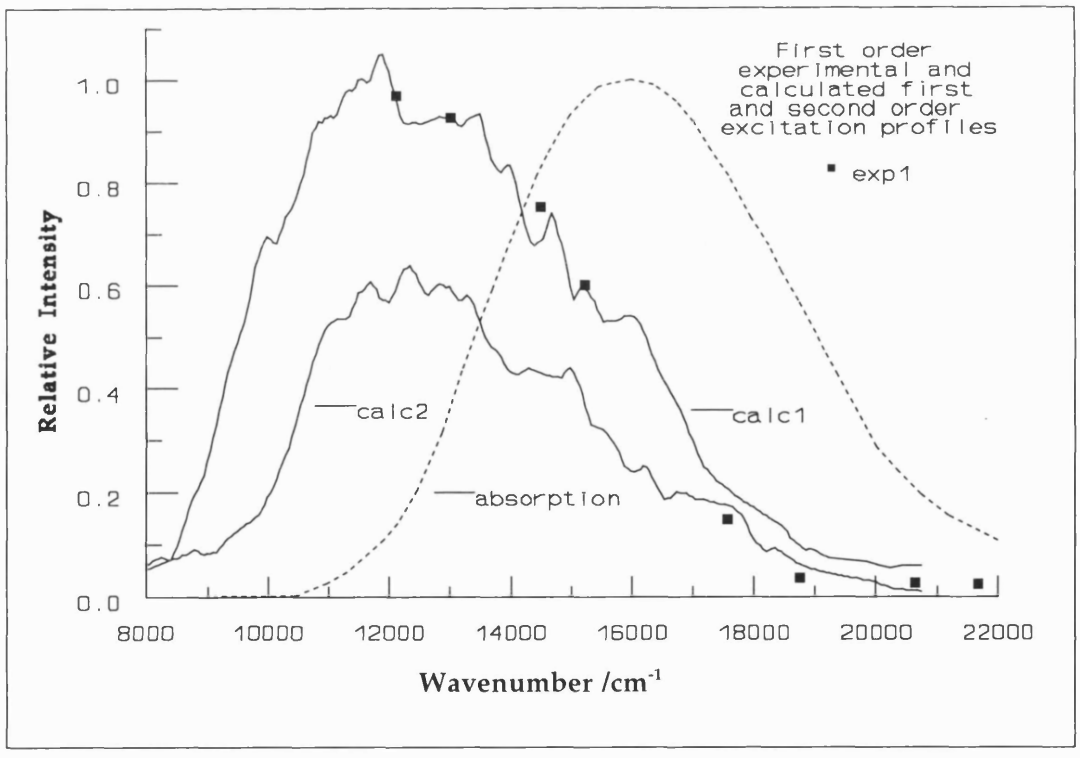

Figures 5.19a (top), 5.19b (bottom).

$[Pt((-)\text{-}dacp)_2][Pt((-)\text{-}dacp)_2Br_2]Br_4$

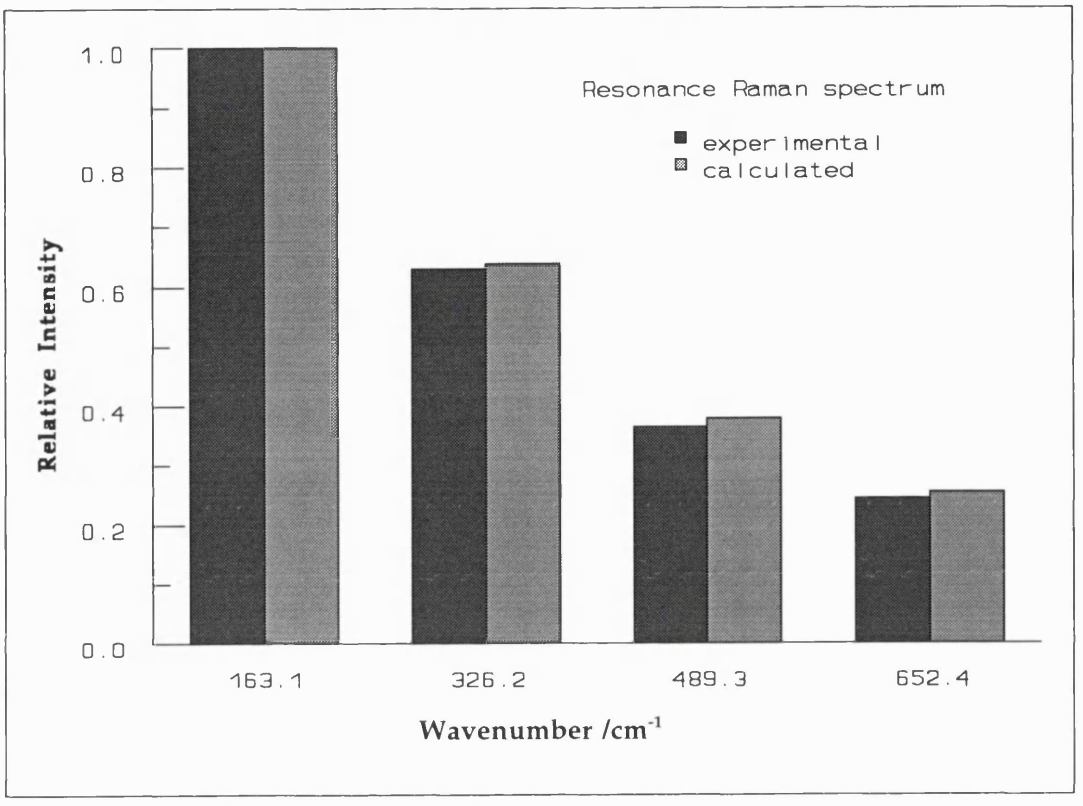

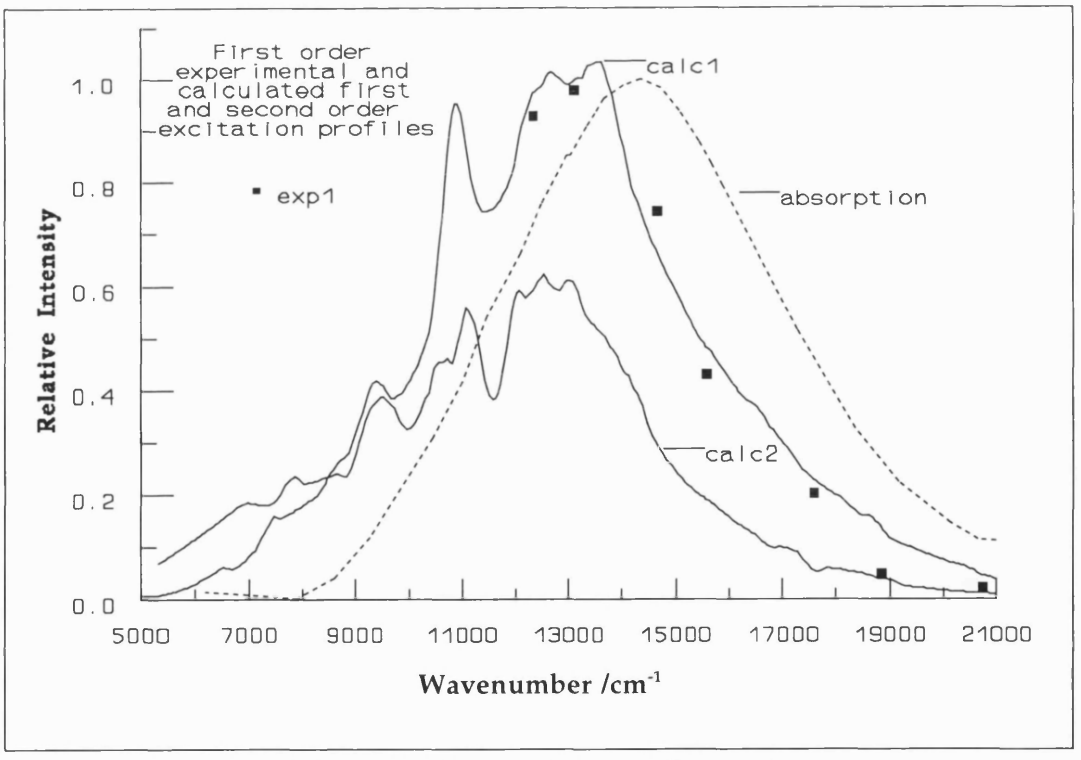

Figures 5.20a (top), 5.20b (bottom).

$[Pt(pn)_2][Pt(pn)_2Br_2](ClO_4)_4$ (red)

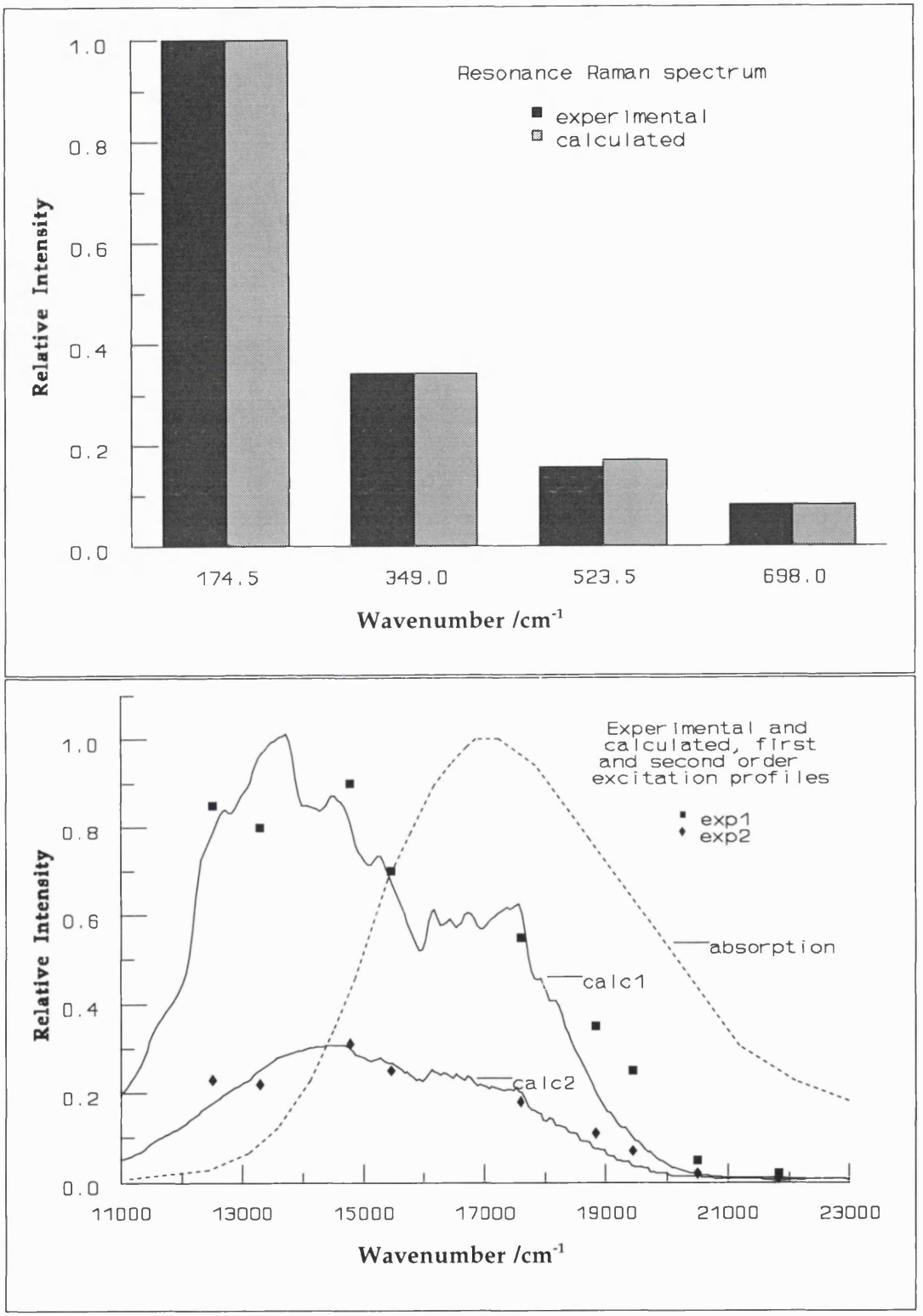

Figures 5.21a (top), 5.21b (bottom).

$[Pt(pn)_2][Pt(pn)_2Br_2](ClO_4)_4$ (blue)

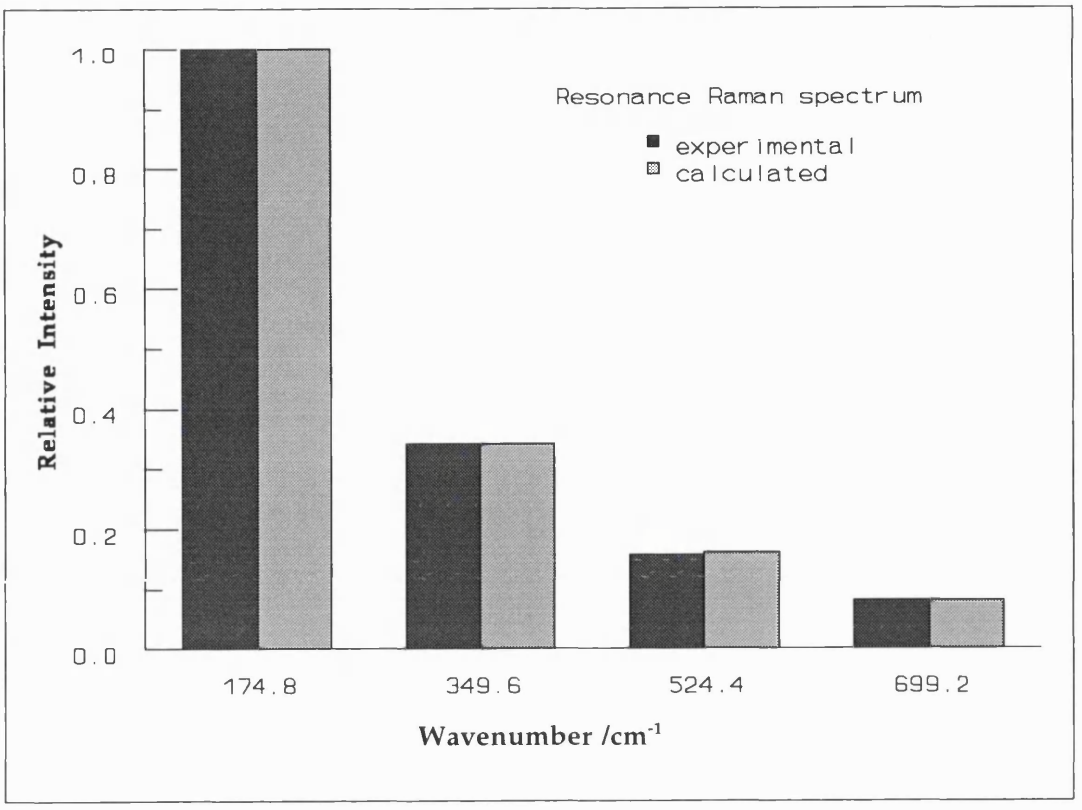

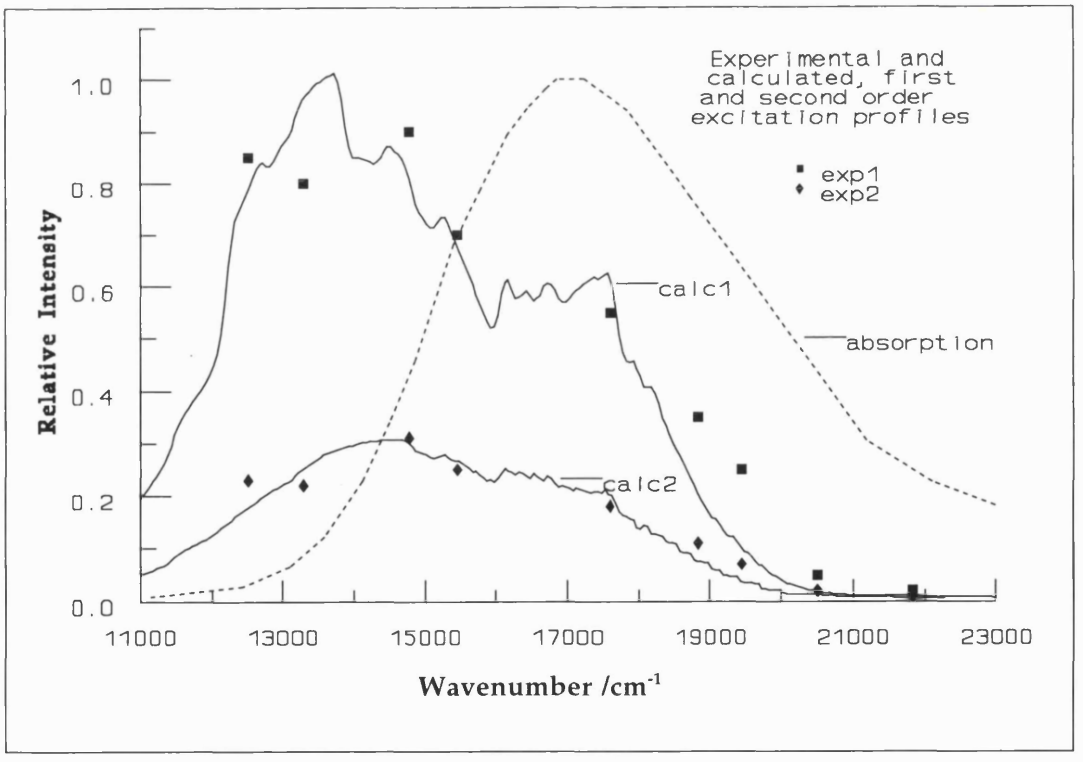

Figures 5.22a (top), 5.22b (bottom).

$[Pt(NH_3)_2(SCN)_2][Pt(NH_3)_2(SCN)_2I_2]$

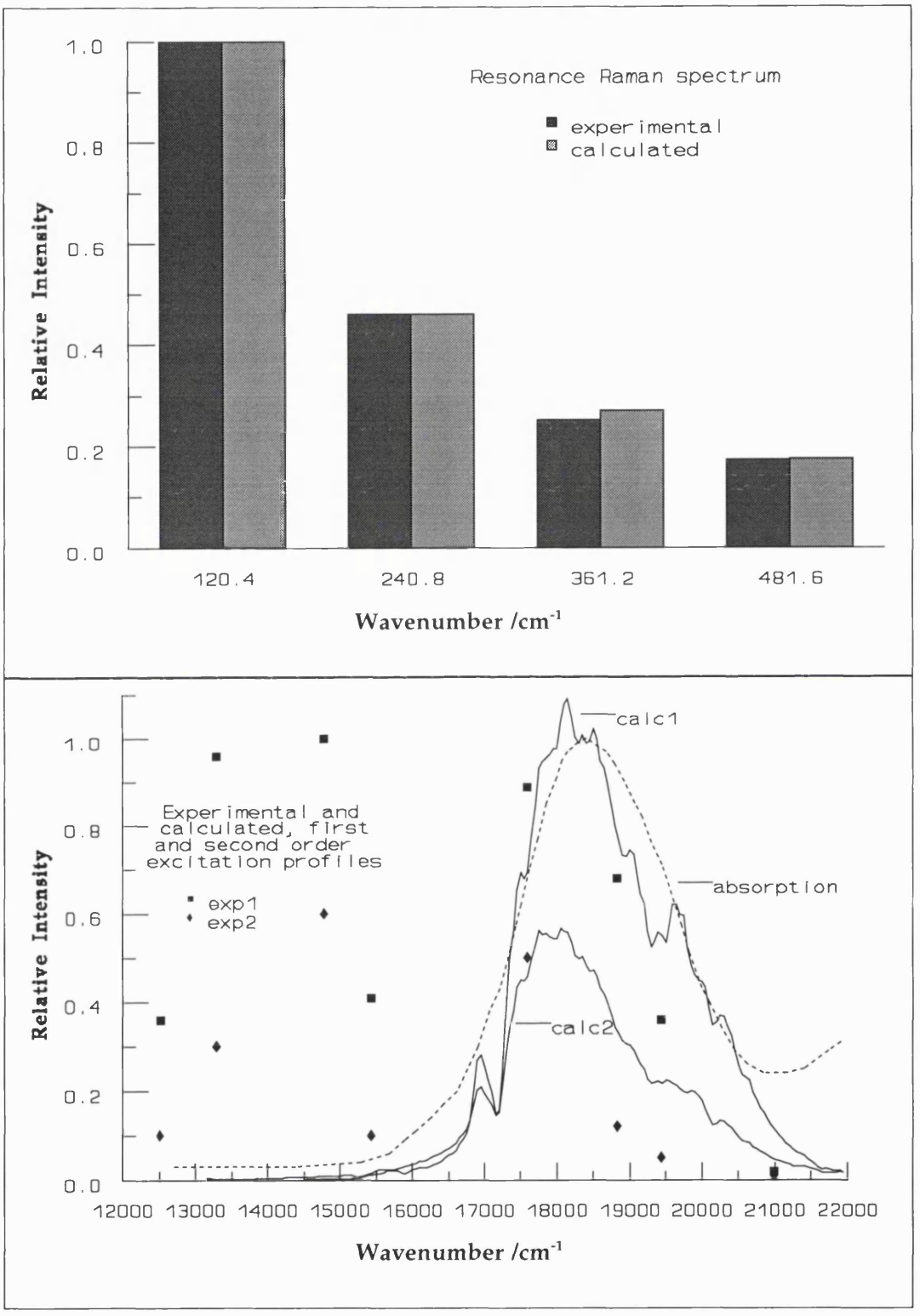

Figures 5.23a (top), 5.23b (bottom).

$[Pt(pn)_2][Pt(pn)_2I_2](ClO_4)_4$

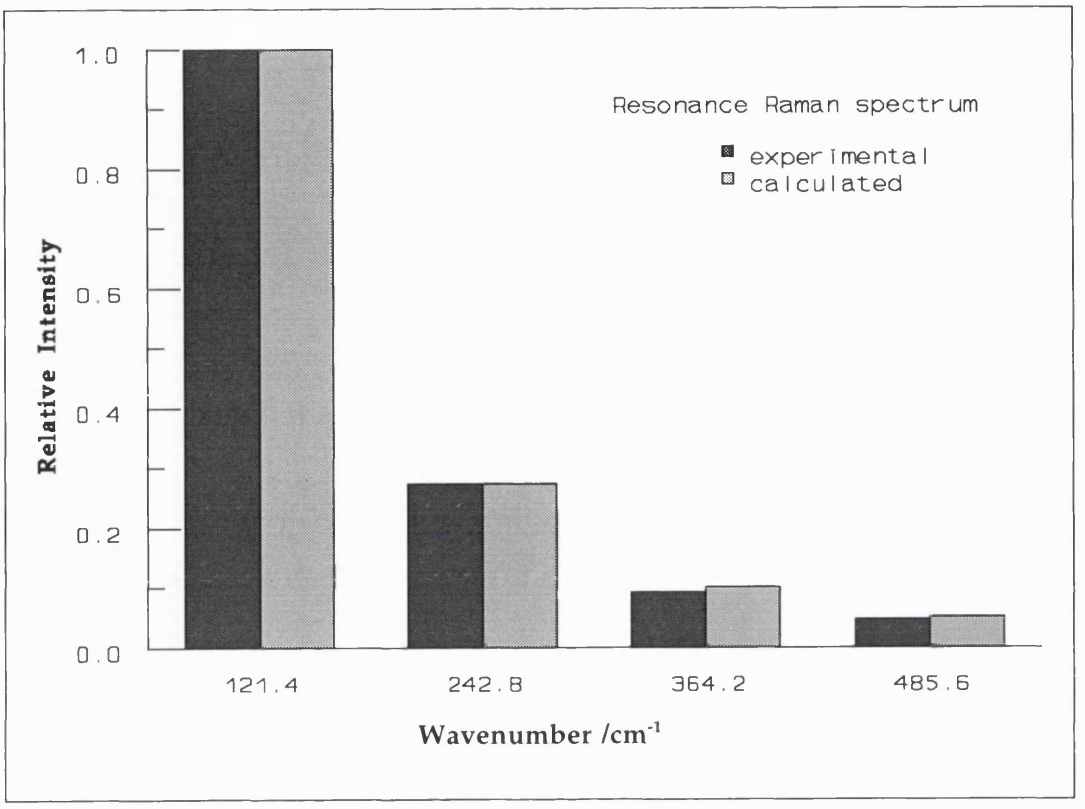

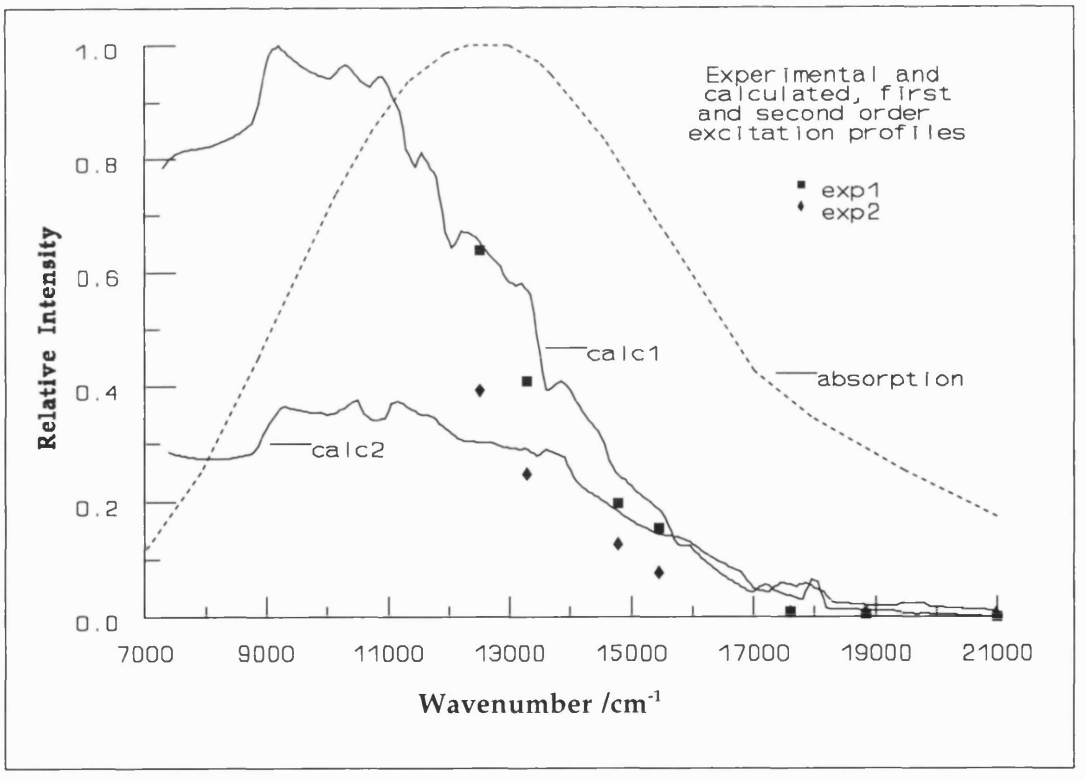

Figures 5.24a (top), 5.24b (bottom).

Conclusions

The present work proposes a new method of obtaining molecular structural, vibrational and vibronic data by linking the resonance Raman excitation profile to the electronic absorption spectrum of the molecule. The mathematical formalism is based on the density matrix of the molecule-radiation interaction and on the Kramers-Kronig transform between the real and imaginary parts of the electronic polarizability.

The foundations of the work are laid in Chapter 1 and Appendix 1, describing the experimental technique, and Chapter 2, which describes the theoretical model employed and its interpretation in terms of Raman and fluorescence radiation. Although original data presented in Appendix 2 shows the importance of resonance fluorescence, only the resonance Raman aspect of secondary radiation is pursued in this thesis.

The original work begins in Chapter 3, relating resonance Raman data to the absorption spectrum through a set of equations depending on microscopic parameters, describing the molecular structure, and macroscopic quantities to be measured experimentally. Chapter 4 proposes a new mathematical method for solving the equation set, and Chapter 5 presents the results of applying the new method to chemical systems belonging to three different geometries.

The transform method proposed here (and introduced in [60]) is the first to provide three vibronic parameters for fitting Raman excitation profiles of any order, or the relative intensities of fundamental and overtone scattering excited at any one wavelength. The potential energy curve displacement parameter Δ, the wavenumber of the Raman mode in the upper potential energy curve $\tilde{\nu}_2$, and the dependence of the transition moment on nuclear coordinate(s) – the non-Condon term (parameter m) – have all been used by others [40-52, 54, 55, 57, 58] in more limited ways. The expressions offered here lead to values for

all three vibronic parameters simultaneously, for scattering of any order.

The formalism also separates the Raman sub-space from the non-Raman space, thereby including temperature dependence and energy-dependent damping in the non-Raman space. The Raman space is treated as one-dimensional in the coordinate of the Raman mode, thus excluding Duschinsky rotation, and thermal excitation of the Raman mode is neglected; this enhances the efficiency of the method, but also creates its most significant limitation. The approximations appear to be realistic for many systems where there is only a single totally symmetric fundamental and for which the vibrational energy considerably exceeds $k_B T$.

The present work represents the first systematic attempt to establish the transform method, within its limitations, as a tool for investigating the geometry and vibrational and vibronic properties of the excited electronic states. A substantial body of experience needs to be accumulated before the method will be fully accepted as a complement to other structural methods used in physical chemistry.

Appendix 1 - Chromatic aberration and Resonance Raman Spectroscopy[4]

It has been noticed in our laboratory that the SPEX R6 instrument does not remain focused throughout a very wide spectral range, suggesting that the collection lens exhibits pronounced chromatic aberration. Tests assessing the chromaticity of this instrument have been conducted on a sample of ethanol, chosen for its wide wavenumber spread between the Raman bands - more than 2000 cm^{-1}; the spectra are shown in Fig. A1.1.

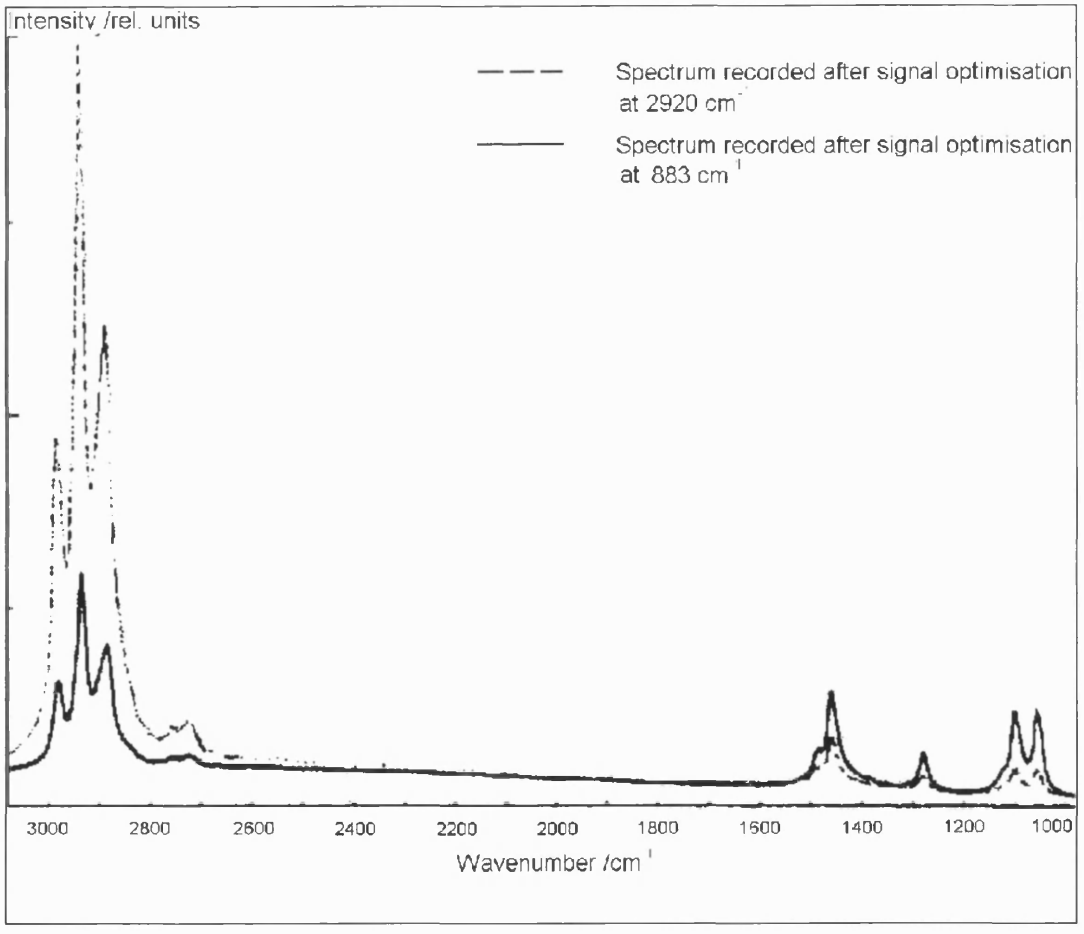

Figure A1.1 - The effect of chromatic aberration on Raman band intensities.

[4] - from a report on the errors introduced in the collected spectra by the chromatic aberration of the collection lens of the Raman spectrometer.

The test procedure is simple, reproducible and unambiguous: the spectrum is recorded first after the signal has been maximised with the monochromator selecting one of the bands, and then after moving the monochromator at the second band and maximising the signal solely by refocusing the collection lens.

If the intensity of the signal remains constant while the lens is refocused, the lens is achromatic and the system is correctly focused for both wavelengths. If refocusing the lens increases the intensity of the signal, the lens is chromatic and the ratio R between the two signal intensities, before and after refocusing, is a measure of the deviation from a truly achromatic behaviour; this ratio is 1.0 for an achromat, and can only be lower than 1.0 for a chromatic lens. The results are summarised in Table A1.1.

Table A1.1

Signal intensity loss due to chromatic aberration.

Spectrometer	Wavelength /nm	R measured after the system is initially focused on the band at:	
		883 cm^{-1}	2930 cm^{-1}
SPEX 1401	406.7	1.000	0.917
	530.2	0.884	0.840
	568.2	0.900	0.793
	647.1	0.826	0.588
SPEX R6	501.7	0.236	0.250
	363.8	0.160	0.158

The results obtained for the SPEX 1401 instrument have been included because its construction is very similar to the SPEX R6, but uses a commercial camera lens (Zeiss Planar T f/1.2 - 50 mm) for light collection; the results show

that such a lens exhibits a small chromatic aberration in the blue and green regions, increasing moderately towards the red region of the visible spectrum, as specified by the manufacturer.

The custom-built collection lens employed on the R6 system exhibits a very large chromatic aberration; as an example of its effects on resonance Raman spectroscopy, the $KMnO_4$ spectrum excited by irradiation with 514.5 nm light loses more than 80% of the intensity of its second overtone, while the intensity of the third overtone becomes too low to be measured. However, the published data [8-10,71-76], as used in Chapter 5, has been recorded in our laboratory with the SPEX 1401 instrument, which does not suffer from pronounced chromatic aberration.

The first possibility for correcting the chromatic aberration of a light collection system is to use a telescope-type objective, built with mirrors, instead of lenses. The main problem with this solution is that these objectives have a short operating distance - typically up to 24 mm - while the current generation of cryostats place the scattering point of the sample at more than 35 mm away from the window through which the Raman scattered light is collected (Fig. 1.3). Thus, telescope-type objectives are ruled out for work involving cryostats and, as low temperature is an important way of improving the signal-to-noise of Raman and resonance Raman spectra, this solution is not suitable to this laboratory at the present time.

A second possible solution to the chromatic aberration exhibited by the collection lens of the SPEX R6 instrument would be to replace its custom-built lens with a commercial camera lens[5] with a 360-900 nm spectral transmittance curve (Fig. 1.4), bringing the model R6 in line with the model 1401 instrument. Optical theory can be used to calculate the extent of the chromatic aberration

[5] - Information obtained from the research departments of Carl Zeiss, Nikon, Canon, Asahi Pentax and Minolta.

and to write a computer program that would permit a more rigorous correction than that achieved solely through the manufacturing process of camera lenses. This correction, used in conjunction with the corrections for the instrumental spectral response (see the dedicated section in Chapter 1) and ν^4 (Eqn 1.8), would result in the experimental precision required by the transform method.

The two main disadvantages of replacing the custom-made lens with a commercially available camera lens would be a frequency-independent decrease in throughput, by 25-30% for a f/1.2 lens as compared with the f/0.95 custom-made lens, and the reduced transmittance in ultraviolet of the commercial lenses, with around 20% at 360 nm (Fig. 1.4). The reduced transmittance in the ultraviolet region would be partly compensated by the ν^4 factor (Eqn 1.8) and increased quantum efficiency of the photomultiplier tube.

To summarise, the chromatic aberration has been proved to introduce significant errors in the measurement of band intensity in Raman spectra, affecting the ability of the transform method to deliver results to its full capabilities. The implementation of the transform method in calculations of excited electronic state parameters requires that the experimental procedure of obtaining resonance Raman spectra should be thoroughly understood, along with all the possible mechanisms for error and ways for their control. As facts presented here suggest, the only realistic solution to chromatic aberration in our experiments is to minimise it by employing commercial camera lenses for collecting Raman scattered light; software can be employed then to correct data even further.

Appendix 2 - Spectroscopy of matrix-trapped molecular species[6]

Introduction

The aim of this study is to establish the structure of the S_4 isomers and to provide reliable Raman and fluorescence 'fingerprints' of all sulphur species produced in an argon discharge and isolated in an argon matrix.

Sulphur vapour has been passed with excess of argon through a microwave discharge and the resulting mixture deposited on a copper plate at a temperature of 14 K. This doped matrix has been irradiated with 40 mW of laser power at several wavelengths and the scattered light analysed with a DILOR XY multichannel spectrometer. Raman and fluorescence spectra of the matrix have been recorded and assignment of some of the bands to S_n and S_n^- species present in the matrix has been carried out. The increased intensity of fluorescence in the spectral region of an absorption system believed to be due to S_4 [92,93], with a maximum at around 530 nm, has been attributed to resonance fluorescence of the same system.

Small sulphur elemental and heteroatomic molecules

The idea of studying small sulphur elemental molecules occurred during preparations for the study of S_mE_n (m,n=2,3,4), where E=O,N,F,Cl, etc. These binary species are interesting for their possible involvement in the combustion of sulphur-containing fossil fuels in an atmosphere of N_2+O_2+small amounts of halogen derivatives like chloro-fluoro-carbons (CFCs). These combustion processes can produce many reactive, short-lived species as intermediates and it has been assumed that similarly rich mixtures can be obtained by passing N_2+S_n or O_2+S_n (1>n>9) in excess of argon through a microwave discharge.

[6] - from a report on experimental work, preliminary to the present thesis.

The resulting mixtures will contain measurable amounts of elemental sulphur species, observable along the binary combinations in any spectroscopic investigation; hence the investigation of the mixtures containing binary species requires investigating the small S,O,N elemental molecules.

Gas-phase investigations using Raman spectroscopy [92,93] found all species of S_n (1>n>9) in open-chain and/or ring configuration; not all Raman bands have been unambiguously assigned, while the Raman and resonance Raman study of the colour centres in ultramarines [94,95] have identified vibrations corresponding to the S_2^-, S_3^- and S_4. Raman studies conducted on the products of a discharged SO_2 stream deposited as a matrix at 80 K [96,97] have assigned the bands at 442 and 218 cm^{-1} to S_8, while 3 strong bands at 585, 601 and 688 cm^{-1} have been assumed to belong to smaller sulphur species. These assignments have been confirmed by infrared spectroscopic studies carried out in the gas phase and in a variety of matrices [98].

The accepted knowledge about the small sulphur clusters is that fundamental Raman vibrations for the rings are to be expected below 500 cm^{-1}, for the anions below 600 cm^{-1}, and for the open chains above 600 cm^{-1}. There is little information about the fluorescence of sulphur molecules; Lenain et al. [92] have observed a feature at 559 cm^{-1} from the 514.5 nm excitation line in the Raman spectrum of overheated sulphur vapour, and assigned it to the resonance fluorescence of S_2.

It is known [99,100] that there are broad electronic absorption bands at 410+15 nm for S_3 and at 520+15 nm for one of the S_4 isotopes. While S_3 is widely believed to be a bent molecule with C_{2v} symmetry, calculations suggest [101,102] that several isomers of S_4 have similar energies; the most stable is thought to be a $^1D_{2h}$ rectangle-shaped ring close to a $(S_2)_2$ structure, while a C_{2h} open chain lies 0.4 eV higher in energy. The same calculations found that all triplet states of S_4 lie well above the $^1D_{2h}$ ground state.

The matrix-isolation technique

The preparation of a matrix requires a high vacuum enclosure containing the substrate - a cold plate maintained at the temperature required by the gas employed to become a solid. A source of gas mixture sends a stream of molecules through the microwave discharge in an Evenson-Broida cavity and the resulting mixture is deposited onto the cold plate. Figures A2.1a,b describe the experimental setup in the two stages of the experiment, the preparation of the sample and the spectroscopic analysis of the resulting matrix.

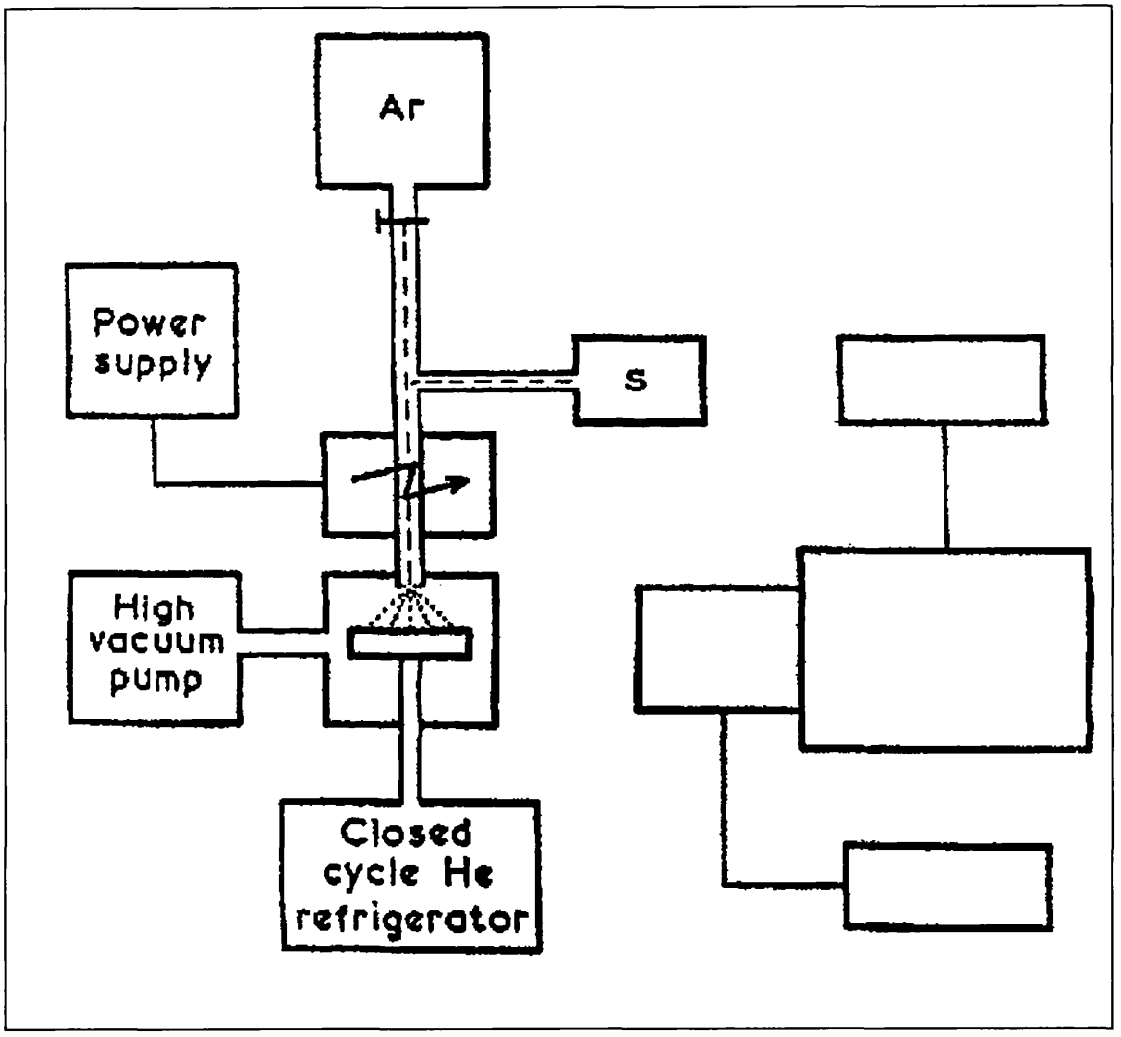

Figure A2.1a - Preparation of solid argon matrices.

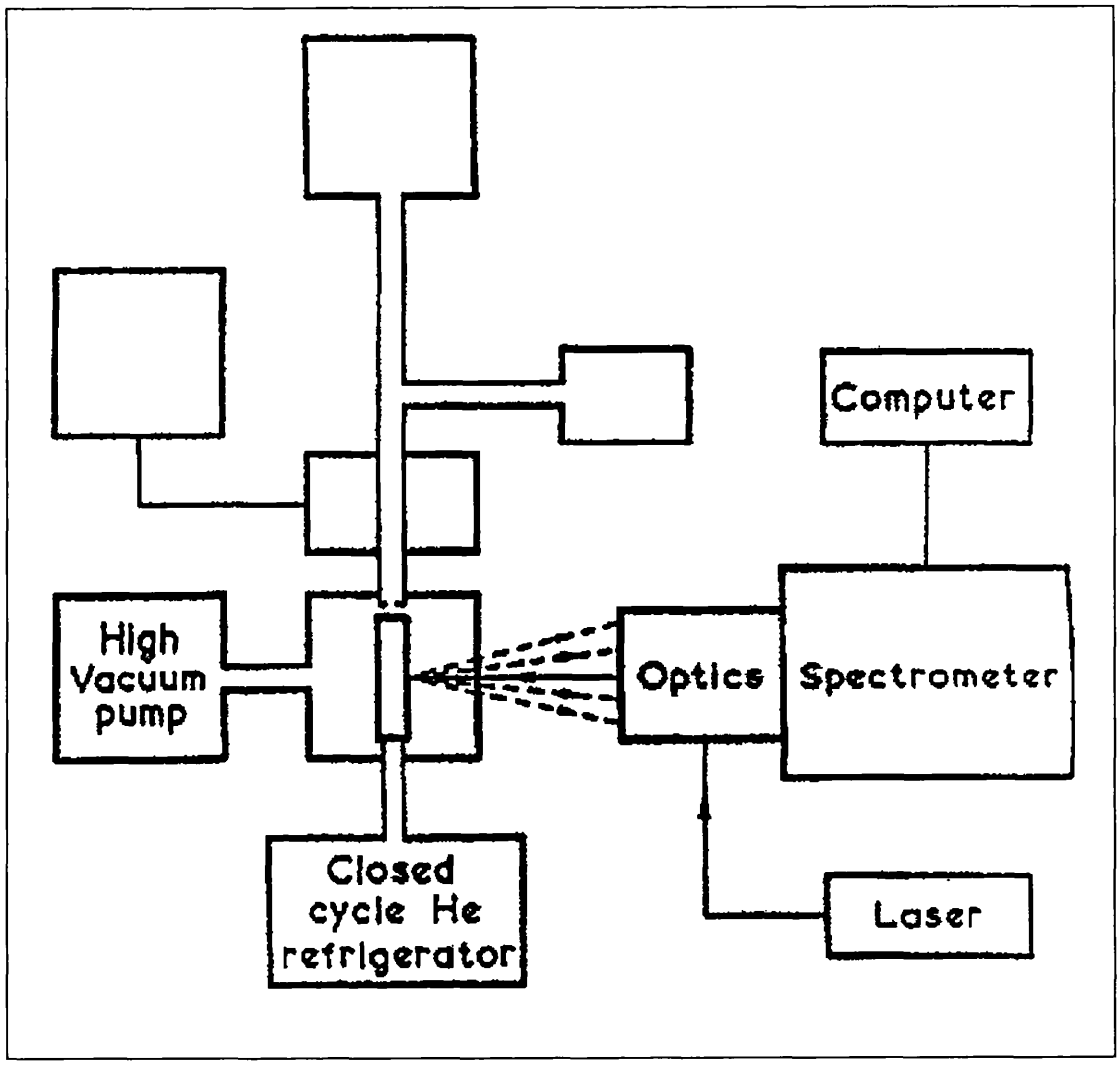

Figure A2.1b - Spectroscopic analysis of a solid argon matrix.

This study has employed a specially shaped quartz tube (Fig. A2.2) to evaporate the sulphur in a flow of argon, the flow of sulphur vapour being controlled through controlling the temperature of the reservoir. The resulting ($Ar + S_n$) mixture is passed through the microwave discharge and the products are deposited as an argon matrix doped with various sulphur clusters. At the end of the deposition process the flow of gas is turned off and the cold plate is turned towards a window of the high-vacuum enclosure for the spectroscopy of the matrix, conducted in a 180° geometry.

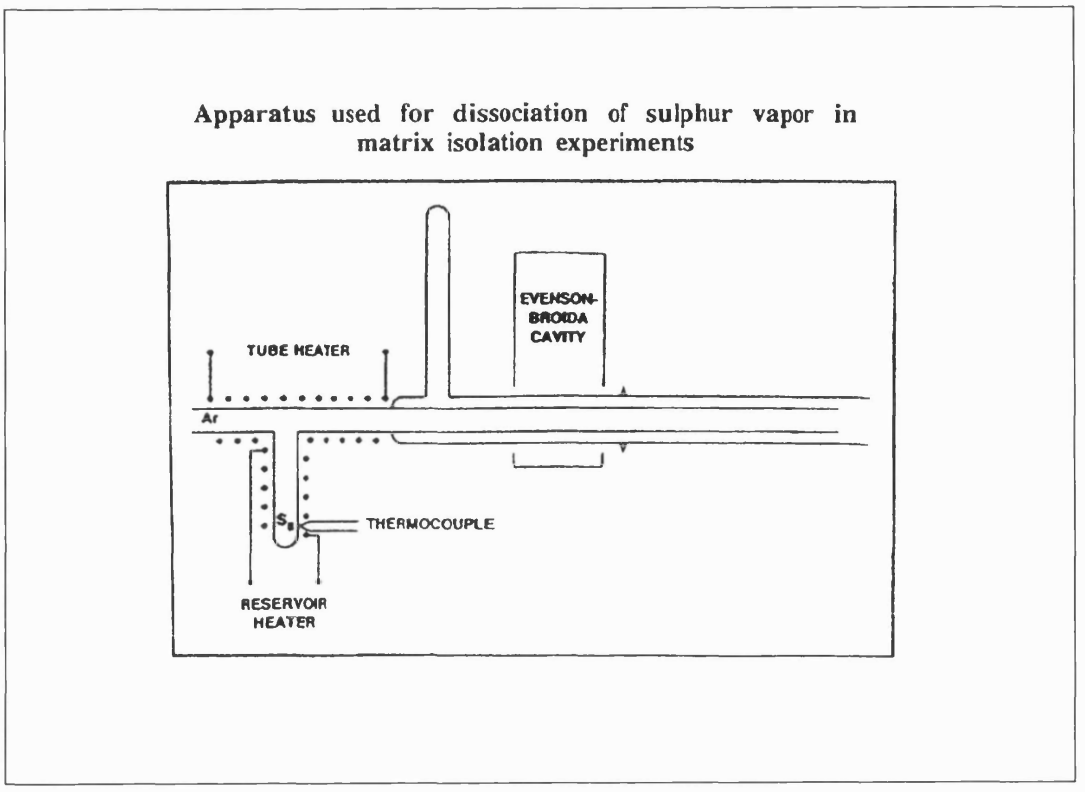

Figure A2.2 - Sulphur vapour generator.

Experimental

The matrices have been deposited on a copper plate in the cold enclosure of an Air Products Displex closed-cycle He refrigerator; the vacuum was better than $3x10^{-5}$ torr at room temperature and better than $6x10^{-6}$ torr at 14 K. Sulphur (flowers) has been heated in the quartz tube (Fig. A2.2) using cascaded variacs plugged directly into the mains. The temperature of the micro-oven has been increased by approximately 1.5 °C min^{-1} from 80 °C up to about 125 °C where it remained stable within 5 °C. The flow of argon was maintained continuously, at a rate of 2 - 4 mmol h^{-1}, and the microwave discharge was also maintained, at about 40 W power and optimal tuning.

Up to 115 °C the discharge looked pink, as a discharge in pure argon; above 115 °C the colour turned progressively to sky-blue, because of S_2 emission.

Matrix deposition lasted for about 3 hours; the estimated Ar:S ratio was between 50:1 and 100:1 and the resulting matrix was coloured light blue.

After the deposition the cold plate carrying the matrix was turned facing the spectrometer and irradiated with laser light, always 40 mW of power measured before the focusing and collection lens, and using no interference filter with any of the laser lines employed. Spectra have been recorded with a DILOR XY triple monochromator fitted with a multichannel diode-array detector.

The first experiment tested for Raman signal between 266 and 800 cm^{-1}, using a 676.4 nm excitation line. With no microwave discharge, all sulphur desublimated on the walls of the tube before reaching the matrix and no signal was seen. By turning the discharge on, all the sulphur from the quartz tube was removed in about 5-10 mins and deposited onto the matrix and onto the walls of the vacuum enclosure. The matrix was then excited with 676.4, 647.1, 568.2 and 530.8 nm and the best spectrum, obtained at 568.2 nm, is shown in Fig. A2.3.

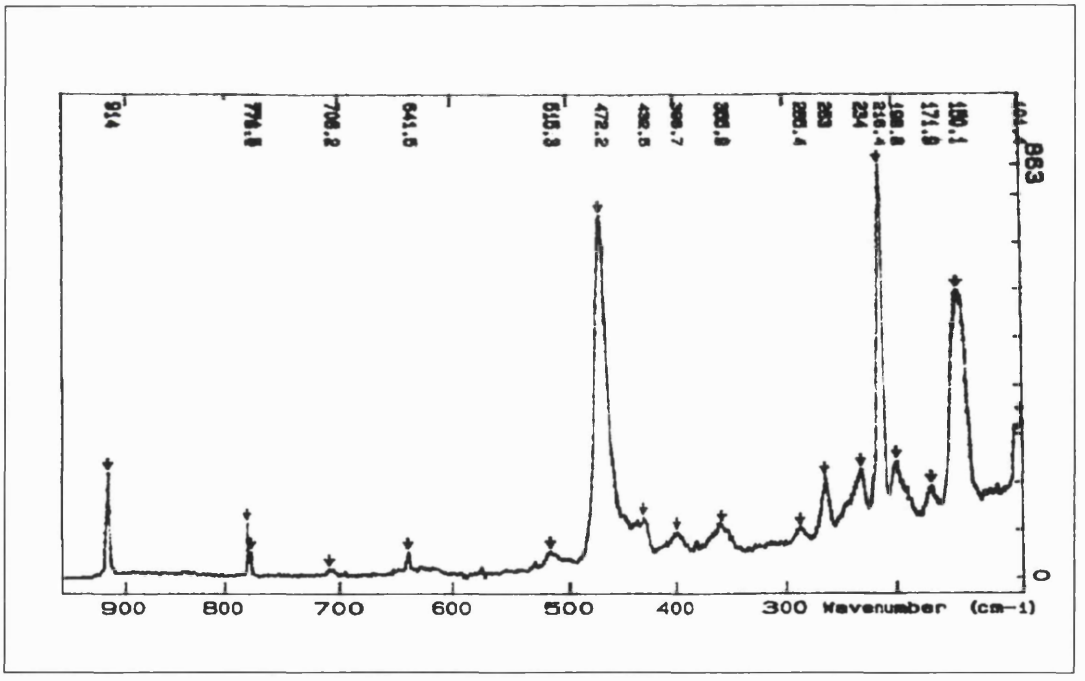

Figure A2.3 - Raman spectrum of a mixture of S_n clusters embedded in a solid argon matrix, excited by the 568.2 nm line of a Kr^+ laser.

The next experiment suffered from initial temperature overshooting up to about 135 - 140 °C for about one minute and some sulphur has been deposited into the matrix as in the first experiment. The following series of experiments was carried out according to the procedure outlined earlier, the resulting matrices being irradiated with 676.4, 647.1, 568.2, 530.8 and 514.5 nm laser light. Apart from the Raman spectra (Fig. A2.3), only one other type of spectrum (Fig. A2.4) has been obtained, for all exciting lines of wavelength shorter than 568.2 nm.

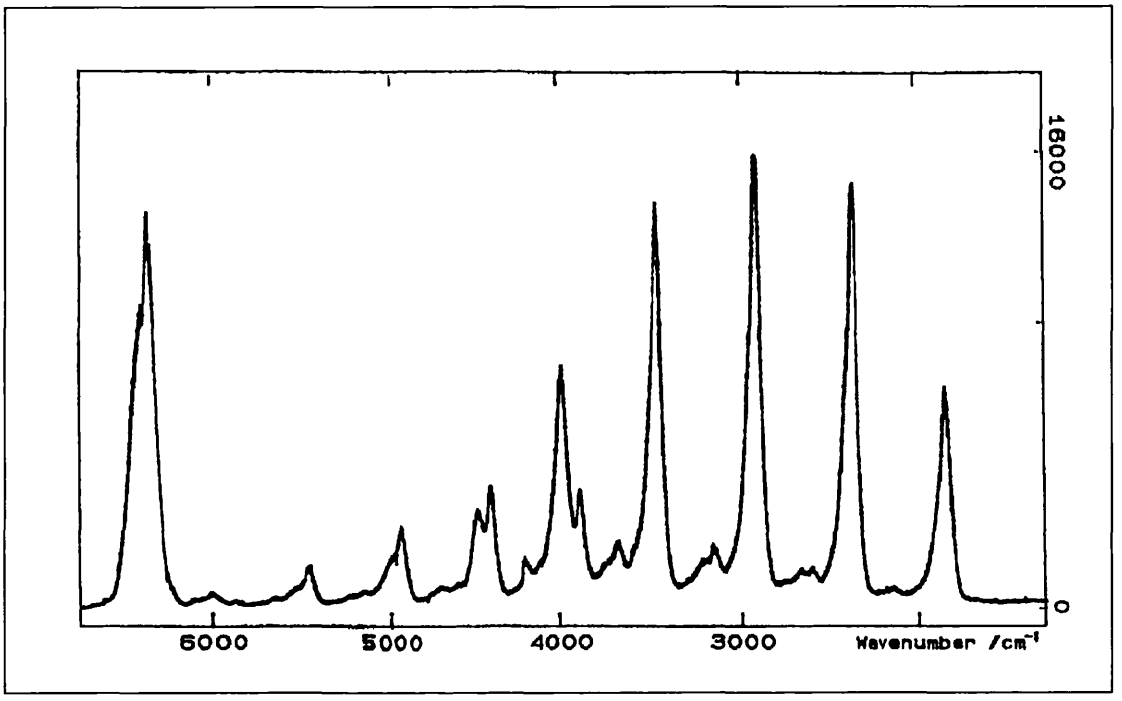

Figure A2.4 - Resonance fluorescence spectrum of a small sulphur cluster (assumed to be an S_4 isomer), trapped in a solid argon matrix excited by the 530.8 nm line of a Kr^+ laser.

Results and discussion

The first experiment gave a good Raman spectrum (Fig. A2.3), showing the main bands reported in the literature [92-98]; the intensity ratios of the 474.2 cm^{-1} versus the 217.2 and 150.5 cm^{-1} bands changes as the excitation wavelength decreases, between 1.6 : 1.6 : 1 at 676.4 nm to 1.4 : 1.4 : 1 at 647.1 nm and 5 : 1.3 : 1 at 530.8 nm. This may indicate that the Raman scattering from S_6 is resonant, removing previous ambiguity [92] in assigning

the 474 cm^{-1} band to S_6 or to S_8. Similarly, the 150 cm^{-1} band is assigned to S_8, ruling out S_7 (see [92]).

The Raman spectrum of the first matrix confirms its composition: mainly S_8, S_7 and S_6 rings and some $S_{>4}^{ch}$ chains. This composition is due to the way the matrix has been deposited, with a high density of sulphur preventing the break-up of the big S_n rings ($5 < n < 9$) and matrix-isolation of the fragments on a large scale; on the contrary, later matrices obtained with a lower concentration of sulphur in the discharge show an increased proportion of small species.

The fluorescence signal obtained by irradiating the matrix with light of 530.8 nm wavelength (Fig. A2.4) consists of 5 different series of peaks from 12830 cm^{-1} to 16990 cm^{-1} (780 to 589 nm), together with a strong feature at about 12550 cm^{-1} (797 nm). The spectra recorded at 514.5, 530.8 and 568.2 nm show a marked increase in the intensity of the respective bands from 514.5 to 530.8 nm and their complete disappearance at 568.2 nm. The intensity of the 12550 cm^{-1} feature, however, is not sensitive to changing the excitation line. While the fluorescence producing the progressions appears to be resonant when excited with 530.8 nm wavelength light, it is clearly not the case with the 797 nm feature. The first part of the signal could be assigned then to one of the S_4 isomers, which absorbs around 530 nm, while the second part remains to be identified.

Conclusions

There are several different methods of preparing the S_n(Ar) matrix suitable for studying small sulphur clusters and both methods used in this study have been proved to be useful; thus the project has provided valuable experience in the technique of matrix isolation of small, unstable species.

Some ambiguities persisting in the literature about the assignment of some Raman bands have been removed by using several excitation lines and

observing the changes in the relative intensity of different bands; the usefulness of Raman spectroscopy is limited, though, by the fact that the S_n(Ar) matrix contains always a mixture of species.

Resonance Raman and resonance fluorescence spectra have been recorded but the UV-VIS spectroscopic data available are not entirely satisfactory for the experiments described here; the UV-VIS spectroscopy of the matrix prior to the resonance experiments would help with the selection of the excitation lines to use. Nonetheless Raman, resonance Raman, and resonance fluorescence have been proven successful in fingerprinting sulphur molecules, as outlined in the introduction of this study.

Appendix 3 - The Manneback equations

The parameters {p, q, r} found in the linear relationship between the raising and lowering operators of two harmonic potential energy curves, the excited state (2) and the ground state (1), need to be related to the two characteristic circular frequencies ω_1 and ω_2 and the relative displacement, Δ, of the minima of the two curves ($\Delta = R_e(2) - R_e(1)$). In 1951 Manneback [103] published key recurrence equations relating the Franck-Condon amplitudes between two harmonic potential energy curves that have different characteristic frequencies ω_1 and ω_2, and displaced minima. The two fundamental formulae, called I and II in [103], are written in the bra/ket notation as

$$\langle b+1|c\rangle = \frac{1}{(b+1)^{1/2}}\left[-b^{1/2}\mathbf{k}_M\langle b-1|c\rangle + c^{1/2}\mathbf{k}_M^{\dagger}\langle b|c-1\rangle - \mathbf{a}_M\langle b|c\rangle\right] \qquad (I)$$

and

$$\langle b|c+1\rangle = \frac{1}{(c+1)^{1/2}}\left[c^{1/2}\mathbf{k}_M\langle b|c-1\rangle + b^{1/2}\mathbf{k}_M^{\dagger}\langle b-1|c\rangle + \mathbf{b}_M\langle b|c\rangle\right] . \qquad (II)$$

The parameters, following the notation from [103], are in bold face and subscripted by "**M**" for Manneback. Equations (2) and (3) of [103] relate these to a measure of the displacement, M, and the two frequencies, according to:

$$\mathbf{a}_M = M\left[\frac{2\omega_1}{\omega_1+\omega_2}\right]^{1/2}, \quad \mathbf{b}_M = M\left[\frac{2\omega_2}{\omega_1+\omega_2}\right]^{1/2},$$
$$\mathbf{k}_M^{\dagger} = \frac{2(\omega_1\omega_2)^{1/2}}{\omega_1+\omega_2}, \quad \mathbf{k}_M = \frac{\omega_1-\omega_2}{\omega_1+\omega_2} . \qquad (A3.1)$$

The dimensionless displacement parameter M is further defined in terms of the actual difference in the location of the harmonic oscillator minima Δ:

$$M = \frac{\Delta}{\lambda}, \quad \text{where } \lambda = \left(\frac{h}{2\pi\mu}\right)^{1/2}\left(\frac{\omega_1+\omega_2}{\omega_1\omega_2}\right)^{1/2} . \qquad (A3.2)$$

Here μ is the reduced mass of the oscillator and the reference distance, λ, is the square root of the average of the mean square displacements of the oscillators in the two potentials. For practical use the units of Δ will be chosen

to be picometers (pm), those of the wavenumber ($\tilde{\nu} = \omega/(2\pi c)$) to be cm^{-1} and those of μ to be atomic mass units (amu) to give:

$$M = 1.7222115 \times 10^{-3}\mu^{1/2}\Delta\left(\frac{\tilde{\nu}_1\tilde{\nu}_2}{\tilde{\nu}_1+\tilde{\nu}_2}\right)^{1/2} . \qquad \text{(A3.3)}$$

Equations I and II will be generated using Eqns (3.31a,b), thereby linking the parameters {*p*, *q*, *r*} to those of [103] and thus relate {*p*, *q*, *r*} to {ω_1, ω_2, Δ}. Given that

$$\hat{a}_2^\dagger = p + q\hat{a}_1^\dagger + r\hat{a}_1 ,$$
$$\hat{a}_2 = p + q\hat{a}_1 + r\hat{a}_1^\dagger , \qquad \text{(A3.4)}$$

with {|b>} the eigenkets of H_2:

$$\hat{a}_2^\dagger|b\rangle = (b+1)^{1/2}|b+1\rangle, \quad \langle b|\hat{a}_2 = (b+1)^{1/2}\langle b+1| ,$$
$$\hat{a}_2|b\rangle = (b)^{1/2}|b-1\rangle, \quad \langle b|\hat{a}_2^\dagger = b^{1/2}\langle b-1| , \qquad \text{(A3.5a)}$$

and similarly with {|c>} the eigenkets of H_1

$$\hat{a}_1^\dagger|c\rangle = (c+1)^{1/2}|c+1\rangle, \quad \langle c|\hat{a}_1 = (c+1)^{1/2}\langle c+1| ,$$
$$\hat{a}_1|c\rangle = (c)^{1/2}|c-1\rangle, \quad \langle c|\hat{a}_1^\dagger = (c-1)^{1/2}\langle c-1| , \qquad \text{(A3.5b)}$$

the matrix element of $\hat{a}_2$ between two arbitrary states b and c can be written, respectively, as

$$\langle b|a_2|c\rangle = (b+1)^{1/2}\langle b+1|c\rangle \qquad \text{(A3.6a)}$$

and

$$\langle b|a_2|c\rangle = \langle b|(p+q\hat{a}_1+r\hat{a}_1^\dagger)|c\rangle$$
$$= p\langle b|c\rangle + c^{1/2}q\langle b|c-1\rangle + (c+1)^{1/2}r\langle b|c+1\rangle \qquad \text{(A3.6b)}$$

or, by eliminating $\langle b|a_2|c\rangle$ between Eqns (A3.6a) and (A3.6b), as

$$(b+1)^{1/2}\langle b+1|c\rangle = p\langle b|c\rangle + c^{1/2}q\langle b|c-1\rangle + (c+1)^{1/2}r\langle b|c+1\rangle . \qquad \text{(A3.7)}$$

Similarly the matrix element of $\hat{a}_2^\dagger$ between two arbitrary states b and c can be written respectively as

$$\langle b|a_2^\dagger|c\rangle = b^{1/2}\langle b-1|c\rangle \qquad \text{(A3.8a)}$$

and

$$\begin{aligned}\langle b|a_2^{\dagger}|c\rangle &= \langle b|(p + q\hat{a}_1^{\dagger} + r\hat{a}_1)|c\rangle \\ &= p\langle b|c\rangle + (c+1)^{1/2}q\langle b|c+1\rangle + c^{1/2}r\langle b|c-1\rangle .\end{aligned} \tag{A3.8b}$$

$\langle b|c+1\rangle$ can be isolated from Eqn (A3.8b) as

$$\langle b|c+1\rangle = \frac{1}{(c+1)^{1/2}}\left[b^{1/2}\left(\frac{1}{q}\right)\langle b-1|c\rangle - c^{1/2}\left(\frac{r}{q}\right)\langle b|c-1\rangle - \left(\frac{p}{q}\right)\langle b|c\rangle\right] \tag{II'}$$

and comparing coefficients of like terms in Eqns (II and II') yields:

$$\mathbf{b_M} = -\frac{p}{q}, \quad \mathbf{k_M^{\dagger}} = \frac{1}{q}, \quad \mathbf{k_M} = -\frac{r}{q} . \tag{A3.9a}$$

Now $\langle b+1|c\rangle$ can be obtained by eliminating $\langle c|b+1\rangle$ between Eqn (A3.7) and Eqn (II') as

$$\langle b+1|c\rangle = \frac{1}{(b+1)^{1/2}}\left[p\frac{q-r}{q}\langle b|c\rangle + c^{1/2}\frac{q^2-r^2}{q}\langle b|c\rangle + b^{1/2}\frac{r}{q}\langle b-1|c\rangle\right]. \tag{I'}$$

Comparing coefficients of like terms in Eqns (I) and (I') yields:

$$\mathbf{a_M} = -p\left(\frac{q-r}{q}\right), \quad \mathbf{k_M^{\dagger}} = \left(\frac{q^2-r^2}{q}\right), \quad \mathbf{k_M} = -\left(\frac{r}{q}\right). \tag{A3.9b}$$

Equations (A3.9a,b) are consistent and with Eqn (A3.1) lead, finally, to

$$p = -M\left[\frac{(\omega_2+\omega_1)}{2\omega_1}\right]^{1/2}, \quad q = \frac{(\omega_2+\omega_1)}{2(\omega_2\omega_1)^{1/2}}, \quad r = \frac{(\omega_2-\omega_1)}{2(\omega_2\omega_1)^{1/2}} \tag{A3.10}$$

and, with Eqn (A3.3),

$$p = -1.2177874 \times 10^{-3}\mu^{1/2}\tilde{\nu}_2^{1/2}\Delta . \tag{A3.11}$$

Based on the expression for r (Eqn (A3.10)), r^2 can be considered small ($r^2 \leq 0.01 \Leftrightarrow r^2 \ll 1$) for a relative frequency change $(\omega_1-\omega_2)/\omega_1 \leq 18.2\%$.

Thus, in Eqns (A3.10,A3.11) the parameters $\{p, q, r\}$, connecting the raising and lowering operators of the excited and ground states, have been expressed in terms of experimentally accessible quantities, ultimately establishing the relationship between the resonance Raman data (ω_1, ω_2) and the molecular structure (μ, Δ).

Appendix 4 - Performance tests for the numerical implementation

The performance is an important factor in establishing a new numerical method and it is one of the aims of the present work to provide an accessible way of obtaining information about molecular structure. As computer implementation can deliver results within a wide performance range, simulation tests have been carried out prior to programming a computer for solving Eqns (3.53a,b, 3.54, 4.2a-c, 4.3a-c, 4.6, 4.7, 4.18), in order to obtain an estimate of the performance to be expected from the program.

The bulk of the computational effort is represented by the calculation of the integral (Eqn (4.18)) and of the polarisability $\alpha_n(\omega)$ for each n = 1,2,3,4 (Eqns (3.53a,b)); the test program has been written to include many operations similar to these tasks, repeated a large number of times through nested loops. The function to be calculated is

$$\sum_{i}^{N} \frac{1}{i} \sum_{j}^{100} \sin\left[\frac{\exp(j\sin(1/j))}{i}\right],$$

where N is the number of outer loops completed in one minute. The program performing the sum above has been compiled in different programming languages and a generic, language-independent version is given below for illustrative purposes:

```
sum = 0
for i = 1 to 50000
     for j = 1 to 100
          sum = sum + ( ( sin( j * exp(sin(1/j) )/i ) /i)
     next j
print i
next i .
```

The results of running the test program on different machines, after recompilation and optimisation, are presented in Table A4.1.

Table A4.1

Performance of different computer systems (in program loops per minute).

Language	IBM PC compatible computers, Intel microprocessors			Sun workstation
	i286	i386SX25+i387	i486DX33	Sparc 5
BASIC	65	1200	1900	n/a
FORTRAN	75	2400	5200	n/a
C	350	3000	7000	16500

The results show that, apart from a marked increase in performance with the power of the hardware, the choice of computer programming language makes a significant difference in the speed of the calculation. Thus, the programs used in implementing the transform method in this thesis have been written in C and run on the hardware available then. As hardware becomes more powerful, the portability of programs written in C ensures that this implementation will not be made obsolete prematurely by the technological progress in computer hardware.

Appendix 5 - Transform program

The program used in Chapter 5 to solve Eqns (4.1a-d) and obtain the parameters $\Delta, \tilde{\nu}_e, m$ for different chemical systems is included here for reference purposes; some of its routines have been included in other programs, used in fitting experimental Raman Excitation Profiles and Resonance Raman spectra.

```
#include <math.h>
#include <stdio.h>
#include <stdlib.h>
#include <string.h>
#include <dos.h>

struct abs {
      int n;
      double x[3000], y[3000], ra[8], ia[8], dfr, xi, m;
      double xi2, mx, dxi2, step, ni, ne;    };

int main(int argc, char *argv[])
{     FILE *stream;
      struct abs absorp, *a = &absorp;
      struct date d;
      struct time t;
      int i;
      char data[30], absorption[30], search[30], output[30];
      char *string;
      void trans(struct abs *);
      double alpha1(struct abs *), alpha2(struct abs *);
      double alpha3(struct abs *), alpha4(struct abs *);
      double miu_r, ct, nr, dsp, rt1, rt21, rt31, rt41;
      double y1, y21, y31, y41, X1, Xm = 1.0;
      double m_min, dsp_min, ne_min, m_max, dsp_max, ne_max;
      double dm, dd, dn, ymin = 1.0, nc = 0;
      strcpy(data, argv[1]);
      strcat(data,"41.dat");
      strcpy(absorption, argv[1]);
      strcat(absorption,".abs");
      strcpy(search, argv[1]);
```

```
strcat(search,".src");
strcpy(output, argv[1]);
strcat(output,"6.out");

stream     = fopen(data, "r");
miu_r      = atof(fgets(string, 10, stream));
nr         = atof(fgets(string, 10, stream));
a->ni      = atof(fgets(string, 10, stream));
y1         = atof(fgets(string, 10, stream));
y21        = atof(fgets(string, 10, stream))/y1;
y31        = atof(fgets(string, 10, stream))/y1;
y41        = atof(fgets(string, 10, stream))/y1;
ct         = (-0.0002435574) * sqrt(miu_r * nr);
fclose(stream);

stream     = fopen(absorption, "r");
a->n       = atoi(fgets(string, 20, stream)) - 1;
for (i = 0; i <= a->n; i++) {
     a->x[i] = atof(fgets(string, 20, stream));
     a->y[i] = atof(fgets(string, 20, stream));
     if (ymin >= a->y[i])  ymin = a->y[i];
}
for (i = 0; i < a->n; i++)
     nc = nc + (a->y[i+1] + a->y[i]) *
                      (a->x[i+1] - a->x[i]) / 2;
nc = nc - ymin * (a->x[a->n] - a->x[0]);
for (i = 0; i <= a->n; i++)
     a->y[i] = a->y[i]/a->x[i]/nc;
fclose(stream);

stream     = fopen(search, "r");
m_min      = atof(fgets(string, 9, stream));
dsp_min    = atof(fgets(string, 9, stream)) + 0.00001;
ne_min     = atof(fgets(string, 9, stream)) + 0.00001;
m_max      = atof(fgets(string, 9, stream));
dsp_max    = atof(fgets(string, 9, stream));
ne_max     = atof(fgets(string, 9, stream));
dm         = atof(fgets(string, 9, stream));
dd         = atof(fgets(string, 9, stream));
dn         = atof(fgets(string, 9, stream));
fclose(stream);
```

```
stream = fopen(output, "a");
getdate(&d);
gettime(&t);
fprintf(stream,"\t%d. %d. %d\t%d:%02d\n",
      d.da_day,d.da_mon,d.da_year,t.ti_hour,t.ti_min);
fprintf(stream,"n0 = %.1f\tnmax = %.1f\tdn = %.1f\n",
      ne_min, ne_max, dn);
fprintf(stream,"d0 = %.2f\tdmax = %.2f\tdd = %.2f\n",
      dsp_min, dsp_max, dd);
fprintf(stream,"m0 = %.3f\tmmax = %.3f\tdm = %.3f\n",
      m_min, m_max, dm);
puts("calculating...");

char *outformat = "%.1f\t%.1f\t%.3f\t%.7f\n";
a->ne = ne_min;
while (a->ne <= ne_max) {
      a->dfr = (a->ne - nr)/(a->ne + nr);
      trans(a);
      dsp = dsp_min;
      while (dsp <= dsp_max) {
            a->xi = ct * dsp * a->ne/(a->ne + nr);
            a->xi2 = a->xi * a->xi;
            a->dxi2 = a->dfr * a->xi2;
            a->m = m_min;
            while (a->m <= m_max) {
                  a->mx = a->m * a->xi;
                  rt1  = alpha1(a);
                  rt21 = alpha2(a)/rt1 - y21;
                  rt31 = alpha3(a)/rt1 - y31;
                  rt41 = alpha4(a)/rt1 - y41;
                  X1 = rt21 * rt21 + rt31 * rt31 +
                                          rt41 * rt41;
                  if (X1 < Xm) {
                        Xm = X1;
                        printf("%.5f\t", X1);
                        fprintf(stream,outformat,
                                    a->ne,dsp,a->m,X1);
                  }
                  a->m = a->m + dm;
            }
            dsp = dsp + dd;
```

```
            }
            a->ne = a->ne + dn;
      }
      gettime(&t);
      fprintf(stream,"\t-------%d:%02d--------\n",
            t.ti_hour,t.ti_min);
      fclose(stream);
      return 0;
}
double alpha1(struct abs *a)
{     double re, im, c0, c1, c2;
      c0 = a->m - a->xi;
      c1 = a->xi * (1 - a->dfr) + a->m;
      c2 = a->dfr * a->xi;
      re = a->ra[2] * c2 + a->ra[1] * c1 + a->ra[0] * c0;
      im = a->ia[2] * c2 + a->ia[1] * c1 + a->ia[0] * c0;
      return (re * re + im * im);
}
double alpha2(struct abs *a)
{     double re, im, c0, c1, c2, c3;
      c0 = a->xi2 - 2 * a->mx - a->dfr;
      c1 = 2 * (a->dxi2  - a->xi2);
      c2 = a->xi2 - 4 * a->dxi2 + 2 * a->mx + a->dfr;
      c3 = 2 * a->dxi2;
      re = a->ra[3] * c3 + a->ra[2] * c2 + a->ra[1] * c1 +
            a->ra[0] * c0;
      im = a->ia[3] * c3 + a->ia[2] * c2 + a->ia[1] * c1 +
            a->ia[0] * c0;
      return ((re * re + im * im)/2);
}
double alpha3(struct abs *a)
{     double re, im, c0, c1, c2, c3, c4;
      c0 = 3 * (a->mx + a->dfr) - a->xi2;
      c1 = 3 * (a->xi2 - a->dxi2 - a->mx - a->dfr);
      c2 = - 3 * (a->xi2 - 3 * a->dxi2 + a->mx + a->dfr);
      c3 = a->xi2 - 9 * a->dxi2 + 3 * (a->mx + a->dfr);
      c4 = 3 * a->dxi2;
      re = a->ra[4] * c4 + a->ra[3] * c3 + a->ra[2] * c2 +
            a->ra[1] * c1 + a->ra[0] * c0;
      im = a->ia[4] * c4 + a->ia[3] * c3 + a->ia[2] * c2 +
            a->ia[1] * c1 + a->ia[0] * c0;
```

```
      return (a->xi2 * (re * re + im * im)/6);
}
double alpha4(struct abs *a)
{     double re, im, c0, c1, c2, c3, c4, c5;
      c0 = a->xi2 - 4 * a->mx - 6 * a->dfr;
      c1 = - 4 * (a->xi2 - a->dxi2 - 2 * a->mx - 3 * a->dfr);
      c2 = 6 * a->xi2 - 16 * a->dxi2;
      c3 = - 4 * (a->xi2 - 6 * a->dxi2 + 2 * a->mx + 3 * a->dfr);
      c4 = a->xi2 - 16 * a->dxi2 + 4 * a->mx + 3 * a->dfr;
      c5 = 4 * a->dxi2;
      re = a->ra[5] * c5 + a->ra[4] * c4 + a->ra[3] * c3 +
            a->ra[2] * c2 + a->ra[1] * c1 + a->ra[0] * c0;
      im = a->ia[5] * c5 + a->ia[4] * c4 + a->ia[3] * c3 +
            a->ia[2] * c2 + a->ia[1] * c1 + a->ia[0] * c0;
      return (a->xi2 * a->xi2 * (re * re + im * im)/24);
}
void trans(struct abs *a)
{     int i, j, j1, j2, j3;
      double ac, bc, cc, en;
      for (i = 0; i <= 5; i++)
      {     j = 0;
            a->ra[i] = 0;
            en = a->ni - i * a->ne;
            while (a->x[j+2] < en) {
                  j1 = j + 1;
                  a->ra[i] = a->ra[i] + (a->y[j1] * (en - a->x[j])
                              + a->y[j] * (a->x[j1] - en))/
                              (a->x[j1] - a->x[j]) *
                              log((en - a->x[j1])/(en - a->x[j]));
                  j = j1;
            }
            j2 = j + 2;
            j3 = j + 3;
            ac = ((a->y[j3] - a->y[j])/(a->x[j3] - a->x[j]) -
                  (a->y[j2] - a->y[j])/(a->x[j2] - a->x[j]))/
                        (a->x[j3] - a->x[j2]);
            bc = (a->y[j3] - a->y[j])/(a->x[j3] - a->x[j]) -
                  ac * (a->x[j3] + a->x[j]);
            cc = a->y[j] - bc * a->x[j] - ac * a->x[j] * a->x[j];
            a->ia[i] = ac * en * en + bc * en + cc;
            a->ra[i] = a->ra[i] + ac * (a->x[j3] * a->x[j3] -
```

```
                    a->x[j] * a->x[j])/2 +
                    (ac * en + bc) * (a->x[j3] - a->x[j]);
          a->ra[i] = a->ra[i] + a->y[a->n] - a->y[j3] + a->y[j]
                    - a->y[0] + a->ia[i] *
                    log((a->x[j3] - en)/(en - a->x[j]));
          j = j3;
          while (j < a->n) {
               j1 = j + 1;
               a->ra[i] = a->ra[i] + (a->y[j1] * (en - a->x[j])
                         + a->y[j] * (a->x[j1] - en))/
                         (a->x[j1] - a->x[j])
                         * log((en - a->x[j1])/(en - a->x[j]));
               j = j1;
          }
          a->ra[i] = a->ra[i]/3.14;
     }
}
```

References

[1] J. H. Van Vleck, *Proc. Natl. Acad. Sci. U.S.* **15**, 754 (1929).

[2] G. Placzek. In E. Marx (ed.), *Handbuch der Radiologie*, Vol. 6, Akademische Verlagsgesellschaft, Leipzig, 1934, Pt. 2, p. 205.

[3] H. Eyring, J. Walter and G. E. Kimball, *Quantum Chemistry*, Wiley(Interscience), New York, 1944.

[4] L. I. Schiff, *Quantum Mechanics*, McGraw-Hill, New York, 1955.

[5] A. Messiah, *Mechanique Quantique*, Dunod, Paris, 1965.

[6] W. Heitler, *The Quantum Theory of Radiation*, Oxford University Press, London and New York, 1954.

[7] W. H. Louisell, *Quantum Statistical Properties of Radiation*, Wiley(Interscience), New York, 1973.

[8] R. J. H. Clark and T. J. Dines, *J. Chem. Soc., Faraday Trans. 2*, **78**, 723 (1982).

[9] R.J.H. Clark, T.J. Dines and J.M. Doherty, *Inorg. Chem.*, **24**, 2088 (1985).

[10] R.J.H. Clark, T.J. Dines and G.P. Proud, *J. Chem. Soc. Dalton Trans.* 2019 (1983).

[11] D. F. Shriver and J. B. R. Dunn, *Appl. Spectrosc.*, **28**, 319 (1974).

[12] T. C. Strekas, D. H. Adams, A. Packer and T. G. Spiro, *Appl. Spectrosc.*, **28**, 324 (1974).

[13] W. Kiefer and H. J. Bernstein, *Mol. Phys.*, **23**, 31 (1972).

[14] W. Kiefer and H. J. Bernstein, *Appl. Spectrosc.*, **25**, 500 (1971).

[15] W. Kiefer and H. J. Bernstein, *Appl. Spectrosc.*, **25**, 609 (1971).

[16] R. J. H. Clark. In R. J. H. Clark and R. E. Hester (eds.), *Advances in Infrared and Raman Spectroscopy*, Vol. 1, Heyden, London, 1975.

[17] H. S. Gold, *Appl. Spectrosc.*, **66**, 649 (1970).

[18] G. H. Atkinson. In R. J. H. Clark and R. E. Hester (eds.), *Advances in Infrared and Raman Spectroscopy*, Vol. 9, Heyden, London, 1982.

[19] S. Howdle and S. P. Best, personal communication.

[20] F. W. Byron and R. W. Fuller, *Mathematics of Classical and Quantum*

Physics, Addison-Wesley, London, 1970.

[21] N. Bloembergen, *Nonlinear Optics*, Benjamin, New York, 1965.

[22] D. L. Huber, *Phys. Rev.* **158**, 843 (1967).

[23] D. L. Huber, *Phys. Rev.* **170**, 418 (1968).

[24] Y. R. Shen, *Phys. Rev. B* **9**, 622 (1974).

[25] P. M. Champion and R. Lange, *J. Chem. Phys.* **73**, 5947 (1980).

[26] D. Lee and A. C. Albrecht. In R. J. H. Clark and R. E. Hester (eds.), *Advances in Infrared and Raman Spectroscopy*, Vol. 12, Wiley Heyden, London (1985).

[27] S. H. Lin and H. Eyring, *Proc. Natl. Acad. Sci. U.S.A.* **74**, 3623 (1977).

[28] S. H. Lin and H. Eyring, *Proc. Natl. Acad. Sci. U.S.A.* **74**, 3105 (1977).

[29] Y. Fujimura and S. H. Lin, *J. Chem Phys.* **70**, 247 (1979).

[30] Y. Fujimura and S. H. Lin, *J. Chem Phys.* **71**, 3733 (1979).

[31] L. D. Ziegler, *Acc. Chem. Res.* **27**, 1 (1994).

[32] S. H. Lin, Y. Fujimura, H. J. Neusser and E. W. Schlag, *Multiphoton Spectroscopy of Molecules*, Academic Press, London, 1984.

[33] U. Fano. In E. R. Caianiello (ed.), *Lectures on the Many-Body Problem*, Vol. 2, Academic Press, New York, 1964.

[34] R. Zwanzig. In P. H. E. Meijer (ed.), *Quantum Statistical Mechanics*, Gordon-Breach, New York, 1966.

[35] Y. Fujimura and S. H. Lin, *J. Chem Phys.* **74**, 3726 (1981).

[36] G. Stock and W. Domcke, *J. Chem. Phys.* **93**, 5496 (1990).

[37] Y. Fujimura, H. Kono, T. Nakajima and S. H. Lin, *J. Chem Phys.* **75**, 99 (1981).

[38] R. L. Kronig, *J. Opt. Soc. Amer.* **12**, 547 (1926).

[39] H. D. Kramers, *Atti. Congr. Int. Fis.* **2**, 545 (1927).

[40] D. L. Tonks and J. B. Page, *Chem. Phys. Lett.* **66**, 449 (1979).

[41] S. Hassing and O. Sonnich Mortensen, *J. Chem. Phys.* **73**, 1078 (1980).

[42] P. M. Champion and A. C. Albrecht, *Chem. Phys. Lett.* **82**, 410 (1981).

[43] D. L. Tonks and J. B. Page, *Chem. Phys. Lett.* **79**, 247 (1981).

[44] H. M. Lu and J. B. Page, *Chem. Phys. Lett.* **131**, 87 (1986).

[45] H. M. Lu and J. B. Page, *J. Chem. Phys.* **88**, 3508 (1988).

[46] H. M. Lu and J. B. Page, *J. Chem. Phys.* **90**, 5315 (1989).

[47] I. J. Tehver, *Opt. Commun.* **38**, 279 (1981).

[48] C. K. Chan, *J. Chem. Phys.* **81**, 1614 (1984).

[49] J. R. Cable and A. C. Albrecht, *J. Chem. Phys.* **84**, 4745 (1986).

[50] D. L. Tonks and J. B. Page, *J. Chem. Phys.* **76**, 5820 (1982).

[49] B. Khodadoost, S. A. Lee, J. B. Page and R. C. Hanson, *Phys. Rev. B* **38**, 5288 (1988).

[50] H. M. Lu and J. B. Page, *J. Chem. Phys.* **92**, 7038 (1990).

[51] D. L. Tonks and J. B. Page, *J. Chem. Phys.* **88**, 738 (1988).

[52] V. Hizhnyakov and I. Tehver, *J. Raman Spectrosc.* **19**, 383 (1988).

[53] A. C. Albrecht, *J. Chem. Phys.* **34**, 1476 (1961).

[54] V. V. Hizhnyakov and I. Tehver, *Phys. Stat Sol.* **21**, 755 (1967).

[55] B. R. Stallard, P. M. Champion, P. R. Callis and A. C. Albrecht, *J. Chem. Phys.* **78**, 712 (1983).

[56] R. Friessner, M. Pettitt and J. M. Jean, *J. Chem. Phys.* **82**, 2918 (1984).

[57] C. K. Chan and J. B. Page, *J. Chem. Phys.* **79**, 5234 (1983).

[58] C. K. Chan and J. B. Page, *Chem. Phys. Lett.* **104**, 609 (1984).

[59] D. J. Tannor and E. J. Heller, *J. Chem. Phys.* **77**, 202 (1982).

[60] A. C. Albrecht, R. J. H. Clark, D. Oprescu, S. J. R. Owens and C. Svendsen, *J. Chem. Phys.* **101**, 1890 (1994).

[61] P. Li and P. M. Champion, *J. Chem. Phys.* **88**, 761 (1988).

[62] J. Cable and A. C. Albrecht, *J. Chem. Phys.* **84**, 1969 (1986).

[63] J. B. Page. In M. Cardona and G. Guntherodt (eds.), *Light Scattering in Solids VI*, Springer, Berlin and New York, 1991, p 17-72.

[64] J. M. Ortega and W. C. Rheinboldt, *Iterative Solution of Nonlinear Equations in Several Variables*, Academic Press, London, 1970.

[65] W. H. Press, S. A. Teukolsky, W. T. Vettering and B. P. Flannery, *Numerical Recipes in C,* Cambridge University Press, Cambridge, 1992.

[66] S. Wolfram, *Mathematica*, Addison-Wesley, Redwood City, California, 1991.

[67] D. Oprescu, *in preparation.*

[68] S.-Y. Lee and E. J. Heller, *J. Chem. Phys.* **71**, 4777 (1979).

[69] E. J. Heller, *Acc. Chem. Res.* **14**, 368 (1981).

[70] R.J.H. Clark and D. Oprescu, *in preparation.*

[71] R. J. H. Clark and B. Stewart, *J. Am. Chem. Soc.*, **103**, 6593 (1981).

[72] R. J. H. Clark, T. J. Dines and M. L. Wolf, *J. Chem. Soc., Faraday Trans. 2*, **78**, 679, (1982).

[73] R. J. H. Clark and T. J. Dines, *Chem. Phys.* **70**, 269 (1982).

[74] R. J. H. Clark and T. J. Dines, *Chem. Phys.* Lett. **64**, 499 (1979).

[75] R. J. H. Clark and T. J. Dines, Inorg. Chem. **19**, 1681 (1980).

[76] R.J.H. Clark and P.D. Mitchell, J. Am. Chem. Soc., **95**, 8300, 1973.

[77] *Tables of Interatomic Distances and Configuration in Molecules and Ions*, L. E. Sutton (ed.), The Chemical Society, London, 1958.

[78] *Handbook of Chemistry and Physics, 73rd edition 1992-1993*, D. R. Lide (ed.), CRC Press, London, 1992, p.9-15 - 9-41.

[79] T. J. Dines, *Spectrochimica Acta A*, **44**, 1087 (1988).

[80] M. C. C. Ribeiro, W. J. Barreto, M. L. A. Temperini and P. S. Santos, *J. Phys. Chem.* **97**, 12153 (1993).

[81] R. J. H. Clark, A. J. Hempleman and D. A. Tocher, *J. Am. Chem. Soc.* **110**, 5968 (1988).

[82] R. J. H. Clark and A. J. Hempleman, *J. Chem. Soc., Dalton Trans.* 2601 (1988).

[83] R. J. H. Clark and A. J. Hempleman, *Inorg. Chem.*, **27**, 2225 (1988).

[84] J. R. Schoonover, D. F. Dallinger, P. M. Killough, A. P. Sattelberger and W. H. Woodruff, *Inorg. Chem* **30**, 1093 (1991).

[85] S. B. Piepho, E. R. Krausz and P. N. Schatz, *J. Am. Chem. Soc.* **100**, 2996 (1978).

[86] K. Prassides and P. N. Schatz, *J. Phys. Chem.* **93**, 8387 (1989).

[87] K. Prassides and P. N. Schatz, *Chem. Phys. Lett.* **178**, 227 (1991).

[88] M. Kurmoo, *PhD Thesis*, University of London, 1983.

[89] K. L. Brown and D. Hall, *Acta Cryst.* **B32**, 279 (1976).

[90] H. Endres, H. J. Keller, R. Martin and S. Notzel, *Z. Naturforsch.* **35b**,1274 (1980).

[91] H. Endres, H. J. Keller, R. Martin, U. Traeger and N. Novotny, *Acta Cryst.* **B36**, 35 (1980).

[92] P. Lenain, E. Picquenard, J. Corset, D. Jensen and R. Steudel, *Berliner Bunsenges. Phys. Chem.* **92**, 859 (1988).

[93] P. Lenain, E. Picquenard, J. Lesne and J. Corset, *J. Mol. Struct.* **142**, 355 (1988).

[94] R. J. H. Clark and D. G. Cobbold, *Inorg. Chem.* **17**, 3169 (1978).

[95] R. J. H. Clark, T. J. Dines and M. Kurmoo, *Inorg. Chem.* **22**, 2766 (1983).

[96] A. G. Hopkins, S.-Y. Tang and C. W. Brown, *J. Am. Chem. Soc.* **96**, 3486 (1973).

[97] S.-Y. Tang and C. W. Brown, *Inorg. Chem.* **14**, 2856 (1975).

[98] L. Andrews, G. D. Brabson and Z. Mielke, *J. Phys. Chem.* **95**, 79 (1991).

[99] B. Meyer, T. Stroyer-Hansen and T. V. Oommen, *J. Mol. Spectrosc.* **42**, 335 (1972).

[100] B. Meyer and T. Stroyer-Hansen, *J. Phys. Chem.* **76**, 3968 (1972).

[101] J. Kao, *J. Inorg. Chem.* **16**, 2085 (1977).

[102] D. Hohl, R. O. Jones, R. Carr and M. Parrinello, *J. Chem. Phys.* **89**, 6823 (1988).

[103] C. Manneback, *Physica* **17**, 1001 (1951).